Department of Chemistry, University College London,
20 Gordon Street, London, WC1H 0AJ, U.K.

Macrocycle-Functionalised SERS Substrates for Sensing Applications

by

Weng I Katherine Chio

A thesis submitted in fulfilment for the degree of Doctor of Philosophy
at University College London (UCL)

July 2020

Declaration

I, Weng I Katherine Chio, confirm that the work presented in this thesis is my own. Where information has been derived from other sources, I confirm that this has been indicated in the thesis.

Abstract

Hierarchical aqueous self-assembly of gold nanoparticles (Au NPs) triggered by macrocyclic molecules, cucurbiturils (CBs), provides a facile method to fabricate surface-enhanced Raman spectroscopy (SERS) substrates for potential applications in homeland security, environmental monitoring, therapeutic drug monitoring and disease diagnostics. In contrast to conventional techniques which suffer from non-specificity and false signals, the Au NP: CB SERS system offers numerous advantages for on-site detection such as high sensitivity, selectivity, reproducibility, cost-effectiveness and minimal sample preparation. The molecular recognition in the system is mediated by a combination of CB host-guest complexation and formation of precise nanojunctions between Au NPs, leading to very strong and reproducible SERS signals. Herein, supramolecular chemistry between CBs and various attractive analyte targets including explosives (2,4-dinitrotoluene, DNT), drugs (methylxanthines, MeX) and biomarkers (creatinine, CRN) was investigated using experimental and computational approaches to quantify the key binding parameters for the subsequent SERS studies. The host-guest complexes can be used to modify the aggregation kinetics of the Au NP: CB nanoaggregates meanwhile bulky guests can be quantified in the SERS system with highly reproducible signals when they are just positioned in close proximity to the plasmonic nanojunctions. The ability of the SERS system to differentiate structurally similar molecules has been verified by multiplexed detection of isomers while the tolerance against possible signal perturbation from background molecules has been investigated in synthetic urine. This research has provided new fundamental insights into the Au NP: CB SERS system and demonstrated its potential to be extended to multiplexed detection of analyte targets in complex media, thus paving the way towards in-field and point-of-care applications.

Impact statement

Current challenges in terrorism, pollution and healthcare facing the contemporary societies have continuously driven the development of high-performance sensors in academic and industrial research around the world. This research has provided new fundamental insights into a promising surface-enhanced Raman spectroscopy (SERS) sensing platform based on aqueous self-assembly of gold nanoparticles (Au NPs) mediated by macrocycles, cucurbiturils (CBs), and explored the potential applications in homeland security, environmental monitoring, therapeutic drug monitoring and disease diagnostics.

In particular, the Au NP: CB nanoaggregates could be dual-triggered by the electrostatic effects of analyte targets in addition to the usual carbonyl portal binding of CBs, implying that the aggregation kinetics can be modified by the host-guest complexes between CBs and analyte targets, and thus allowing new possibilities in the design of the SERS system. The scenario of bulky guests in the Au NP: CB SERS system, which has not been properly addressed in previous studies, was clarified in our work, meanwhile the relatively rare neutral host-guest complexation would extend the range of attractive analyte targets available for this system. Multiplexed detection of isomers has also been successfully demonstrated, which could be easily extended to a wide range of structurally similar molecules. Our findings would potentially impact the subsequent research in relevant fields such as supramolecular chemistry, SERS and nanosensors.

In a nutshell, this research has set very promising examples in utilising the Au NP: CB SERS system towards real sample testing or applications in real environments that could be potentially achieved in the next few years, whereas commercialisation might also be possible in the long run.

Acknowledgements

I would like to express my deepest gratitude to my principal supervisor, Dr. Tung Chun John Lee, for his guidance, insightful advice and massive support throughout my PhD. Without his profound knowledge and patience, this research would not be possible. Of particular mention, I very much appreciate his contributions to the TEM images and the computational studies. I would like to extend my deepest gratitude to my co-supervisor, Prof. Ivan Parkin, for his extensive knowledge, patient guidance, encouragement and support along these four years. I am extremely grateful to my supervisor in SBIC, Prof. Malini Olivo, for her valuable advice, encouragement and guidance during the very enjoyable two-year attachment in Singapore. Many thanks to the Studentship funded by the A*STAR-UCL Research Attachment Programme through the EPSRC M3S CDT.

I am very grateful to all former and current members of the research groups of Dr. Lee and Prof. Parkin for their practical contributions and generous discussions, in particular, Dr. William Peveler for the CB synthesis, Dr. Suresh Moorthy for the NMR measurements of nitroexplosives and biomarkers, and Ms Jia Liu for the NMR measurements of drugs. I would like to extend my thanks to other members of UCL Chemistry, Dr. Steve Firth for his patience in providing SERS and TEM support, Dr. Senio Campos de Souza for his assistance in DLS and Dr. Zhimei Du for her continuous support on CDT-related matters.

I must thank all members of LBOI in SBIC for their helpful advice and practical suggestions, particularly Dr. Dinish U. S. and Dr. Jayakumar Perumal for their unparalleled knowledge and support on SERS, Mr. Douglas Goh for his kind assistance in laboratory-related matters, Dr. Dave Wong for his willingness to share resources and experiences. Thanks should also go to the administrative staffs of SBIC, Ms Wendy Kan and Ms Jenny See, for their assistance and friendliness.

I gratefully acknowledge our collaborators, Dr. Khaleel Assaf and Prof. Werner Nau, for the UV-Vis titrations and ITC measurements of nitroexplosives.

I also wish to thank my family, especially my parents and sister, and friends for their love, support and encouragement through all the ups and downs during my PhD, and my cat for accompanying me during the write-up process.

Table of Contents

List of Publications

1. Chio, W.-I. K.; Davison, G.; Jones, T.; Liu, J.; Parkin, I. P.; Lee, T.-C. Quantitative SERS Detection of Uric Acid via Formation of Precise Plasmonic Nanojunctions within Aggregates of Gold Nanoparticles and Cucurbit[*n*]uril. *J. Vis. Exp.* **2020**. (Accepted)

2. Chio, W.-I. K.; Moorthy, S.; Perumal, J.; Dinish, U. S.; Parkin, I. P.; Olivo, M.; Lee, T.-C. Dual-Triggered Nanoaggregates of Cucurbit[7]uril and Gold Nanoparticles for Multi-Spectroscopic Quantification of Creatinine in Urinalysis. *J. Mater. Chem. C.* **2020**, *8*, 7051−7058.

3. Chio, W.-I. K.; Peveler, W. J.; Assaf, K. I.; Moorthy, S.; Nau, W. M.; Parkin, I. P.; Olivo, M.; Lee, T.-C. Selective Detection of Nitroexplosives Using Molecular Recognition within Self-Assembled Plasmonic Nanojunctions. *J. Phys. Chem. C* **2019**, *123*, 15769–15776. (Front cover)

4. Peveler, W. J.; Jia, H.; Jeen, T.; Rees, K.; Macdonald, T. J.; Xia, Z.; Chio, W.-I. K.; Moorthy, S.; Parkin, I. P.; Carmalt, C. J.; et al. Cucurbituril-Mediated Quantum Dot Aggregates Formed by Aqueous Self-Assembly for Sensing Applications. *Chem. Commun.* **2019**, *55*, 5495–5498.

5. Ellis, E.; Moorthy, S.; Chio, W.-I. K.; Lee, T.-C. Artificial Molecular and Nanostructures for Advanced Nanomachinery. *Chem. Commun.* **2018**, *54*, 4075–4090. (Feature article, front cover)

List of Abbreviations

5HT	Serotonin
AAO	Anodic alumina oxide
$AdNH_2$	Adamantylamine
Au NP	Gold nanoparticle
CAF	Caffeine
CARS	Coherent anti-Stokes Raman spectroscopy
CB	Cucurbituril
CD	Cyclodextrin
CE	Crown ether
CHEM	Chemical
CRN	Creatinine
CTAB	Cetyltrimethylammonium bromide
CTAC	Cetyltrimethylammonium chloride
CX	Calixarene
DA	Dopamine
DAS	Diaminostilbene
DFT	Density functional theory
DLS	Dynamic light scattering
DMF	Dimethylformamide
DNT	2,4-dinitrotoluene
EC-SERS	Electrochemical surface-enhanced Raman spectroscopy
EF	Enhancement factor
EG	Ethylene glycol

EM	Electromagnetic
EMIT	Enzyme multiplied immunoassay technique
EPI	Epinephrine
HPLC	High-performance liquid chromatography
IR	Infrared
ITC	Isothermal titration calorimetry
LSPR	Localised surface plasmon resonance
Mag	Magnetic
MBA	Mercaptobenzonic acid
MD	Molecular dynamics
MeX	Methylxanthines
MPBA	Mercaptopheylboronic acid
MV	Methyl viologen
NC	Nanocube
NMR	Nuclear magnetic resonance
NNP	Nanogapped nanoparticle
NPoM	Nanoparticles on mirror geometry
NR	Nanorod
NS	Nanostar
NT	Nanotriangle
PA	Picric acid
PAH	Polyaromatic hydrocarbon
PC	Packing coefficient
PDA	Polydopamine
PIERS	Photo-induced enhanced Raman spectroscopy

PMMA	Poly(methylmethacrylate)
PVP	Poly(vinyl pyrrolidone)
R6G	Rhodamine 6G
RRS	Resonance Raman spectroscopy
RS	Raman spectroscopy
SEROA	Surface-enhanced Raman optical activity
SERS	Surface-enhanced Raman spectroscopy
SHINERS	Shell-isolated nanoparticle-enhanced Raman spectroscopy
SNR	Signal-to-noise ratio
SPR	Surface plasmon resonance
SU	Synthetic urine
TBR	Theobromine
TCB	1a,2a,3b,4b-tetrakis(4-aminophenyl)cyclobutane
TEM	Transmission electron microscopy
TERS	Tip-enhanced Raman spectroscopy
TNT	2,4,6-trinitrotoluene
TPH	Theophylline

List of Figures

List of Tables

Chapter 1. Introduction and Literature Review

This Chapter first provided insights into the motivations of the research, followed by the introduction of the fundamental knowledge and critical review of the current developments in the relevant fields. The objectives of the research and thesis structure were given in the latter part of this Chapter.

1.1 Motivations

The growing demand for trace detection of explosives, environmental pollutants, drugs and biomarkers in different fields including homeland security, environmental monitoring, on-site healthcare monitoring and early disease diagnostics, has driven the continuous development of academic and industrial research for high-performance sensors to tackle real-world problems. Conventional techniques for rapid detection of small molecules mainly rely on colourimetry, immunoassay and ion mobility of the species, which suffer from non-specificity and are prone to false signals. In contrast, surface-enhanced Raman spectroscopy (SERS) is a promising analytical technique that offers a good combination of merits for on-site detection, including high sensitivity and selectivity, rapid response, cost-effectiveness, portability, ease-of-use, minimal sample preparation and wider information window. However, the existing SERS substrates often face a dilemma of complicated fabrication procedures and low signal reproducibility which hinders the practical applications of the SERS sensors.

Aqueous self-assembled nanoaggregates of gold nanoparticles (Au NPs) and cucurbit[*n*]urils (CBs) initially reported by Lee and Scherman[1] provides a facile method to fabricate SERS substrates with precise plasmonic nanojunctions, which leads to very strong and reproducible SERS signals. While there have been a few illustrative examples[2–5] exploiting the Au NP: CB nanoaggregates for SERS studies, the fundamental science and the potential applications of the Au NP: CB SERS system remain largely unexplored. For instance, "Can it detect weaker CB guests?", "What happens if there are stronger binders of CB or Au NPs?", "How does the CB cavity size affect molecular recognition?", "Can it detect structurally similar molecules simultaneously?", "How do the encapsulated guests affect the self-assembly of the Au NP: CB nanoaggregates?", "Can it detect analyte molecules in a complex matrix?" and "What are the potential future applications?".

Herein, highly reproducible SERS substrates (i.e. Au NP: CB nanoaggregates) were fabricated to investigate the quantitative detection of various small molecules via CB host-guest complexation and formation of precise plasmonic nanojunctions within the nanoaggregates, with the aim to provide new fundamental insights into the Au NP: CB SERS system and explore the potential field and clinical applications.

1.2 Current sensing techniques

Numerous analytical techniques have been developed for qualitative and quantitative detection of small molecules in practical applications, however, most of them fail to offer a combination of advantages such as rapid response, high sensitivity, specificity, cost-effectiveness, portability and ease-of-use. In the following, the current techniques for the detection of analyte molecules studied in our research, namely 2,4-dinitrotoluene (DNT), methylxanthines (MeX) and creatinine (CRN), were briefly introduced.

1.2.1 DNT

Common sensors for nitroexplosives (e.g. DNT) are based on techniques such as colourimetry, ion mobility spectrometry and X-ray.[6] Colourimetric technique (e.g.

Expray) is popular for rapid screening against nitroexplosives, in which a colour change is observed when a reagent is sprayed onto a sample-containing surface swipe, but it may not be able to differentiate certain type of explosives and is prone to false-positive (e.g. fertilisers containing nitrates).[7] Ion mobility spectrometry correlates the drift velocity of ions from a vapour sample in an electric field to the mass-to-charge ratio to identify the presence of nitroexplosives.[6] This technique is widely-used for its high-sensitivity, portability, rapid response and ability to differentiate major explosives although volatilisation is required for non-vapour (solution or solid) samples and a radioactive source is usually used for ionisation.[7] X-ray detectors are commonly used for security checks in airports to identify any material with a similar effective atomic number to explosives by irradiating the luggage with an X-ray source to generate an image.[8] A trained person is required to interpret the image for any suspected item while exposure to X-ray radiation is potentially hazardous.

1.2.2 MeX

Enzyme immunoassay such as enzyme multiplied immunoassay technique (EMIT) and high-performance liquid chromatography (HPLC) are used to quantify MeX, including caffeine (CAF), theobromine (TBR) and theophylline (TPH), for therapeutic drug monitoring and toxicity testing.[9–12] EMIT is a homogenous assay based on the change in enzyme activity due to competitive binding of enzyme-labelled (e.g. glucose-6-phosphate dehydrogenase) drug and free drug in the sample with the antibody.[13] A change in absorbance associated with the change in enzyme activity can be measured via spectroscopic techniques. HPLC is used to quantify MeX in the sample by separating different components in the matrix using eluent solvent.[12] Immunoassay techniques are moderately sensitive, expensive and prone to interferences with structurally similar compounds,[14] while HPLC is time-consuming and requires expensive instrument.[15]

1.2.3 CRN

The current clinical method for quantification of an important biomarker CRN is a colourimetric technique based on the Jaffe reaction, in which a reddish-orange complex is formed when CRN reacts with picric acid in an alkaline solution.[16,17] A blood serum sample is extracted to determine the routine CRN level while a urine sample is collected over 24 hours for CRN clearance test. The major drawback of this technique is its non-specificity as picric acid forms the coloured complex with a wide variety of other molecules including glucose, ascorbic acid and proteins, and thus interferes with the CRN signals.[18]

1.3 Raman spectroscopy

Raman spectroscopy (RS) is an optical spectroscopic technique developed in 1928[19] which allows us to identify and differentiate target analytes via their vibrational fingerprints in a similar way to infrared (IR) spectroscopy (Figure 1.1). In RS, a single mode laser illuminates the sample after passing through sets of mirrors and slits, most photons are elastically (Rayleigh) scattered by the molecules whereas a very small number of photons are inelastically (Raman) scattered and collected by a CCD detector (Figure 1.2a). The Rayleigh scattered photon has the same energy as the incident photon while the Raman scattered photon has either a lower (Stokes) or higher energy (anti-Stokes) than the incident photon (Figure 1.2b). The Stokes Raman scattering is more intense than the anti-Stokes Raman scattering, and is more commonly used in RS.[20] The selection rule for RS is that the molecular vibration needs to be coupled to a change in the polarisability of the molecule.[21] The probability of Raman scattering (and hence scattering cross-section) is very low as it depends on whether the incident light is in resonance with the energy transition between the ground and excited electronic states of the molecule.[22] The Raman signal shows the intensity of photons collected as a function of Raman shift, that is the energy difference between the incident and inelastically scattered photons and is given in wavenumber (Figure 1.2c). RS offers advantages such as no or minimal sample preparation, high spatial resolution, fast response and tolerance to water, which merit its applications in different areas including geology,[23] pharmaceuticals[24] and polymer analysis[25]. However, RS is not suitable for diluted samples due to its inherently weak signals, thus limiting its application to bulk solid or liquid samples or materials.

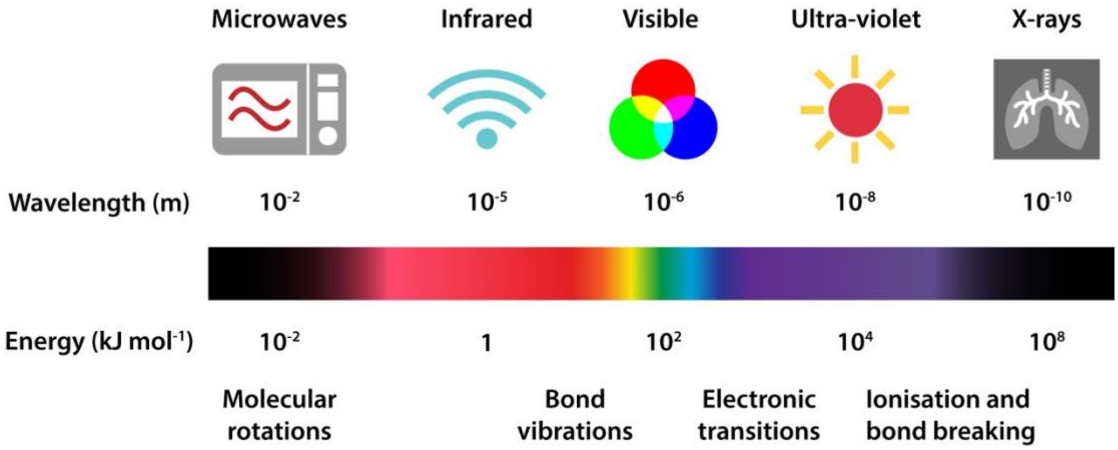

Figure 1.1. Schematic illustration of the electromagnetic spectrum, showing the energies and material phenomena across a range of wavelengths (not to scale).

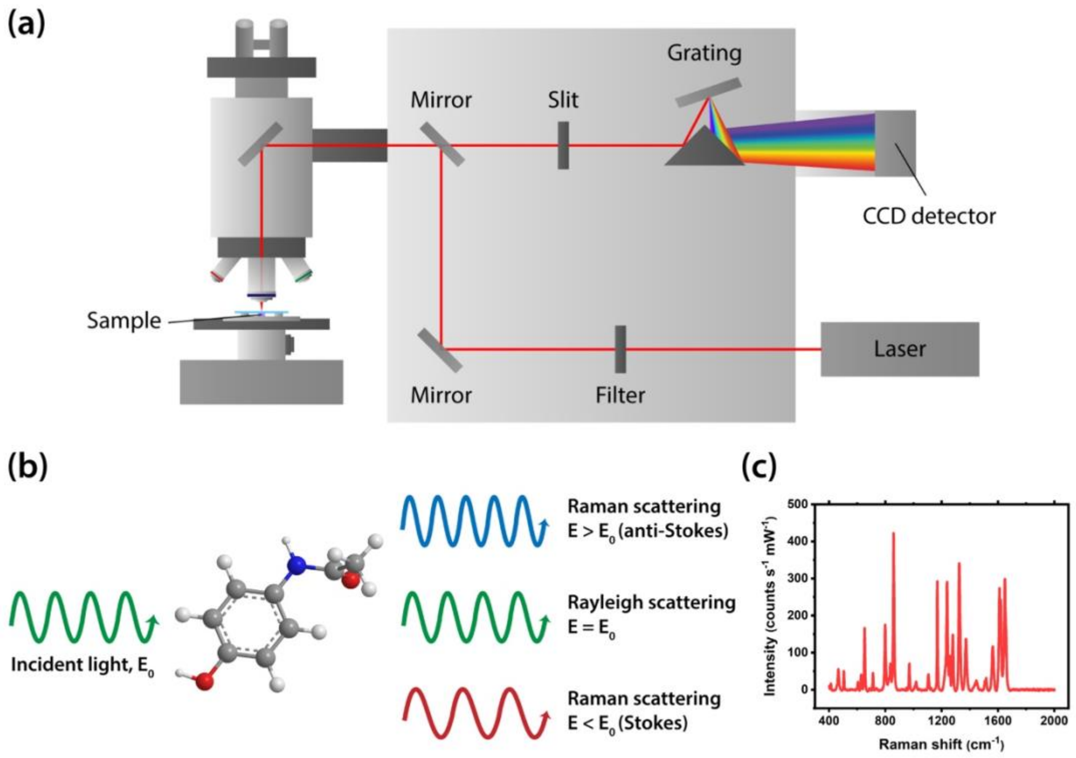

Figure 1.2. (a-b) Schematic illustrations of (a) set-up of Raman spectroscopy and (b) scattering of light by a molecule (paracetamol). (c) An example of Raman spectrum (paracetamol).

1.4 SERS

SERS was first observed by Fleischmaan and co-workers[26] during the measurement of Raman signals of pyridine on a roughened Ag electrode in 1974 and the phenomenon was interpreted by two groups, Jeanmaire and Van Duyne[27] and Albrecht and Creighton[28], in 1977. Over the past 45 years, SERS has sparked great interests across different disciplines including chemistry, physics, biology, materials and analytical science. SERS overcomes the poor signals caused by the intrinsically low scattering cross-sections in RS with metallic nanoparticles (NPs) or nanostructured surfaces such as Au and Ag serving as substrates to reach an average enhancement factor (EF) of $\sim 10^5$ - 10^6. The overall EF is contributed by the electromagnetic (EM) enhancement of the incident light absorbed on or near the surface of metallic NPs via localised surface plasmon resonance (LSPR) and the chemical (CHEM) enhancement associated with the increase in polarisability of the analyte molecules during charge transfer between the metallic NPs and the analyte molecules (Figure 1.3). The overall EF (G_{SERS}) is then given by:[29]

$$G_{SERS} = G_{Em} G_{Chem} \tag{1}$$

where G_{Em} and G_{Chem} are the contributions from the EM and CHEM enhancements respectively.

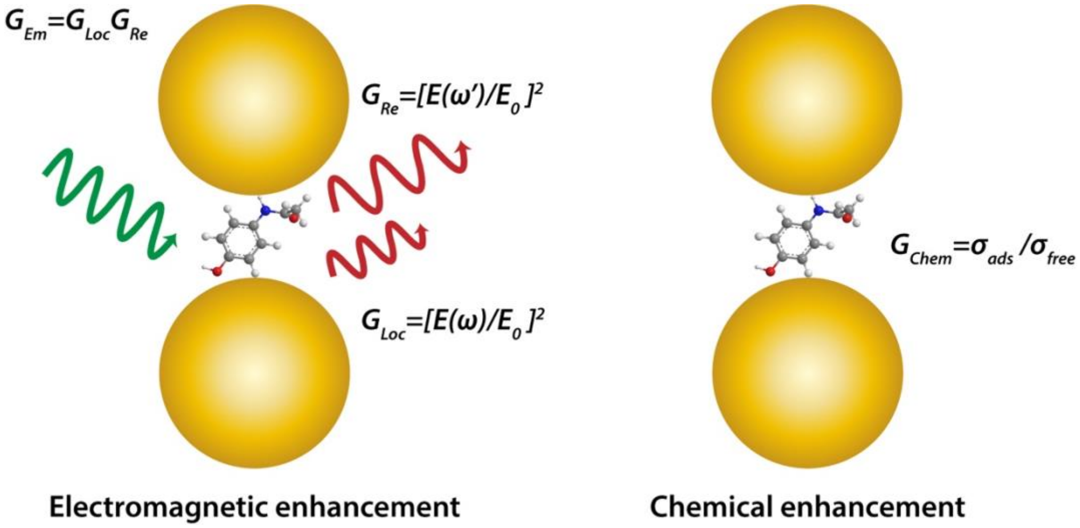

Figure 1.3. Schematic illustration of the electromagnetic enhancement (local electric field enhancement and dipole re-radiation enhancement) and the chemical enhancement in SERS. Reproduced with permission from ref. 30. Copyright 2016 Nature Publishing Group.

1.4.1 EM enhancement

The EF is mainly contributed by the EM enhancement (~10^4 - 10^{11}), which is a two-step process involving local electric field and re-irradiation enhancements due to LSPR of the metallic NPs with the incident light (see section 1.5).[29–31] When the analyte molecules are located in close proximity to the metallic NPs, the local electric field (E) oscillating at an incident frequency of ω is enhanced and the enhancement (G_{Loc}) is defined by:

$$G_{Loc} = \left[\frac{E(\omega)}{E_0}\right]^2 \tag{2}$$

where E_0 is the incident electric field.

The metallic NPs then transfer the Raman signals, which are proportional to the square of the enhanced local electric field at a scattered frequency of ω', from near field to far field due to the mutual excitation between the dipole of the metallic NPs and the induced dipole of the molecules.[30,31] This dipole re-irradiation enhancement (G_{Re}) is defined by:

$$G_{Re} = \left[\frac{E(\omega')}{E_0}\right]^2 \tag{3}$$

For small Raman shifts (small frequency or wavelength differences between incident and scattered photons),

$$G_{Em} = G_{Loc}G_{Re} = \left[\frac{E(\omega)}{E_0}\right]^2 \left[\frac{E(\omega')}{E_0}\right]^2 = \left[\frac{E(\omega)}{E_0}\right]^4 \tag{4}$$

The EM enhancement is approximately proportional to the fourth power of the local electric field enhancement. This commonly used $|E(\omega)|^4$ approximation is valid for most applications but one may also need to account for the non-local effects caused by the sub-nm spacing between the NPs (quantum confinement effects), the anisotropic nanostructures and the random orientations of molecules under certain circumstances (polarisation effects).[30,32–34] Furthermore, the EM enhancement is strongly dependent on the distance from the surface of the metallic NP (r), which is given by:[29,31]

$$\frac{G_{Em}(r)}{G_{Em}(0)} = \left[\frac{a}{a+r}\right]^{12} \tag{5}$$

where a is radius of the metallic NP. The SERS enhancement decreases significantly for a small increase in the distance between the analyte molecules and the metallic NPs

(Figure 1.4), hence it is very important to bring the molecules close to the surface of the SERS substrate.

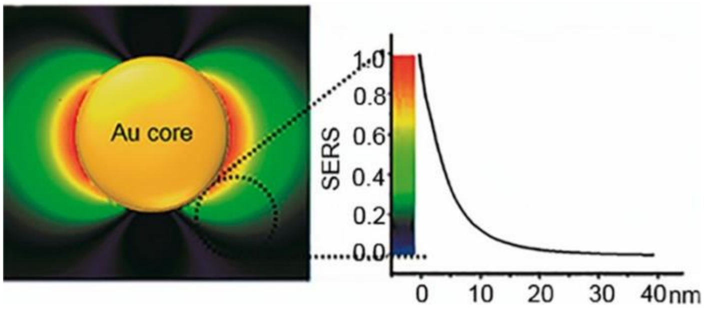

Figure 1.4. Finite difference time domain simulation of spatial distribution of local electric field of the Au NP, showing the dependence of EM enhancement on the distance from the Au NP surface. Reproduced with permission from ref. 31. Copyright 2018 American Chemical Society.

1.4.2 CHEM enhancement

The contribution of the CHEM enhancement (10 – 100) to the EF is much smaller than that of the EM enhancement,[22,31] however, it is still important to understand the chemical mechanisms in order to optimise the SERS signals for the desired applications. When the analyte molecules are adsorbed onto the substrate, the polarisability and hence the cross-sections of the vibration modes of the molecules are modified by the surface interaction with the metallic NPs (Figure 1.3).[22,29] The CHEM enhancement (G_{Chem}) is defined by:

$$G_{Chem} = \frac{\sigma_{ads}}{\sigma_{free}} \tag{6}$$

where σ_{ads} and σ_{free} are the cross-sections of adsorbed and free (unbound) molecules respectively. The non-resonant interaction (ground state interaction between molecule and metallic NP), the molecular resonance (resonance of incident light with molecule) and the charge transfer resonance (resonance of incident light with metal-molecule coupling) are the mechanisms contributing to the overall CHEM enhancement.[35,36]

Electronic structure methods such as time-dependent density functional theory (DFT) have been used to describe the CHEM enhancement by modelling the metallic NP as a cluster of several atoms. This method can calculate the static polarisability derivatives of the metal-molecule system (ground state) but fails to interpret the weakly-coupled (long-range) charge transfer correctly (strongly mixed with LSPR).[36,37] Recently, semi-empirical molecular orbital methods such as Intermediate Neglect of Differential Overlap Hamiltonian and the singles configuration interaction approaches have been used to describe the CHEM enhancement from charge transfer by separating the LSPR and charge transfer resonance in the calculations.[22,38]

1.4.3 Hotspots

The SERS EF is dependent on the nanoscale geometry of the metallic NP substrate and the distance and relative orientation between the analyte molecules and the substrate. The EM enhancement is highly localised in a very small spatial volume on or in close proximity to the SERS substrate which is known as a hotspot. The hotspots are usually located at the nanogaps between two metallic NPs (or NP and substrate) or at the sharp tips or corners of anisotropic nanostructures such as nanocubes (NCs) and nanostars (NSs).[39,40] The enhancement of the local electric field is much stronger in the nanogaps than on the surface of NPs and thereby aggregated NPs are usually used as SERS substrates instead of isolated NPs.[29]

The SERS signals can be enhanced significantly when the analyte molecules are located in close proximity to the plasmonic hotspots. For instance, the SERS EF increases by four orders of magnitudes when the nanogap between the Au NP dimer is reduced from 10 nm to 2 nm (Figure 1.5a,b).[30,41,42] The dependence of EM enhancement on the size of the nanogap (g) is given by the power-law:[42,43]

$$G_{Em} \sim \frac{1}{g^n} \tag{7}$$

where n ~2.

However, the EF can be reduced by an order of magnitude due to quantum tunnelling when the nanogap is at sub-nm scale (< 0.7 nm) (Figure 1.5c).[42,44,45]

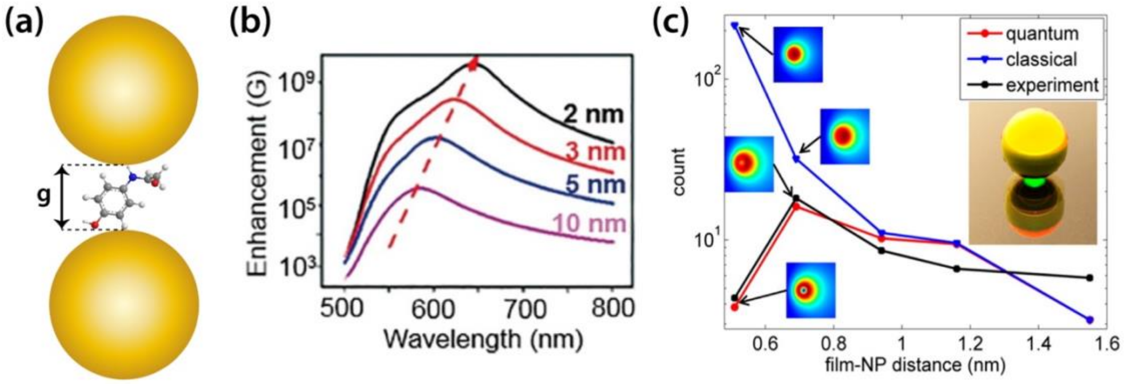

Figure 1.5. (a) Schematic illustration of a nanogap between two Au NPs. (b) The dependence of the SERS EM enhancement on the size of the nanogap between two Au NPs. (c) The quantum tunnelling effect on the SERS EM enhancement for < 0.7 nm distance between Au NP and Au film. Reproduced with permissions from ref. 31, 45. Copyright 2014, 2018 American Chemical Society.

1.5 Surface plasmon resonance

The very first applications of the metallic NPs were over a millennium ago though the modern research has just begun in the past century. The Lycurgus Cup, which was manufactured by the Roman craftsmen in 4th century, is the most well-known example of ancient artefacts composing of metallic NPs (Figure 1.6). Interestingly, the Lycurgus Cup resembles jade with an opaque greenish-yellow colour when light is illuminated from outside but resembles a translucent ruby red colour when illuminated from inside. The dichroic nature of the Lycurgus Cup under illumination is due to the presence of nanocomposites of Au and Ag NPs at a ratio of 3:7.[46]

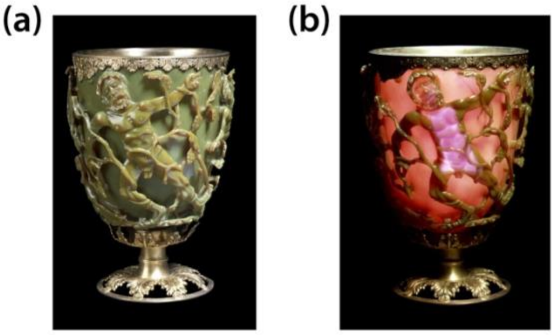

Figure 1.6. The Lycurgus Cup in (a) reflected light and (b) transmitted light. Copyright The Trustees of the British Museum.

The distinct colour appeared on the metallic NPs is resulted from a photophysical process termed surface plasmon resonance (SPR), in which the free (conduction band) electrons within the NPs are polarised by the electric field of the incident light to create a coherent multipolar (e.g. dipolar) oscillation between the opposite charges of the NPs (Figure 1.7).[47] When the coherent oscillation is highly localised to a particular position (e.g. on the NP surface), it is known as localised SPR (LSPR).

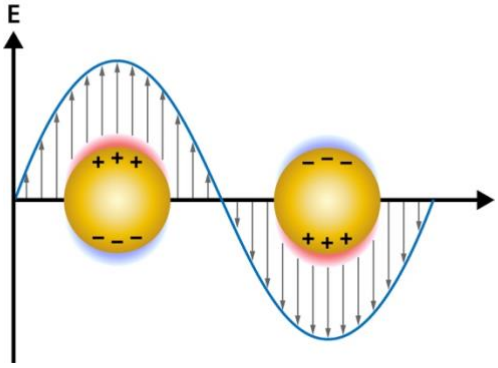

Figure 1.7. Schematic illustration of localised surface plasmon resonance of Au NPs.

In 1908, Mie[48] provided the first explanation to the ruby-red colour of Au NPs by solving Maxwell's equations for interaction of small metallic NPs with monochromatic electromagnetic wave. The extinction cross-section σ_{ext} of a metallic NP, which is the sum of its absorption σ_{abs} and scattering cross-sections σ_{sca}, is given by the following equations:[29,49]

$$\sigma_{ext}(\omega) = \sigma_{abs}(\omega) + \sigma_{sca}(\omega) \tag{8}$$

$$\sigma_{abs}(\omega) = 4\pi k a^3 i \left[\frac{\varepsilon(\omega)-\varepsilon_m}{\varepsilon(\omega)+2\varepsilon_m}\right] \tag{9}$$

$$\sigma_{sca}(\omega) = \frac{8\pi}{3} k^4 a^6 \left|\frac{\varepsilon(\omega)-\varepsilon_m}{\varepsilon(\omega)+2\varepsilon_m}\right|^2 \tag{10}$$

where k is wavevector, a is radius of the metallic NP, $\varepsilon(\omega)$ is complex dielectric constant of the metallic NP and ε_m is dielectric constant of the surrounding medium. For a metallic NP with radius much smaller than the wavelength of incident light ($2a \ll \lambda$), i.e. $a < 10$ nm, it experiences a time-dependent but spatial-independent (homogeneous) electric field under the quasi-state approximation. The electric field inside the metallic NP (E_{in}) is thus given by:[29,49]

$$E_{in} = E_0 \frac{3\varepsilon_m}{\varepsilon(\omega)+2\varepsilon_m} \tag{11}$$

In this case, a dipolar charge distribution is generated on the NP surface and the extinction cross-section is mainly contributed by light absorption (Figure 1.8a), which can be described by the equation below:[49,50]

$$\sigma_{ext}(\omega) = \frac{9{\varepsilon_m}^{3/2} V\omega}{c} \frac{\varepsilon_2(\omega)}{(\varepsilon_1(\omega)+2\varepsilon_m)^2+{\varepsilon_2}^2(\omega)} \tag{12}$$

where V is volume of the metallic NP, c is speed of light, ε_1 and ε_2 are the real and imaginary parts of the dielectric constant of the metallic NP. When ε_2 is sufficiently small, σ_{ext} is maximised at a resonance frequency when

$$\varepsilon_1(\omega) = -2\varepsilon_m \tag{13}$$

The position and bandwidth of the LSPR peaks are determined by real and imaginary parts of the dielectric constant of the metallic NP.[50,51] For example, the LSPR peaks of Au NPs and Ag NPs lie within the visible range, at ~520 nm and ~420 nm respectively. The loss factor (optical losses mainly due to interband and intraband transitions) of the metallic NPs is also described by the imaginary part of the dielectric constant.[52] Ag NPs have lower losses than Au NPs in the visible range, as the band edge frequency (at which interband transition becomes allowed) in Ag NPs is above the LSPR frequency, implying that the localised surface plasmons cannot decay into electron-hole pairs.[53,54] This results in relatively stronger EM field enhancement and better plasmonic photothermal properties and hence stronger SERS signals. In contrast, the localised surface plasmons in Au NPs can delay into electron-hole pairs due to overlapping of the band edge and LSPR frequencies, resulting in higher losses.[53,54] Nevertheless, Au NPs are preferred for theranostic applications for their biocompatibility, chemical stability and low cytotoxicity.[55]

When the size of the NPs is greater than their electron mean free path (e.g. ~40 nm for Au NPs), the electrons are scattered in all directions. The contribution from the scattering cross-section starts to appear and the extinction cross-section becomes more complex (Figure 1.8b).[50,56] There are approximately equal contributions from absorption and scattering to the extinction cross-section when the size of Au NPs reaches 80 nm (Figure 1.8c).[50,54,56] The LSPR peak is redshifted and broadened as the particle size increases (Figure 1.9a).

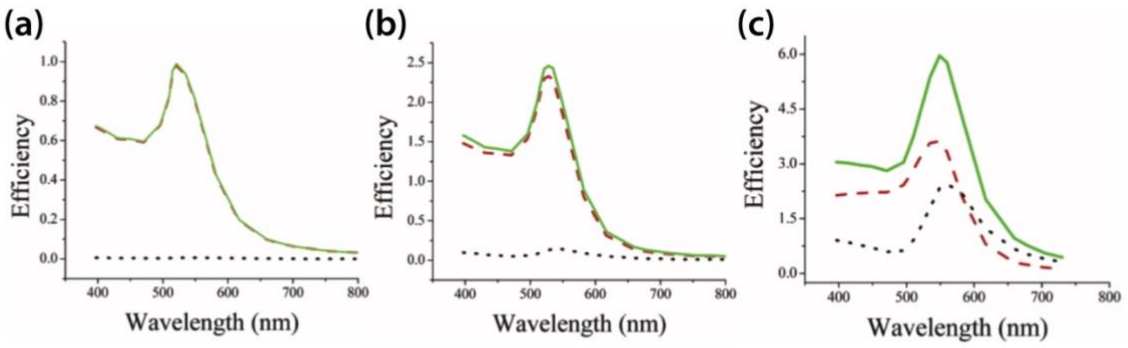

Figure 1.8. Efficiency of absorption (red dashed), scattering (black dotted) and extinction (green solid) for Au NPs with a diameter of (a) 20 nm, (b) 40 nm and (c) 80 nm. Reproduced with permission from ref. 56. Copyright 2006 American Chemical Society.

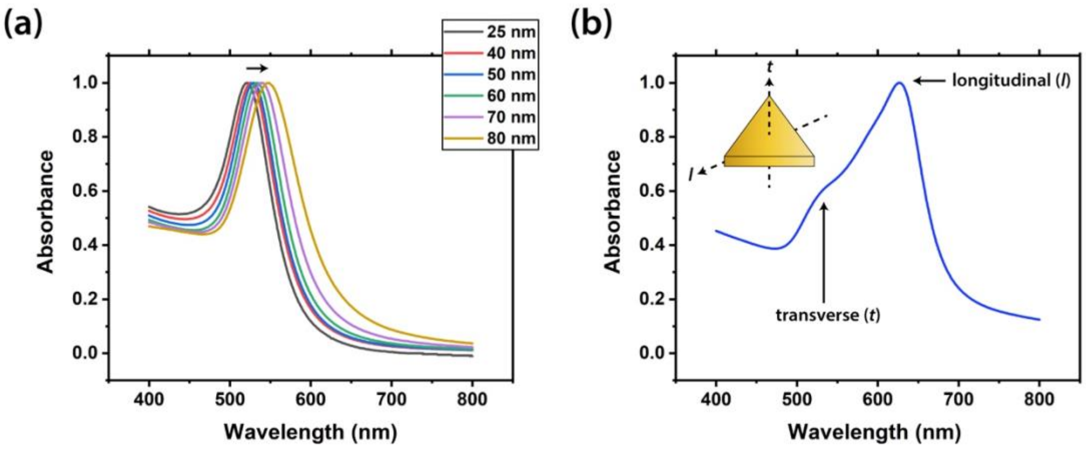

Figure 1.9. (a) UV-Vis spectra of Au NPs with sizes from 25 to 80 nm, showing gradual red-shift in the LSPR peak with increasing particle size. (b) UV-Vis spectra of Au NTs showing the transverse and longitudinal LSPR peaks.

When the shape of the metallic NPs derivates from sphericity, such as nanorods (NRs) and nanotriangles (NTs), the resonances in the transverse and longitudinal directions are no longer equivalent and there are two distinct LSPR peaks, with the lower and higher wavelengths corresponding to the transverse and longitudinal LSPR respectively (Figure 1.9b).[49,57] Herein, the LSPR and hence SERS EM enhancement are dependent on the dielectric constant, size and shape of the metallic NPs. For instance, the wavelength of the LSPR peak can be tuned into the near infrared range (650 - 900 nm) to improve the penetration depth for biomedical applications, which is advantageous over fluorescence probes as no UV excitation is required.[58]

1.6 Other SERS related techniques

In the past years, various optical techniques based on or related to SERS have been developed, including but not limited to, coherent anti-Stokes Raman spectroscopy (CARS), resonance Raman spectroscopy (RRS), surface-enhanced Raman optical activity (SEROA), electrochemical surface-enhanced Raman spectroscopy (EC-SERS) and tip-enhanced Raman spectroscopy (TERS), for a wide range of applications.

CARS is a third-order non-linear process that utilises multiple lasers (photons) at different frequencies to generate vibrational coherences via laser-sample interactions (i.e. when the energy of a photon equals the energy difference between two photons).[59] This technique is particularly useful for biomedical imaging as no staining or chemical labelling is required due to its intrinsic vibrational contrast.[60] RRS is a technique based on the normal RS in which the frequencies of the incident photons and the electronic transition of the molecule overlap and the electrons are excited to a higher electronic state (i.e. a subset of the Raman-active modes is enhanced).[61] This technique allows selective monitoring of a molecule in a complex matrix, such as biological chromophores embedded in membrane proteins.[60]

SEROA is a chiral-sensitive vibrational technique combining SERS and Raman optical activity (ROA), in which a tiny difference in the Raman intensity of a chiral molecule in right- and left-circularly polarised light is measured.[62] The potential applications of SEROA include protein and RNA studies.[63] EC-SERS integrates SERS with electrochemical techniques to produce CHEM enhancement from charge transfer that occurs when the energy of the incident photons overlaps with the transition between the Fermi level in metal-molecule couplings.[22] Examples of EC-SERS studies include surface adsorption, structure of interfacial water, surface redox reactions and electrodeposition.[64] TERS, which combines SERS with scanning probe microscopy, utilises nanoscale metallic tips to generate a strong EM enhancement at the tip apex as to increase the spatial resolution (to a few nm) with intramolecular chemical resolution for studying biomaterials, carbon materials and polymers.[22,65,66]

1.7 SERS substrates

To develop a high-performance SERS sensor, it is essential to understand how the enhancement and reproducibility of the SERS signals are affected by the features of the SERS substrates, including substrate type, material, size, shape and fabrication method. Though the ultra-high SERS enhancement (e.g. single-molecule level) is of numerous interests in the research community, other aspects such as reproducibility, uniformity, ease-of-fabrication, stability and cost-effectiveness are critical to most practical applications. Herein, different SERS substrates based on the state of matters, i.e. solution and solid, are presented in the following subsections.

1.7.1 Solution-based substrates

Colloidal NPs such Au NPs and Ag NPs, which can be synthesised via bottom-up approaches (e.g. sodium citrate reduction of the corresponding metal precursor, see section 1.8)[67,68], are the most commonly used solution-based SERS substrates. Colloidal Au NPs and Ag NPs are easy to synthesise (also commercially available), highly reproducible and cost-effective, meanwhile allowing surface functionalisation and tunable plasmonics by varying their size and shape. However, unaggregated (single) spherical NPs suffer from low SERS signal enhancement due to their high symmetry. The SERS signals of colloidal NPs can be enhanced via aggregation to form a 3D network of plasmonic hotspots, which can be triggered by adding salt (e.g. NaCl)[69] or using molecular linkers (e.g. DNA and biotin-streptavidin)[70,71]. Unfortunately, it may be difficult to control the aggregation process and the measurement window for colloidal nanoaggregates is rather limited due to its dynamic nature.

The SERS signals can be further enhanced by using anisotropic nanostructures such as Au nanorods (NRs)[72], Au nanotriangles (NTs)[73], Ag nanocubes (NCs)[74], Au nanostars (NSs)[75] and nanogapped nanoparticles (NNPs)[76,77] (Figure 1.10), due to an increase in the number of plasmonic hotspots at the sharp edges or corners. Typically, Au NRs are synthesised in the presence of a cationic surfactant, cetyltrimethylammonium bromide (CTAB).[78] The synthesised Au NRs can be used as SERS substrates after removing the excess CTAB by centrifugation and the surface-bound CTAB by HCl treatment.[72] Au NTs can be synthesised in the presence of NaI and cetyltrimethylammonium chloride (CTAC), which act as the shape directing agent and surfactant respectively. The Au NTs were then purified, flocculated overnight and the precipitated NTs were redispersed in CTAC before SERS measurements.[73] SERS substrates based on Ag NCs can be prepared by ethylene glycol (EG) reduction of $AgNO_3$ in the presence of poly(vinyl pyrrolidone) (PVP) and HCl.[79] EG and excess PVP were removed by washing with acetone and ethanol before redispersion in water.[74] Notably, the Ag NCs can also be used to prepare Au nanocages via galvanic replacement reaction.[80] Au NSs, which are sometimes known as Au nanoflowers[81], nanoporous Au NPs[82], Au tetrapods[83], etc., have a higher number of sharp tips or branches and hence plasmonic hotspots, making them promising for SERS applications. For instance, Au NSs can be synthesised via a PVP-mediated approach, in which the PVP-coated Au seeds in ethanol were injected into a growth solution of dimethylformamide (DMF). Excess PVP and DMF were then removed by centrifugation in ethanol.[75]

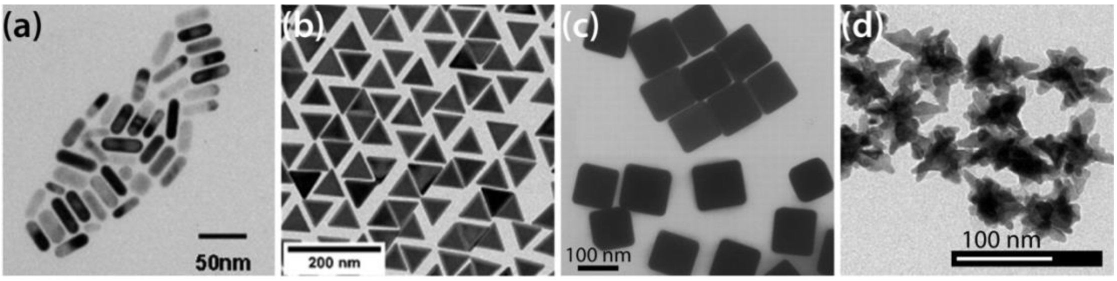

Figure 1.10. TEM images of different SERS substrates (a) Au NRs, (b) Au NTs, (c) Ag NCs and (d) Au NSs. Reproduced with permissions from ref. 72, 73, 75, 79. Copyrights 2010 Elsevier B.V., 2008, 2014 American Chemical Society, 2002 American Association for the Advancement of Science.

Au NNPs can be synthesised by the reaction of DNA-modified Au cores[84] with $NH_2OH–HCl$ and $HAuCl_4$ in the presence of PVP (Figure 1.11a).[76] The analyte molecules can be loaded into the ~1 nm hollow gap between the Au core and Au shell for SERS sensing. In addition, SERS substrates based on multi-shell Au NNPs and hybrid NNPs can be achieved by repetitive polydopamine (PDA) coating on a wide variety of cores such as spherical Au NPs, Au NRs, metal–organic frameworks, and magnetic polymer NPs (Mag NPs) and subsequent purification (Figure 1.11b).[77] Hence, SERS substrates based on anisotropic nanostructures can significantly enhance the SERS signals, but the synthetic methods are relatively complicated, as compared to the spherical NPs.

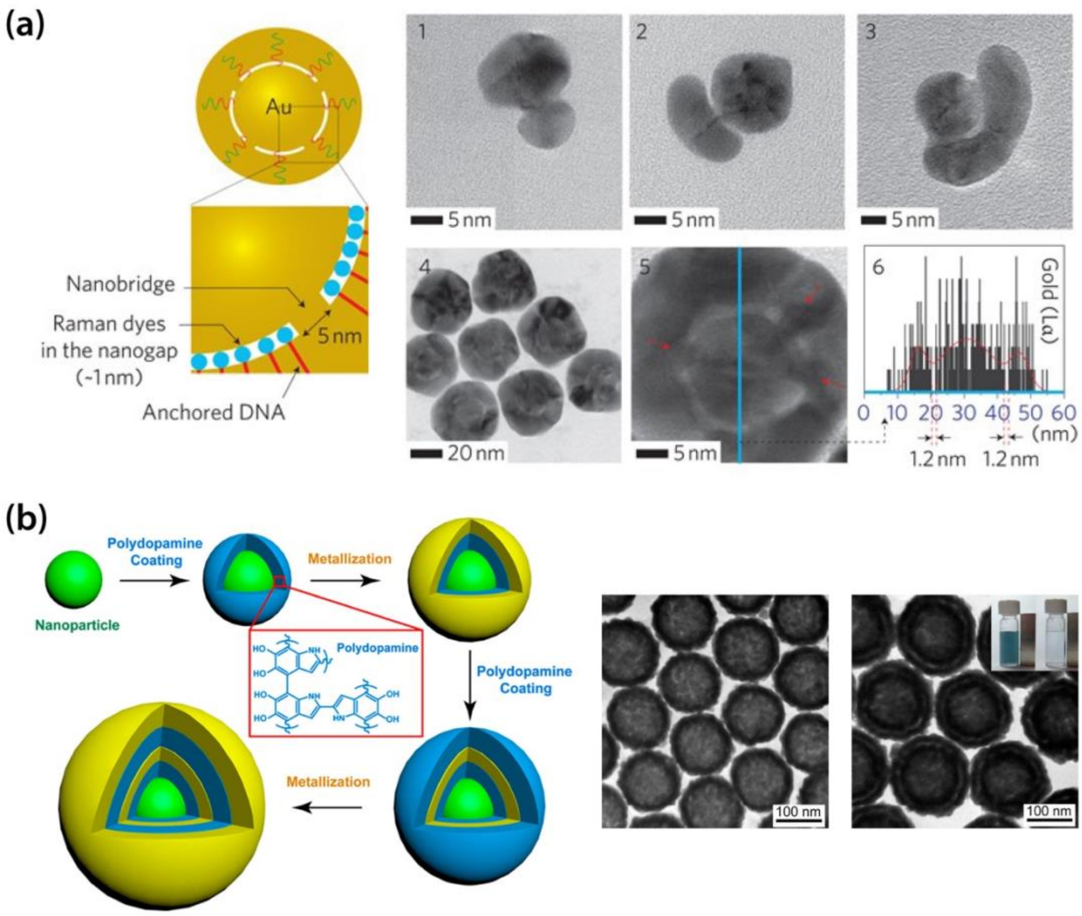

Figure 1.11. (a) Schematic illustration of Au NNPs mediated by DNA, TEM images of the intermediates (1-3) and Au NNPs (4-5) and elemental line mapping of the ~1.2 nm nanogap within Au NNPs (6). (b) Schematic illustration of multi-shell NNPs mediated by PDA and TEM images of Mag NP@PDA@Au and Mag NNPs. Reproduced with permissions from ref. 76, 77. Copyrights 2011 Nature Publishing Group, 2016 American Chemical Society.

1.7.2 Solid-based substrates

The first ever SERS substrate was fabricated by electrochemical roughening,[26] in which very small regions of metal (e.g. Ag, Au or Cu) from the working electrode are dissolved upon a positive potential and the dissolved metal is then redeposited back onto the electrode upon a more negative potential in a three-electrode system.[85] Electrochemical roughening is useful for large-scale fabrication and can be easily adopted to different electronic conductors with the major drawback being lack of precise control in the surface roughness.[85] Solid-based SERS substrates generally involve sophisticated fabrication procedures and hence are more expensive than solution-based substrates.[22]

Template-based techniques (e.g. anodic alumina oxide, AAO) and lithography (e.g. electron-beam lithography) are other commonly used fabrication methods for SERS substrates. An AAO template can be easily fabricated by dissolving alumina in acidic solution upon a high voltage to form a porously hexagonal pattern.[86] Electrodeposition of metal (e.g. Ag , Au or Pt) is then performed before dissolving the AAO film in phosphoric acid to form the elongated nanostructures. Template-based techniques are particularly useful for large-scale fabrication.[85] In e-beam lithography, the regions of a resist, which is an electron-sensitive polymer (e.g. poly(methylmethacrylate), PMMA), exposed to a focused beam of electrons are either dissolved or remained (Figure 1.12).[29,87] The metallic nanostructures can then be constructed via different routes, etching or lifting off. The former involves reactive ion etching of the resist pattern into the substrate before removing the resist and depositing metal (e.g. Ag or Au) onto it, whereas the latter involves metal deposition before removing the resist, to generate metallic nanopatterns. The geometry of the SERS substrates can be precisely controlled using this technique with a relatively good reproducibility as opposed to electrochemical roughening, while being very expensive and not suitable for large-scale fabrication.[29]

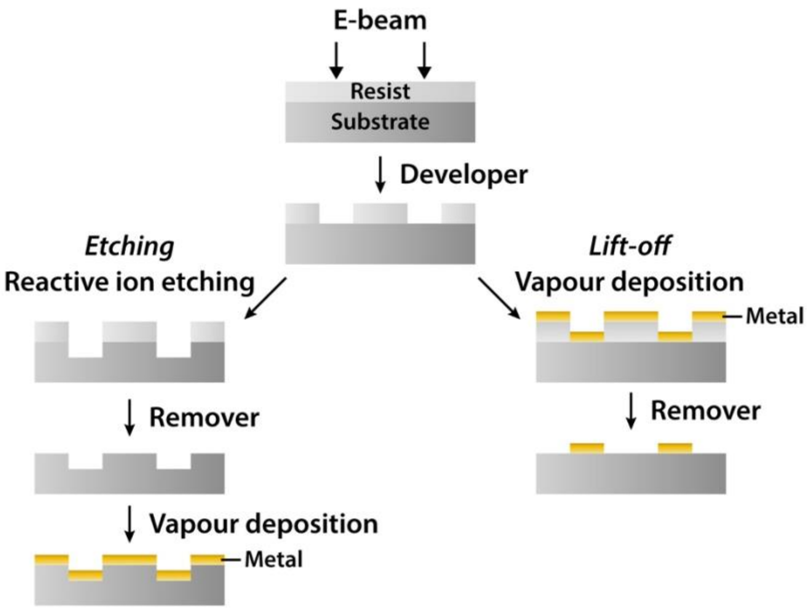

Figure 1.12. Schematic illustration of fabrication of SERS substrates by e-beam lithography. Reproduced with permission from ref. 87. Copyright 1998 Elsevier B.V.

Colloidal NPs can be immobilised on solid supports as SERS substrates, which are relatively stable and easy to handle. For instance, the surface of a glass slide can be chemically modified by 3-aminopropyltrimethoxysilane before immersing into a solution of Au NPs or Ag NPs to form a self-assembled monolayer (Figure 1.13).[88,89] The idea of self-assembled monolayer can be extended to multi-layers using a layer-by-layer approach, in which the substrate is immersed into a solution of bifunctional cross-linkers after forming the first self-assembled monolayer of NPs and the process of alternate immersion is repeated until the desired number of layers is formed.[90] The reproducibility of the SERS signals using multi-layered substrates is relatively higher than the monolayered substrates at the expense of uniformity issues due to aggregations of NPs. The SERS substrates based on self-assembly of NPs can be optimised for different applications by varying the features of NPs (e.g. material, size and shape), type of solid supports (e.g. glass, silicon, metal and paper), cross-linkers and immersion time.

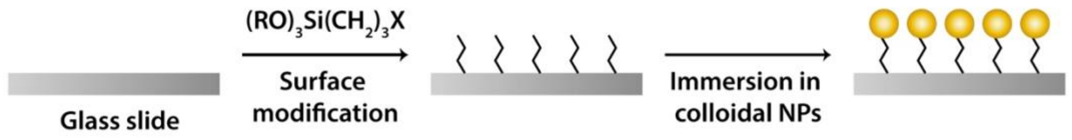

Figure 1.13. Schematic illustration of immobilisation of colloidal NPs onto a glass slide. Reproduced with permission from ref. 89. Copyright 1995 American Association for the Advancement of Science.

Shell-isolated nanoparticle-enhanced Raman spectroscopy (SHINERS) is a technique developed for 'smart dust' SERS substrates, in which Au@SiO_2 or Au@Al_2O_3 core-shell NPs is spread over the surface of interests to form a monolayer (Figure 1.14).[91] The chemically inert SiO_2 or Al_2O_3 shell can protect the Au NPs from aggregating or direct contact with the analyte molecules (e.g. methyl parathion). This method offers flexibility in probing analyte molecules anchored on materials of various sizes and shapes (e.g. orange) with strong SERS signal enhancement.

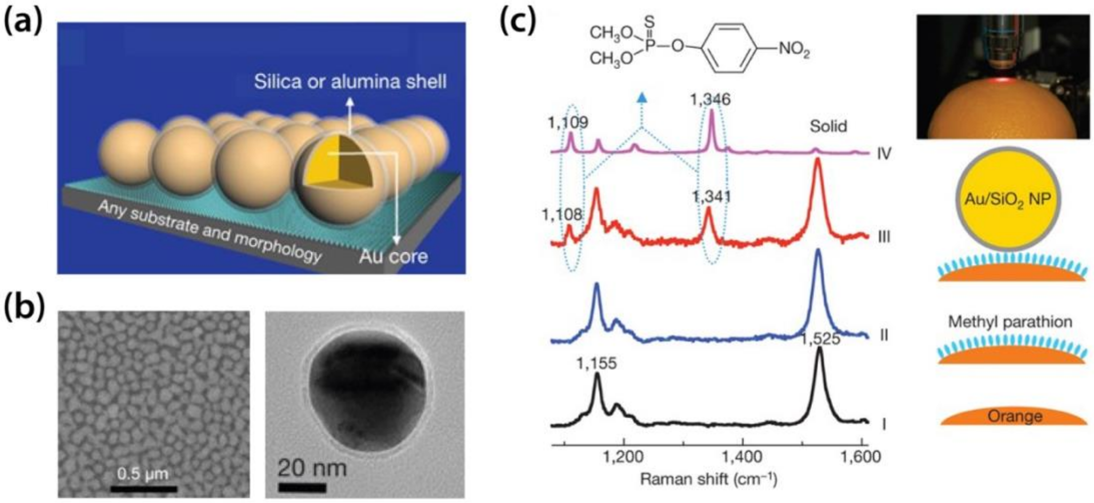

Figure 1.14. (a) Schematic illustration of SHINERS. (b) SEM image of the Au@SiO_2 NP monolayer on Au surface (left) and TEM image of the Au@SiO_2 NP (right). (c)

SHINERS measurements of pesticide residues (methyl parathion) on an orange. Reproduced with permission from ref. 91. Copyright 2010 Nature Publishing Group.

1.8 Synthesis of Au NPs

Though the very first applications of Au NPs dates back to 4th century, no synthetic method has been reported until 1857 when Faraday[92] synthesised Au NPs via phosphorus reduction of $AuCl_3$ solution in a two-phase CS_2-water mixture. Many techniques have been developed for the preparation of NPs from bulk materials (top-down approach) or from atoms, molecules and clusters (bottom-up approach) since then. Bottom-up approach such as colloidal self-assembly is more popular than top-down approach for its relatively narrow size distribution and high uniformity. There have been countless reports on the synthetic methods of Au NPs, but the Turkevich method developed in 1951 and the Brust-Schiffrin method developed in 1994 remain as the most popular and standard methods for Au NP synthesis to date. While the synthesis of non-spherical Au nanostructures is of numerous research interests, it often involves the use of surfactants such as CTAC that restricts further functionalisation by CBs. The recent advances in Au nanostructures can be found in the literature.[93]

1.8.1 The Turkevich method

The first breakthrough in the synthetic method of Au NPs did not take place until a century after Faraday's initial report. In 1951, Turkevich and co-workers[67] developed a similar approach to synthesise Au NPs with a typical size of 20 nm via sodium citrate reduction of $HAuCl_4$ in aqueous solution. Later in 1973, Frens[94] refined the Turkevich method to produce Au NPs with sizes ranging from 16 to 147 nm by varying the ratio of sodium citrate to $HAuCl_4$. However, this method results in polydispersity when the particle size is greater than 20 nm. Continued effort in the modification of the Turkevich method (e.g. temperature, pH, ratio of reactants and order of addition) and the understanding of the mechanism has been made in the recent decades, aiming to synthesise monodispersed Au NPs tailored for different applications.[95–100] Of particular mention, Puntes and co-workers[101] developed a kinetically-controlled seeded growth method to synthesise monodispersed Au NPs with controllable sizes from 10 to 180 nm (Figure 1.15), simply by varying temperature and seed concentration. An exhaustive list of other modifications on the Turkevich method can be found in a recent publication.[102]

Herein, the Au NPs synthesised via the Turkevich method are suitable for further functionalisation by CBs as the citrate-capping layer is only loosely bound to the surface of Au NPs. For instance, citrate-capped Au NPs with sizes ≥ 40 nm formed via the kinetically-controlled seeded growth method could be a good candidate for SERS substrates after CB functionalisation.

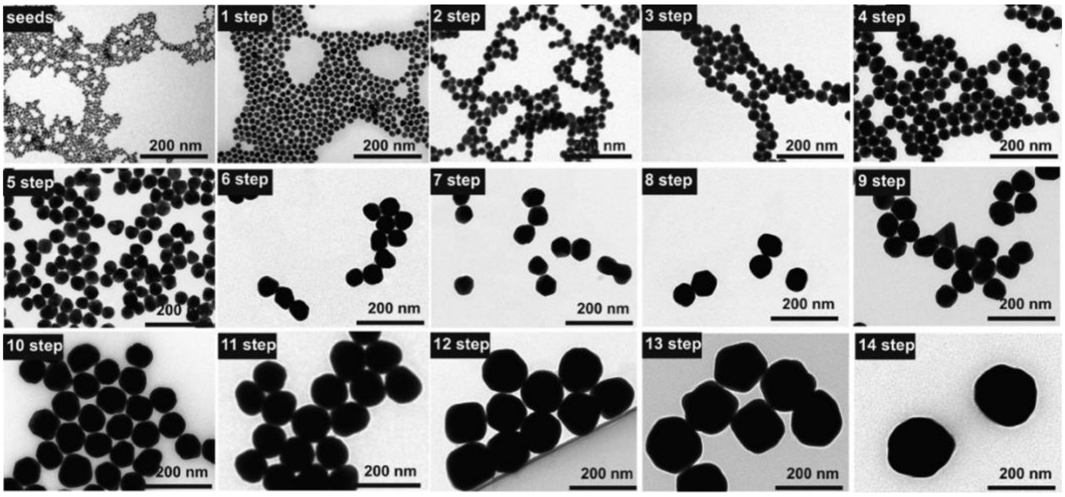

Figure 1.15. TEM images of the Au NPs synthesised via the kinetically-controlled seeded growth method. The Au NPs increased from 8.4 nm to 180.5 nm after 14 growing steps. Reproduced with permission from ref. 101. Copyright 2011 American Chemical Society.

1.8.2 The Brust-Schiffrin method

The Turkevich method has been widely used for Au NP synthesis but the synthetic method for sub-10 nm remained an open challenge until Schiffrin and co-workers[103] reported an one-step method to synthesise thiol-functionalised Au NPs of 1-3 nm in 1994. The Brust-Schiffrin method involves the reduction of $HAuCl_4$ by sodium borohydride in the presence of dodecanethiol at water-toluene interface with tetraoctylammonium bromide acting as phase-transfer reagent. Though this method has impacted the subsequent development in the field,[104,105] it is not suitable for our studies as the strong interaction between Au and thiol prohibits further functionalisation by CBs and the small sizes of Au NPs synthesised are not optimised for SERS sensing.

1.9 Functionalisation of Au NPs

Bare Au NPs tend to aggregate to lower their surface energy owing to the nature of their incredibly high surface area. It is necessary to precisely control the aggregation of Au NPs as to ensure the formation of reproducible SERS substrates. Functional ligands and linkers such as citrate[98], alkylthiols[106], carboxylates[107], amines[108], DNA[70] and biotin-streptavidin[71] have been used to aggregate Au NPs for a wide range of applications. However, these strategies fail to produce a controllable and consistent inter-particle spacing between Au NPs or provide access to plasmonic hotspots, resulting in irreproducible plasmonics and hence are not desirable for use as SERS substrates.[2] In 2010, Lee and Scherman[1] first defined a precise inter-particle spacing of 0.91 nm between Au NPs by capping a supramolecular host molecule, cucurbit[5]uril (CB5), which has led to the subsequent applications of the Au NP: CB nanoaggregates as substrates for SERS sensing (see section 1.15).

1.10 Supramolecular hosts

Supramolecular chemistry describes the non-covalent interactions between two or more molecules or ions to form a structural complex.[109] Macrocyclic hosts such as crown ethers (CEs)[110], calixarenes (CXs)[111], cyclodextrins (CDs)[112] and CBs[113] (Figure 1.16), which can trap small analyte molecules or ions inside their cavities to form host-guest complexes, have attracted great attention for their wide-range applications. CBs outweigh the classical supramolecular hosts for their higher selectivity towards the shape and charge of guest molecules.[1] Among all, CB7 stands out for its remarkably high binding affinity for neutral guests in water (similar to biotin-avidin pair) whereas similar binding affinities can only be obtained for host-guest complexation between molecules of high and opposite charges in other supramolecular systems.[114]

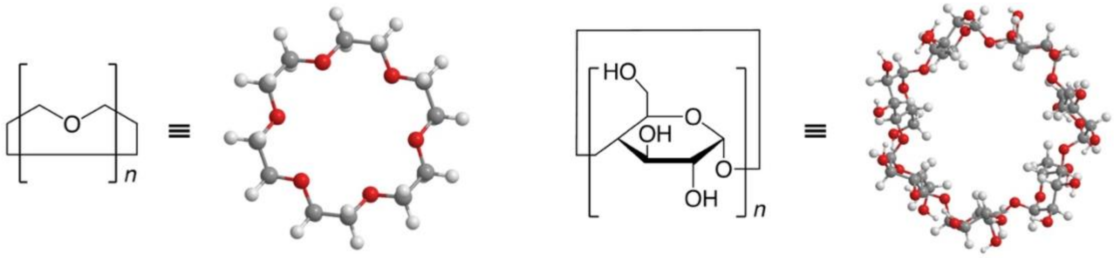

18-crown-6 **β-cyclodextrin**

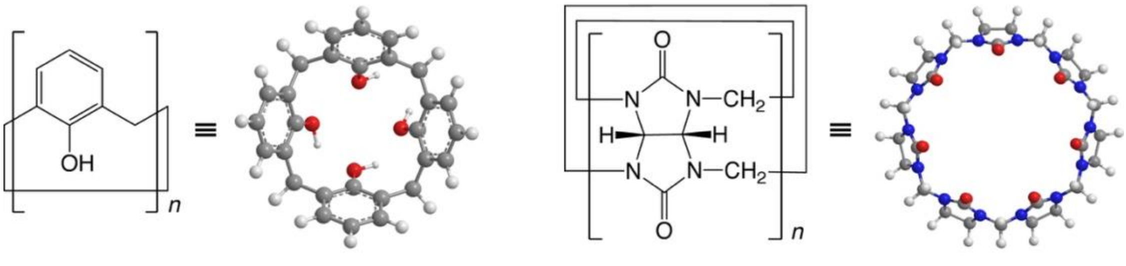

Calix[4]arene **Cucurbit[7]uril**

Figure 1.16. Chemical structures and molecular models (top view) of different macrocycles. (Colour code: grey = C atom, white = H atom, red = O atom and blue = N atom.)

1.11 Synthesis of CBs

The first CB homologue (CB6) was reported by Behrend and co-workers[115] as a condensation product of glycoluril and formaldehyde in 1905 but the existence of CBs was not widely known until Mock and co-workers[116] reported the molecular structure of CB6 (i.e. 6 glycoluril units bound together by 12 methylene bridges) in 1981. The name "cucurbituril" was proposed by Mock for the resemblance of the CB molecular structure to a pumpkin, which belongs to the plant family cucurbitaceae.[116] In 2000-2002, the research groups of Kim[117] and Day[118,119] reported the synthesis and isolation of other CB homologues, including CB5, CB7, CB8 and CB10·CB5 (i.e. CB5 encapsulated within the cavity of CB10), with different number of glycoluril units (Figure 1.17), by modifying the reaction conditions such as reagent (H_2SO_4/HCl), temperature (80-100 °C) and time (10-100 h).[120,121] The isolation of CB homologues is based on their extent of solubilities in water, water/methanol and diluted HCl, with CB6 being the major product.[120]

CB10 can be isolated from CB10·CB5 (Figure 1.18) via competitive guest binding to displace CB5 and subsequent removal of the new guests. The first isolation was performed by Issacs and co-workers in 2005,[122,123] using an excess amount of melamine diamine to form a 2:1 complex with CB10. The two guests were then removed by washing with methanol and reaction with acetic anhydride, followed by washing with methanol, dimethyl sulfoxide and water. A few years later, a simpler approach was reported by Day and co-workers[124] in which the commercially available 1,12-diaminododecane was used to displace CB5 at low pH. 1,12-diaminododecane was removed by repetitive washing with NaOH/methanol solution and CB10 was recrystallised from HCl.

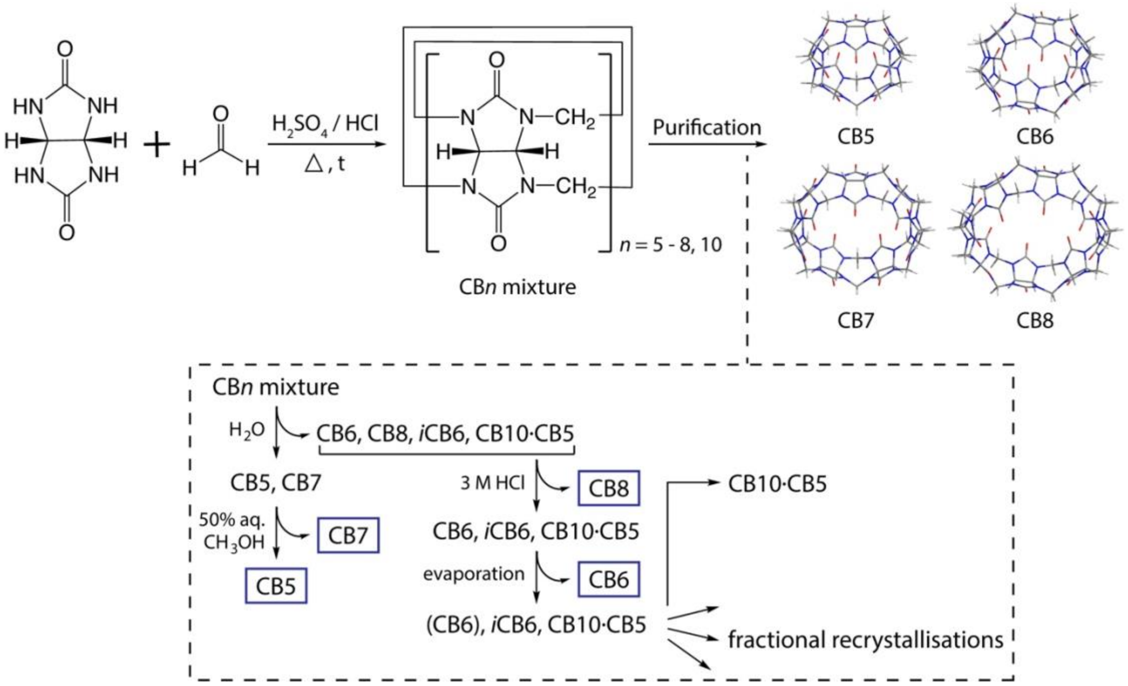

Figure 1.17. General synthesis and isolation of CBs, showing the four smallest CB homologues (CB5 - 8). *i*CB6 is the abbreviation for inverted CB6. Curved arrows indicate precipitation. The purification step is reproduced with permission from ref. 120. Copyright 2012 The Royal Society of Chemistry.

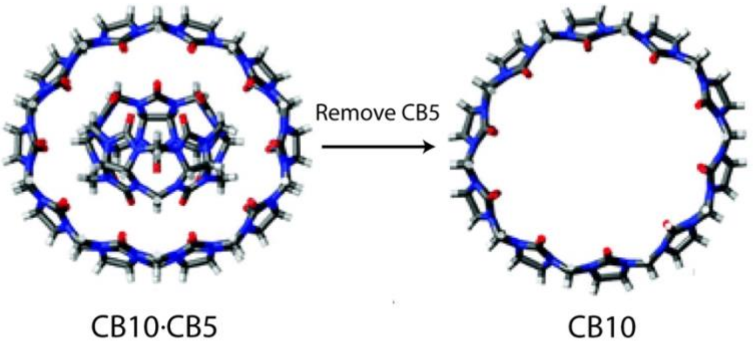

Figure 1.18. X-ray crystal structure of CB10·CB5 (left) and CB10 (right). Reproduced with permission from ref. 123. Copyright 2009 The Royal Society of Chemistry.

The larger members of the CB family, CB13, 14, 15, which adopt twisted conformations, have been isolated in 2013 and 2016 (Figure 1.19, Table 1.1).[125,126] The recent discovery of the twisted CB13-15 indicates there is a trace amount of larger CB homologues formed in the course of CB synthesis, which is still based on the acid-catalysed condensation of glycoluril and formaldehyde reported by Behrend to date.

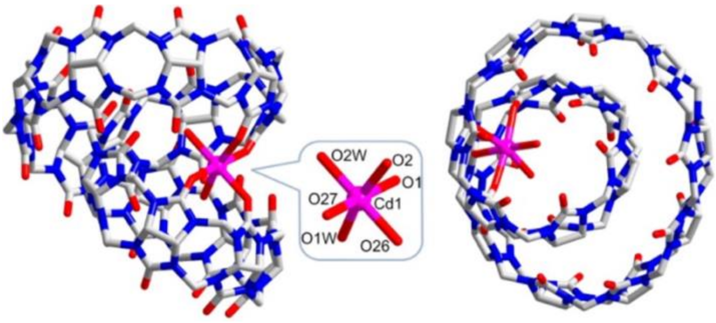

Figure 1.19. Side (left) and top view (right) of the X-ray crystal structure of Cd^{2+}/CB15 complex. CB15 is the current largest member of the CB family. Reproduced with permission from ref. 126. Copyright 2016 American Chemical Society.

Table 1.1. Timeline of the discovery of homologues in the main CB family (CB derivatives are excluded). Reproduced with permission from ref. 121. Copyright 2015 The Royal Society of Chemistry.

Year	CB homologue	Research group	Ref.
1905	CB6 (not structurally known)	Behrend	115
1981	CB6	Mock	116
2000	CB5, 7, 8	Kim	117
2002	CB10·CB5	Day	119
2005	CB10	Issacs	122
2013	CB14	Tao	125
2016	CB13, 15	Tao	126

Apart from the main CB family, numerous CB*n* derivatives, including functionalised CB*n*[127–133], inverted CB*n* (*iCBn*)[134], nor-*seco*-CB*n*[135,136] and congeners such as bambus[6]uril and hemicucurbit[*n*]uril[137,138], have also been synthesised by various research groups since the first synthesis of CB derivatives (decamethyl-CB5) by Stoddart and co-workers[139] in 1992. Details on the synthesis and structures of CB derivatives can be found in recent reviews.[121,140]

1.12 Fundamental properties of CBs

CBs are defined by their characteristic rigid and highly symmetric structures, with two negatively charged carbonyl portals and a hydrophobic cavity. The functionality of CBs as cation-receptors is illustrated by the electron-rich carbonyl oxygens at the portals in the electrostatic potential map (Figure 1.20).[121,141] The non-dipolar nature of CBs and the lack of functional groups and lone electron pairs pointing towards the inside of the cavity result in limited hydrogen bonding interactions and hence a highly hydrophobic cavity.[121,141] The electrostatic potentials at the portals and inside the cavity of CBs are significantly more electronegative than CDs, CBs have a distinct preference to bind to cationic guests over neutral guests and even more over anionic guests, in contrast to CDs which exhibit a preference for neutral or anionic guests.[113]

Similar to other macrocycles (e.g. CDs), different members in the CB family have the same height (0.91 nm) but their size (portal diameter, cavity diameter, outer diameter and cavity volume) increases systematically with the number of glycoluril units (Figure 1.21, Table 1.2). Despite CB15 being the current largest member of the CB family in terms of number of glycoluril units (Figure 1.19), CB10 remains as the homologue with the largest effective cavity size (Figure 1.18). The number of main CB family members have outweighed that of CDs with CB6, 7, 8 having comparable cavity volumes to α, β, γ-CD respectively. The CB portals are approximately 0.2 nm smaller than the equatorial regions which restrict the size of guests binding to CB. Interestingly, CB*n* with an odd number of *n* (i.e. *n* = 5, 7) have fairly good water solubility of 20-30 mM (comparable to β-CD) but those with an even number of *n* (i.e. *n* = 6, 8, 10) have poor water solubility. Nonetheless, the solubility of CBs can be improved in acidic solutions or in the presence of metal cations or upon formation of inclusion complexes with amphiphilic guests.[120,123]

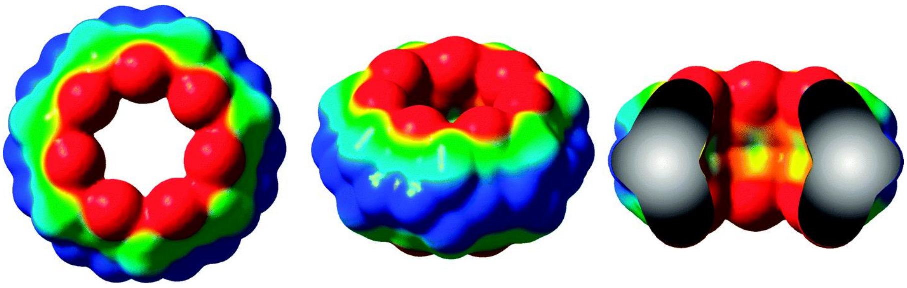

Figure 1.20. Electrostatic potential map (top and side view) of CB7, showing the negatively charged carbonyl regions (red) and the electron-deficient equatorial region (blue). Reproduced with permission from ref. 121. Copyright 2015 The Royal Society of Chemistry.

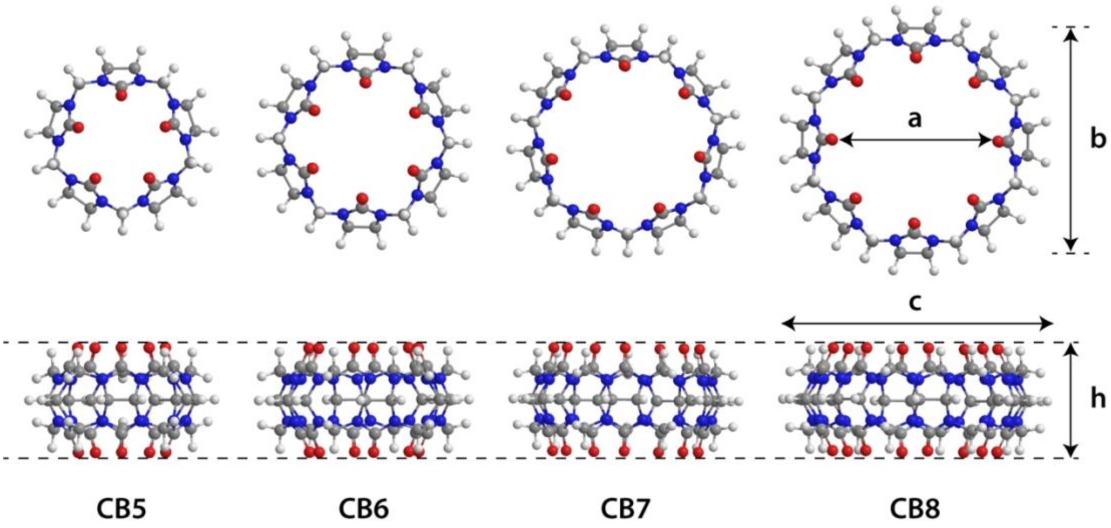

Figure 1.21. Molecular structures (top and side view) of major CB*n* (*n* = 5 – 8) homologues, with increasing cavity size from CB5 to CB8. a = portal diameter, b = cavity diameter, c = outer diameter and h = height of CB.

Table 1.2. Structural parameters (a = portal diameter, b = cavity diameter, c = outer diameter and h = height), volume and water solubility (S_{water}) of CBs and CDs.

	a (Å)	b (Å)	c (Å)	h (Å)	Volume ($Å^3$)	S_{water} (mM)
CB5	2.4[142]	4.4[142]	13.1[142]	9.1[142]	82[142]	20 - 30[142]
CB6	3.9[142]	5.8[142]	14.1[142]	9.1[142]	164[142]	0.018[142]
CB7	5.4[142]	7.3[142]	16.0[142]	9.1[142]	279[142]	20 - 30[142]
CB8	6.9[142]	8.8[142]	17.5[142]	9.1[142]	479[142]	< 0.01[142]
CB10	10.0[123]	11.7[123]	20.0[121]	9.1[123]	870[123]	< 0.05[122]
α-CD	4.7[143]	5.3[143]	14.6[143]	7.9[143]	174[143]	145[143]
β-CD	6.0[143]	6.5[143]	15.4[143]	7.9[143]	262[143]	18.5[143]
γ-CD	7.5[143]	8.3[143]	17.5[143]	7.9[143]	427[143]	232[143]

The likelihood of CB to form a host-guest inclusion complex can be estimated from the packing coefficient (PC),[144] which is the volume ratio of the guest molecule to the inner cavity (i.e. the confined volume between the two carbonyl portals) of CB.[141] An optimum PC of 55% was found to give the best binding affinity for host-guest complexes in solution, with a lower or higher PC resulting in a lower binding affinity.[144] Depending on the inner cavity volume, CB*n* can host between 2 to 22 water molecules as estimated from the 55% PC and similar results were obtained using molecular dynamics (MD) simulations (Table 1.3). The number of water molecules (N_{water}) CB5 and CB8 can accommodate is analogous to α-CD and γ-CD respectively. β-CD can accommodate 6-7 water molecules which is in between CB6 and CB7, though CB6 is analogous to α-CD in terms of cavity size.[141]

Table 1.3. Occupancy of the inner cavity of CBs by water molecules.[141] [a] The potential energy difference for removal of all water molecules in the CB cavity and transfer of those to a spherical cavity in bulk water.[121]

	Inner cavity (Å^3)	N_{water}		ΔE_{pot}[a] (kJ mol^{-1})
		MD simulations	PC analysis	
CB5	68[141]	2[141]	2[141]	-41.6 ± 28.8[121]
CB6	142[141]	4[141]	4[141]	-51.1 ± 29.0[121]
CB7	242[141]	7[141]	8[141]	-102.4 ± 31.3[121]
CB8	367[141]	10[141]	12[141]	-66.2 ± 10.7[121]
CB10	691[141]	20[141]	22[141]	--

The water molecules inside the weakly polarisable CB cavity are of high energy (i.e. enthalpically and entropically unfavourable) due to the weak dispersion interactions and the deficiency of hydrogen bonding.[121] The release of high-energy water molecules from the CB cavity is the main driving force for the formation of host-guest inclusion complexes in aqueous solution (Figure 1.22). The gain in potential energy for removing all water molecules from the CB cavity is determined by the compromise between the absolute number of water molecules and their engagement in hydrogen bonding.[114] The potential energy of individual water molecules decreases with increasing cavity size as there is a higher chance to form hydrogen bonds. However, the maximum potential energy is reached for CB7 which does not allow the water molecules within its cavity to arrange in an energetically stable hydrogen-bond network as in the case of CB8 (i.e. structurally similar to bulk water).[114,121] This may provide a rationale for the ultra-high binding affinities of CB7 despite the fact that it has a smaller cavity size than CB8.

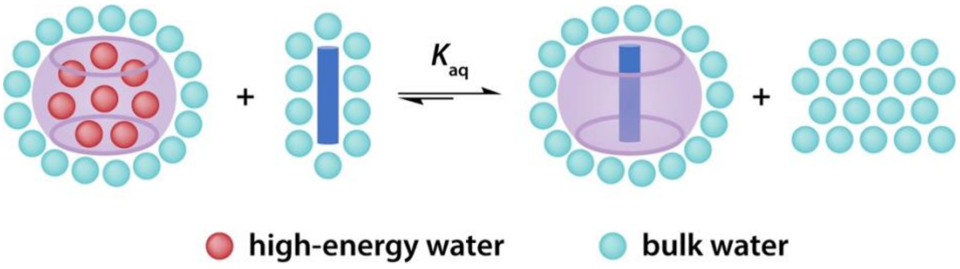

Figure 1.22. The release of high-energy water molecules from the CB cavity upon host-guest complexation. Reproduced with permission from ref. 114. Copyright 2012 American Chemical Society.

1.13 Host-guest chemistry of CBs

The molecular recognition properties of CBs have not only sparked interests in fundamental research but also practical applications, including but not limited to, drug delivery[145], catalysis[146], reaction containers[147], molecular machines[148] and sensing[149]. The host-guest chemistry of CBs has been widely studied since the first report of host-guest complexations between alkylammonium and alkyldiammonium ions and CB6 in aqueous formic acid by Mock and Shin[150] in 1983, two years after they have identified the CB6 molecular structure[116]. The first X-ray structure of CB host-guest complex was reported by Freeman and co-workers[151] shortly after the work of Mock and Shin (Figure 1.23).

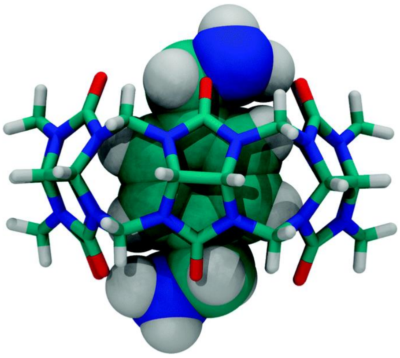

Figure 1.23. X-ray structure of the host-guest complex between CB6 and *p*-xylylenediammonium ion. Reproduced with permission from ref. 121. Copyright 2015 The Royal Society of Chemistry.

The binding of guest molecules to CBs is due to a combination of driving forces, the hydrophobic effect (i.e. the release of high-energy water molecules from the cavity), the ion-dipole interactions and hydrogen bonding between the electron-rich carbonyl portals and the guest molecules, unlike other macrocycles such as CDs, in which the hydrophobic effect alone dominates.[152]

In general, the smaller CB*n* (*n* = 5 – 7) homologues form 1:1 binary complexes with the guest molecules while the larger CB8 can also form 1:2 and 1:1:1 ternary host-guest complexes (Figure 1.24).

Figure 1.24. Schematic illustrations showing 1:1, 1:2 and 1:1:1 CB host-guest inclusion complexes.

For instance, CB5, the smallest member in the CB family, can bind to alkali, alkaline earth, transition metal and ammonium cations (e.g. Na^+, Ca^{2+}, Fe^{3+}, NH_4^+),[153,154] and gas molecules (e.g. N_2, O_2, N_2O, CO_2 and CH_4)[155] with 1:1 stoichiometry. CB6, the first and most-abundant CB member, also binds strongly to aliphatic amines (e.g. formation of rotaxanes and pseudorotaxanes)[156] and five-membered aromatic rings (e.g. thiophenes)[150] though it is usually not able to accommodate six-membered aromatic rings.[157]

The larger CB members, CB7 and CB8, have been extensively studied in the last couple of decades for their unique host-guest binding properties. CB7 shows ultra-high binding affinities towards a wide variety of guest molecules such as ferrocene[142,158,159], adamantanes[160,161] and diamantanes[162] derivatives which have reached and even surpassed that of the biotin-avidin pairs (~10^{15} M^{-1})[163]. A remarkable binding constant between CB7 and diamantine diammonium ion (7.2×10^{17} M^{-1} in D_2O and 1.9×10^{15} M^{-1} in 50 mM NaO_2CCD_3), which is caused by the optimal size and shape complementarity between the rigid CB7 cavity and the diamantine core, was reported by Issacs and co-workers[162] in 2014 (Figure 1.25). CB7 is also well-known to bind a wide range of aromatic guests.

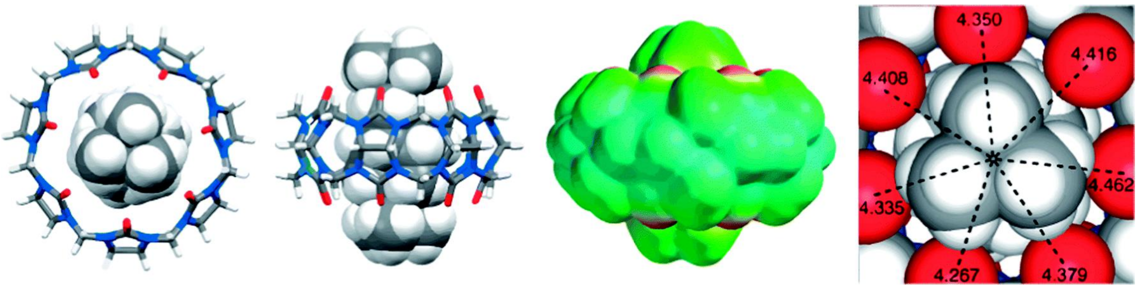

Figure 1.25. X-ray structure of the host-guest complex between CB7 and diamantine diammonium ion (top and side view). Reproduced with permission from ref. 162. Copyright 2014 WILEY-VCH Verlag GmbH & Co. KGaA, Weinheim.

CB8 is characterised by its ability to host two guest molecules, with its inner cavity volume being about 1.5 times larger than CB7. A stable CB8 ternary complex can be achieved when one guest is electron-rich (π-acceptor) and the other is electron-deficient (π-donor).[164] The first 1:1:1 ternary complex was reported by Kim and co-workers[165] in 2001, just a year after the isolation of CB8 from the CB*n* mixture. The electron-deficient guest, methyl viologen (MV^{2+}), first binds to CB8 before the electron-rich second guest, 2,6-dihydroxynaphthalene, which cannot bind to CB8 alone, is encapsulated via charge-transfer interactions. The use of CB8 in supramolecular polymers and 3D networks has also been demonstrated.[166,167]

The examples above are to show the wide variety of guest molecules available to CBs while extensive reviews on the host-guest chemistry of CBs and their applications can be found in recent publications.[113,120,121,157,168–170]

1.14 Capping of CBs by Au NPs

While the idea of encapsulating Au NPs within the CB cavity was suggested by Corma and co-workers[171] in 2007, the capping of CBs by Au NPs has not been reported until Lee and Scherman[1] synthesised Au NPs via $NaBH_4$ reduction of $HAuCl_4$ in the presence of

CB5 and demonstrated the feasibility to form Au NP: CB5 nanoaggregates both before and after the reduction of $HAuCl_4$. They also investigated the capping with different CB*n* homologues (*n* = 5 – 8) via formation of metastable Au NPs in follow-up work.[172] The self-assembled Au NPs can singly-cap (non-bridging) or doubly-cap (bridging) CBs with a constant spacing of 0.91 nm (i.e. height of CBs) between the adjacent Au NPs depending on the ratio of Au NP: CB (Figure 1.26). CBs bind to the surface of Au NPs via their electron-rich carbonyl portals as in the case of attaching CBs onto a flat Au surface reported by Li and co-workers[173]. The electron-rich carbonyl portals donate electrons to the surface of Au NPs upon binding and weaken the C=O bond.[1] The capping of CBs by Au NPs is mainly driven by the enthalpic gain from the interaction between carbonyl and Au, and the entropic gain from the release of surrounding water molecules.[1] The interaction of Au NPs with CBs is stronger than other macrocycles due to their rigid and highly symmetric structures.[172,174]

The kinetics of Au NP: CB5 nanoaggregates as a function of CB5 concentration was studied shortly after the initial report on capping of CBs by Au NPs.[2] At high CB5 concentration (1:80 Au NP: CB5), open and elongated chain-like structures were initially formed before joining together as quasi-fractal networks (Figure 1.27a). The colliding particles cannot reach the centre of the nanoclusters but coagulate with the outermost particles, following the diffusion-limited colloidal growth regime. On the other side, slow formation of compact nanoclusters was observed at low CB5 concentration (1:60 Au NP: CB5) which follows the reaction-limited colloidal growth regime (Figure 1.27b).

Nevertheless, the formation of precise nanogaps of 0.91 nm (> 0.7 nm where quantum tunnelling takes place) between Au NPs within the nanoaggregates results in greatly enhanced electric field (see section 1.4) and thereby leads to important plasmonic applications such as SERS (see section 1.15).

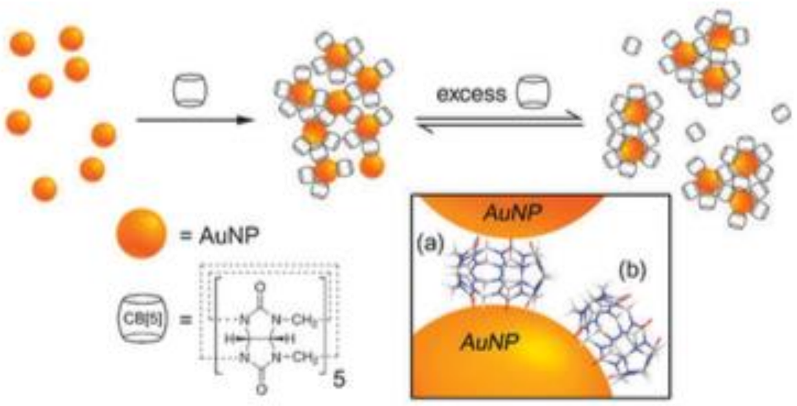

Figure 1.26. Schematic illustration of Au NP: CB5 nanoaggregates. Either one or both carbonyl portals of CB5 can be capped by the Au NPs. Reproduced with permission from ref. 1. Copyright 2010 The Royal Society of Chemistry.

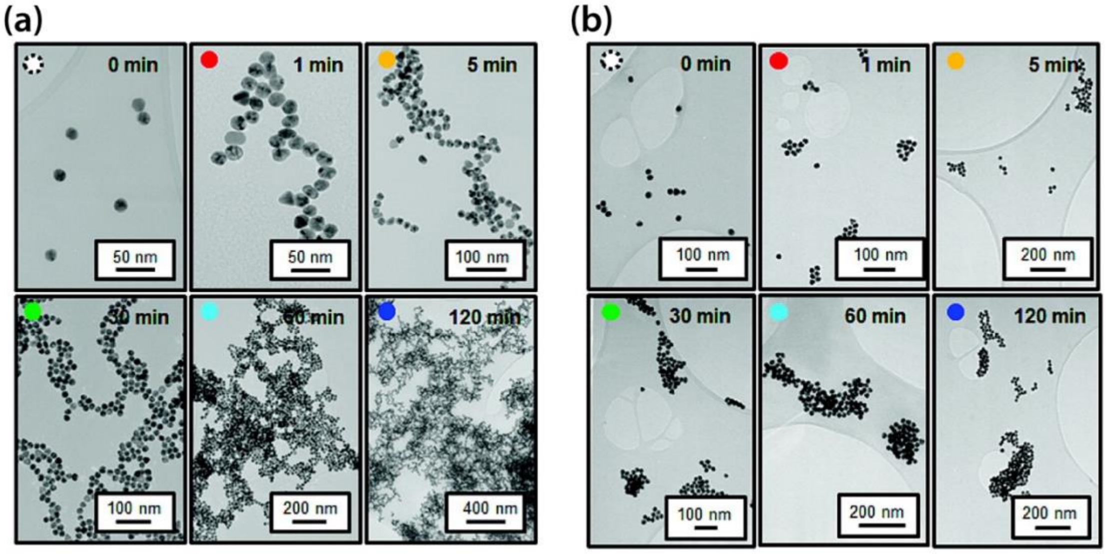

Figure 1.27. TEM images of (a) 1:80 (diffusion-limited) and (b) 1:60 (reaction-limited) Au NP: CB5 nanoaggregates formed at the indicated time. Reproduced with permission from ref. 2. Copyright 2011 American Chemical Society.

1.15 Au NP: CB nanoaggregates as SERS substrates

The ability of CBs to simultaneously mediate the formation of precise plasmonic nanojunctions and recognise small molecules via host-guest complexation is particularly important for the detection of analyte targets with low affinities to Au surface. The Au NP: CB nanoaggregates are promising candidates as powerful SERS substrates and their applications have been recently explored (Table 1.4).

The first use of Raman and SERS to characterise and differentiate major CB*n* (*n* = 5 – 8) homologues was reported by Mahajan and co-workers[175] in 2010. The two major characteristic peaks of CBs at ~450 and 830 cm^{-1} observed in the Raman spectra are attributed to the ring scissor and ring deformation modes respectively (Figure 1.28). Interestingly, the CB*n* characteristic peaks show systematic (red- and blue-) shifts as the ring size of CB increases. Similar results were observed in the SERS spectra of Au NP: CB nanoaggregates which paved the way for the subsequent SERS applications.

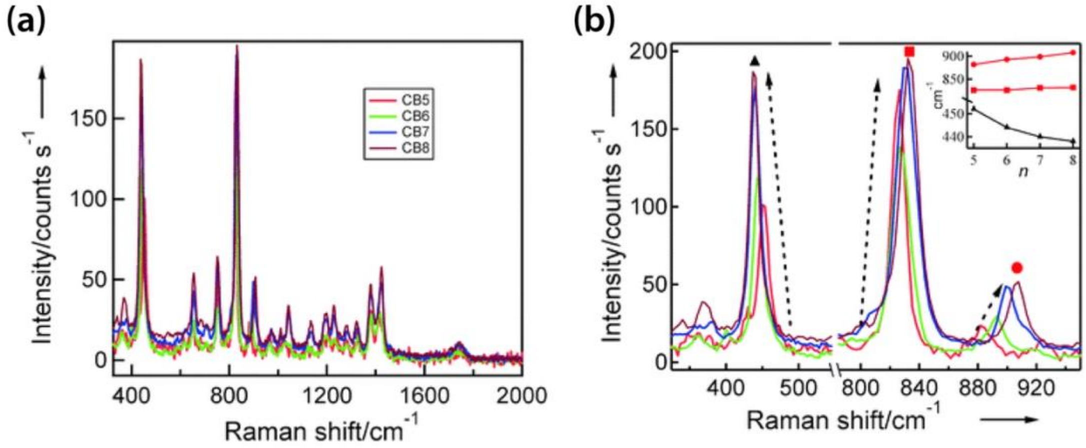

Figure 1.28. (a) Full range and (b) zoom-in Raman spectra of CB*n* (*n* = 5 – 8) showing systematic peak shifts as the number of glycoluril unit increases. Reproduced with permission from ref. 175. Copyright 2010 The PCCP Owner Societies.

The SERS detection of a dye molecule, rhodamine 6G (R6G), based on the formation of precise plasmonic nanojunctions between Au NPs and the size-specific host-guest binding of CBs was demonstrated in 2011.[2] For instance, CB7 can form 1:1 host-guest complexes with R6G which cannot be accommodated by the small cavity of CB5. The combined use of CB5 to align and aggregate Au NRs, and CB7 to form host-guest complexes with R6G was also reported in 2014.[176] CBs were preferentially bound to the (111) end facet of the NRs as the (100) longitudinal facet was strongly capped by CTAB and cannot be easily displaced.

Scherman, Abell and co-workers[177] reported a novel one-step fabrication of microcapsules held together by 1:1:1 ternary host-guest complexes of CB8 with methyl viologen (MV^{2+}) as the electron-deficient first guest and naphthol-containing copolymers as the electron-rich second guest at the liquid-liquid interface of microdroplets. This is an illustrative example of indirect interaction between Au NPs and CBs via host-guest complexation with the molecules anchored on the surface of Au NPs, in contrast to the direct interaction of Au NPs with the CB portals.[178] The microcapsules could potentially be used as SERS substrates for the encapsulated molecules. In addition, Scherman and co-workers[3] reported the use of Au NP: CB8 nanoaggregates as solution-based SERS substrates to detect trace amount of polyaromatic hydrocarbons (PAHs), including anthracene, 2-naphthol, phloroglucinol and 2,3-naphthalenediol, which is a class of pollutants, via formation of 1:1:1 ternary complexes with CB8 and MV^{2+} (Figure 1.29a). In a separate study, they also monitored the phototransformation of trans-diaminostilbene (trans-DAS) partly encapsulated in CB7 and CB8 by SERS.[4] Trans-DAS forms 1:1 inclusion complexes with CB7 but 2:1 complexes with the larger CB8, resulting in different reactions, i.e. photoisomerisation into cis-DAS in CB7 and photodimerisation into syn-1a,2a,3b,4b-tetrakis(4-aminophenyl)cyclobutane (syn-TCB) in CB8, upon UV excitation (Figure 1.29b). It is worth noting that the photodimerisation of trans-DAS in CB8 takes place at pH 7 whereas there is no photoreaction in basic (pH 11) or acidic (pH 5) solution. The uncharged DAS amines at pH 11 remain as 2:1 complexes while they are protonated at pH 5 and form 1:1 complexes with CB8 due to strong charge repulsion.

The feasibility of multiplexed SERS detection of neurotransmitters, including dopamine (DA), epinephrine (EPI) and serotonin (5HT), of ~1 μM levels spiked in water and synthetic urine using Au NP: CB7 nanoaggregates as substrates has been demonstrated by Scherman and co-workers[5] (Figure 1.29c). However, it is very challenging to visualise the contribution from the individual neurotransmitter to the SERS spectra. Very recently, it has been shown that the detection limit of analyte molecules such as tetrahydrocannabinol encapsulated by CBs in aqueous solution can be lowered by removing excess binding sites.[179]

Table 1.4. SERS substrates based on aqueous self-assembly of Au NP: CB nanoaggregates.

SERS substrate	Analyte molecule	Detection limit	Ref.
Au NP: CB7	R6G	-	2
Au NP: CB8	PAHs (anthracene, 2-naphthol, phloroglucinol and 2,3-naphthalenediol)	1 μM	3
Au NP: CB7 / Au NP: CB8	Trans-DAS, cis-DAS and syn-TCB	-	4
Au NP: CB7	Neurotransmitters (DA, EPI and 5HT)	~ 0.5 μM	5

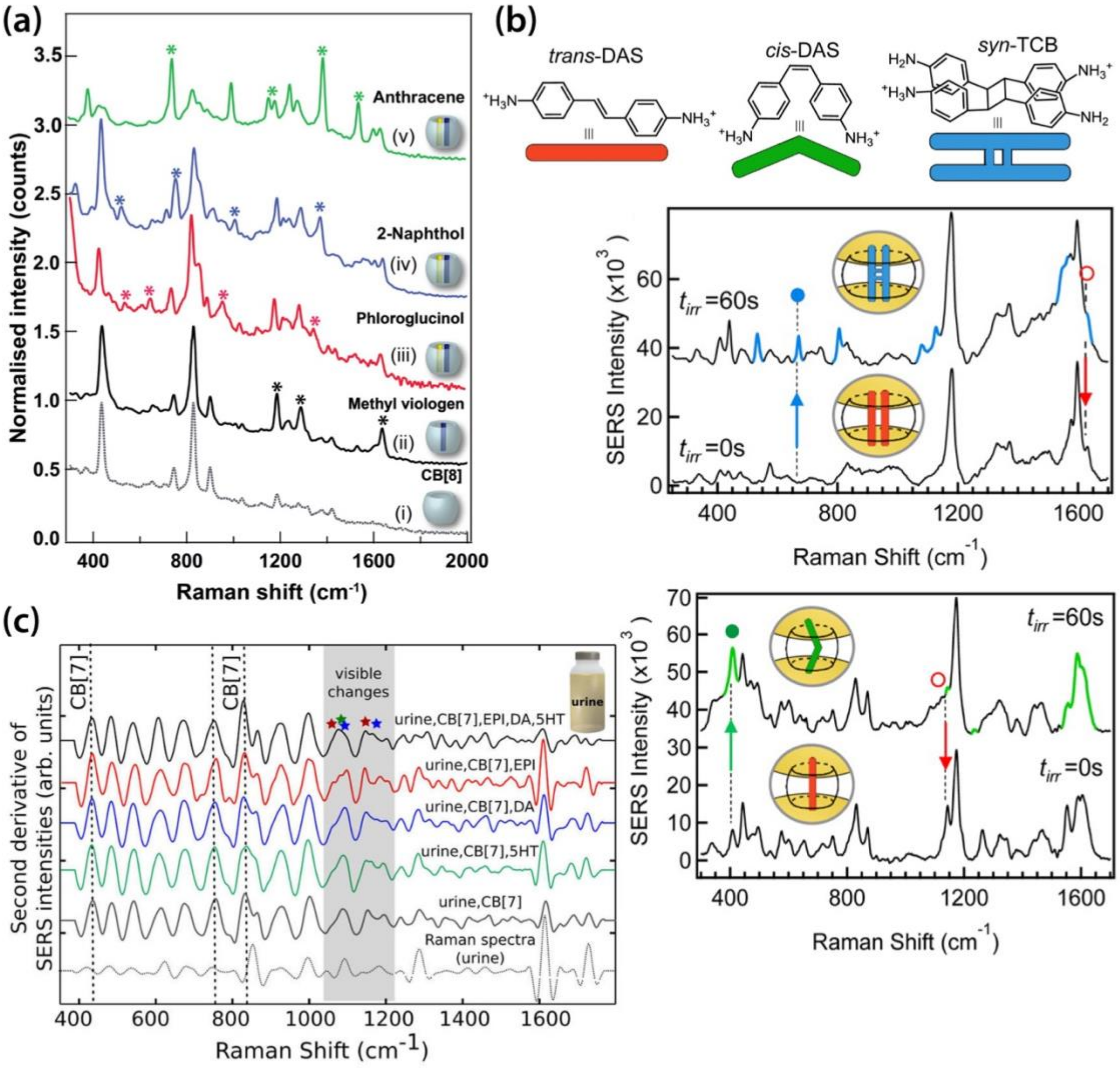

Figure 1.29. (a) SERS detection of PAHs with Au NP: CB8 nanoaggregates and an electron-deficient first guest MV^{2+}. Reproduced with permission from ref. 3. Copyright 2012 American Chemical Society. (b) SERS monitoring of photoisomerisation of trans-DAS into cis-DAS within Au NP: CB7 nanoaggregates, and photodimerisation of trans-DAS into syn-TCB within Au NP: CB8 nanoaggregates when excited with UV light. Reproduced with permission from ref. 4. https://pubs.acs.org/doi/full/10.1021/nl403164c. (Note: further permissions related to the material excerpted should be directed to American Chemical Society.) (c) Multiplexed SERS sensing of neurotransmitters spiked into synthetic urine. Reproduced with permission from ref. 5. Copyright 2014 Nature Publishing Group.

Apart from aqueous Au NP: CB nanoaggregates, solid-based SERS substrates exploiting the plasmonic nanojunctions defined by CBs have also been explored. For instance, Li and co-workers[180] investigated the SERS detection of ferrocene, which has no affinity for Au surfaces but strongly binds to CBs, via deposition of Au NP: CB7 dimers on a glass substrate. A localised EF up to 10^9 was achieved but the dimers were in random orientations and non-uniformly distributed. Baumberg and co-workers[181] used NPs on mirror geometry (NPoM), i.e. Au NPs on Au film sandwiched by CB7, to study the presence or absence of various guest molecules within the CB7 cavity via SERS. The SERS signals of Au NP: CB nanoaggregates deposited on different underlying substrates (Au, Si and SiO_2) were also studied.[182] Optimal SERS signals were observed for the Au substrate which was only 2-fold higher than that of the glass substrate.

1.16 Research objectives

The aim of the research was to provide new fundamental insights into aqueous self-assembly of Au NP: CB nanoaggregates and exploit the system for rapid detection of multiple trace analyte molecules, in order to develop a high-performance SERS sensing platform for potential applications in different areas such as homeland security, environmental monitoring, on-site healthcare monitoring and early disease diagnostics. The objectives were as follows:

- To fabricate SERS substrates via aqueous self-assembly of Au NPs mediated by CBs, as to provide precise plasmonic hotspots and hence strong and reproducible SERS signals of the analyte molecules.
- To identify, using experimental and computational approaches, analyte molecules of fundamental and practical interests, as to investigate the novel CB host-guest complexes and their impacts on the formation of Au NP: CB nanoaggregates.

- To demonstrate the potential SERS detection of neutral and bulky molecules as to investigate the feasibility of extending the Au NP: CB sensing scheme to detect larger sets of analyte molecules that are of practical interests.
- To demonstrate the SERS detection of analyte molecules with different CB homologues as to study the role of CB cavity size on the enhancement of SERS signals and further exploit the molecular recognition properties of CBs in the Au NP: CB nanoaggregates.
- To demonstrate multiplexed detection of isomers as to investigate the ability of the Au NP: CB SERS system to distinguish structurally similar molecules for potential applications such as drug monitoring and quality control.
- To demonstrate the SERS detection of analyte molecules in complex media, as to investigate the possible signal perturbations from background molecules, which is relevant to molecular recognition in field and clinical applications.

1.17 Thesis structure

Chapter 1 described the motivations of the research and discussed the existing techniques for the detection of analyte molecules of interests. The fundamental background of RS and SERS was introduced with particular focus on the rationale behind the enhancement of the SERS signals. Other relevant optical techniques were also briefly introduced. The fabrication of SERS substrates was described together with the existing synthetic methods and properties of Au NPs and CBs, as well as the interactions between Au NPs and CBs via comparisons with classical supramolecular hosts. Previous examples of Au NP: CB nanoaggregates as SERS substrates were also critically reviewed.

Chapter 2 listed all materials used in this research, followed by full descriptions of the sample preparations, and the computational and characterisation methods used to quantify the key binding parameters between CBs and the analyte molecules. The quantitative SERS sensing of the host-guest complexes was described in detail.

Chapter 3 reported the supramolecular chemistry of CB7 and an explosive marker, 2,4-dinitrotoluene (DNT), using experimental and computational techniques. The importance of the formation of precise plasmonic nanojunctions mediated by CBs in SERS was demonstrated using NaCl as aggregating agent for Au NPs in a control experiment. The surface-enrichment effect of CB7 was illustrated by a competitive binding experiment with a stronger CB7 binder, 1-adamantylamine. In addition, the selectivity and robustness of the SERS sensor were demonstrated with a structurally similar nitroaromatic explosive, picric acid, and organic contaminants, 4-mercaptobenezoic acid and 4-mercaptophenylboronic acid, respectively.

Chapter 4 reported the supramolecular chemistry of CB*n* (*n* = 7, 8) and three structurally similar drug molecules in the purine family, methylxanthines (MeX), including caffeine (CAF), theobromine (TBR) and theophylline (TPH), using experimental and computational techniques. The quantitative SERS sensing of MeX was demonstrated with different CB homologues, CB7 and CB8, via formation of Au NP: CB nanoaggregates. The multiplexing ability of the SERS sensor was also demonstrated with the larger CB homologue, CB8, and the two isomers, TBR and TPH.

Chapter 5 reported the supramolecular chemistry of CB7 and an important biomarker, creatinine (CRN), using experimental and computational techniques. A novel multi-spectroscopic sensing approach (i.e. UV-Vis spectroscopy and SERS) was developed to quantify CRN in water and highly diluted synthetic urine (SU) of clinically relevant concentrations with the lowest detection limit among the state-of-the-art methods. The formation of Au NP: CB nanoaggregates in this system was also mediated by the neutralisation of surface charges on the citrate-capped Au NPs, in addition to the carbonyl portal binding of CB7 to the Au NP surface, as verified by the dynamic light scattering and zeta potential measurements. The tolerance to matrix effect (against the presence of proteins and other biomolecules) was then discussed by comparing the SERS signals of CRN after sequential dilutions of SU.

Chapter 6 provided the conclusions of the research outcomes and discussed the potential future work.

Chapter 2. Materials and Methods

This Chapter first listed the materials used in the experiments including storage and safety notes. The sample preparation methods were fully described, followed by the descriptions of the experimental and computational methods used to measure the binding parameters of cucurbit[*n*]urils (CB*n*) and the analyte molecules. Quantitative detection of the CB host-guest complexes via UV-Visible spectroscopy and surface-enhanced Raman spectroscopy (SERS) was described in the latter part of this Chapter.

2.1 Materials

40 nm gold nanoparticles (Au NPs) were purchased from nanoComposix (0.05 mg mL^{-1} in aqueous 2 mM sodium citrate, storage note: should be kept at 2 – 8°C). Gold (III) chloride trihydrate ($HAuCl_4$), sodium citrate tribasic dihydrate, paraformaldehyde, HCl, 2,4-dinitrotoluene (DNT), 1-adamantylamine ($AdNH_2$), picric acid (PA, safety note: should be kept wetted at all times), 4-mercaptophenylboronic acid (4-MPBA), 4 mercaptobenzonic acid (4-MBA), caffeine (CAF), theobromine (TBR), theophylline (TPH), creatinine (CRN), urea, uric acid, citric acid, sodium phosphate monobasic and albumin from human serum were purchased from Sigma-Aldrich. Methanol, ethanol and KCl were purchased from VWR. Glycoluril was purchased from Acros Organics. NaCl was purchased from Kanto Chemical. All chemicals were used as received without further purification. Milli-Q water was used in all experiments.

2.2 Synthesis of Au NPs

Au NPs (Au seeds) were first synthesised via the conventional Turkevich method[67] and grown to 40 nm according to literature with modifications[101] (see section 1.8).

2.2.1 Synthesis of Au seeds

99.5 mL of a 0.25 mM $HAuCl_4$ solution was refluxed in a 250 mL three-necked round-bottomed flask equipped with a condenser at 90℃ for 15 min. 0.5 mL of a 500 mM sodium citrate solution was then injected into the flask and refluxed until the colour of the solution turned ruby red.

2.2.2 Seeded growth of Au NPs

The Au seeds were cooled to 70℃, 0.67 mL of a 25 mM $HAuCl_4$ solution and 0.67 mL of a 60 mM sodium citrate solution were sequentially injected with a time interval of 2 min. This sequential injection process was repeated to gradually increase the size of Au NPs up to 40 nm (see Figure A.1 in appendix). It should be noted that larger Au NPs can be achieved via the dilution method[101].

Though the synthesised Au NPs were highly uniform, reproducible and cost-effective, commercial Au NPs were chosen for the subsequent SERS studies in this research as they are more readily available by us and other researchers, thus eliminating the variations between different laboratory set-up and increasing the reproducibility of the SERS data.

2.3 Synthesis of CBs

CB7 and CB8 were synthesised and isolated according to literature[113] (see Section 1.11) by Dr. William Peveler.

2.4 Preparation of synthetic urine

Synthetic urine (SU) mimicking the normal and excess CRN levels in human urine were prepared according to literature[183] with modifications. For 100 mL SU, 0.9 g urea, 16 mg uric acid, 0.5 g NaCl, 0.45 g KCl, 40 mg citric acid, 0.48 g sodium phosphate, 5 mg albumin from human serum and 0 - 300 mg CRN were dissolved in 90 mL water. The prepared SU was diluted with water for subsequent UV-Vis and SERS measurements.

2.5 Nuclear magnetic resonance spectroscopy

Nuclear magnetic resonance (NMR) measurements were performed to verify the formation of host-guest complexes between CBs and the analyte molecules. Chemical shifts (in ppm) were referenced to D_2O with $\delta = 4.79$ ppm for ^1H.

2.5.1 DNT

2 mM CB7 solution was prepared in D_2O. DNT was added to the CB7 solution with 1:1 or 1.2:1 molar ratio. PA was added to the CB7 solution with 1:1 molar ratio. The samples were sonicated for 3 hours. ^1H NMR spectra were measured using a Bruker Avance III 600 Cryo spectrometer.

2.5.2 MeX

1 mM CB7, CAF, TBR, TPH, CB7-CAF, CB7-TBR and CB7-TPH solutions with 1:1 molar ratio were prepared in D_2O. Similarly, 1 mM CB8, CAF, TBR, TPH, CB8-CAF,

CB8-TBR and CB8-TPH solutions with 1:1 molar ratio were prepared in 1 mM DCl. ^1H NMR spectra were measured using a Bruker Avance III 400 spectrometer.

2.5.3 CRN

4 mM CB7, CRN and CB7-CRN solutions with 1:1 molar ratio were prepared in D_2O. ^1H NMR spectra were measured using a Bruker Avance III 400 spectrometer.

2.6 Computer simulations

Computer simulations were performed to study the host-guest complexation between CBs and the analyte molecules. Restricted (closed-shell) models were used in all quantum mechanical calculations. The binding energy of an inclusion complex was calculated from the energy difference between the complex and the total energies of CB and analyte molecule optimised and calculated at the same level of theory.

2.6.1 DNT

Density functional theory (DFT) calculations were performed using Spartan'16 Parallel Suite. Force-field calculations were performed using Chem3D. Geometry optimisation was first performed using MMFF94, followed by full optimisation at the required level of theory (HF/3-21G, wB97X-D/6-31G* and wB97X-D/6-311+G**). Raman spectra were simulated at the HF/3-21G level of theory. A scaling factor of 0.90 was applied to correct the calculated vibrational frequencies.

2.6.2 MeX

DFT calculations were performed using Spartan'16 Parallel Suite. Force-field calculations were performed using Chem3D. Geometry optimisation was first performed using MMFF94, followed by full optimisation at the required level of theory (wB97X-D/6-31G*).

2.6.3 CRN

DFT calculations were performed using Gaussian 09 using the UCL computer cluster Thomas. Force-field calculations were performed using Chem3D. Geometry optimisation was first performed using MMFF94, followed by full optimisation using dispersion-corrected functional (wB97X-D/6-31G* and CPCM/wB97X-D/6-31G*). Raman spectra were simulated at CPCM/wB97X-D/6-31G* level of theory.

2.7 Isothermal titration calorimetry

Isothermal titration calorimetry (ITC) measurements were performed at 25°C to study the binding equilibria between CB7 and DNT using a MicroCal VP-ITC. 0.1 mM DNT solution was prepared in (unbuffered) water to which a 1.0 mM CB7 solution was titrated. 27 consecutive injections of 10 μL were typically used, and all solutions were degassed before titration. The first data point was removed from the data set before curve fitting according to a one-set-of-sites model. The standard free energy ($\Delta G°$) and entropy changes ($\Delta S°$) were calculated from the complex stability constant (K_a) and molar reaction enthalpy ($\Delta H°$) according to $\Delta G° = -RT \ln K_a = \Delta H° - T\Delta S°$.

2.8 UV-Visible spectroscopy

UV-Vis spectroscopy was used to quantify the binding constants of CB7 and the analyte molecules, and the concentrations of CRN in water and diluted SU.

2.8.1 DNT

For CB7-DNT binding studies, 10 μM DNT solution was prepared in water and placed in a cuvette with 1 cm optical path length to which small amounts of a 1 mM CB7 stock solution were added up to 4-5 equivalents. The CB7 concentration was increased gradually while that of DNT was kept approximately constant. The UV-Vis binding titrations were performed using a Varian Cary 4000 UV-Visible spectrophotometer.

2.8.2 CRN

For CB7-CRN binding studies, 50 μM CRN solution was prepared in water and placed in a cuvette with 1 cm optical path length to which small amounts of a 5 mM CB7 stock solution were added up to 2 equivalents. The CB7 concentration was increased gradually while that of CRN was kept approximately constant. The UV-Vis binding titrations were performed on a Shimadzu UV-3600 UV-Vis-NIR spectrophotometer.

For quantitative sensing of CRN, the prepared SU (or water) with varying CRN concentrations of 0 – 300 mg dL^{-1} (see section 2.4 for SU preparation) was diluted with water before adding 1 mL to 1 mL of a 0.2 mM CB7 solution in a 2 mL Eppendorf tube. 20 μL of the premixed CB7-CRN solution was then added to a 180 μL Au NP solution in a 0.5 mL tube to give a final CRN concentration of 0 – 1.50 μg mL^{-1} (2000 or 5000-fold diluted). Controls were prepared in the absence of CB7. The sample solution was vortexed for 30 s before placing 100 μL into a cuvette with 1 cm optical path length. Five spectra were measured for each sample using a Boeco S-200 Vis spectrophotometer and an averaged value was calculated.

2.9 Transmission electron microscopy

A 0.2 mL drop of the pre-mixed 0.1 mM CB7-DNT stock solution was added to a 1.8 mL Au NP solution in a 2 mL Eppendorf tube to form Au NP-CB7-DNT nanoaggregates. The sample solution was vortexed for 30 s before drop-casting one or two 5 μL drops onto a C-coated 300-mesh Cu grid and drying with Ar gas. The transmission electron microscopy (TEM) images were taken using a JEOL JEM-2100 system with an accelerating voltage of 200 kV.

2.10 Dynamic light scattering and zeta potential measurements

1 mL of the CRN stock solution with varying concentration of 0 – 30 μg mL^{-1} was added to 1 mL of a 0.2 mM CB7 solution in a 2 mL Eppendorf tube. 0.2 mL of the pre-mixed solution was then added to a 1.8 mL Au NP solution in a 2 mL tube to give a final CRN concentration of 0 – 1.50 μg mL^{-1}. Controls were prepared in the absence of CB7. 0.5 mL of the Au NP-CRN or Au NP-CB7-CRN solution was placed in a semi-micro cuvette to measure the hydrodynamic size while 0.75 mL of the same sample solution was placed in a folded capillary zeta cell to measure the zeta potential using a Malvern ZEN 3600 instrument. Five measurements were taken for each sample and an average was calculated.

2.11 Raman spectroscopy and SERS

Raman and SERS spectra were acquired using a Reinshaw Raman InVia Microscope with a 633 nm He–Ne laser (9.3 mW - 11.36 mW). The laser was focused onto the sample via a 50 × objective lens (N.A. = 0.75). The grating used was 1800 lines mm^{-1} which gave a spectral resolution of 1 cm^{-1}. All spectra were calibrated with respect to Si and acquired at room temperature. The sample solution (see subsections below for sample preparations) was vortexed for 30 s before dropping 15 μL onto a custom-made sample holder for SERS measurements (Figure 2.1). Three accumulations of 30 s scan were acquired on each measurement for solution samples while single 30 s scan with 10% laser power was acquired on each measurement for powder samples. Five measurements were taken across different regions of interest per sample. The spectra were averaged and baseline corrected using an asymmetric least squares plugin in Origin.

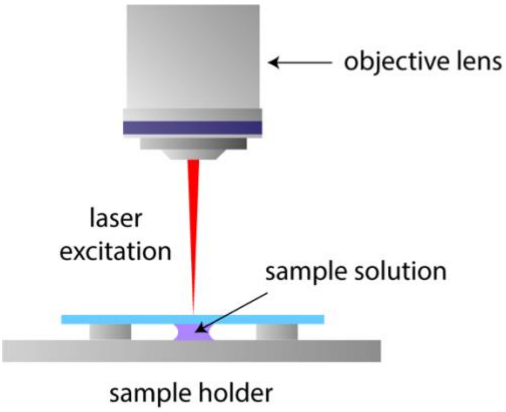

Figure 2.1. Schematic illustration of the SERS measurements.

2.11.1 DNT

1 mL of the DNT stock solution with varying concentration of 0 – 0.4 mM was added to 1 mL of a 0.2 mM CB7 solution in a 2 mL Eppendorf tube. 20 μL of the pre-mixed solution was then added to a 180 μL Au NP solution in a 0.5 mL tube to give a final DNT concentration of 0 – 20 μM. Controls were prepared in the presence of 0.1 M NaCl instead of CB7. Similar procedures were used to prepare sample solutions containing $AdNH_2$, 4-MBA or 4-MPBA.

2.11.2 MeX

For CB7 studies, 1 mL of the CAF stock solution with varying concentration of 0 – 0.2 mM was added to 1 mL of a 0.2 mM CB7 solution in a 2 mL Eppendorf tube. 20 μL of the pre-mixed solution was then added to a 180 μL Au NP solution in a 0.5 mL tube to give a final CAF concentration of 0 – 10 μM. For CB8 studies, 1 mL of the CAF stock solution with varying concentration of 0 – 0.1 mM was added to 1 mL of a 0.1 mM CB8 solution (prepared in 10 mM HCl) in a 2 mL Eppendorf tube. 20 μL of the pre-mixed solution was then added to a 180 μL Au NP solution in a 0.5 mL tube to give a final CAF concentration of 0 – 5 μM. Similar procedures were used to prepare sample solutions of TBR and TPH.

2.11.3 CRN

The sample solutions were prepared by the same procedures as for UV-Vis spectroscopy (see section 2.8.2). A set of sample solutions containing 1000-fold diluted SU was also prepared to study the matrix effect on the SERS signals of CRN.

Chapter 3. Quantitative Sensing of Nitroaromatic Explosives

This Chapter first reported the host-guest complexation between cucurbit[7]uril (CB7) and an explosive marker, 2,4-dinitrotoluene (DNT), using various characterisation techniques including nuclear magnetic resonance (NMR) spectroscopy, UV-Visible spectroscopy and isothermal titration calorimetry (ITC), and computer simulations based on density functional theory (DFT). Quantitative surface-enhanced Raman spectroscopy (SERS) detection of DNT using nanoaggregates of gold nanoparticles (Au NPs) and CB7 as substrates was fully studied. The role of CB7 in the formation of precise plasmonic nanojunctions for DNT detection was illustrated by control experiments in the absence of any aggregating agent or in the presence of NaCl. In addition, the surface-enrichment effect of CB7 was described by the reduction in the SERS signals of DNT in the presence of 1-adamantylamine ($AdNH_2$), which is a stronger binder of CB7. The selectivity of the SERS sensor was demonstrated with a structurally similar nitroaromatic explosive, picric acid (PA), while the robustness was demonstrated with model organic contaminants, 4-mercaptobenezoic acid (4-MBA) and 4-mercaptophenylboronic acid (4-MPBA) in the latter part of this Chapter.

3.1 Introduction

Rapid detection of trace explosives remains a great challenge in homeland security and environmental monitoring around the world.[184–192] Nitroaromatic compounds such as 2,4-dinitrotoluene (DNT) and 2,4,6-trinitrotoluene (TNT) are directly associated with bombs and landmines used in terrorist attacks and military activities,[189–192] and present as contaminants in surface water, groundwater and soils at munitions manufacturing sites and military ranges.[193,194] DNT is also produced as a major degradation product of TNT with much higher vapour pressure.[195] In addition, DNT and TNT exhibit toxicity upon exposure, resulting in adverse health effects including decreased neurological, haematological, hepatic, renal and reproductive functions.[196–199] Development of highly sensitive and selective nitroexplosive sensors is thus of great importance for the rise in global threats of terrorism and environmental safety concerns. Common explosive sensors to date have utilised techniques based on mass spectrometry, fluorescence, colorimetry, voltammetry and surface plasmon resonance,[200–203] but not all of these methods allow on-site detection in real-time with high performance.

In contrast, SERS can significantly enhance the Raman signals of analyte molecules located in close proximity to the plasmonic nanostructures (e.g. Au NPs) and thus offers numerous advantages for explosive detection such as rapid response, cost-effectiveness, high chemical stability, minimal sample preparation and wider information window of the analyte molecules via their vibrational fingerprints. (see section 1.4).[188,204–206] Attachment of cucurbiturils (CBs) onto the surface of Au NPs can further enhance the sensitivity by controlling the inter-particle spacing between Au NPs and localising the explosive markers at the plasmonic hotspots via formation of host-guest complexes.[1,2,172] Previous SERS studies based on Au NP: CB nanoaggregates focused on good CB guests that are positively charged and entirely (or mostly) encapsulated within the CB cavity. Weaker guests, in particular poly-substituted nitroaromatics that are neutral and bulky, remain largely unexplored in such SERS sensing platforms, despite being an important class of analytical targets.[190]

Herein, the host-guest complexation between CB7 and an explosive marker DNT was investigated in water using experimental and computational techniques to quantify the key binding parameters for the first time (Figure 3.1). Quantitative SERS detection of DNT was demonstrated down to 1 μM with highly reproducible signals via formation of precise plasmonic hotspots within the Au NP: CB7 nanoaggregates.[207] Surprisingly, the molecular recognition phenomena of CB in the SERS system of Au NP: CB nanoaggregates have not been systematically studied since the first experimental observation.[2] Our SERS sensor was highly selective against a similar nitroexplosive, picric acid (PA), which is too bulky to be encapsulated by the CB7 cavity. The SERS sensor was also tolerant against the presence of model organic contaminants that strongly bind to Au NPs.

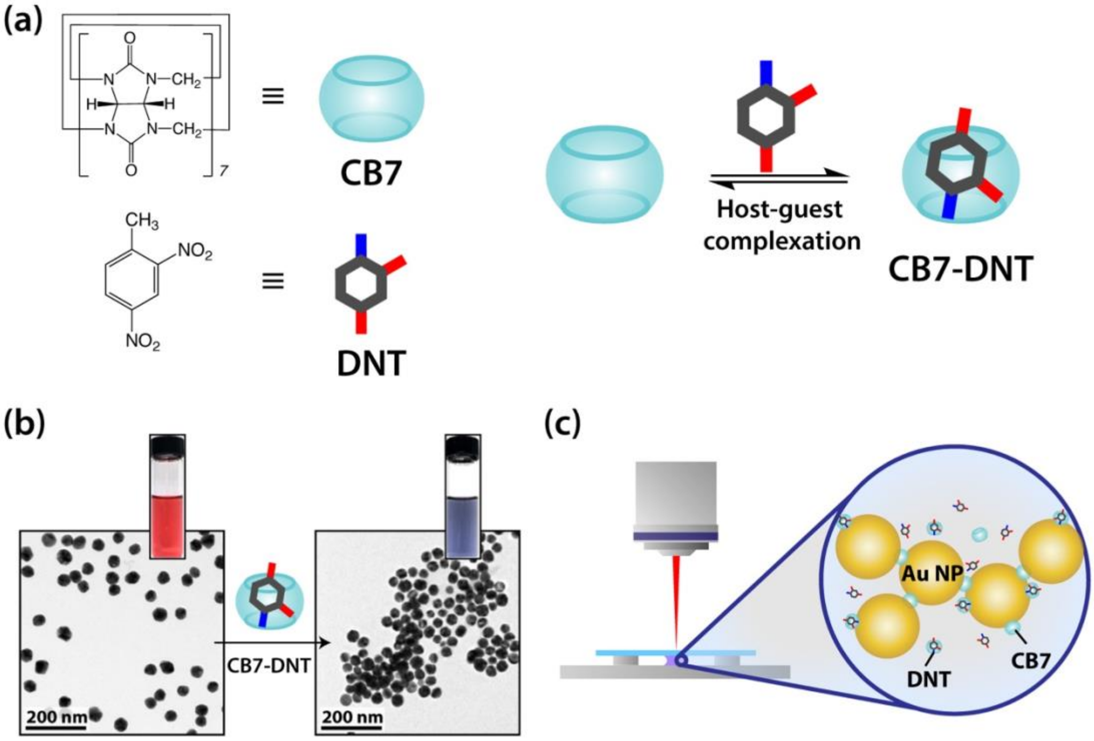

Figure 3.1. (a) Schematic illustration of the formation of a 1:1 host-guest complex between CB7 and DNT. (b) TEM images and photographs showing the 40 nm Au NP solution upon addition of the CB7-DNT complexes. (c) Schematic illustration of the SERS measurements of the Au NP-CB7-DNT sample solution.

3.2 Supramolecular chemistry of CB7 and DNT

When CB7 and DNT were mixed in D_2O with 1:1 stoichiometry, characteristic upfield shifts of all DNT proton signals (H_a, H_b, H_c and H_d) were observed in the ^{1}H NMR spectra, verifying the formation of host-guest complexes between CB7 and DNT (Figure 3.2). NMR titration experiments were then performed by adding excess DNT (1.2 equivalent) to CB7, in which the proton signals of both complexed (H_a, H_b, H_c and H_d) and free ($H_{a'}$, $H_{b'}$, $H_{c'}$ and $H_{d'}$) DNT were observed, further revealing that the complexation-dissociation dynamics falls into the slow exchange regime on the NMR time scale at 298 K (Figure 3.3). The change in chemical shift ($\Delta\delta$) for H_d/H_c ($\Delta\delta_d = –0.86$ ppm and $\Delta\delta_c = –1.1$ ppm) of DNT is greater than for H_b/H_a ($\Delta\delta_b = –0.12$ ppm and $\Delta\delta_a = –0.7$ ppm) after host-guest complexation, which indicates H_d/H_c are deep inside the CB7 cavity, whereas H_b/H_a are much closer to the carbonyl rim. Interestingly, the anisotropic binding of DNT leads to desymmetrisation of the CB7 protons and therefore splits the corresponding NMR signals in the CB7-DNT complex. The energy-minimised molecular model of the complex in water calculated at CPCM/wB97XD/6-311+G** level of theory supports the host-guest binding geometry derived from NMR (Figure 3.2, see appendix for details). The binding energy of a discrete CB7-DNT complex was calculated to be –26.9 kcal mol$^{–1}$ (see Table A3 in appendix for details), which is consistent to previous report on similar neutral complexes.[147] Notably, the NO_2 group at the 4-position of DNT is sticking out through the CB7 portal, blocking its potential interaction with Au NPs. Nevertheless, the other CB7 portal can still bind to the surface of Au NPs which is critical to the subsequent SERS studies.

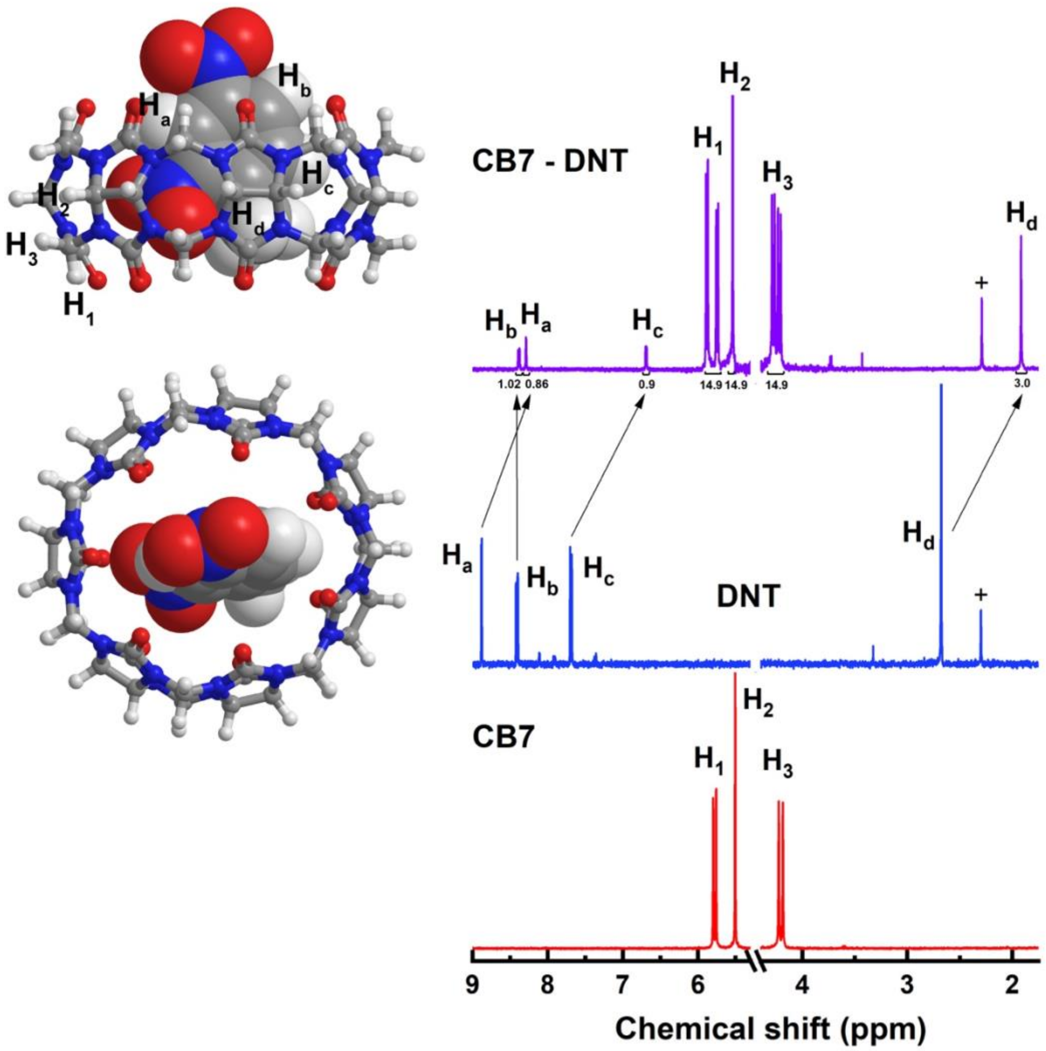

Figure 3.2. ^{1}H NMR spectra of CB7, DNT and 1:1 CB7-DNT host-guest complex in D_2O. The impurity in the DNT sample is marked by +. Inset: DFT molecular model of a CB7-DNT host-guest complex in water.

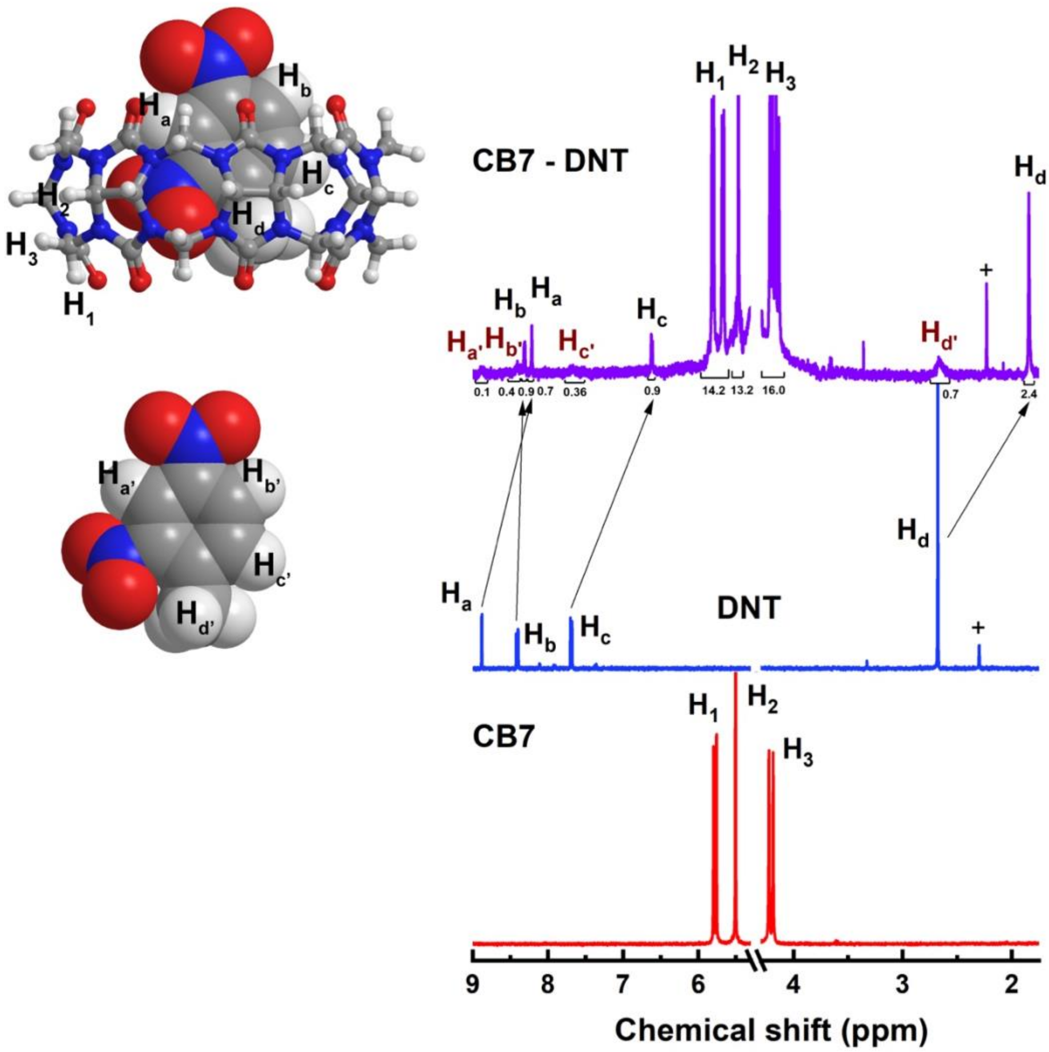

Figure 3.3. ^{1}H NMR spectra of CB7, DNT and 1:1 CB7-DNT host-guest complex with excess DNT in D_2O. The impurity in the DNT sample is marked by +. Inset: DFT molecular model of a CB7-DNT host-guest complex and a free DNT molecule in water.

Due to the relatively low water solubility of DNT (0.19 mg mL^{-1} at 22 °C)[208] and the relatively high aqueous binding constant, it was challenging to extract an accurate binding constant with CB7 via NMR titration. Hence, the system was further characterised by UV-Vis titration of 10 μM DNT with up to 4-5 equivalents of CB7, in which a binding constant of $(1.6 \pm 0.2) \times 10^{6}$ M^{-1} was obtained by assuming a 1:1 binding model (Figure 3.4a). The thermodynamics of the binding was also determined by ITC, verifying the postulated 1:1 binding mode. A binding constant of $(4.94 \pm 0.34) \times 10^{5}$ M^{-1} was obtained, which is consistent with UV-Vis titration within methodological error (Figure 3.4b). The ITC data also revealed that the binding is enthalpically driven ($\Delta H° = -11.37$ kcal mol^{-1}), indicating that the displacement of high-energy water molecules by DNT is the major driving force for the complexation, which is typical for CB7 host-guest complexes (see section 1.12).[114] In addition, the dispersion interactions between the highly polarisable nitroaromatics and the hydrophobic cavity of CB7 are likely contributors to the complex formation.[209,210] Negative entropic contributions ($\Delta S° = -0.012$ kcal mol^{-1} K^{-1} or $T\Delta S° = -3.61$ kcal mol^{-1}) reflect the formation of a conformationally restricted and tight inclusion complex, which matches well with the deformed, ellipsoidal shape of CB7 in the energy-minimised molecular model (Figure 3.2).

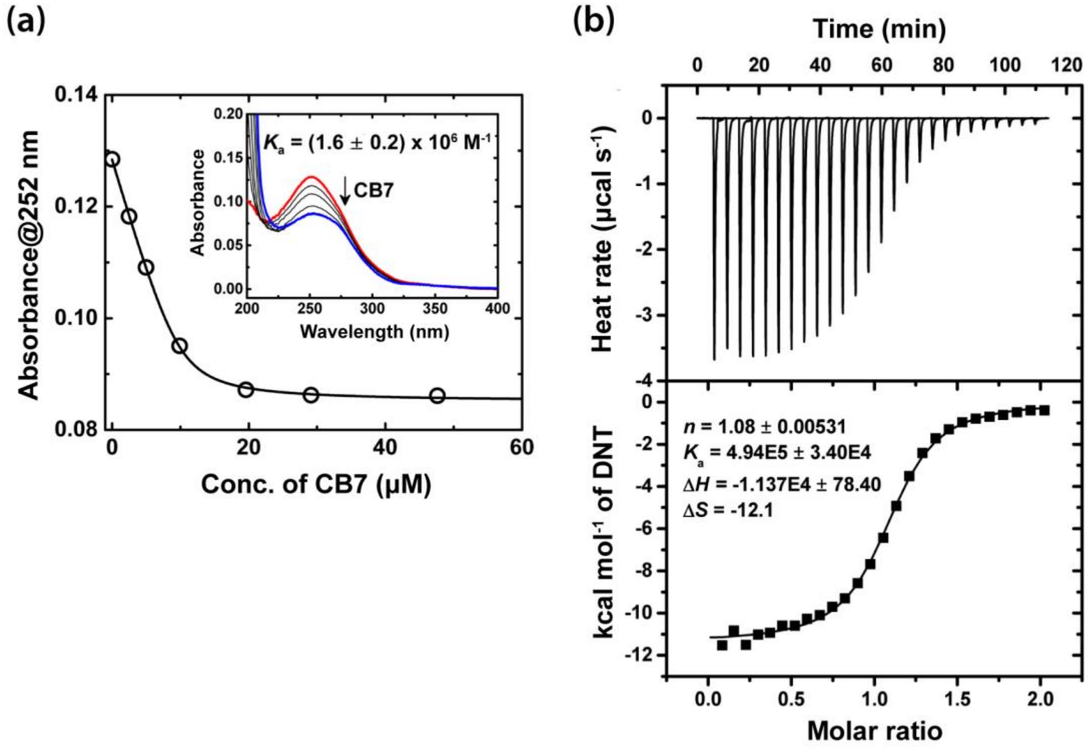

Figure 3.4. (a) UV-Vis titration of 10 μM DNT with CB7. Inset: UV-Vis spectra of CB7-DNT. (b) ITC data showing binding isotherms of CB7 and DNT. The apparent reaction heats were obtained from integration of the calorimetric traces.

3.3 Raman spectroscopy of CB7-DNT host-guest complexes

The Raman spectrum of solid DNT is characterised by a strong peak at 1348 cm^{-1} which corresponds to symmetric NO_2 stretching vibration (Figure 3.5a).[211] The two peaks at 1544 cm^{-1} and 1611 cm^{-1} are attributed to asymmetric NO_2 stretching vibration and aromatic NO_2 conjugation respectively.[211] The Raman spectrum of solid CB7 is characterised by two major peaks at 444 cm^{-1} and 833 cm^{-1}, corresponding to ring scissor and ring deformation modes respectively.[175] The Raman peaks of the 1:1 CB7-DNT host-guest complex in aqueous solution show slight shifts in positions when compared to those of the solid CB7 and solid DNT. In addition, the DNT signals are dominant in the Raman spectrum of the CB7-DNT complex, probably due to the fact that DNT is more Raman-active than CB7. The Raman spectra of CB7, DNT and the CB7-DNT complex were also modelled in the gas phase at the HF/3-21G level of theory (Figure 3.5b), which show general consistency with the experimental results. The calculated Raman spectrum of the CB7-DNT complex is roughly equal to the sum of that of CB7 and DNT with slight shifts in some peaks.

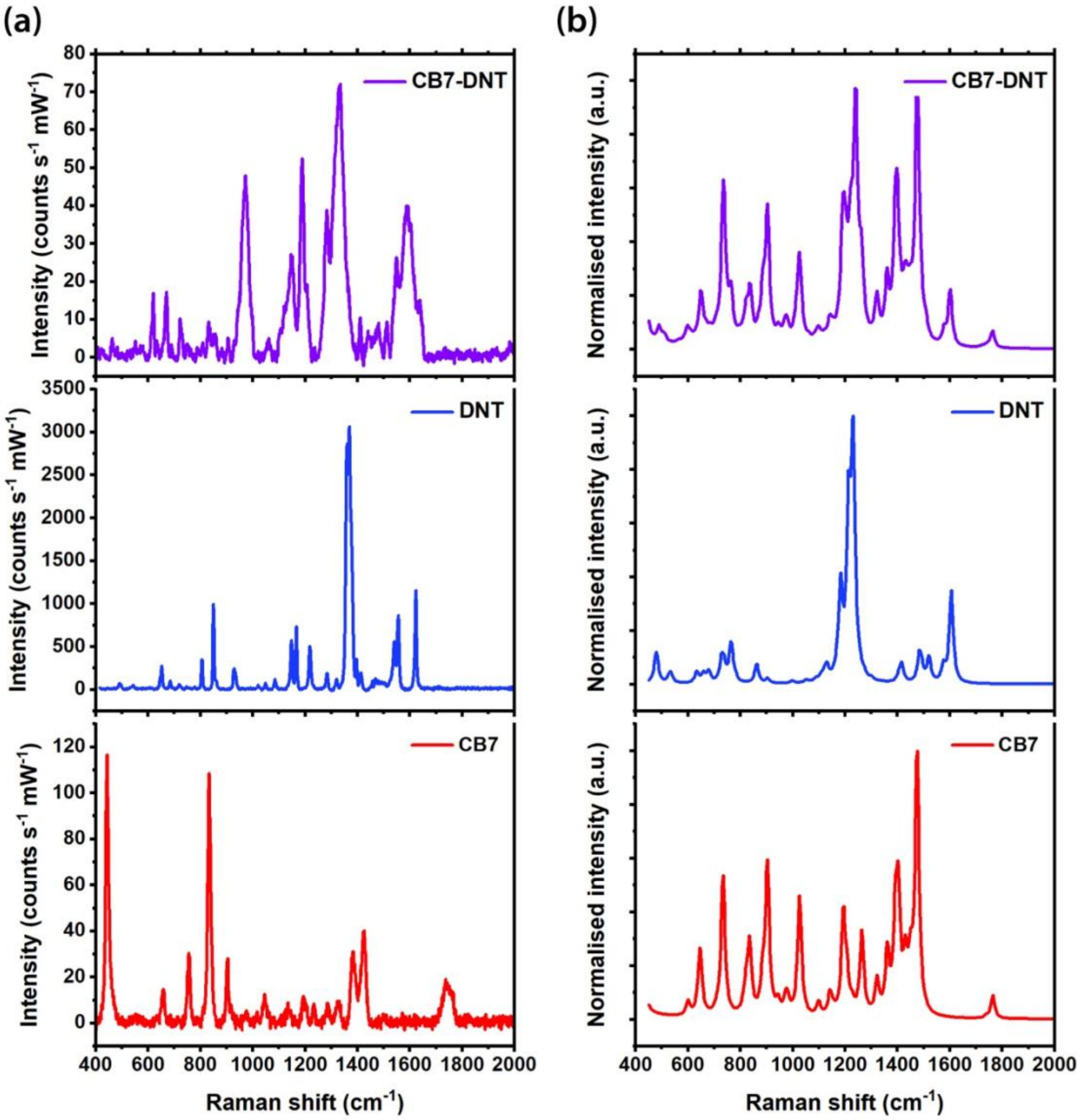

Figure 3.5. (a) Experimental Raman spectra of solid CB7, solid DNT and 1:1 CB7-DNT host-guest complex of 2 mM in water. (b) Calculated Raman spectra of CB7, DNT and 1:1 CB7-DNT host-guest complex in gas phase at HF/3-21G level of theory.

3.4 SERS sensing of CB7-DNT host-guest complexes

The potential SERS detection of the explosive marker DNT was investigated by adding a pre-mixed 1:1 CB7-DNT solution into a 40 nm citrate-capped Au NP solution. The aggregation of Au NPs was mediated by CB7 as evidenced by the colour change in the Au NP solution from red to purple and the formation of ~1.0 nm plasmonic nanojunctions in the transmission electron microscopy (TEM) images (Figure 3.1,3.6), which is consistent with our previous findings.[1,2,172] The characteristic Raman peak of DNT at 1334 cm^{-1} was clearly observed in the presence of CB7 while there was no aggregation of Au NPs in the absence of CB7, thus illustrating the importance of CB7 on DNT detection (Figure 3.7a). It is noted that the broad peak at ~1640 cm^{-1} in the Raman spectrum of DNT is attributed to the H-O-H bending mode of liquid water (Figure 3.7b).[212]

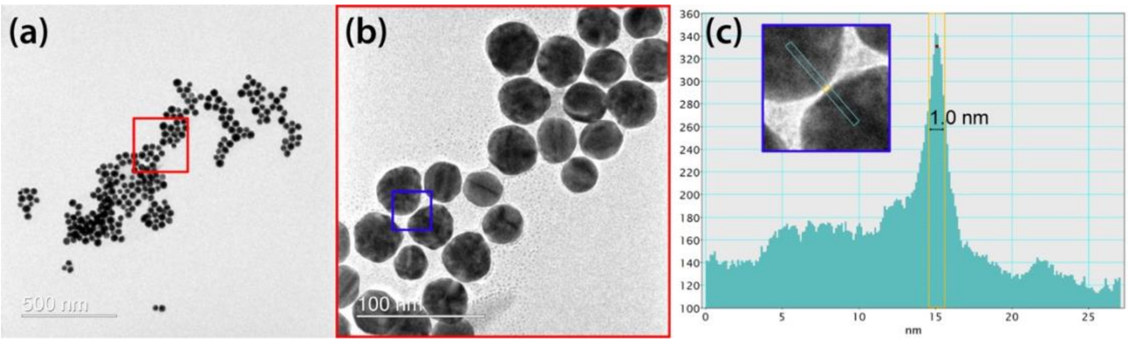

Figure 3.6. (a-c) Stepwise zoom-in TEM images of 40 nm Au NPs after addition of the CB7-DNT complex. (c) Plot of grayscale against pixel. (Grayscale refers to the brightness of a pixel. Total white = 255 for 8-bit depth and total dark = 0.)

SERS titration was then performed by adding different concentrations of the 1:1 CB7-DNT host-guest complexes into the Au NP solution (Figure 3.7c,d). The characteristic DNT signals remain readily observable for concentrations down to ~10 μM. Nevertheless, no aggregation of Au NPs and hence no SERS signals can be observed at very low concentrations of the CB7-DNT complexes due to the insufficient amount of CB7 to trigger the self-assembly of Au NPs.

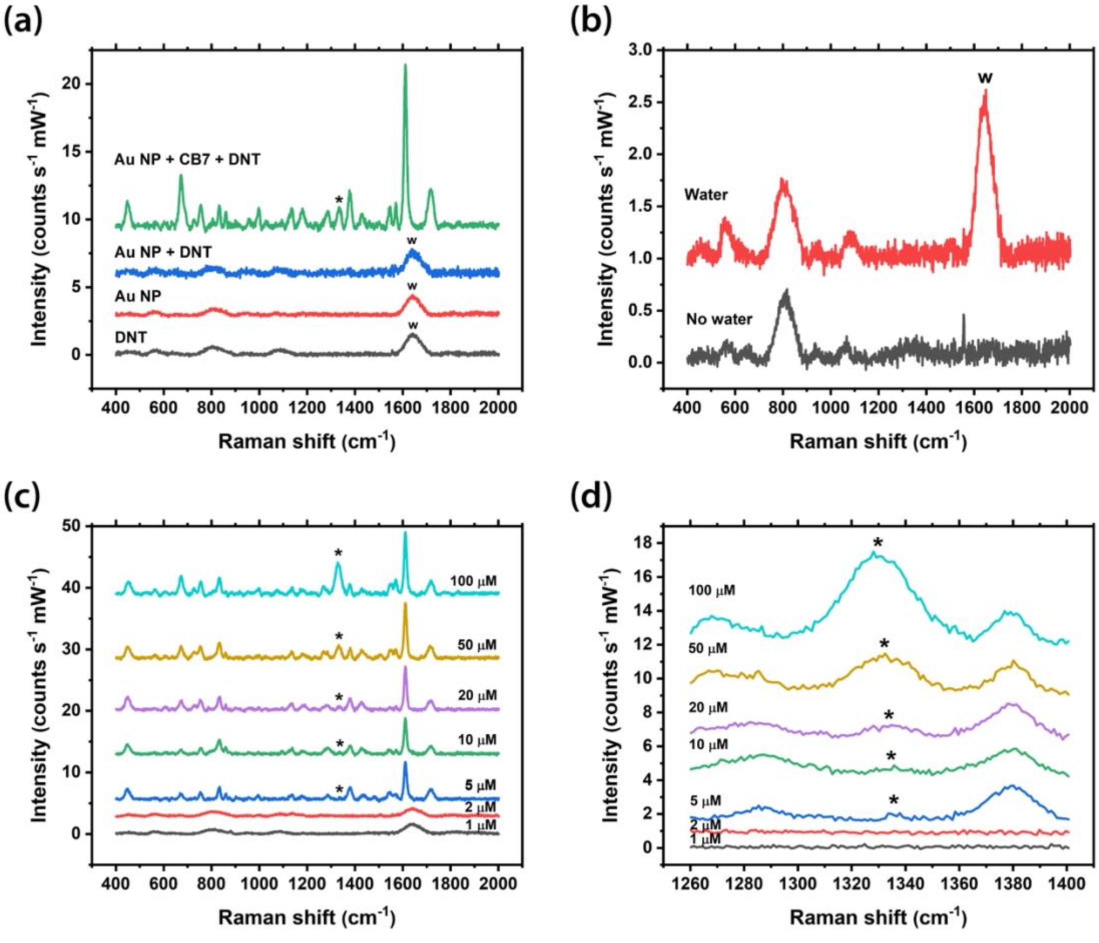

Figure 3.7. (a) Raman and SERS spectra of DNT in the presence or absence of CB7. Main Raman peak of DNT is marked by *. (b) Raman spectrum of water in the custom-made sample holder. The H-O-H bending peak of liquid water is marked by w. (c) Full-range and (d) zoom-in SERS spectra of the 1:1 CB7-DNT complexes from 1 μM to 100 μM. Spectra were baseline corrected and offset for clarity.

To test the detection limit of our nitroexplosive sensor, SERS titrations of DNT were performed at a constant CB7 concentration of 10 μM as to ensure the formation of reproducible nanoaggregates, i.e. the SERS substrates, since the aggregation kinetics is determined by the ratio of Au NP: CB (Figure 3.8a,b).[2] The main peak of DNT attributed to symmetric NO_2 stretching vibration can be clearly observed in the SERS spectra even when the concentration is down to 2 μM (Figure 3.8c). The detection limit of DNT in our SERS system was found to be ~1 μM with a strong correlation (R^2 ~ 0.97) between the SERS intensity and log concentration of DNT across a wide range (Figure 3.8d), which is comparable to other solution-based SERS techniques.[5,186]

Notably, the aggregation of Au NPs should be mostly caused by empty CB7, which is present at dynamic equilibrium of host-guest complexation, in the Au NP-CB7-DNT system. As opposed to a number of previous reports using small analyte molecules that can be entirely encapsulated deep inside the CB cavity, the CB7-DNT complex alone could not mediate the aggregation of Au NPs because one of the CB7 portals is blocked by the bulky nitro group of DNT, as evidenced by the ^1H NMR spectra and the energy-minimised molecular model of the CB7-DNT complex (Figure 3.2). Nevertheless, the CB7-DNT complexes can still stay in close proximity to the plasmonic hotspots through binding to the Au NP surface via the accessible portal (Figure 3.8a). This phenomenon is reflected in the relatively large error bar and the slight departure from linearity in the sample with 20 μM DNT (Figure 3.8d), where the concentration of empty CB7 is lower than that in the other samples due to a shift in equilibrium position caused by the excess DNT.

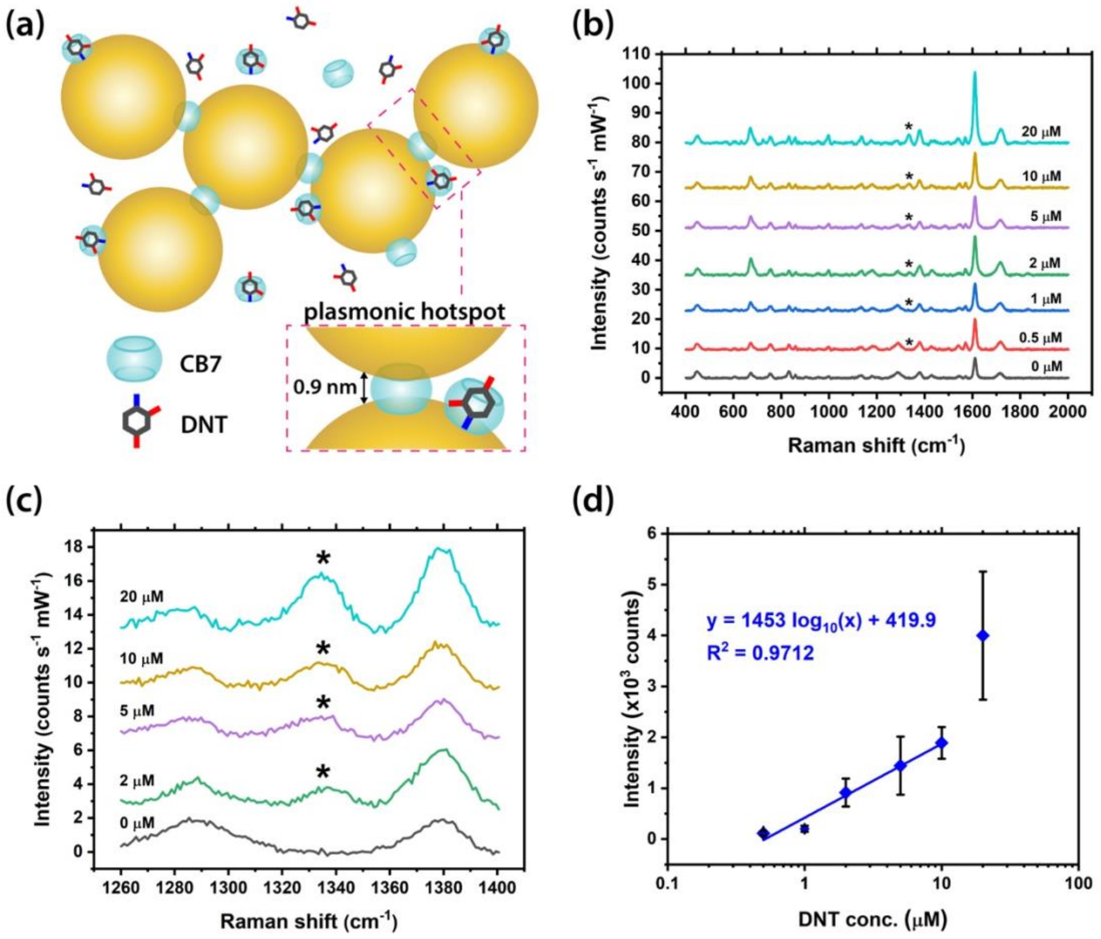

Figure 3.8. (a) Schematic illustration of the precise plasmonic hotspots within Au NP: CB7 nanoaggregates for DNT detection (not to scale). (b) Full-range and (c) zoom-in SERS spectra of DNT with concentrations from 0 to 20 μM. Main Raman peak of DNT is marked by *. Spectra were baseline corrected and offset for clarity. (d) Corresponding plot of SERS intensity of the main DNT peak (marked by * in (b)) against DNT concentration. Logarithmic fittings were performed to reveal correlation between SERS intensity and DNT concentration from 0.5 to 10 μM DNT.

CB7 plays two major roles in enhancing the SERS signals of DNT. Firstly, the rigid molecular structure of CB7 defines precise nanojunctions of 0.91 nm between the Au NPs, resulting in very strong and localised plasmonic hotspots. A control experiment with 0.1 M NaCl as the aggregation agent for Au NPs was performed to support this phenomenon (Figure 3.9a). Though the main DNT peak can be clearly observed in the SERS spectra (Figure 3.9b,c), the Raman features are significantly broader and more importantly, a correlation between the SERS intensity and DNT concentration is lacking, owing to the random plasmonic hotspots resulted from uncontrolled aggregation of Au NPs.

Secondly, the surface-bound CB7 can encapsulate DNT within its cavity, leading to an enriched DNT concentration on the Au NP surface and in close proximity to the plasmonic hotspots. This effect is particularly important for analyte targets such as nitroaromatics, that have low intrinsic affinities to Au surface, in contrast to many of the previous examples using analyte molecules with high affinities to Au surface.[4,5] A competitive binding experiment with 1-adamantylamine ($AdNH_2$), which is a strong binder to CB7, was performed to verify the surface-enrichment effect of CB7 (Figure 3.9a). The SERS signal of the main DNT peak was reduced by 67% in the presence of equimolar (10 μM) $AdNH_2$ which effectively displaced DNT from the CB7 cavity (Figure 3.9c,e).

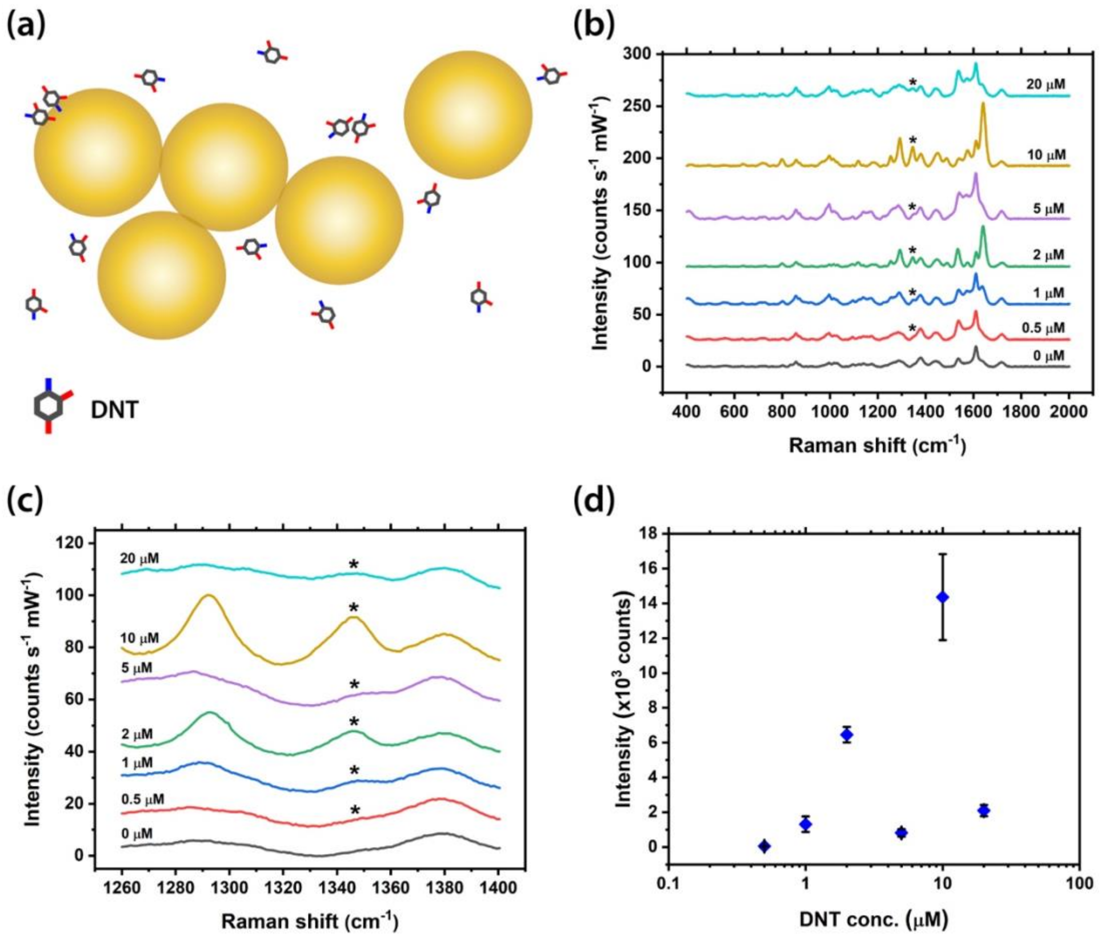

Figure 3.9. (a) Schematic illustration of the random plasmonic hotspots formed by NaCl-aggregated Au NPs for DNT detection (not to scale). (b) Full-range and (c) zoom-in SERS spectra of DNT with different concentrations from 0 μM to 20 μM. Main Raman peak of DNT is marked by *. Spectra were baseline corrected and offset for clarity. (d) Corresponding plot of SERS intensity of the main DNT peak (marked by * in (b)) against DNT concentration.

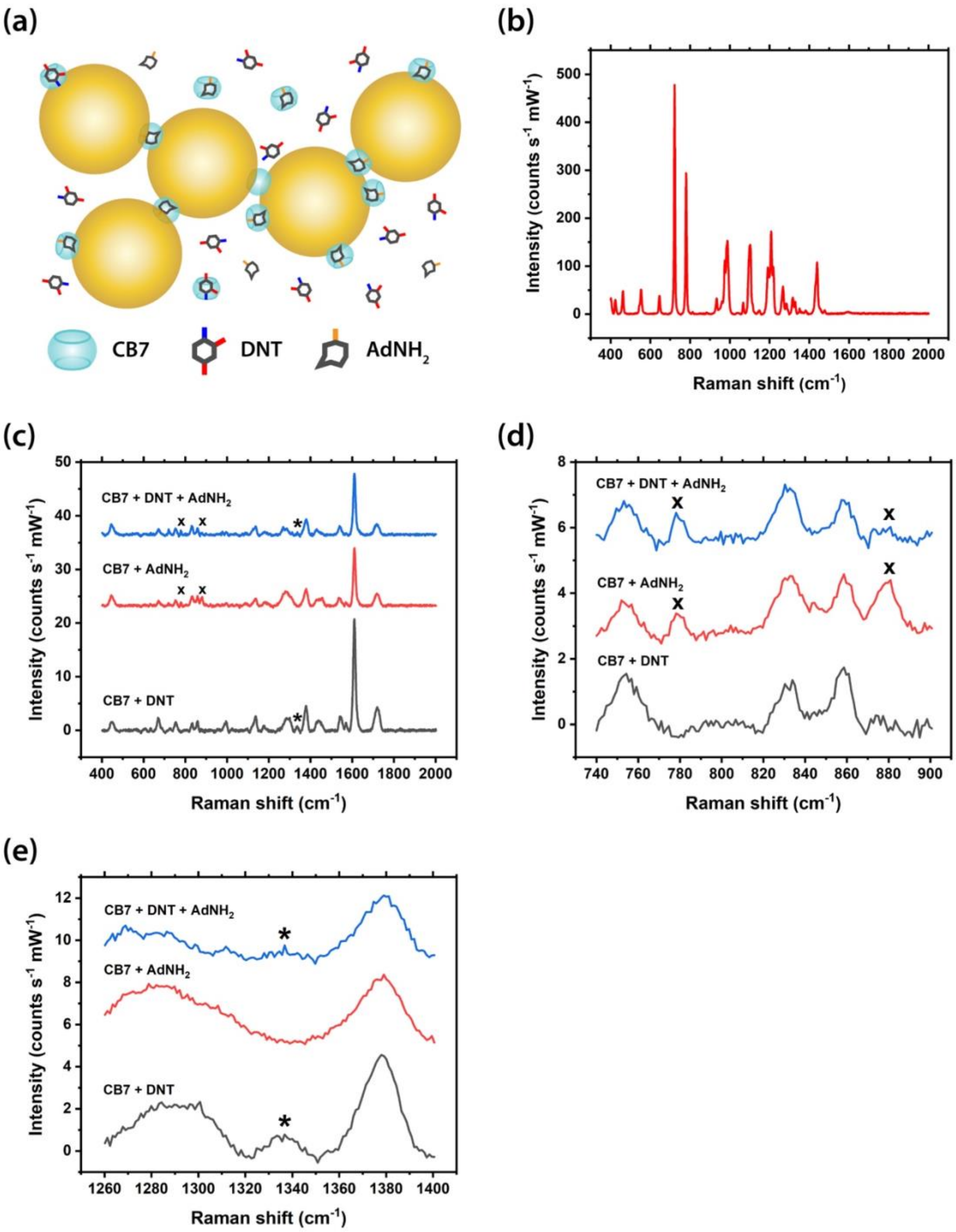

Figure 3.10. (a) Schematic illustration of competitive formation of CB7-DNT and CB7-AdNH$_2$ host-guest complexes (not to scale). (b) Raman spectrum of AdNH$_2$ powder. (c) Full-range and (d,e) zoom-in SERS spectra showing competitive formation of CB7-DNT and CB7-AdNH$_2$ host-guest complexes. Main Raman peaks of DNT and AdNH$_2$ are marked by * and x respectively. Spectra were baseline corrected and offset for clarity.

3.5 Selectivity of the nitroaromatic explosive SERS sensor

The selectivity of our SERS system was demonstrated by control experiments with another nitroaromatic explosive, picric acid (PA), which is structurally similar to DNT but too bulky to fit inside the CB7 cavity. When CB7 and PA were mixed in D_2O with 1:1 stoichiometry, no characteristic upfield shift of the PA proton signals can be observed in NMR, verifying the absence of host-guest complexation between CB7 and PA (Figure 3.11).

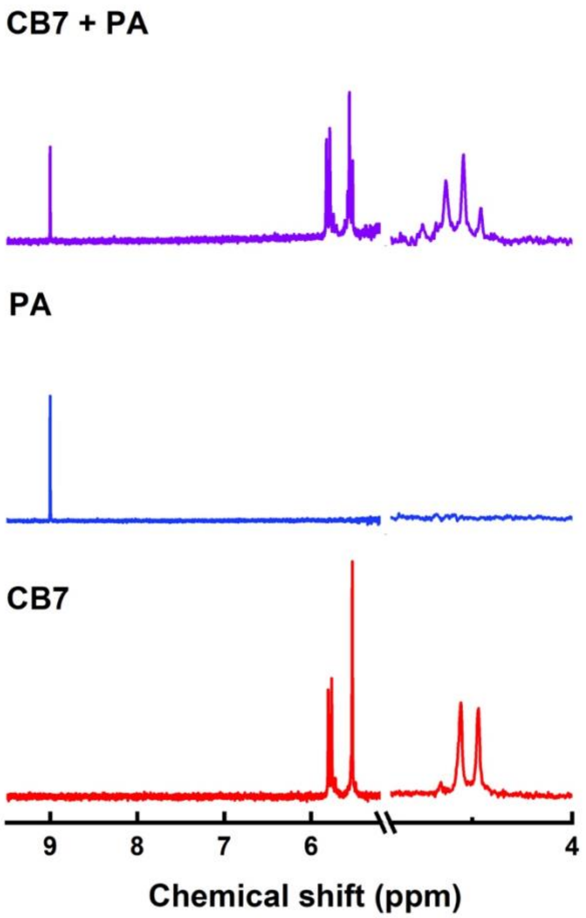

Figure 3.11. ^{1}H NMR spectra of CB7, PA and 1:1 CB7 and PA in D_2O.

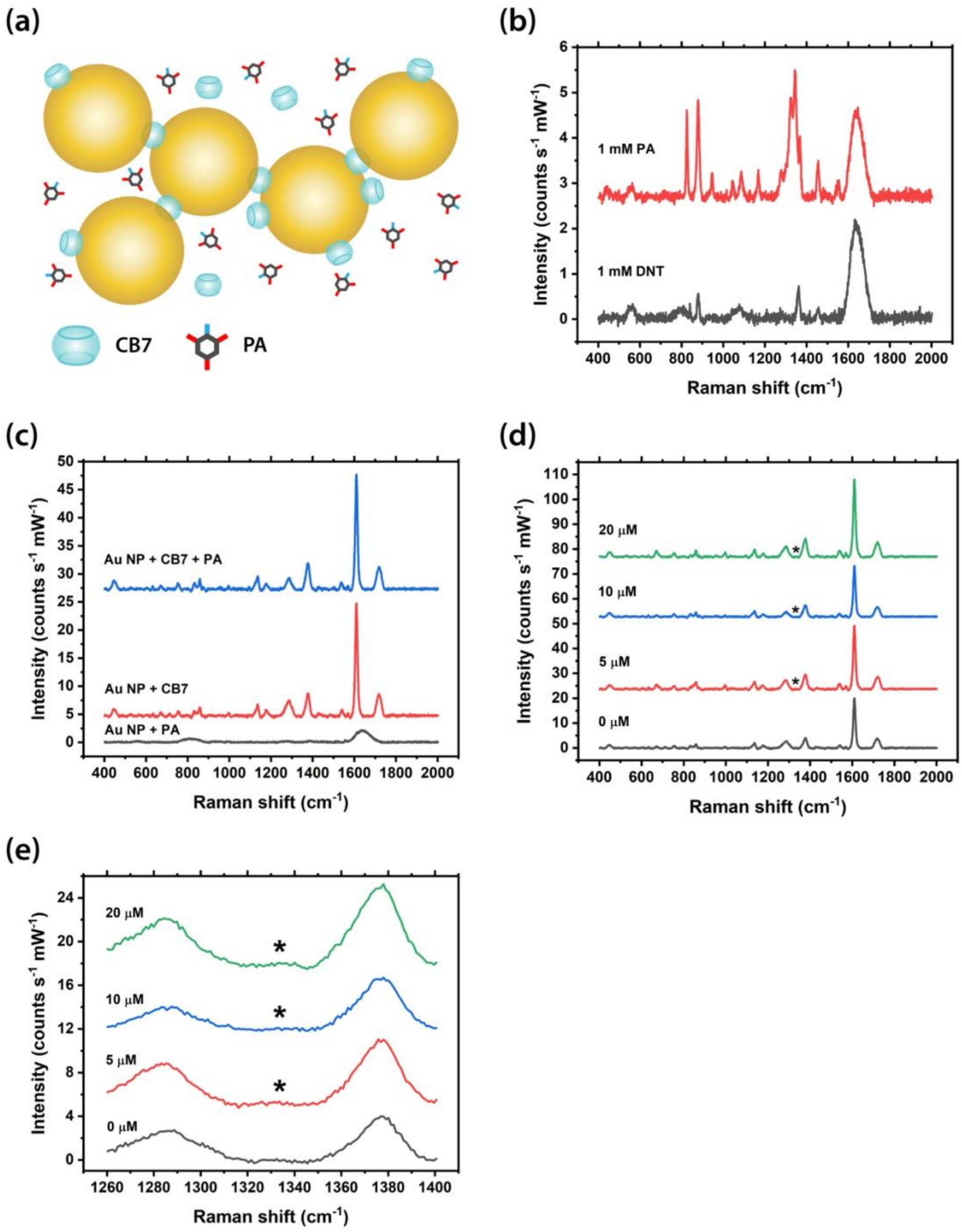

Figure 3.12. (a) Schematic illustration showing the absence of host-guest complex of CB7 and PA (not to scale). (b) Raman spectra of 1 mM PA and 1 mM DNT. (c) SERS spectra of PA in the presence or absence of CB7. (d) Full-range and (e) zoom-in SERS spectra of PA with concentrations from 0 μM to 20 μM. Spectra were baseline corrected and offset for clarity.

The overall negative charge and high water solubility of PA also disfavour its binding with CB7. Despite being 3.5 times more Raman-active than DNT in aqueous solution (Figure 3.12b), PA did not exhibit any observable SERS signals in the presence of 10 μM CB7 (Figure 3.12a,c,d,e), thus illustrating the importance of host-guest complexation in our sensing scheme.

3.6 Robustness of the nitroaromatic explosive SERS sensor

Finally, the SERS detection of DNT was performed in the presence of strong Au NP ligands, 4-mercaptobenezoic acid (4-MBA) and 4-mercaptophenylboronic acid (4-MPBA) respectively, to mimic strongly binding environmental impurities that might feature in field applications, as proof-of-concept experiments (Figure 3.13, 3.14). Although 4-MBA can strongly bind to Au NPs, no SERS signal of 1 μM 4-MBA can be observed in the absence of CB7 (Figure 3.13c). In contrast, the 4-MBA signals can be readily observed when CB7 was used to mediate the formation of precise plasmonic hotspots as aforementioned (Figure 3.13a). Multiplexed SERS detection of 10 μM DNT and 1 μM 4-MBA was demonstrated in the presence of CB7 and the characteristic peaks of 4-MBA and DNT can be clearly observed in the SERS spectra (Figure 3.13d,e,f). Similar results were obtained with 4-MPBA, which reflects the tolerance of our SERS system in detecting trace nitroaromatic explosives (Figure 3.14). Therefore, the interference from various contaminants in the background can be eliminated by extracting the Raman shift information, as opposed to the classical on/off-type sensing techniques which are more prone to false-positive results.

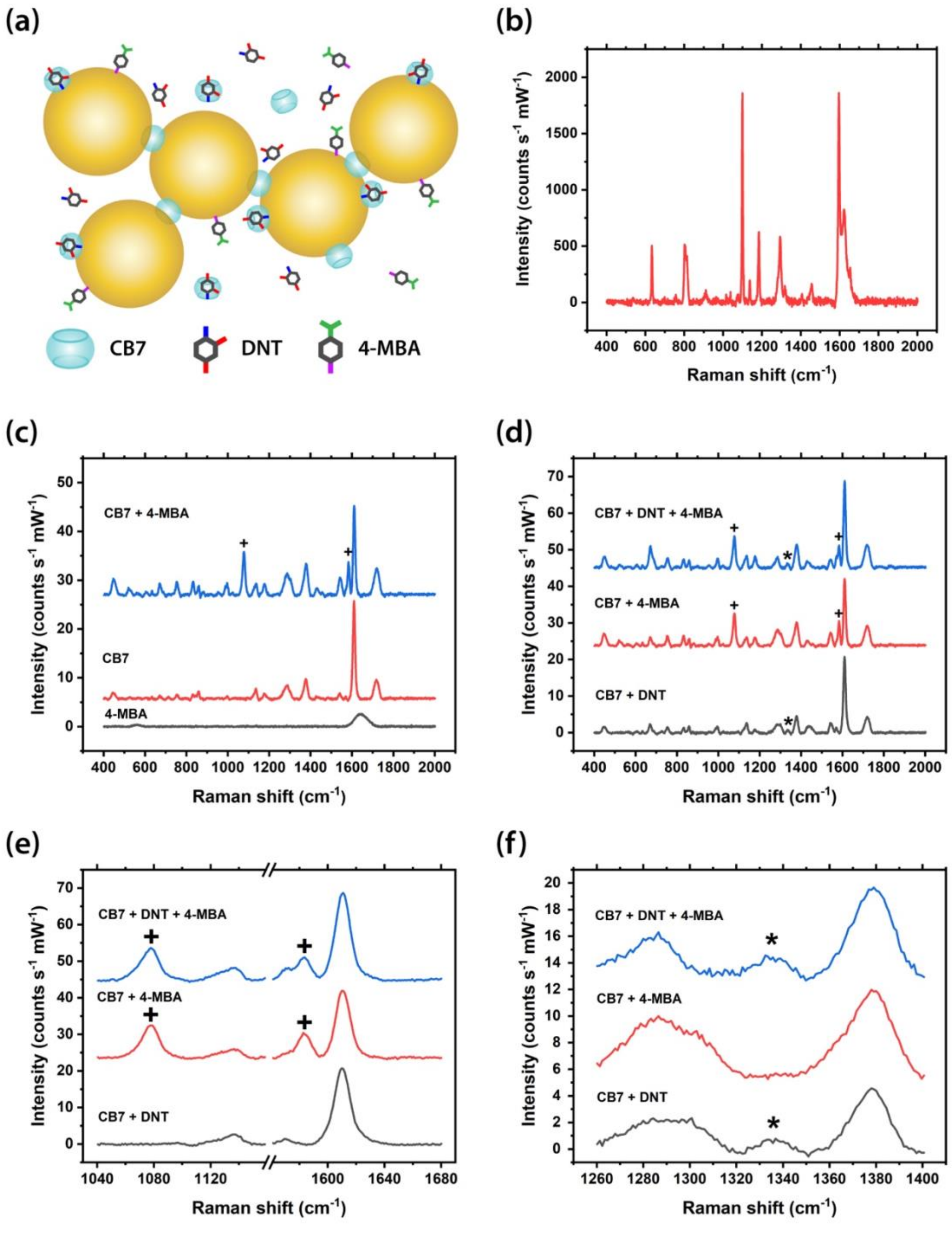

Figure 3.13. (a) Schematic illustration of the precise plasmonic hotspots within Au NP: CB7 nanoaggregates with DNT encapsulated inside the CB7 cavity and 4-MBA bound to Au NPs (not to scale). (b) Raman spectrum of 4-MBA powder. (c) SERS spectra of 4-MBA in the presence or absence of CB7. (d) Full-range and (e-f) zoom-in SERS spectra of 10 μM DNT in the presence of 1 μM 4-MBA. Main Raman peaks of DNT and 4-MBA

are marked by * and + respectively. Spectra were baseline corrected and offset for clarity.

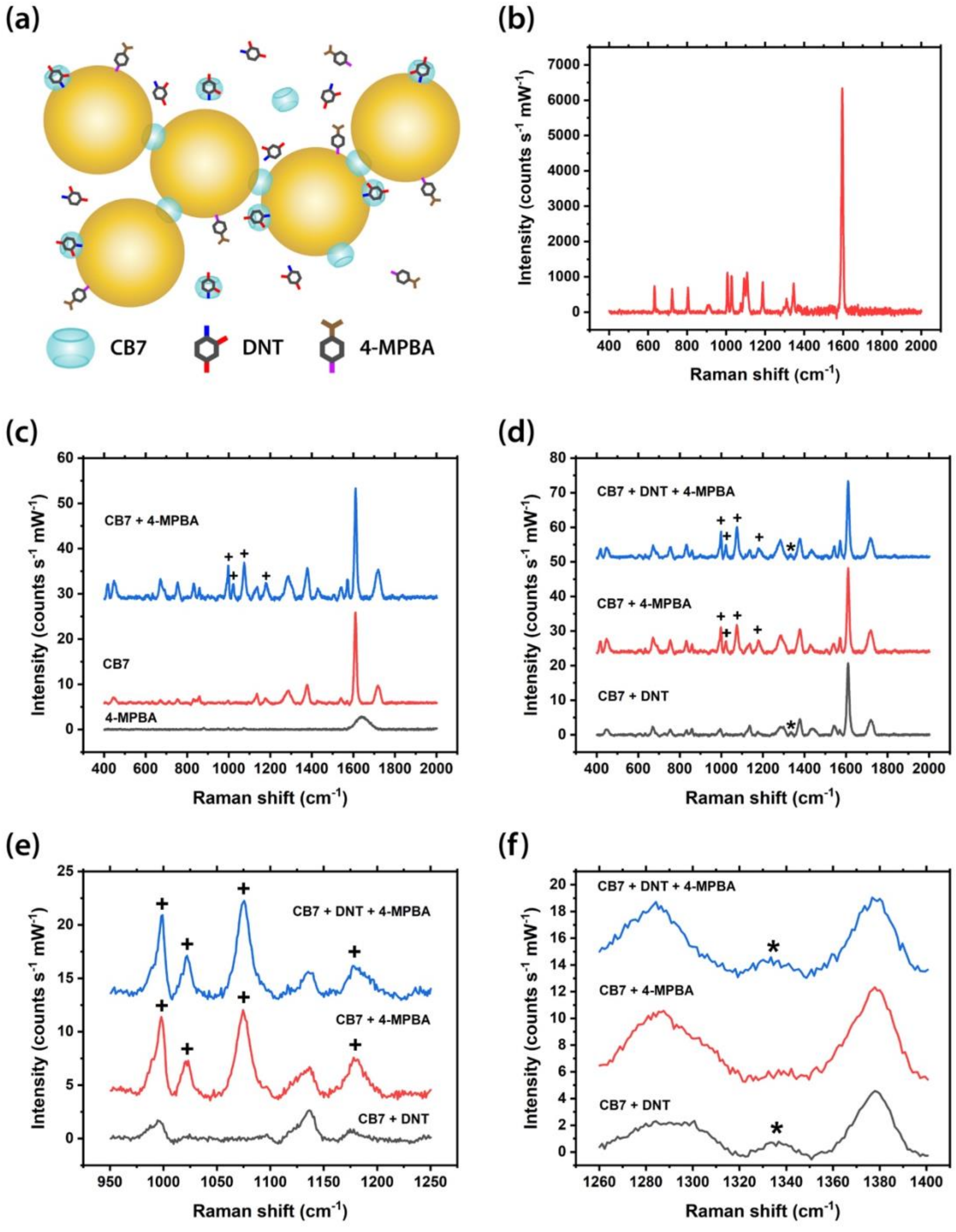

Figure 3.14. (a) Schematic illustration of the precise plasmonic hotspots within Au NP: CB7 nanoaggregates with DNT encapsulated inside the CB7 cavity and 4-MPBA bound to Au NPs (not to scale). (b) Raman spectrum of 4-MPBA powder. (c) SERS spectra of 4-MPBA in the presence or absence of CB7. (d) Full-range and (e-f) zoom-in SERS

spectra of 10 μM DNT in the presence of 1 μM 4-MPBA. Main Raman peaks of DNT and 4-MPBA are marked by * and + respectively. Spectra were baseline corrected and offset for clarity.

3.7 Conclusions

In this Chapter, a novel SERS sensor that exploits a neutral host-guest complexation between CB7 and an explosive marker DNT has been developed. The key binding parameters of the CB7-DNT complexes have been quantified using NMR, UV-Vis titrations and ITC measurements, and supported by DFT molecular models. While CB7 is known to bind a wide variety of positively charged guests, its binding with neutral guests is much rarer. Our results have demonstrated new possibilities in utilising aqueous supramolecular chemistry of CB7 for poly-substituted nitroaromatics, which is an important class of explosive compounds for terrorism and military applications. The CB7-DNT host-guest complexation allows a sensing scheme based on aqueous SERS via formation of precise plasmonic hotspots, offering rapid response, high reproducibility and signal linearity. Our system has achieved a detection limit of ~1 μM, consistent to other solution-based SERS sensors. Notably, the molecular recognition properties of CB7 is retained after capping onto the surface of Au NPs, which has been verified by a competitive binding experiment with 1-adamantylamine and a negative control experiment with picric acid. Proof-of-concept experiments have also showed that our SERS sensor is tolerant against the presence of model organic contaminants, 4-mercaptobenezoic acid and 4-mercaptophenylboronic acid, paving the way towards its potential applications in on-site environmental monitoring.

Chapter 4. Quantitative Sensing of Methylxanthine Drugs

This Chapter first reported the host-guest complexations between cucurbit[*n*]urils (CB*n*, *n* = 7, 8) and three structurally similar drugs, methylxanthines (MeX), in the purine family, namely caffeine (CAF), theobromine (TBR) and theophylline (TPH), using nuclear magnetic resonance (NMR) spectroscopy and computer simulations based on density functional theory (DFT). Quantitative surface-enhanced Raman spectroscopy (SERS) detection of MeX using nanoaggregates of gold nanoparticles (Au NPs) and CBs as substrates was fully studied. The ability of the SERS sensor to differentiate structurally similar molecules was demonstrated via multiplexed detection of isomers, TBR and TPH, using Au NP: CB8 nanoaggregates in the latter part of this Chapter.

4.1 Introduction

Caffeine (CAF, 1,3,7-trimethylxanthine), theobromine (TBR, 3,7-dimethylxanthine) and theophylline (TPH, 1,3-dimethylxanthine), which are structurally similar family members of purine alkaloids, are naturally present in foods and beverages such as coffee, tea, and chocolate. Interestingly, TBR and TPH are also two of the three major metabolites of CAF.[15] Methylxanthines (MeX) act as central nervous system stimulants for sustaining alertness by blocking adenosine receptors and inhibiting phosphodiesterases,[213,214] while showing antitumoral and anti-inflammatory properties.[215] For instance, CAF is widely used in the formulations of prescription and over-the-counter medications, whereas TBR and TPH are active ingredients of bronchodilator drugs taken to widen the airways in the lungs for asthma and other respiratory tract problems.[216] Though MeX are generally safe for human consumptions except in the cases of severe overdose[217], they are potentially toxic to small animals such as cats and dogs.[218]

Development of a high-performance MeX sensor with multiplexing ability is thus essential for therapeutic drug monitoring, quality control of consumer products in the food and pharmaceutical industries, as well as for forensics and veterinary science. Conventional methods for MeX detection are based on high-performance liquid chromatography, near infrared spectroscopy, immunoassay, voltammetry and fluorescence,[216,219–227] but not all of these methods allow multiplexed detection of MeX in real-time with minimal sample preparation and high performance.

SERS is an analytical technique capable to quantitatively discriminate multiple structurally similar analyte molecules located in close proximity to the plasmonic nanostructures (e.g. Au NPs and Ag NPs) via their vibrational fingerprints, with additional advantages such as rapid response, high sensitivity, selectivity and reproducibility (see section 1.4). Surprisingly, most of the previous SERS studies on MeX detection were based on Ag NPs[228–237] for their relatively strong signals despite Au NPs having higher chemical stability, reproducibility and biocompatibility.[238–240] This is probably due to the poor sensitivity and reproducibility of the SERS signals resulted from bare Au NPs or uncontrolled aggregation triggered by NaCl.[15,241] The inter-particle spacing between Au NPs can be precisely controlled via cucurbituril (CB) mediated aggregation, thus localising the analyte molecules at the centre of the plasmonic hotspots via formation of host-guest complexes. Previous work on MeX detection mainly focused on CAF, while TBR and TPH, in particular their multiplexed SERS sensing, remains largely unexplored.

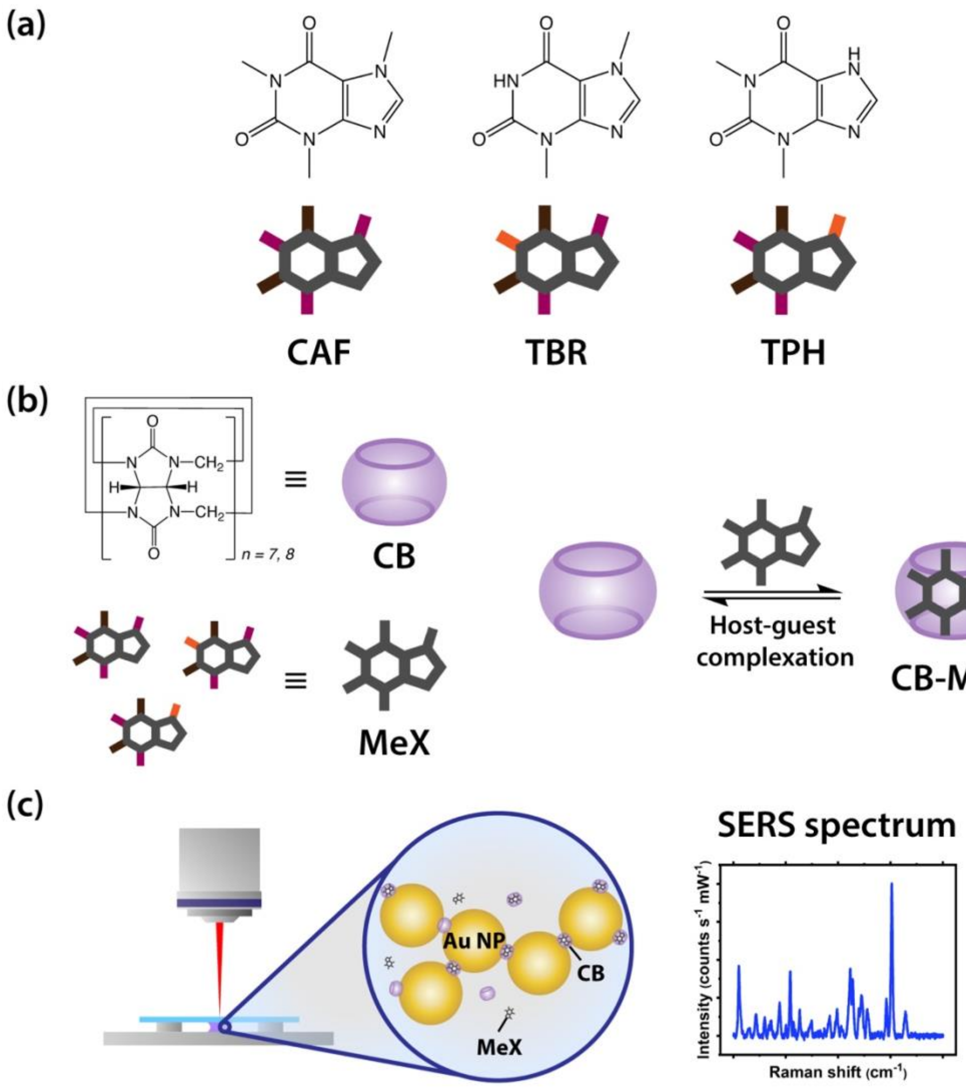

Figure 4.1. Schematic illustrations of (a) MeX (CAF, TBR and TPH), (b) the formation of a 1:1 host-guest complex between CB and MeX and (c) the SERS measurement of the Au NP-CB-MeX sample solution.

Herein, the host-guest complexations between CB*n* (*n* = 7, 8) and structurally similar drug molecules, MeX (CAF, TBR and TPH), were investigated in solution using experimental and computational techniques to quantify the key binding parameters for the first time (Figure 4.1). Quantitative SERS detection of MeX was demonstrated with highly reproducible signals via formation of precise plasmonic hotspots within the Au NP: CB nanoaggregates. The detection limit of CAF is down to ~1 μM while those of its demethylated analogues, TBR and TPH, have reached ~50 nM, which are comparable to, if not better than, other similar SERS techniques in the literature.[15,230–232,236–238,240,241] Notably, multiplexed detection of TBR and TPH at sub-μM concentrations was also demonstrated with CB8 using our SERS sensing platform.

4.2 Supramolecular chemistry of CB and MeX

The conjugated acid of CAF, $[\text{CAF-H}]^+$, has a pKa of 10.4,[214] implying that CAF exists in its protonated form in solution under our experimental condition. TBR and TPH, which have pKa of 10.0 and 8.8 respectively,[214] also exist in their protonated forms, $[\text{TBR-H}]^+$ and $[\text{TPH-H}]^+$, in our studies. The binding of CB7 to CAF was first suggested by Issacs and co-workers[242] in 2009, however, no NMR studies or DFT models have been reported. Meanwhile, the host-guest complexations of CB8-CAF, CB7-TBR, CB8-TBR, CB7-TPH and CB8-TPH were studied for the first time.

4.2.1 Supramolecular chemistry of CB and CAF

When CB7 and CAF were mixed in D_2O with 1:1 stoichiometry, characteristic upfield shifts of the CAF proton signals (H_a, H_b, H_c and H_d) were observed in the ^1H NMR spectra, verifying the formation of host-guest complexes between CB7 and CAF (Figure 4.2b). Interestingly, splitting of the NMR signal of H_d was observed after host-guest complexation, resulting in two different values for the change in chemical shift ($\Delta\delta$) for H_d ($\Delta\delta_d$ = -0.002 ppm and -0.010 ppm). $\Delta\delta$ for H_d is greater than that for H_c/H_b/H_a ($\Delta\delta_c$ = -0.002 ppm, $\Delta\delta_b$ = -0.002 ppm and $\Delta\delta_a$ = -0.003 ppm) which indicates H_d is deep inside the CB7 cavity, whereas H_c/H_b/H_a are much closer to the carbonyl rim.

Similarly, characteristic upfield shifts of the CAF proton signals (H_b, H_c and H_d) were observed in the ^1H NMR spectra when CAF was mixed with the larger CB homologue, CB8, in DCl, verifying the formation of host-guest complexes between CB8 and CAF (Figure 4.3b). $\Delta\delta_d$ (-0.010 ppm) is greater than $\Delta\delta_c$ (-0.008 ppm) and $\Delta\delta_b$ (-0.006 ppm), indicating H_d is deep inside the CB8 cavity, whereas H_c/H_b are closer to the carbonyl rim. Notably, H_a was downfield shifted ($\Delta\delta_a$ = 0.002 ppm), which implies it is around the portal region.

The energy-minimised molecular models of the $[CB7\text{-}CAF\text{-}H]^+$ and $[CB8\text{-}CAF\text{-}H]^+$ complexes calculated at wB97X-D/6-31G* level of theory both support the host-guest binding geometries derived from NMR (Figure 4.2a,4.3a, see appendix for details), with the cavity of CB8 being large enough to fully encapsulate CAF. The binding energies of the $[CB7\text{-}CAF\text{-}H]^+$ and $[CB8\text{-}CAF\text{-}H]^+$ complexes in gas phase were calculated to be -88.51 kcal mol^{-1} and -94.11 kcal mol^{-1} respectively (see Table A10 in appendix for details), which are consistent to previous report on similar host-guest complexes.[147]

CAF is fully or almost fully encapsulated within the cavity of CB7 and CB8, leaving both of the CB portals available for binding to the surface of Au NPs and hence localising CAF at the centre of the plasmonic hotspots, which is critical to the subsequent SERS studies.

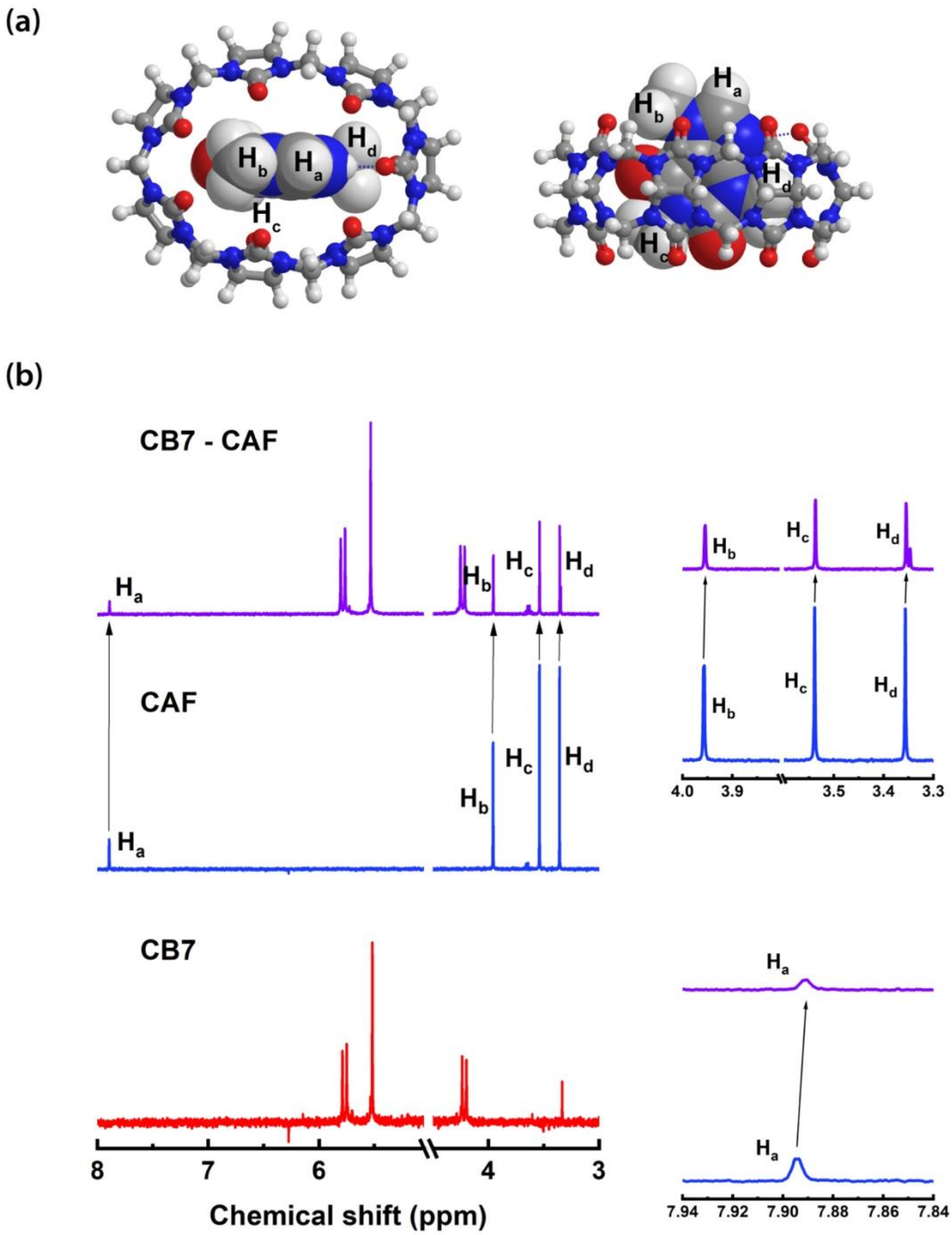

Figure 4.2. (a) DFT molecular model of a $[CB7\text{-}CAF\text{-}H]^+$ host-guest complex in gas phase. (b) ^1H NMR spectra of CB7, CAF and 1:1 CB7-CAF host-guest complex in D_2O. Inset: Zoom-in NMR spectra.

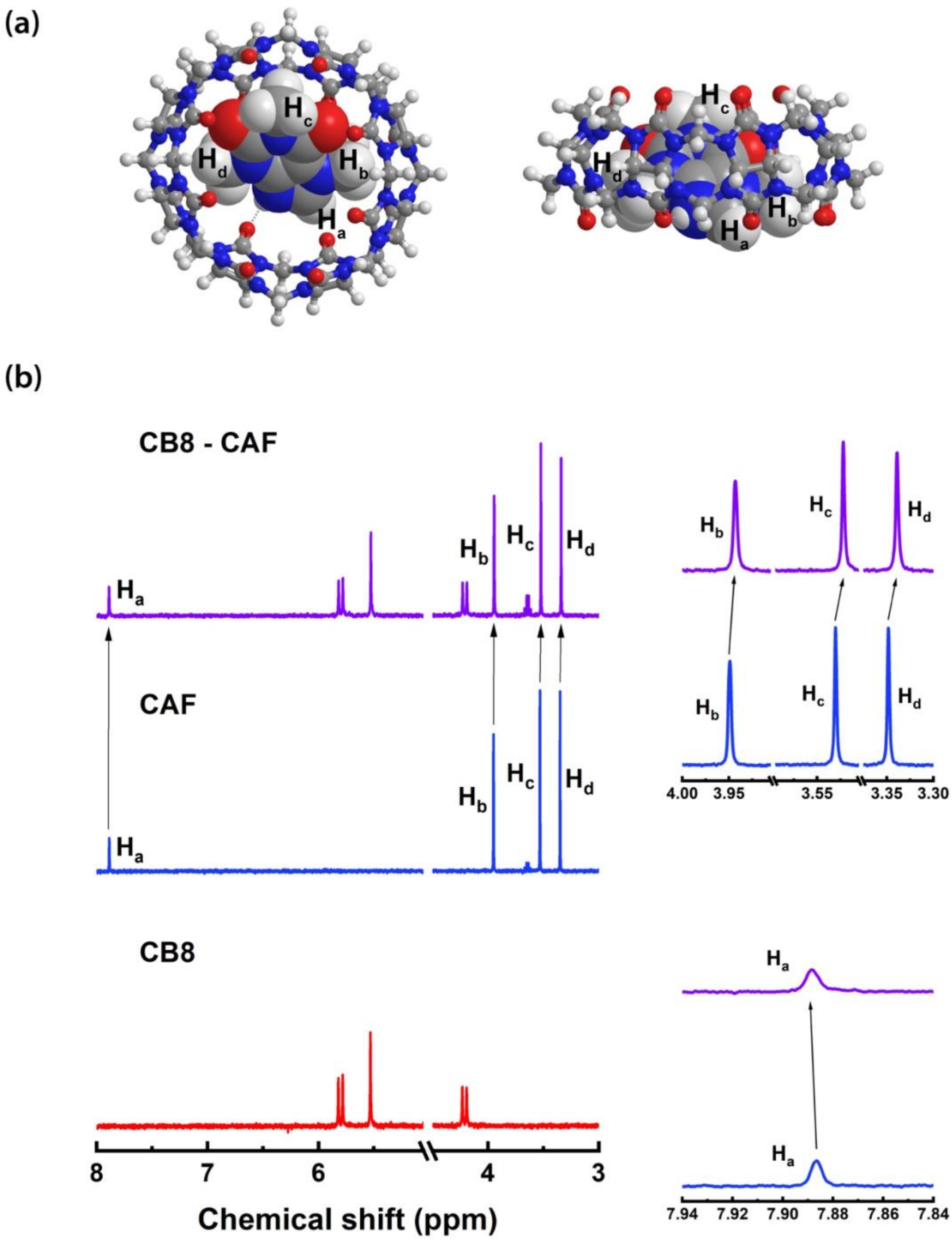

Figure 4.3. (a) DFT molecular model of a $[\text{CB8-CAF-H}]^+$ host-guest complex in gas phase. (b) ^{1}H NMR spectra of CB8, CAF and 1:1 CB8-CAF host-guest complex in DCl. Inset: Zoom-in NMR spectra.

4.2.2 Supramolecular chemistry of CB and TBR

Host-guest complexations between the demethylated analogues of CAF, TBR and TPH, with CB7 and CB8 were also studied.

When CB7 and TBR were mixed in D_2O with 1:1 stoichiometry, characteristic upfield shifts of the TBR proton signals (H_b and H_c) were observed in the ^1H NMR spectra, verifying the formation of host-guest complexes between CB7 and TBR (Figure 4.4b). The NMR signal of H_b was strongly broadened after host-guest complexation ($\Delta\delta_b$ = -0.099 ppm), probably due to the binding kinetics falling into the intermediate exchange regime on the NMR time scale at 298 K. This implies the H_a signal may be so broad that it could not be observed in the NMR spectra. The energy-minimised molecular model of the $[CB7\text{-}TBR\text{-}H]^+$ complex calculated at wB97X-D/6-31G* level of theory supports the formation of host-guest complexes between CB7 and TBR (Figure 4.4a, see appendix for details). The binding energy of the $[CB7\text{-}TBR\text{-}H]^+$ complex in gas phase was calculated to be -88.87 kcal mol^{-1} (see Table A10 in appendix for details), which is consistent to that of the $[CB7\text{-}CAF\text{-}H]^+$ complex.

In addition, characteristic upfield shifts of the TBR proton signals (H_a, H_b and H_c) were observed when TBR was mixed with CB8, verifying the formation of 1:1 CB8-TBR host-guest complexes (Figure 4.5b). $\Delta\delta$ for H_a ($\Delta\delta_a$ = -0.014 ppm) is greater than that for H_c/H_b ($\Delta\delta_c$ = -0.010 ppm and $\Delta\delta_b$ = -0.011 ppm) which indicates H_a is deeper inside the CB8 cavity, whereas H_c/H_b are closer to the carbonyl rim. The energy-minimised molecular model of the $[CB8\text{-}TBR\text{-}H]^+$ complex calculated at wB97X-D/6-31G* level of theory supports the host-guest binding geometry derived from NMR (Figure 4.5a, see appendix for details). The binding energy of the $[CB8\text{-}TBR\text{-}H]^+$ complex in gas phase was calculated to be -79.40 kcal mol^{-1} (see Table A10 in appendix for details), which is consistent to that of the $[CB8\text{-}CAF\text{-}H]^+$ complex.

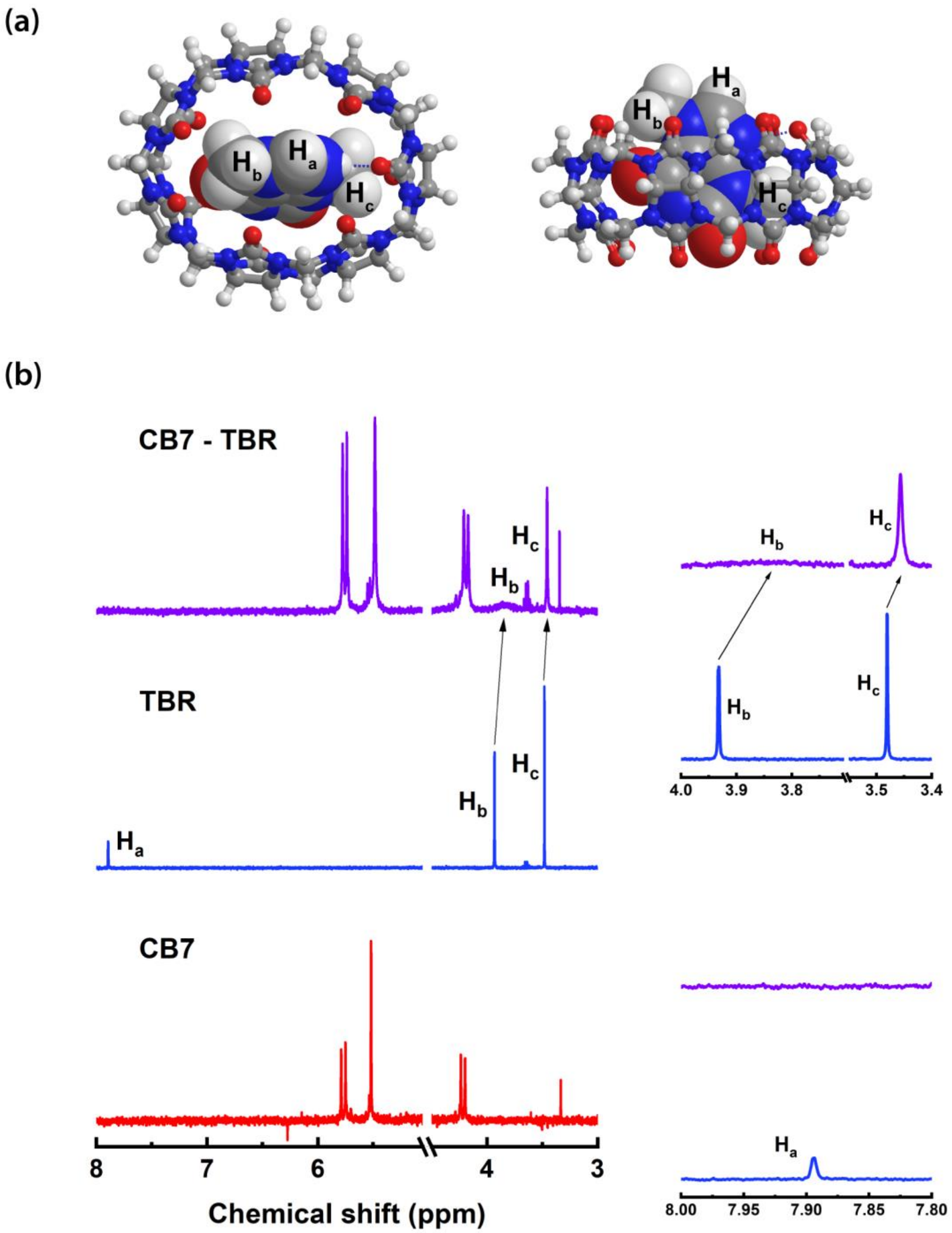

Figure 4.4. (a) DFT molecular model of a $[\text{CB7-TBR-H}]^+$ host-guest complex in gas phase. (b) ^1H NMR spectra of CB7, TBR and 1:1 CB7-TBR host-guest complex in D_2O. Inset: Zoom-in NMR spectra.

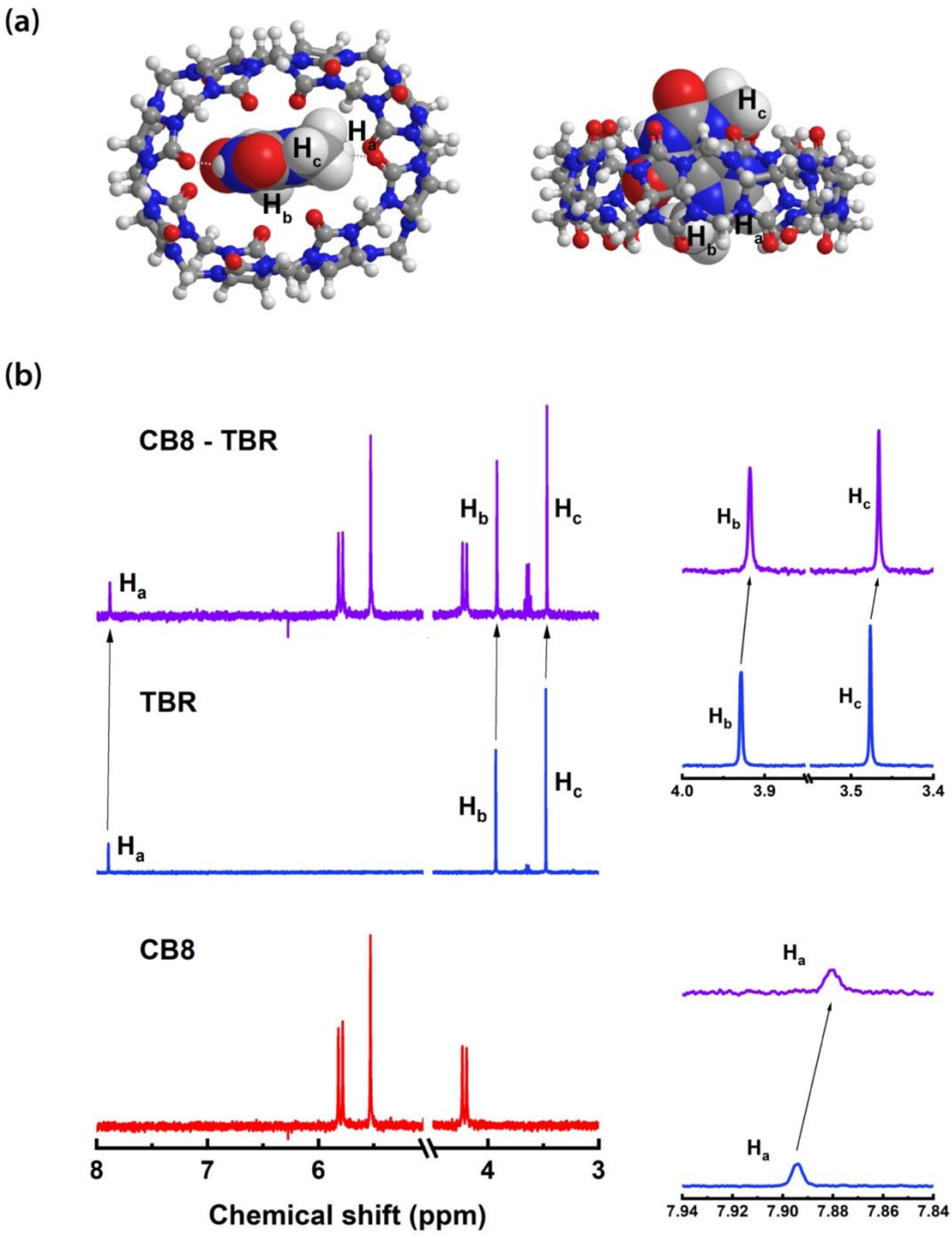

Figure 4.5. (a) DFT molecular model of a $[CB8\text{-}TBR\text{-}H]^+$ host-guest complex in gas phase. (b) ^1H NMR spectra of CB8, TBR and 1:1 CB8-TBR host-guest complex in DCl. Inset: Zoom-in NMR spectra.

4.2.3 Supramolecular chemistry of CB and TPH

Though TBR and TPH are isomers, strong broadening of proton signals after host-guest complexation between CB and TPH was not observed in the ^{1}H NMR spectra (Figure 4.6b). When CB7 and TPH were mixed in D_2O with 1:1 stoichiometry, characteristic shifts (H_a, H_b and H_c) of the TPH proton signals were observed, verifying the formation of host-guest complexes between CB7 and TPH. In particular, H_a was downfield shifted ($\Delta\delta_a = 0.021$ ppm) after host-guest complexation, implying it should be around the portal region in a similar way to the case of [CB8-CAF-H]$^+$. However, H_a is deep inside the CB7 cavity in the energy-minimised model of the [CB7-TPH-H]$^+$ complex calculated at wB97X-D/6-31G* level of theory which suggests the model could be at local minimum (Figure 4.6a, see appendix for details).

The host-guest complexation between CB8 and TPH is very similar to that of CB7 and TPH, in which characteristic upfield shifts of H_b and H_c, and downfield shift of H_a signals were observed in the ^{1}H NMR spectra (Figure 4.7b), whereas H_a is deep inside the CB8 cavity in the energy-minimised model of the [CB8-TPH-H]$^+$ complex calculated at wB97X-D/6-31G* level of theory (Figure 4.7a, see appendix for details). The binding energies of the [CB7-TPH-H]$^+$ and [CB8-TPH-H]$^+$ complexes in gas phase were calculated to be -81.47 kcal mol^{-1} and –85.38 kcal mol^{-1} respectively (see Table A10 in appendix for details), which are consistent to those of the [CB-CAF-H]$^+$ and [CB-TBR-H]$^+$ host-guest complexes.

The two isomers, TBR and TPH, are fully or almost fully encapsulated within the cavity of CB7 and CB8, leaving both of the CB portals available for binding to the surface of Au NPs as in the case of CAF, and hence TBR and TPH are localised at the centre of the plasmonic hotspots which are critical to the subsequent SERS studies.

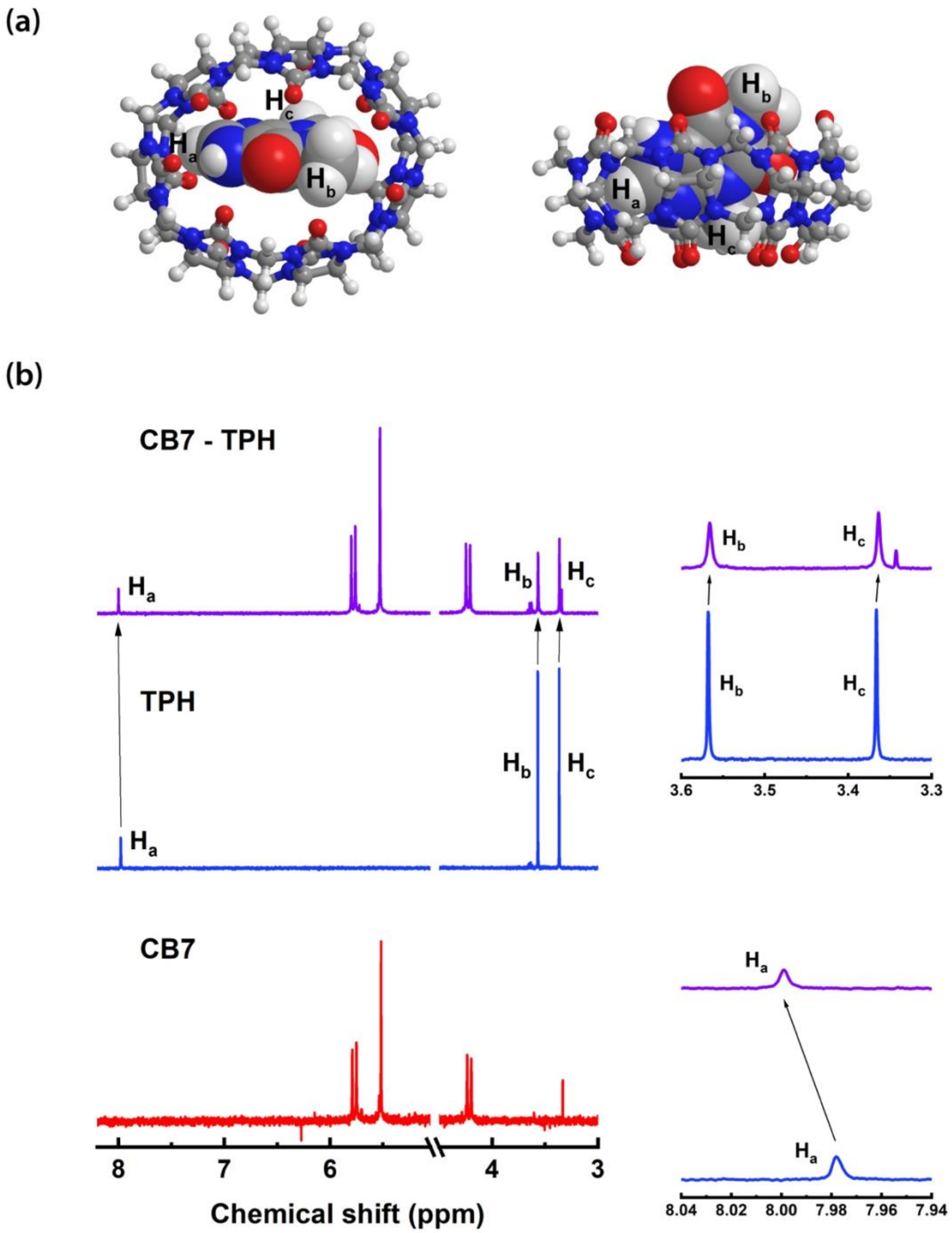

Figure 4.6. (a) DFT molecular model of a $[CB7\text{-}TPH\text{-}H]^+$ host-guest complex in gas phase. (b) ^1H NMR spectra of CB7, TPH and 1:1 CB7-TPH host-guest complex in D_2O. Inset: Zoom-in NMR spectra.

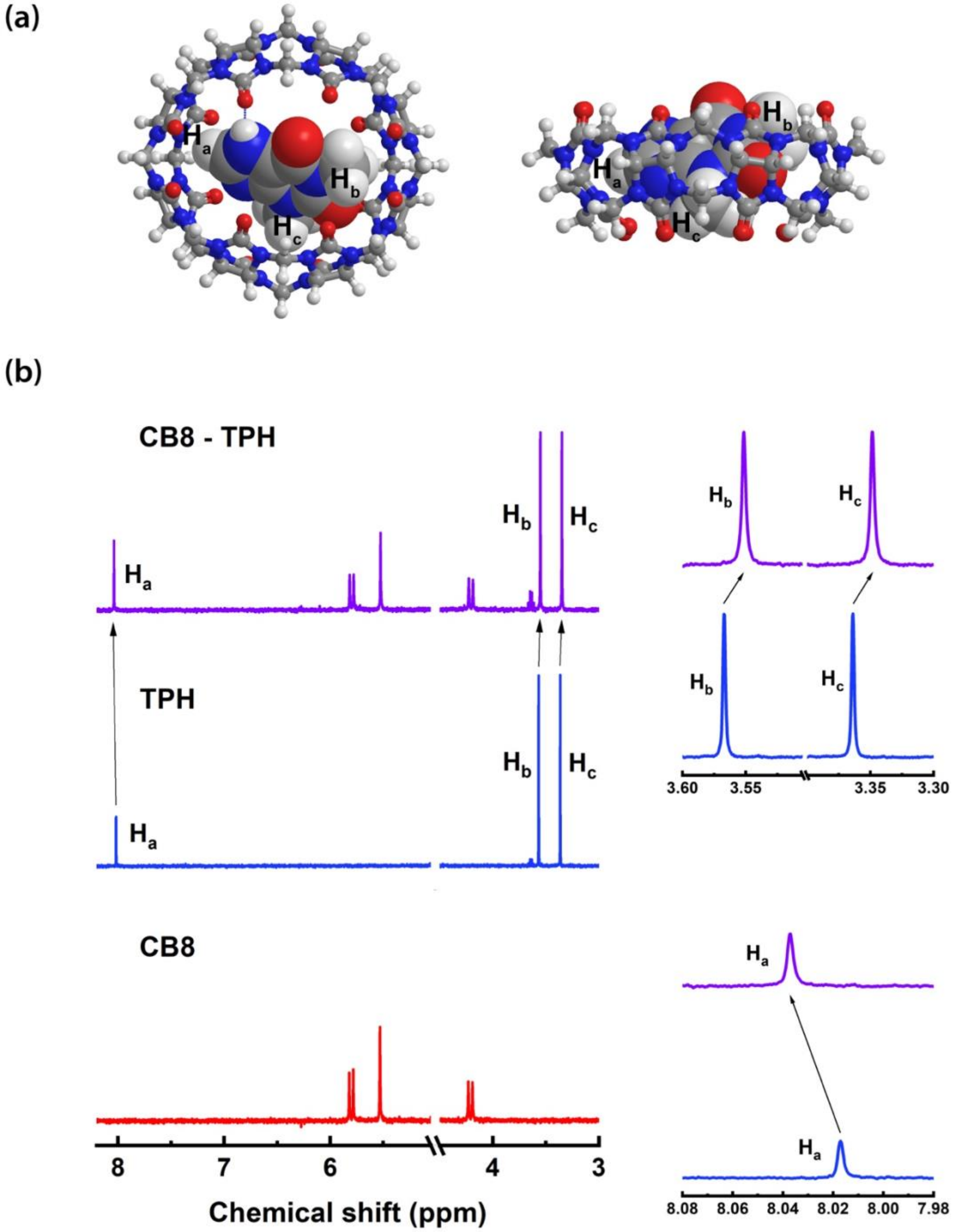

Figure 4.7. (a) DFT molecular model of a $[CB8\text{-}TPH\text{-}H]^+$ host-guest complex in gas phase. (b) ^1H NMR spectra of CB8, TPH and 1:1 CB8-TPH host-guest complex in DCl. Inset: Zoom-in NMR spectra.

4.3 Raman spectroscopy of MeX and SERS of CB

The Raman spectrum of CAF powder is characterised by two major peaks at 558 cm^{-1} and 1330 cm^{-1}, corresponding to pyrimidine ring deformation + C-N-C deformation + CH_3 rocking and imidazole ring stretching vibration respectively (Figure 4.8a).[236,243] Similarly, the Raman spectrum of TBR powder is characterised by two major peaks at 622 cm^{-1} and 1334 cm^{-1}, which are attributed to C=C-C deformation and imidazole ring stretching vibration respectively (Figure 4.8b).[243,244] The Raman spectrum of TPH powder is characterised by a main peak at 557 cm^{-1}, which corresponds to pyrimidine ring deformation + C-N-C deformation + CH_3 rocking (Figure 4.8c). The other peaks at 668 cm^{-1} and 1316 cm^{-1} are assigned to O=C-N deformation + pyrimidine imidazole ring deformation and imidazole ring stretching vibration respectively.[243]

The two characteristic Raman peaks of CB7 at 444 cm^{-1} and 833 cm^{-1}, which correspond to ring scissor and ring deformation modes respectively, were clearly observed in the SERS spectra of CB7 at 447 cm^{-1} and 833 cm^{-1} (Figure 4.8d). The slight shifts in peak position and peak broadening could be due to the solution effect and the molecular interaction between Au NPs and CB7. Notably, the ring scissor mode of CB8 is at a slightly lower wavenumber of 444 cm^{-1} whereas its ring deformation mode is at a slightly higher wavenumber of 834 cm^{-1} than that of CB7, which is consistent with the previous report.[175]

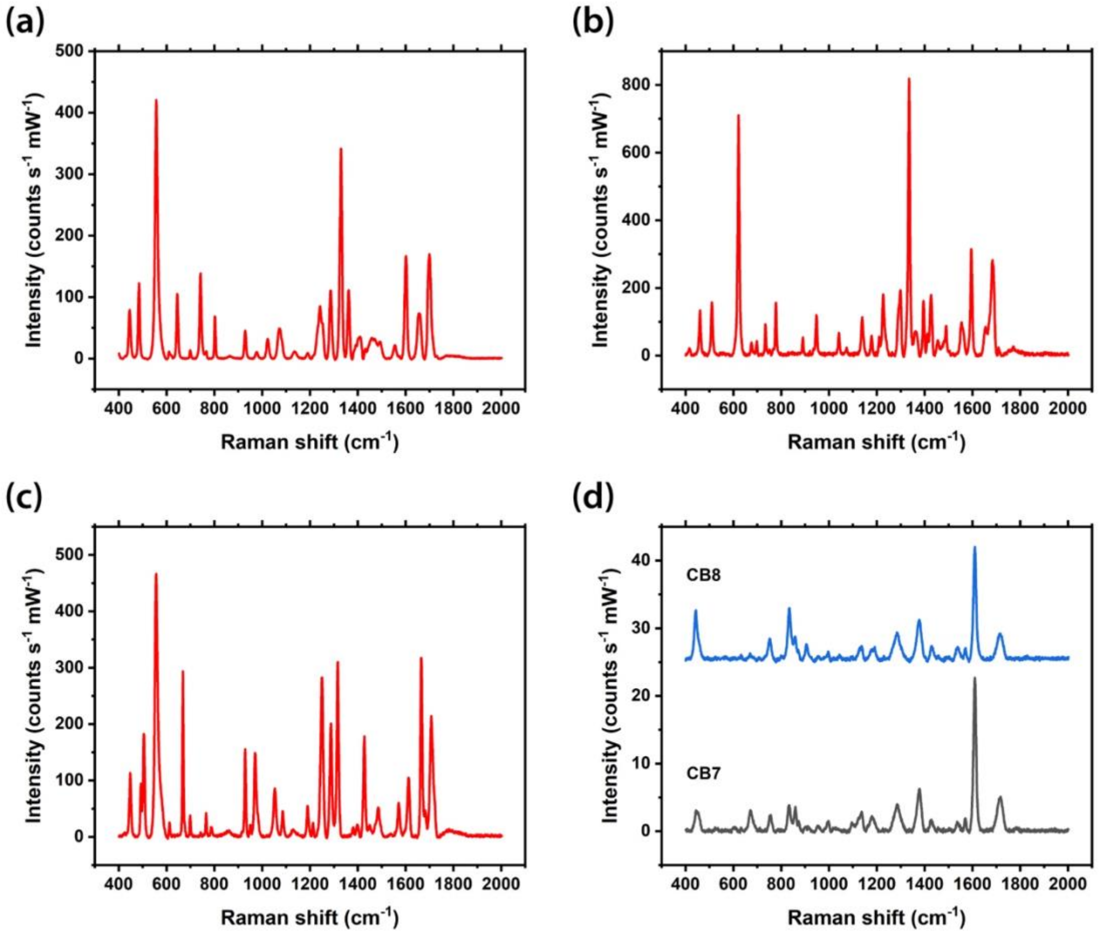

Figure 4.8. (a-c) Raman spectra of (a) CAF, (b) TBR and (c) TPH powder respectively. (d) SERS spectra of 10 μM CB7 and 5 μM CB8.

4.4 SERS sensing of CB-CAF host-guest complexes

The potential SERS detection of CAF was first performed with CB7 by adding a pre-mixed CB7-CAF solution into the 40 nm citrate-capped Au NP solution, at a constant CB7 concentration of 10 μM as to ensure the formation of reproducible nanoaggregates, i.e. SERS substrates, since the aggregation kinetics is determined by the ratio of Au NP: CB. As CB7 defines precise nanojunctions between Au NPs while CAF is fully or almost fully encapsulated within the CB7 cavity (see section 4.2.1), CAF is localised at the plasmonic hotspots within the Au NP: CB7 nanoaggregates (Figure 4.9a). The characteristic Raman peak of CAF at 1330 cm^{-1}, which is attributed to imidazole ring stretching vibration, can be observed in the SERS spectra down to 5 μM (Figure 4.9c,d). It should be noted that no aggregation of Au NPs can be triggered and no SERS signals can be observed in the absence of CB7 (Figure 4.9b), thus illustrating the importance of CB on CAF sensing.

The sensitivity of our SERS system for CAF detection can be enhanced by using the larger CB homologue, i.e. CB8. The calculated binding energy of the $[\text{CB8-CAF-H}]^+$ complex is lower than that of the $[\text{CB7-CAF-H}]^+$ complex (see section 4.2.1), and CAF is located deeper inside the cavity of CB8 than that of CB7. The SERS detection of CAF was performed by adding a pre-mixed CB8-CAF solution into the Au NP solution, at a constant CB8 concentration of 5 μM, to form precise plasmonic nanojunctions as in the case of CB7 (Figure 4.10a). The main peak of CAF attributed to imidazole ring stretching vibration can be clearly observed in the SERS spectra down to 1.25 μM (Figure 4.10c,d) while no aggregation of Au NPs can be triggered in the absence of CB8 (Figure 4.10b). A good correlation ($R^2 \sim 0.93$) between the SERS intensity and log concentration of CAF was found by performing power-law fittings (Figure 4.10e).

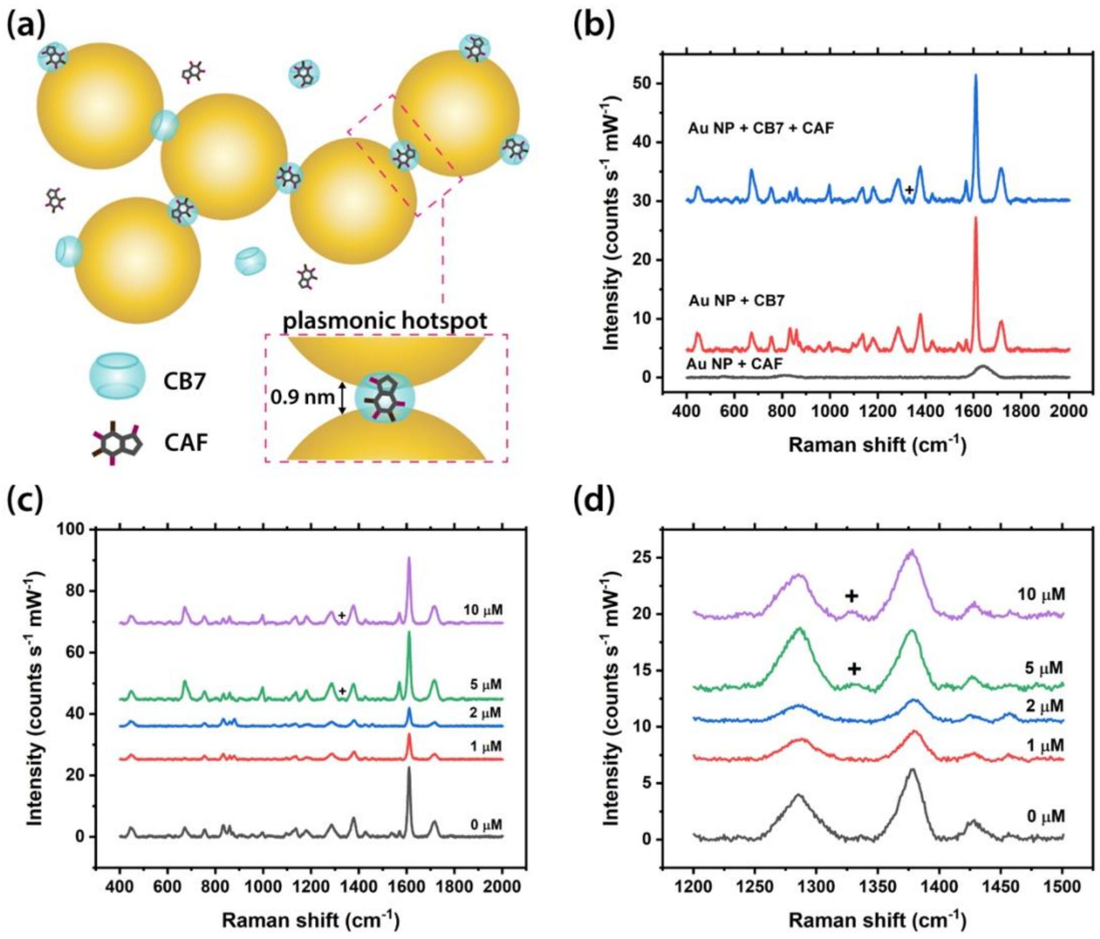

Figure 4.9. (a) Schematic illustration of the precise plasmonic hotspots within Au NP: CB7 nanoaggregates for CAF detection (not to scale). (b) SERS spectra of CAF in the presence or absence of CB7. (c) Full-range and (d) zoom-in SERS spectra of CAF with different concentrations from 0 to 10 μM. Main Raman peak of CAF is marked by +. Spectra were baseline corrected and offset for clarity.

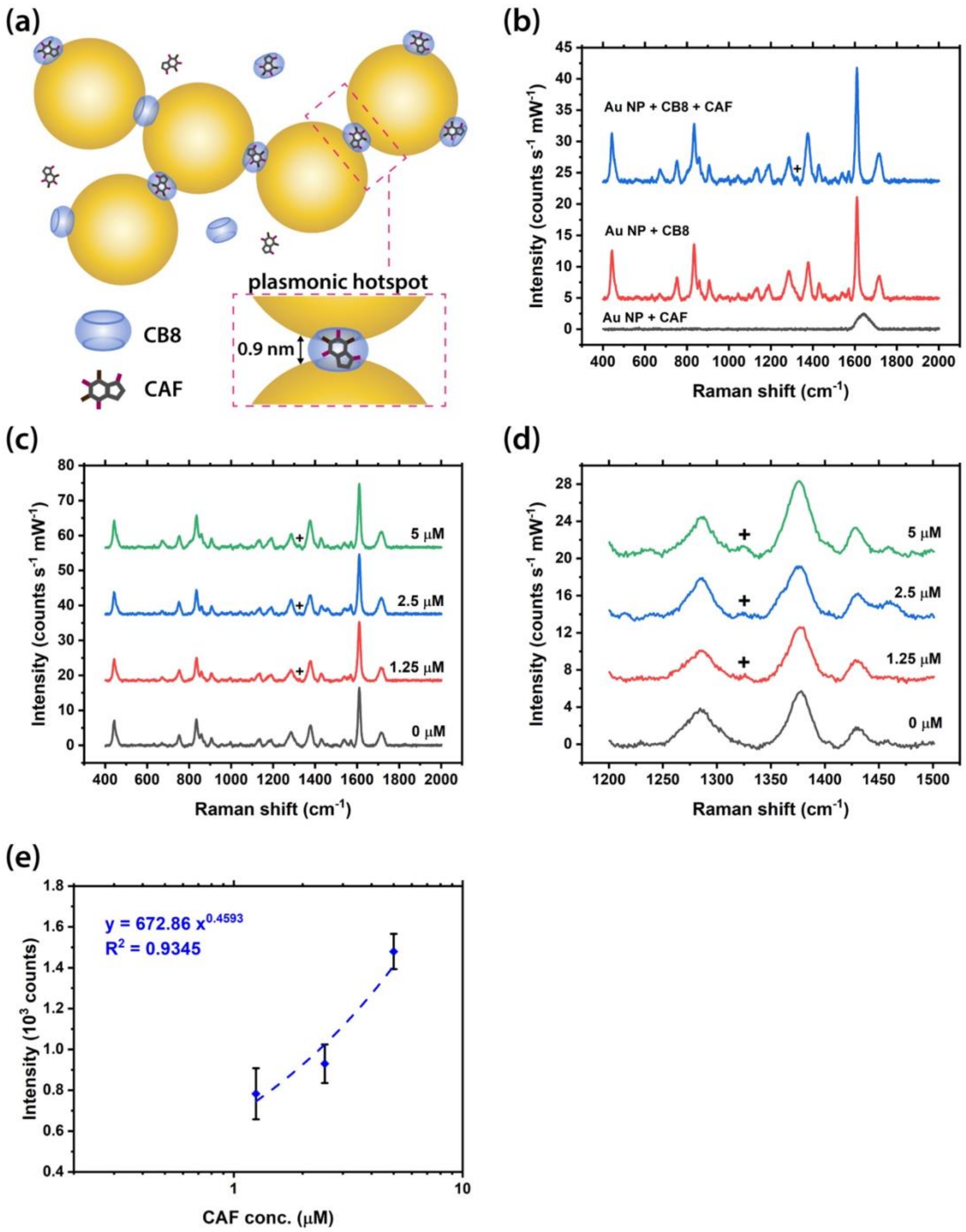

Figure 4.10. (a) Schematic illustration of the precise plasmonic hotspots within Au NP: CB8 nanoaggregates for CAF detection (not to scale). (b) SERS spectra of CAF in the presence or absence of CB8. (c) Full-range and (d) zoom-in SERS spectra of CAF with different concentrations from 0 to 5 μM. Main Raman peak of CAF is marked by +. Spectra were baseline corrected and offset for clarity. (e) Corresponding plot of SERS

intensity of the main CAF peak (marked by **+** in (d)) against CAF concentration. Power-law fittings were performed to reveal correlation between SERS intensity and CAF concentration.

4.5 SERS sensing of CB-TBR host-guest complexes

The SERS detection of the demethylated analogues of CAF, i.e. TBR and TPH, was subsequently investigated in our studies, at a constant concentration of CB7 (or CB8). TBR and TPH are fully or almost fully encapsulated within the cavity of CB7 and CB8 as in the case of CAF while no aggregation of Au NPs can be triggered in the absence of CB (Figure 4.11–4.14). In the Au NP: CB7 system, the characteristic Raman peak of TBR at 1334 cm^{-1}, which is attributed to imidazole ring stretching vibration, can be clearly observed in the SERS spectra down to 0.5 μM (Figure 4.11c,d). A good correlation (R^2 ~ 0.94) between the SERS intensity and log concentration of TBR was found by performing power-law fittings (Figure 4.11e).

In addition, the detection limit of TBR was found to be 10-fold lower (i.e. down to ~50 nM) in the Au NP: CB8 system (Figure 4.12c,d), which is the lowest among all similar SERS platforms in the literature,[15,230] with a strong correlation (R^2 ~ 0.97) between the SERS intensity and log concentration of TBR across a wide range (Figure 4.12e). Notably, the binding geometries of $[CB7\text{-}TBR\text{-}H]^+$ and $[CB8\text{-}TBR\text{-}H]^+$ complexes are also very similar (see section 4.2.2).

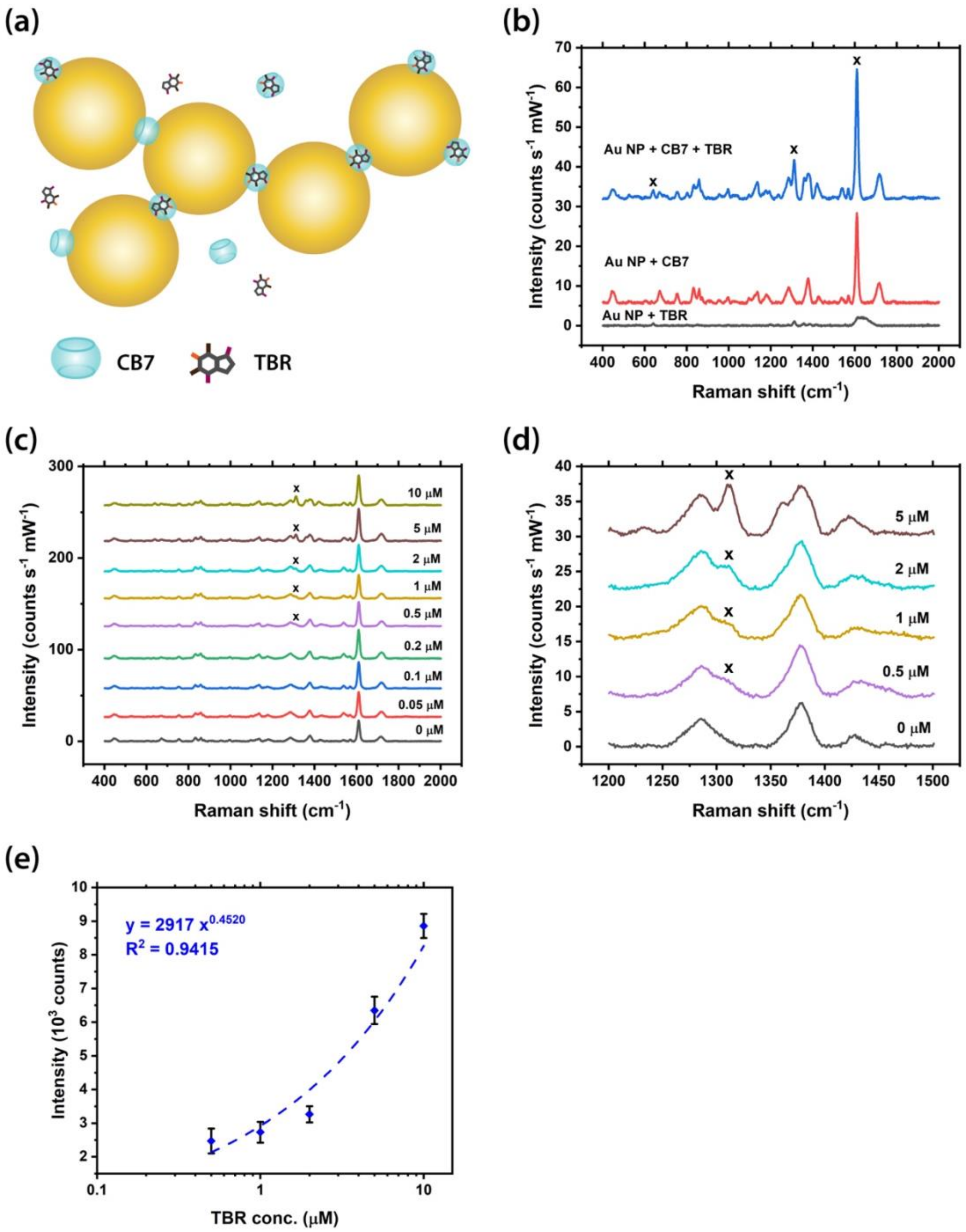

Figure 4.11. (a) Schematic illustration of the precise plasmonic hotspots within Au NP: CB7 nanoaggregates for TBR detection (not to scale). (b) SERS spectra of TBR in the presence or absence of CB7. (c) Full-range and (d) zoom-in SERS spectra of TBR with different concentrations from 0 to 10 μM. Main Raman peak of TBR is marked by x. Spectra were baseline corrected and offset for clarity. (e) Corresponding plot of SERS

intensity of the main TBR peak (marked by x in (d)) against TBR concentration. Power-law fittings were performed to reveal correlation between SERS intensity and TBR concentration.

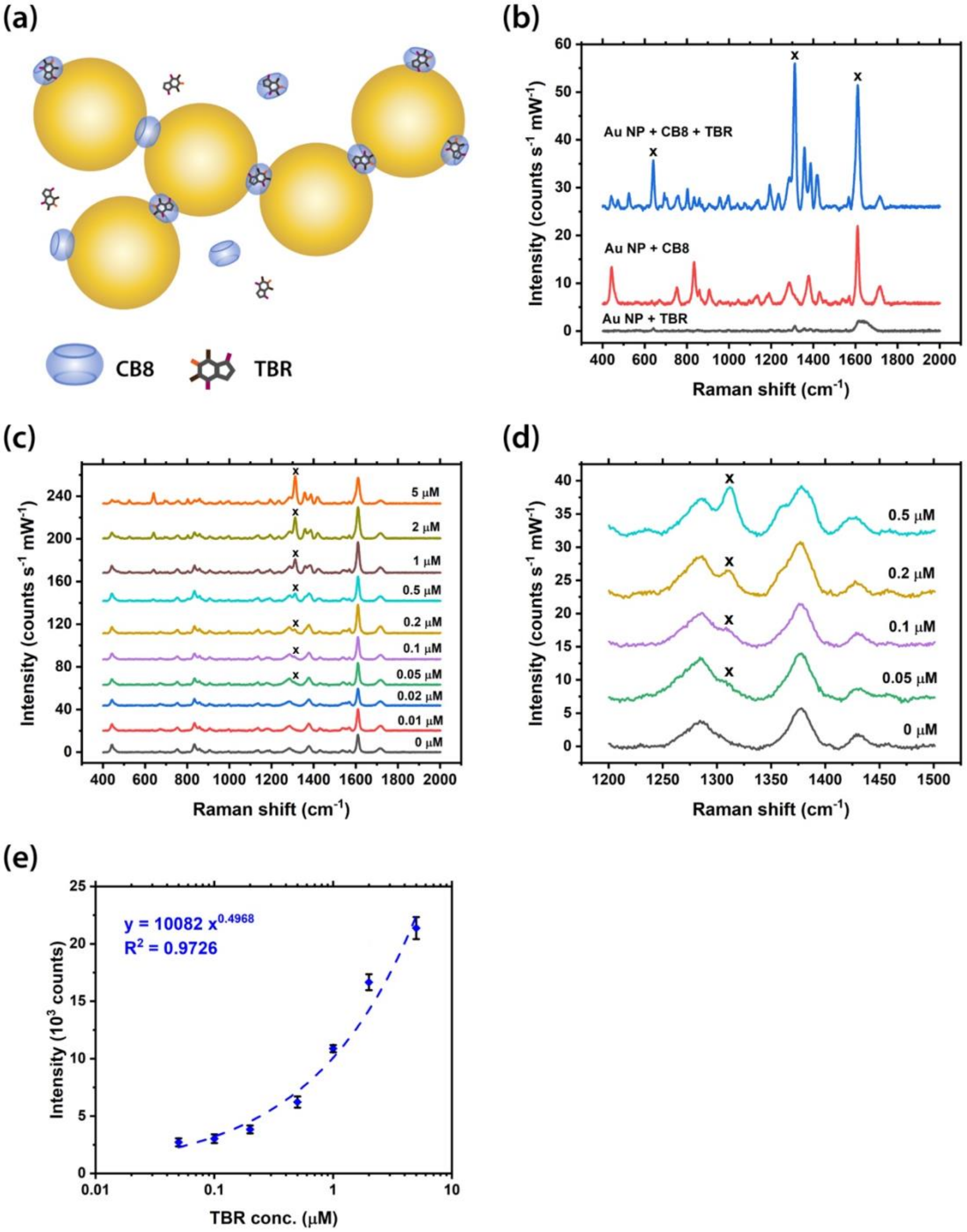

Figure 4.12. (a) Schematic illustration of the precise plasmonic hotspots within Au NP: CB8 nanoaggregates for TBR detection (not to scale). (b) SERS spectra of TBR in the presence or absence of CB8. (c) Full-range and (d) zoom-in SERS spectra of TBR with different concentrations from 0 to 5 μM. Main Raman peak of TBR is marked by x. Spectra were baseline corrected and offset for clarity. (e) Corresponding plot of SERS intensity of the main TBR peak (marked by x in (d)) against TBR concentration. Power-law fittings were performed to reveal correlation between SERS intensity and TBR concentration.

4.6 SERS sensing of CB-TPH host-guest complexes

The characteristic Raman peak of TPH at 557 cm^{-1}, which corresponds to pyrimidine ring deformation + C-N-C deformation + CH_3 rocking, can be clearly observed in the SERS spectra down to 50 nM in the presence of CB7 (Figure 4.13c,d), with a strong correlation (R^2 ~ 0.98) between the SERS intensity and log concentration of TPH (Figure 4.13e). Interestingly, the detection limit of TPH in the Au NP: CB7 SERS system is 10-fold better than that of its isomer, TBR, despite being less Raman-active (Figure 4.8b,c). This could be due to the difference in the binding geometries of the two complexes (see section 4.2.2, 4.2.3).

Moreover, the $[CB8\text{-}TPH\text{-}H]^+$ complex has a similar binding geometry to that of the $[CB7\text{-}TPH\text{-}H]^+$ complex (see section 4.2.3), with a detection limit of ~0.1 μM (Figure 4.14c,d) and a very strong correlation (R^2 ~ 1.00) between the SERS intensity and log concentration of TPH from 0.1 to 2 μM (Figure 4.14e). It should be noted that the 5 μM data point deviates from the trendline, probably due to the LSPR peak shifting away from the 633 nm excitation or the difference in pH, which requires further investigations.

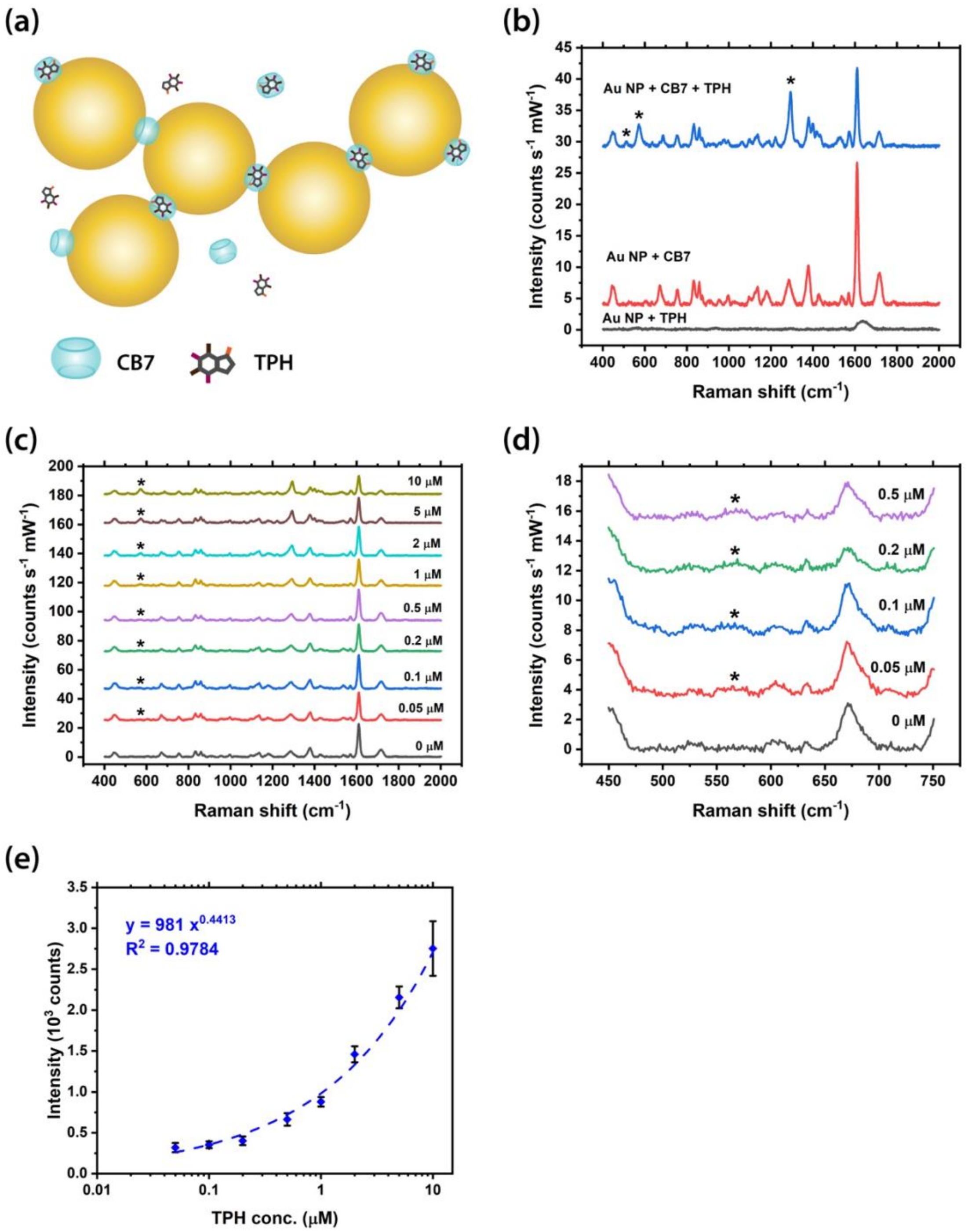

Figure 4.13. (a) Schematic illustration of the precise plasmonic hotspots within Au NP: CB7 nanoaggregates for TPH detection (not to scale). (b) SERS spectra of TPH in the presence or absence of CB7. (c) Full-range and (d) zoom-in SERS spectra of TPH with different concentrations from 0 to 10 μM. Main Raman peak of TPH is marked by *. Spectra were baseline corrected and offset for clarity. (e) Corresponding plot of SERS

intensity of the main TPH peak (marked by * in (d)) against TPH concentration. Power-law fittings were performed to reveal correlation between SERS intensity and TPH concentration.

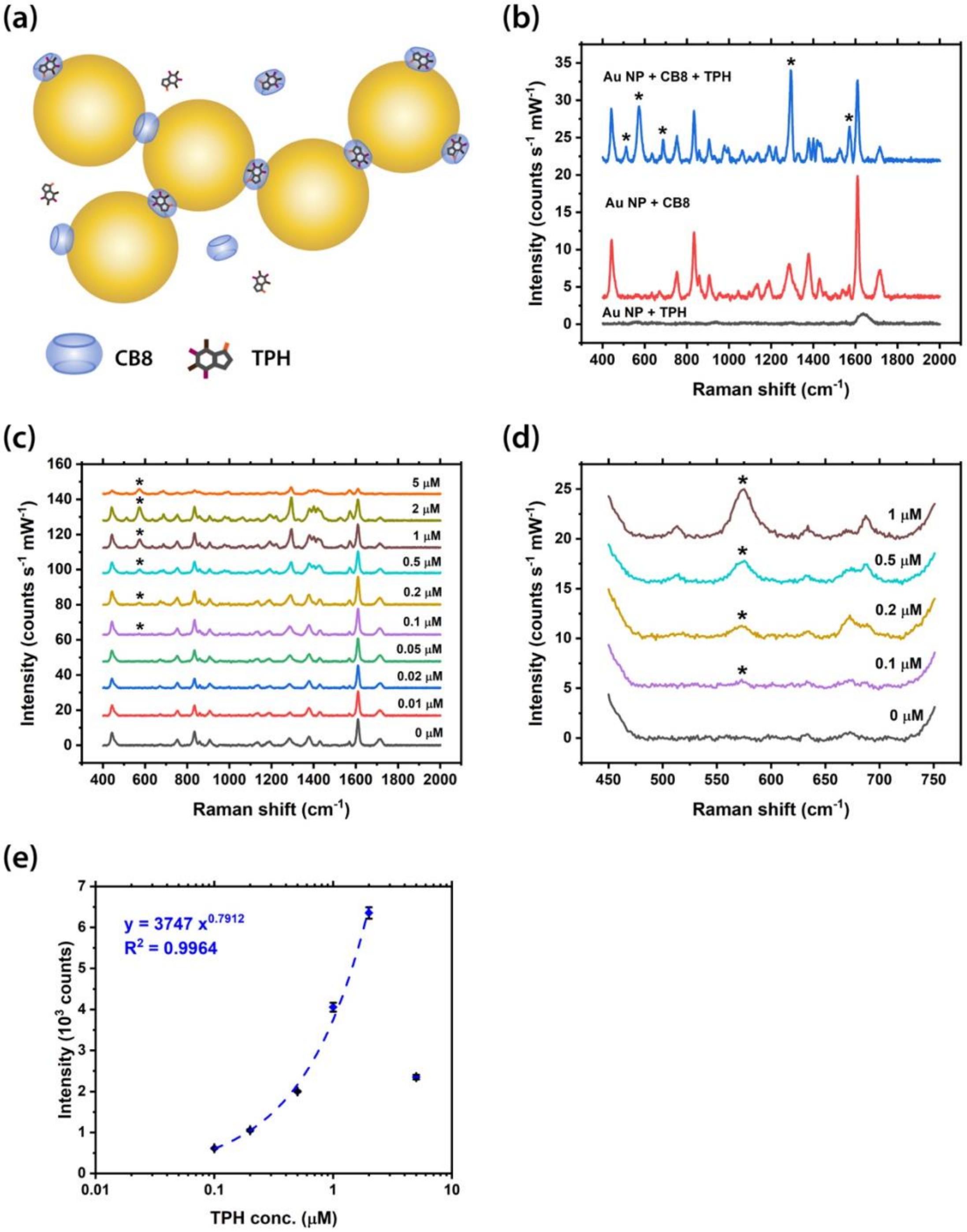

Figure 4.14. (a) Schematic illustration of the precise plasmonic hotspots within Au NP: CB8 nanoaggregates for TPH detection (not to scale). (b) SERS spectra of TPH in the presence or absence of CB8. (c) Full-range and (d) zoom-in SERS spectra of TPH with different concentrations from 0 to 5 μM. Main Raman peak of TPH is marked by *. Spectra were baseline corrected and offset for clarity. (e) Corresponding plot of SERS intensity of the main TPH peak (marked by * in (d)) against TPH concentration. Power-law fittings were performed to reveal correlation between SERS intensity and TPH concentration.

4.7 Multiplexed SERS sensing of isomers

Furthermore, the potential multiplexed detection of structurally similar molecules using our SERS system was demonstrated with the two isomers, TBR and TPH, at various concentrations within the Au NP: CB8 nanoaggregates (Figure 4.15a). The main peaks of TPH and TBR, at 557 cm^{-1} and 1334 cm^{-1} respectively, can be clearly observed in all SERS spectra (Figure 4.15b). Good correlations (R^2 ~ 0.89 – 1.00) between the SERS intensity and log concentration of TBR and TPH were found for all mixtures (Figure 4.15c). Meanwhile, the small error bars in Figure 4.11–4.15 indicate the high reproducibility of the SERS signals of TBR and TPH in our sensing scheme. Notably, the multiplexed detection of MeX at sub-μM levels was performed using Au NP-based SERS system, in contrast to precedent examples using Ag NPs,[15,230] with improved detection limit but without using advanced data analysis model. Therefore, it is possible to distinguish isomers using our SERS sensors by identifying their characteristic Raman peaks, as opposed to other techniques which do not allow molecular fingerprinting.

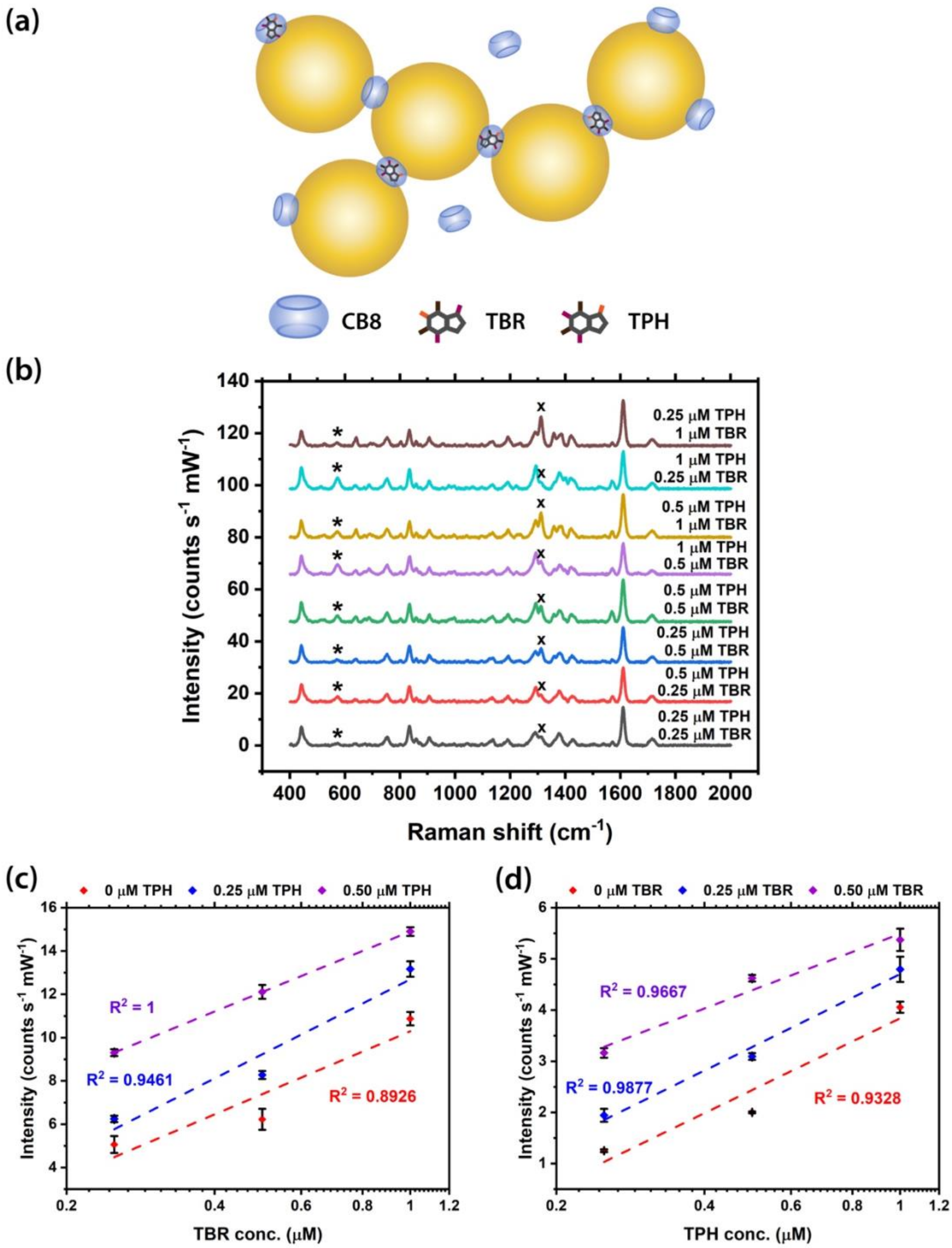

Figure 4.15. (a) Schematic illustration of the multiplexed detection of TBR and TPH within Au NP: CB8 nanoaggregates (not to scale). (b) SERS spectra of different mixtures of TBR and TPH. Main Raman peaks of TBR and TPH are marked by x and * respectively. Spectra were baseline corrected and offset for clarity. (c) Corresponding plot of SERS intensity of the main TBR peak (marked by x in (b)) against TBR

concentration in the presence of different concentrations of TPH. (d) Corresponding plot of SERS intensity of the main TPH peak (marked by * in (b)) against TPH concentration in the presence of different concentrations of TBR. Logarithmic fittings were performed to reveal correlation between SERS intensity and concentration of TBR or TPH.

4.8 Conclusions

In this Chapter, a novel multiplexed SERS sensing platform that utilises various host-guest complexations between two CB homologues, CB7 and CB8, and three structurally similar drug molecules, CAF, TBR and TPH, has been developed. The key binding parameters of the six different CB-MeX complexes have been quantified using NMR and supported by DFT molecular models for the first time. The binding affinities of the complexes will also be measured by UV-Vis titrations in the near future. The potential SERS detection of CAF, TBR and TPH has been demonstrated with CB7 and CB8 mediating the formation of precise plasmonic hotspots within the Au NP: CB nanoaggregates. The detection limit of CAF using our SERS system is down to ~1 μM whereas those of the demethylated analogues, TBR and TPH, have reached ~50 nM, with highly reproducible SERS signals. This is enabled by the relatively large cavity size of CB8, which can fully encapsulate MeX inside its cavity and localise them at the centre of the plasmonic hotspots within the Au NP: CB8 nanoaggregates. The capability of our SERS system to simultaneously detect multiple structurally similar molecules or isomers (TBR and TPH) holds great potential for a wide range of applications including therapeutic drug monitoring, food processing, forensics and veterinary science.

Chapter 5. Quantitative Sensing of Biomarkers in Urinalysis

This Chapter first reported the host-guest complexation between cucurbit[7]uril (CB7) and an important biomarker, creatinine (CRN), using various characterisation techniques including nuclear magnetic resonance (NMR) spectroscopy, UV-Visible spectroscopy and computer simulations based on density functional theory (DFT). Quantitative detection of CRN in water and highly diluted (2000 and 5000-fold) synthetic urine (SU) of clinically relevant concentrations were fully studied by UV-Vis spectroscopy and surface-enhanced Raman spectroscopy (SERS) using nanoaggregates of gold nanoparticles (Au NPs) and CB7 as plasmonic substrates. In addition, the formation of Au NP: CB7 nanoaggregates via neutralisation of surface charges on the citrate-capped Au NPs and carbonyl portal binding of CB7 was verified by dynamic light scattering (DLS) and zeta potential measurements. The tolerance of the SERS sensor against the presence of other biomolecules and proteins was demonstrated in the latter part of this Chapter.

5.1 Introduction

Urine is one of the major body fluids where metabolic information of the body and renal function can be extracted.[245,246] It is readily available and can be obtained in a non-invasive way as opposed to blood serum. Creatinine (CRN), the end product of muscle metabolism, is a critical biomarker used to monitor the kidney filtration function in renal clearance test.[247,248] CRN is used as the internal standard to normalise the variations of water and other analytes in urine for its almost constant excretion rate.[249,250] Early detection of urinary biomarkers can help to diagnose life-threatening diseases and improve the efficiency of medical treatment, for instance, to prevent the progression from renal diseases to kidney failure. Elevated CRN level is also related to diseases such as muscular dystrophy, hyperthyroidism and poliomyelitis.[251–253]

The standard clinical method for CRN quantification is based on the Jaffe reaction developed in 1886.[16,17] However, this method suffers from a major drawback of non-specificity, as picric acid also forms reddish-orange complexes with a wide range of other biomarkers besides CRN in basic solution.[18,250,254,255] Other clinical methods for CRN include enzymatic methods, capillary electrophoresis, high-performance liquid chromatography and isotope dilution mass spectrometry,[256–259] but not all of these methods allow point-of-care diagnosis in real-time with high sensitivity and specificity.

On the contrary, SERS is a promising technique for diagnostic applications as it offers advantages including rapid response, high-sensitivity, cost-effectiveness, ease of use, minimal sample preparation and wider information window of the biomolecules via their vibrational fingerprints (see section 1.4).[260–262] It can dramatically amplify the Raman signals of the biomolecules located at or in close proximity to the plasmonic nanostructures (e.g. Au NPs).[204] Despite the strong merits of using nanostructured SERS substrates for CRN quantification in urinalysis, its applications have been greatly limited by the relatively low reproducibility in solution-based systems or the complicated fabrication procedures involved in solid-based systems.[248,252,257,263–268]

Poor sensitivity and reproducibility result from uncontrolled aggregation of colloidal Au NPs can be overcome by attaching cucurbiturils (CBs) onto the surface of Au NPs to control the inter-particle spacing and localise CRN at the centre of the plasmonic hotspots via formation of host-guest complexes.[1,2,172] Surprisingly, there is only one illustrative example of the Au NP: CB SERS system on biosensing[5] in the literature, thus leaving plenty of room for more application-oriented studies.

Herein, the host-guest complexation between CB7 and an important urinary biomarker CRN was investigated in water using experimental and computational techniques to quantify the key binding parameters for the first time. The formation of nanoaggregates in previous Au NP: CB systems was only mediated by the portal binding of CB7 on the surface of Au NPs, whereas it is also mediated by the electrostatic effects of CRN molecules in addition to CB7 portal binding in this study.[269] The quantitative detection of CRN in water and diluted synthetic urine (SU) of clinically relevant levels was demonstrated using a facile multi-spectroscopic approach, i.e. UV-Vis spectroscopy and SERS, in which a single sample solution exhibits two independent spectral signatures and thus allows rapid cross-validation of the results (Figure 5.1).

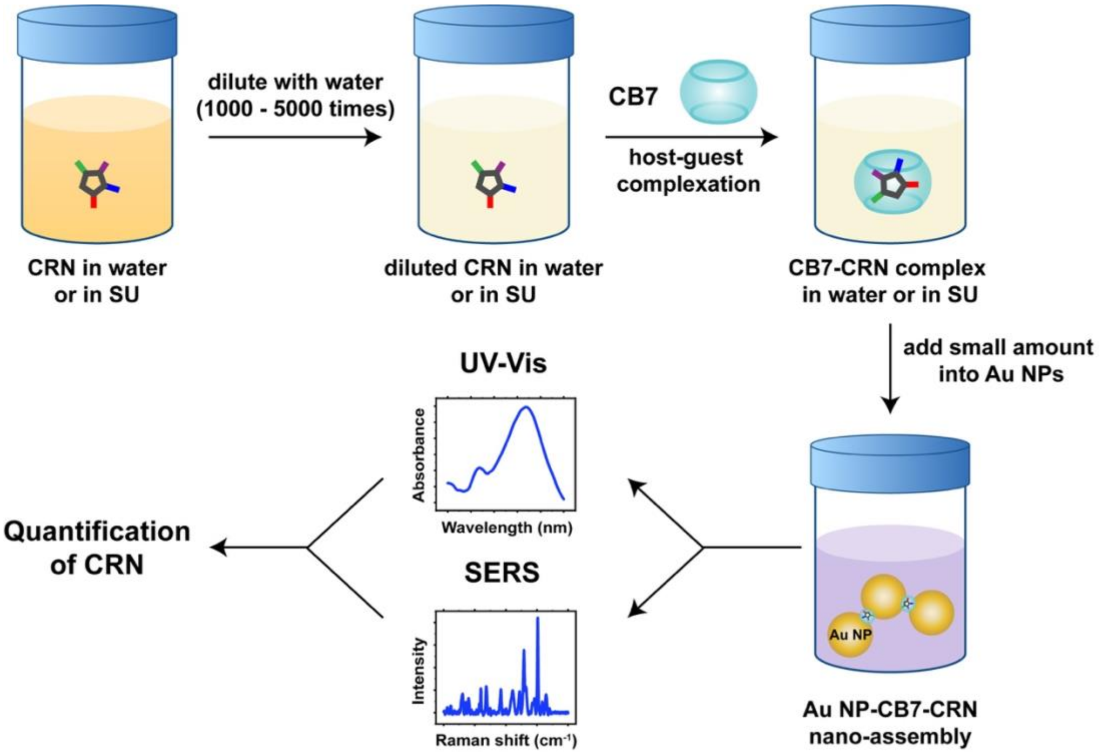

Figure 5.1. Schematic illustration of the dual UV-Vis and SERS detection scheme triggered by the formation of host-guest complexes between CB7 and CRN in water or highly diluted SU, and the self-assembly of Au NPs mediated by portal binding of CB7 and electrostatic interactions with CRN.

Notably, our SERS system for CRN quantification in urinalysis is highly sensitive with a sub-μM detection limit of 12.5 ng mL^{-1} (111 nM), which is the lowest among all current state-of-the-art methods.[269] The CRN signals are also highly reproducible (< 5% error) and tolerant against the presence of other biomolecules and proteins in the complex matrix (SU).

5.2 Supramolecular chemistry of CB7 and CRN

When CB7 and CRN were mixed in D_2O with 1:1 stoichiometry, characteristic upfield shifts of the CRN proton signals (H_a and H_b) were observed in the ^1H NMR spectra, verifying the formation of host-guest complexes between CB7 and CRN (Figure 5.2). The change in chemical shift ($\Delta\delta$) for H_b ($\Delta\delta_b$ = -0.15 ppm) of CRN is much greater than that for H_a ($\Delta\delta_a$ = -0.02 ppm) after host-guest complexation, which indicates H_b (methyl group) is deep inside the CB7 cavity, whereas H_a (CH_2 group) is closer to the carbonyl rim. The formation of CB7-CRN host-guest complexes is mainly driven by the release of high-energy water from the CB7 cavity,[114] together with ion-dipole interactions and hydrogen bonding between the electron-rich carbonyl portal of CB7 and the protonated site on CRN (see section 1.12). A binding constant of $(1.17 \pm 0.03) \times 10^4$ M^{-1} was obtained for the CB7-CRN complex via UV-Vis titration of 50 μM CRN with up to 2 equivalents of CB7, assuming a 1:1 binding model (Figure 5.3). The relatively low binding affinity is probably due to the high water solubility and small molecular size of CRN.

The conjugated acid of CRN, $[CRN\text{-}H]^+$, has a pKa of 9.2,[270] implying that CRN exists in its protonated form in water and SU under our experimental conditions where the pH is between 5 and 7. The energy-minimised molecular models of the complex in gas phase (MMFF94 and wB97XD/6-31G*) and in water (CPCM/wB97XD/6-31G*) both support the host-guest binding geometry derived from NMR (Figure 5.2, see appendix for details). The binding energy of the $[CB7\text{-}CRN\text{-}H]^+$ complex in gas phase and in water was calculated to be -85.00 kcal mol^{-1} and -36.12 kcal mol^{-1} respectively (see Table A13 in appendix for details), which is consistent to previous report on similar host-guest complexes.[147] Notably, CRN is fully encapsulated within the CB7 cavity, leaving both of the CB7 portals available for binding to the surface of Au NPs and hence localising CRN at the centre of the plasmonic hotspots which is critical to the subsequent SERS studies.

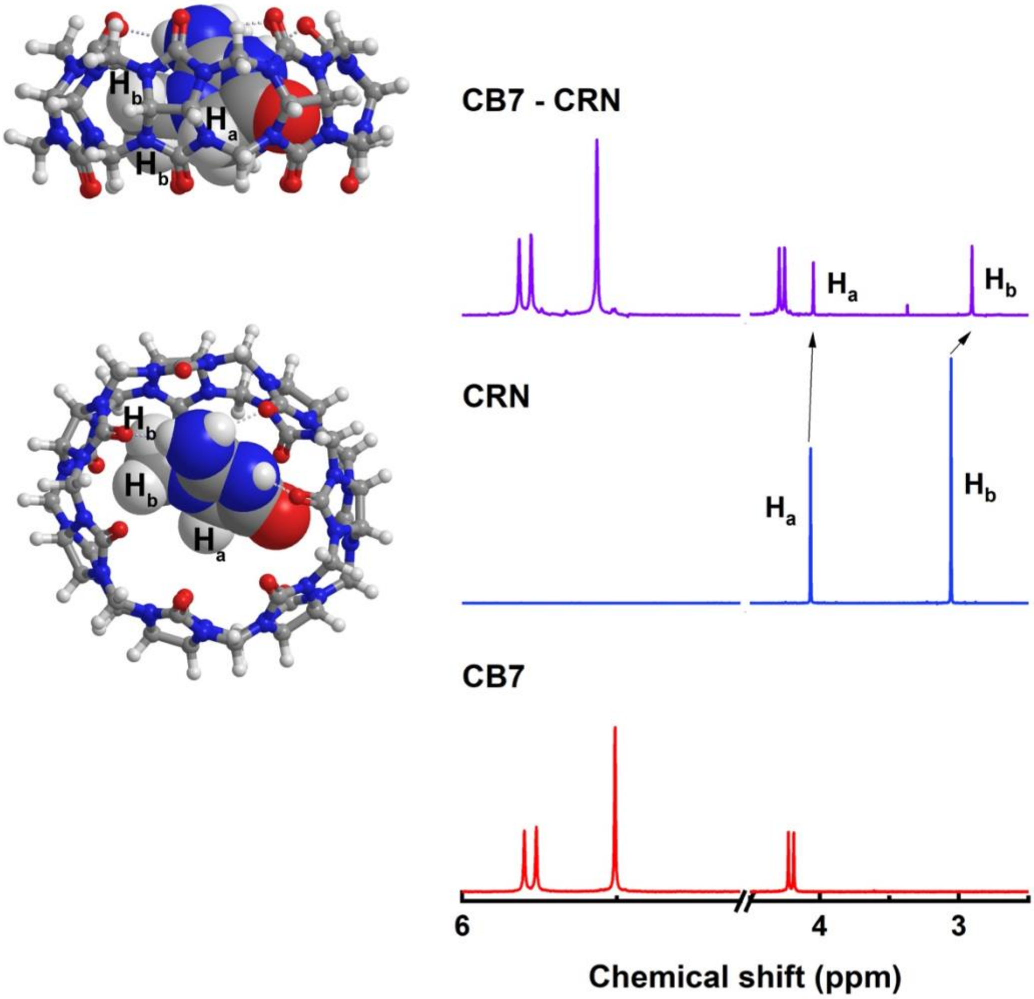

Figure 5.2. ^1H NMR spectra of CB7, CRN and 1:1 CB7-CRN host-guest complex in D_2O. Inset: DFT molecular model of a $[CB7\text{-}CRN\text{-}H]^+$ host-guest complex in water.

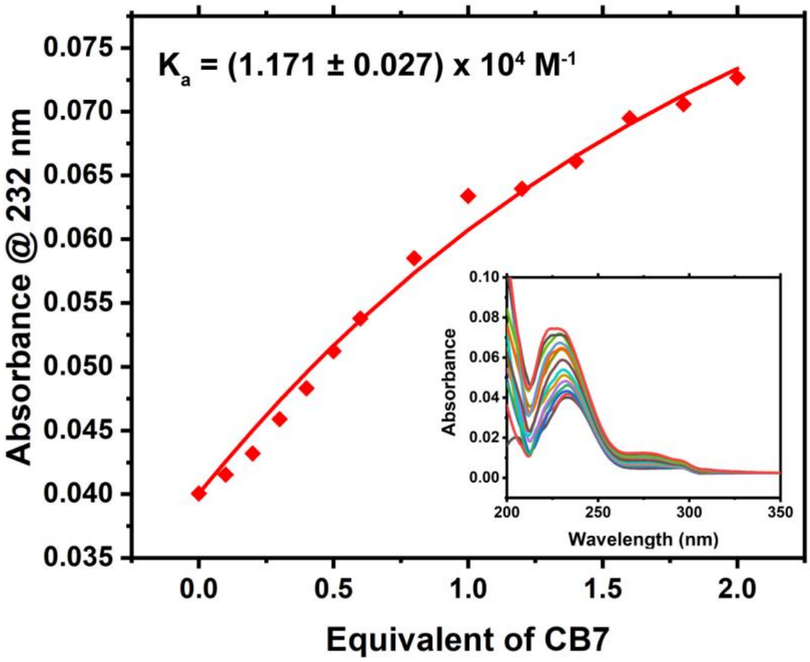

Figure 5.3. UV-Vis titration of 50 µM CRN with CB7. Inset: UV-Vis spectra of CB7-CRN.

5.3 Colourimetric sensing of CB7-CRN host-guest complexes

CRN of clinically relevant concentrations from 0 to 300 mg dL^{-1} (from normal to excess) was prepared in water and SU (see section 2.4). Quantification of CRN was first investigated by UV-Vis titrations in water, 2000 and 5000-fold diluted SU with a constant CB7 concentration of 10 µM as to ensure the formation of reproducible nanoaggregates and signal reproducibility (Figure 5.4). The aggregation of the 40 nm citrate-capped Au NPs was mediated by CB7 as evidenced by the colour change in the Au NP solution from red to purple and the appearance of a secondary localised surface plasmon resonance (LSPR) peak between 690 – 760 nm in the UV-Vis spectra (see section 1.5). The new LSPR peak is attributed to the longitudinal plasmonic resonance, suggesting the formation of chain-like Au nanoaggregates where CB7 is doubly-capped by the Au NPs.[1,2]

Strong correlations between the LSPR peak wavelength (λ_{LSPR}) and log concentration of CRN were found in water ($R^2 \sim 0.93$) and 2000-fold diluted SU ($R^2 \sim 0.98$) while reasonable correlation ($R^2 \sim 0.81$) can still be observed in 5000-fold diluted SU (Figure 5.4). Notably, the low detection limit of 0.06 μg mL^{-1} (0.53 μM) allows quantification of CRN in highly diluted SU, and hence minimising signal perturbation from other biomolecules and proteins in the sample (i.e. matrix effects, see section 5.6). Surprisingly, CRN can also trigger the aggregation of Au NPs in the absence of CB7 when its concentration is > 0.30 μg mL^{-1} in water but the correlation between λ_{LSPR} and log concentration of CRN was less robust (Figure 5.5a). In contrast, CB7 plays the critical role in the formation of nanoaggregates in SU as CRN alone fails to aggregate Au NPs due to preferential surface crowding by other biomolecules and proteins present in the complex matrix (Figure 5.5b).[265]

Attachment of the $[CB7\text{-}CRN\text{-}H]^+$ complexes onto the citrate-capped Au NPs can further speed up the aggregation via neutralisation of the negative surface charges, leading to a decrease in the long-range electrostatic repulsion between Au NPs and thus lowering the colloidal stability, as opposed to the pure CB-mediated aggregations via carbonyl portal binding in the previous examples.[1,2,172] This was verified by the increase in hydrodynamic size of the nanoaggregates and the decrease in the magnitude of the zeta potential in the presence of CB7 (Figure 5.6). In addition, $[CRN\text{-}H]^+$ alone can trigger aggregation of Au NPs via a similar electrostatic self-assembly mechanism, upon electrostatic interactions or chemisorption with the surface of Au NPs via its nitrogen containing groups.

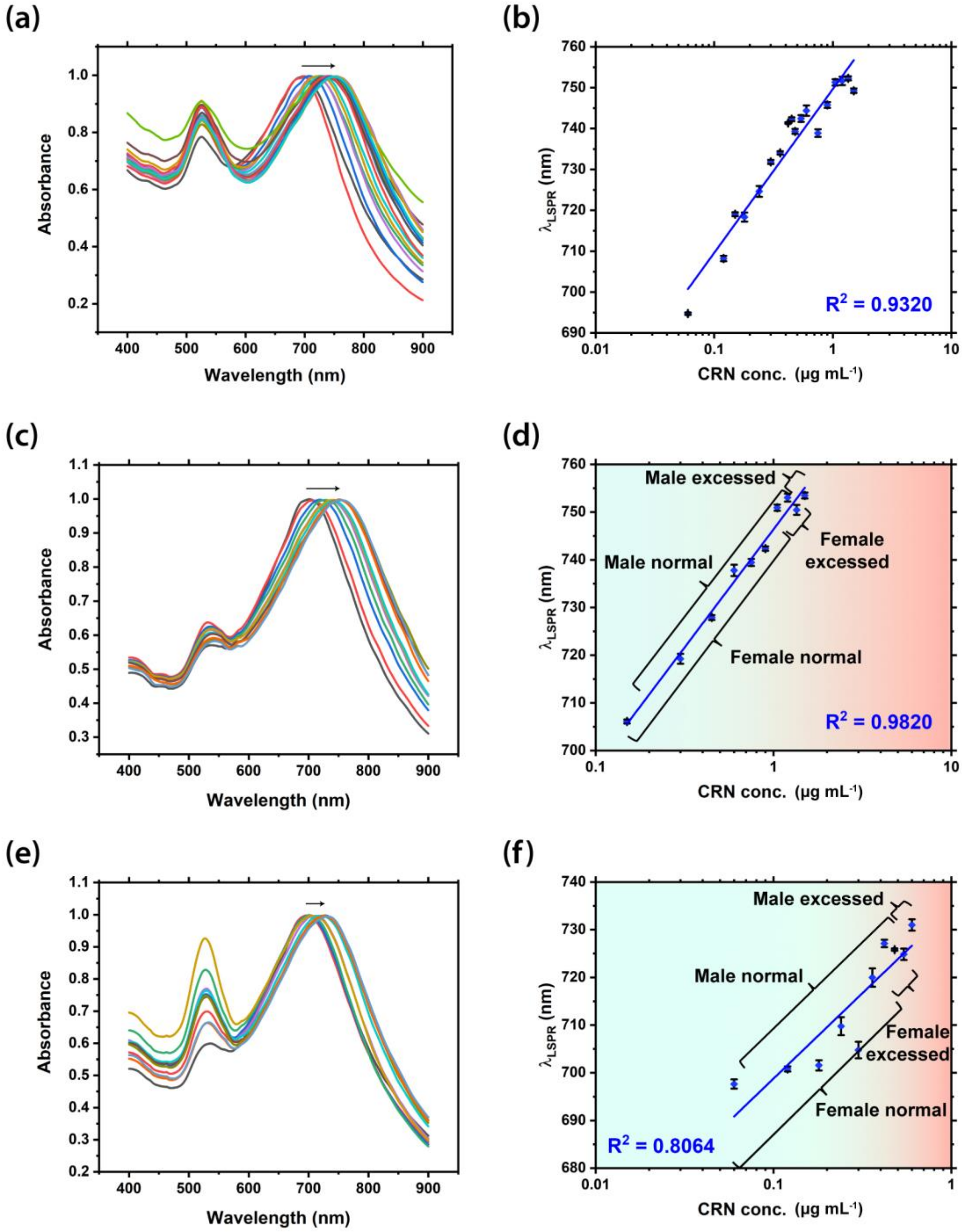

Figure 5.4. (a,c,e) UV-Vis spectra of CRN in (a) water, (c) 2000-fold diluted SU and (e) 5000-fold diluted SU with arrows indicating the shifting of the LSPR peaks. (b,d,f) Corresponding plots of λ_{LSPR} in (a,c,e) against CRN concentration respectively. Logarithmic fittings were performed to reveal correlation between λ_{LSPR} and CRN concentrations. (Note: 1 μg mL^{-1} in measurement samples in (d) corresponds to 2000 μg

mL^{-1} of the actual CRN concentration in undiluted patient samples while 1 µg mL^{-1} in measurement samples in (f) corresponds to 5000 µg mL^{-1} in the undiluted patient samples.)

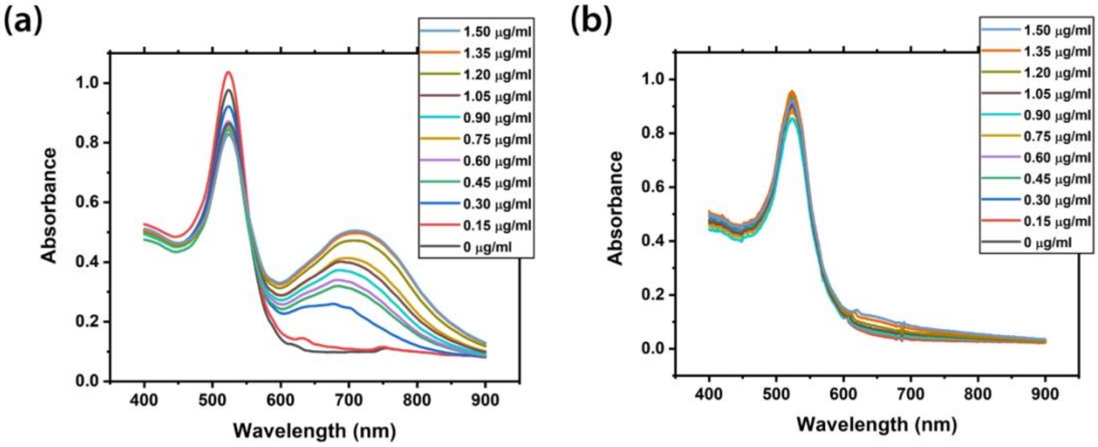

Figure 5.5. UV-Vis spectra of Au NP-CRN in (a) water and (b) 2000-fold diluted SU, with CRN concentrations from 0 to 1.50 µg mL^{-1} in the absence of CB7.

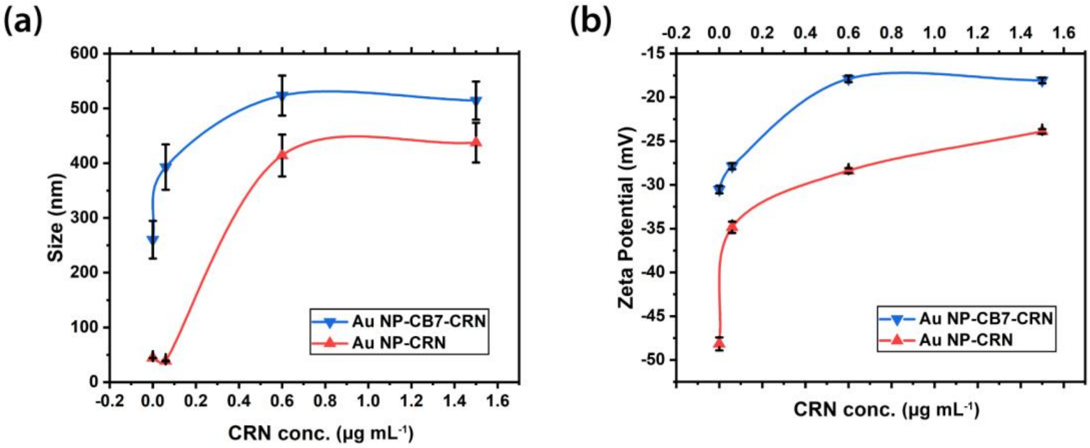

Figure 5.6. (a) Hydrodynamic size and (b) zeta potential of Au NP-CRN and Au NP-CB7-CRN at different concentrations of CRN from 0 to 1.50 µg mL^{-1}. (Note: solid lines are to guide the eyes.)

Colourimetric sensing of CRN via UV-Vis spectroscopy can be potentially useful for clinical applications, however, there is no direct evidence to show whether the shift in λ_{LSPR} is caused by CRN or other biomolecules in the matrix. For instance, the λ_{LSPR} of 0.60 μg mL^{-1} CRN is at 738 nm in 2000-fold diluted SU but at 731 nm in 5000-fold diluted SU. Nevertheless, this detection scheme can still be used as a rapid test to complement and cross-validate the results from quantitative SERS sensing (see section 5.5).

5.4 SERS sensing of CB7-CRN complexes in water

In contrast to colourimetric sensing, SERS is a highly specific technique for CRN quantification as it allows identification of CRN via its vibrational fingerprints and hence differentiation from other biomolecules in the matrix. The Raman spectrum of CRN powder is characterised by multiple peaks at 608, 674, 839, 904, 1416, 1657 and 1712 cm^{-1} (Figure 5.7a). The Raman spectrum of solid CB7 is characterised by two major peaks at 444 cm^{-1} and 833 cm^{-1}, corresponding to ring scissor and ring deformation modes respectively (Figure 5.7b). Due to the intrinsically low Raman scattering cross-sections, it was challenging to measure the Raman signals of CB7, CRN and CB7-CRN in water.

SERS signals were then measured by adding the CB7, CRN and pre-mixed 1:1 CB7-CRN solution into the 40 nm citrate-capped Au NP solution respectively. CB7 defines precise nanojunctions between Au NPs via interactions with their electron-rich carbonyl portals, resulting in very strong and localised plasmonic hotspots. The SERS peaks of CB7 and CRN in solution are broadened and show slight shifts in positions when compared to those of CB7 and CRN powder, owing to the solution effect and the molecular interaction between Au NPs and CB7 (Figure 5.8a).[175]

Notably, the SERS signals of the CB7-CRN complex are approximately equal to the sum of CB7 and CRN, indicating that the major tautomer of CRN in aqueous solution (i.e. amino tautomer, 2-amino-1-methyl-2-imidazoline-4-one)[271] should stay the same upon binding to CB7. The Raman spectra of CB7, CRN and the CB7-CRN complex were also modelled in water at CPCM/wB97XD/6-31G* level of theory (Figure 5.8b), which show general consistency with the experimental results.

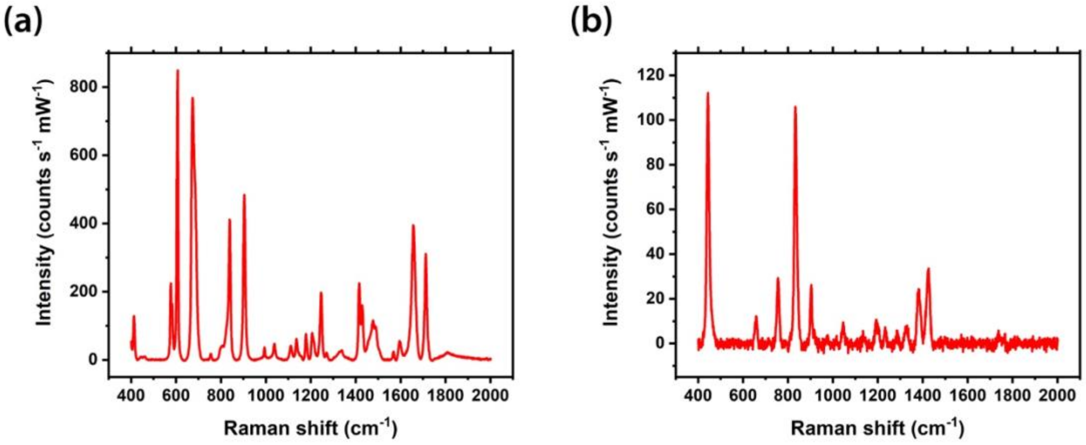

Figure 5.7. Raman spectra of (a) CRN powder and (b) CB7 powder.

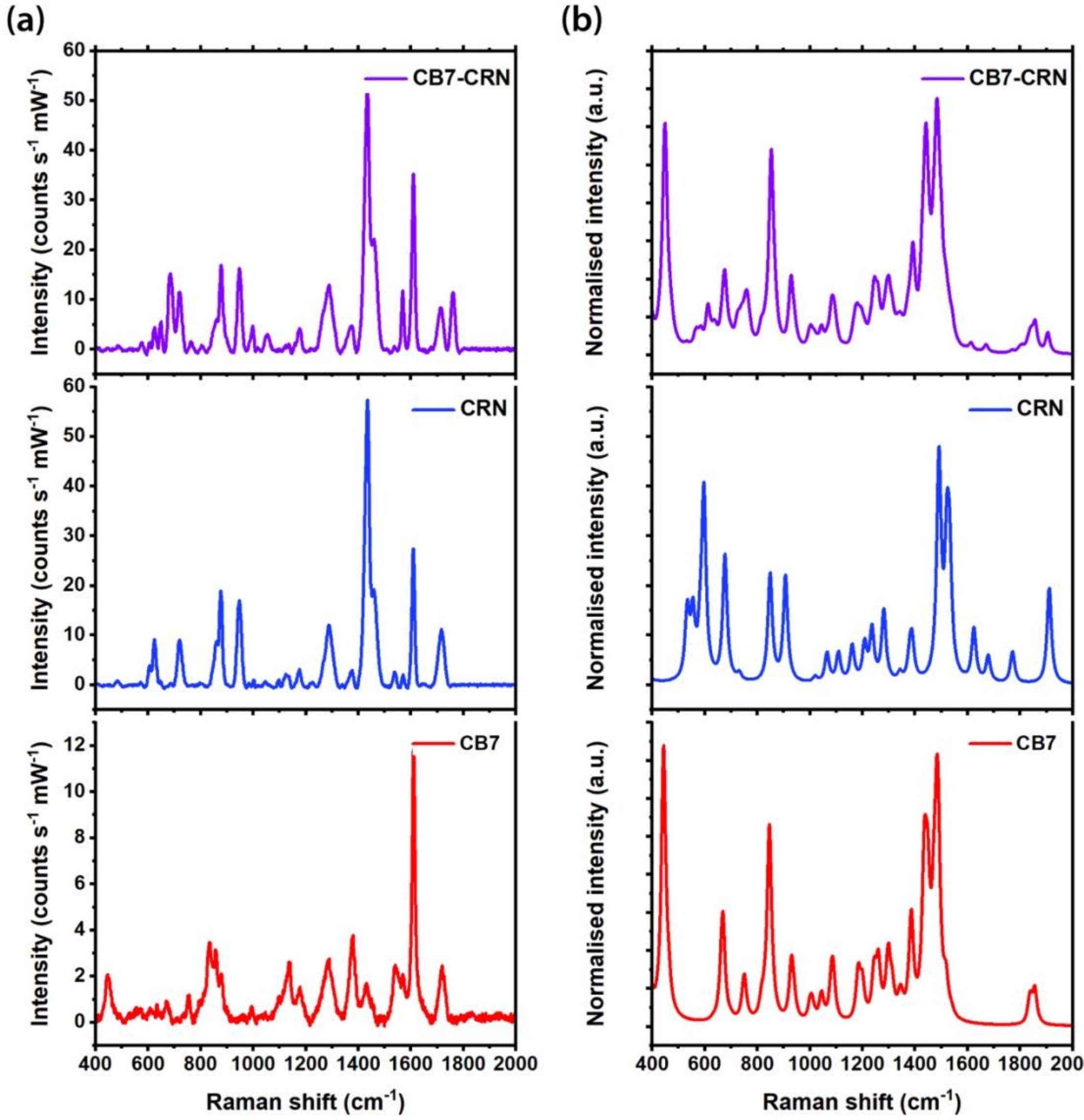

Figure 5.8. (a) Experimental SERS spectra of CB7, CRN and 1:1 CB7-CRN host-guest complex added to 40 nm Au NP solution. (b) Calculated Raman spectra of CB7, CRN and 1:1 CB7-CRN host-guest complex in water at CPCM/wB97XD/6-31G* level of theory.

SERS titrations of CRN with concentrations from 0 to 1.50 μg mL^{-1} (13.3 μM) were performed in water at a constant CB7 concentration of 10 μM as to ensure the formation of reproducible nanoaggregates, i.e. SERS substrates (Figure 5.9). Most of the CRN molecules should be fully encapsulated within the CB7 cavity, however, there might be a tiny amount of free (i.e. uncomplexed) CRN trapped within the Au NP: CB7 nanoaggregates, which can only happen at relatively high concentrations of CRN (i.e. CRN is in excess). The CRN signals can be clearly observed in the SERS spectra even when the concentration is down to 0.06 μg mL^{-1} (0.53 μM) with a good signal-to-noise ratio (SNR) of 12.8, implying that the actual detection limit could be down to 4.69 ng mL^{-1} (41.5 nM). The SNR is the ratio of the intensity of the major CRN peak at 1434 cm^{-1} (i.e. signal) to the background signal at 1800 – 2000 cm^{-1} (i.e. noise). Good correlations (R^2 ~ 0.78 – 0.91) between the SERS intensity and log concentration of CRN were found for multiple characteristic peaks at 721, 877, 947, 1435 and 1461 cm^{-1} respectively (Figure 5.9c). Notably, there is a slight drop in linearity when the CRN concentration is ≥ 1.05 μg mL^{-1} (9.28 μM), probably due to the LSPR peak shifting away from the 633 nm excitation.[2] Furthermore, the CRN signals can still be observed in the SERS spectra in the absence of CB7 due to the aggregation of Au NPs caused by the electrostatic interactions or chemisorption of CRN with the surface of Au NPs, but a correlation between the SERS intensity and concentration of CRN is lacking (Figure 5.10a).

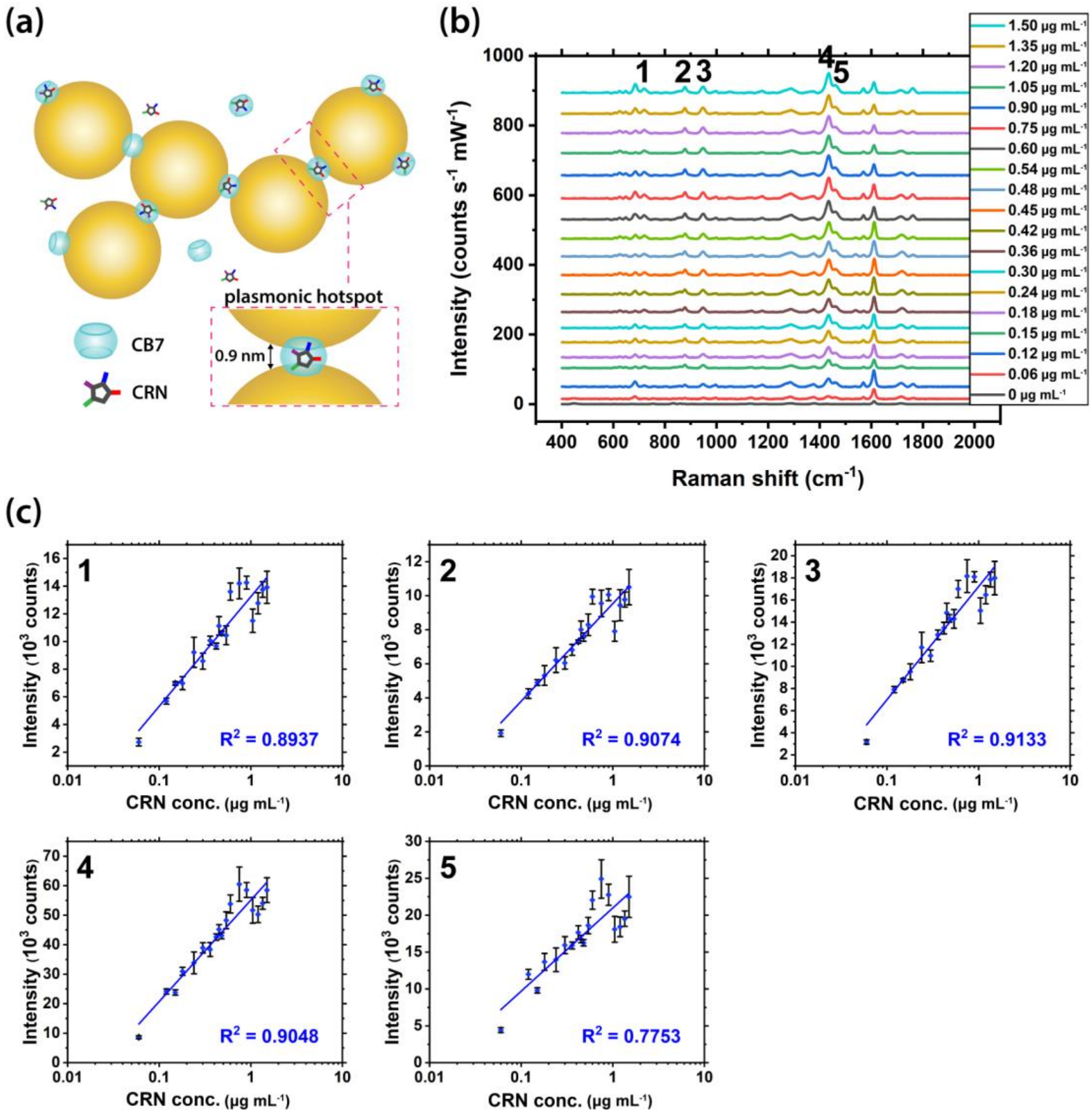

Figure 5.9. (a) Schematic illustration of the precise plasmonic hotspots within Au NP: CB7 nanoaggregates for CRN detection in water (not to scale). (b) SERS spectra of CRN in water with concentrations from 0 to 1.50 μg mL^{-1} (13.3 μM). Spectra were baseline corrected and offset for clarity. (c) Corresponding plots of SERS intensity of the five characteristic CRN peaks in (b) against CRN concentration. Logarithmic fittings were performed to reveal correlation between SERS intensity and CRN concentration.

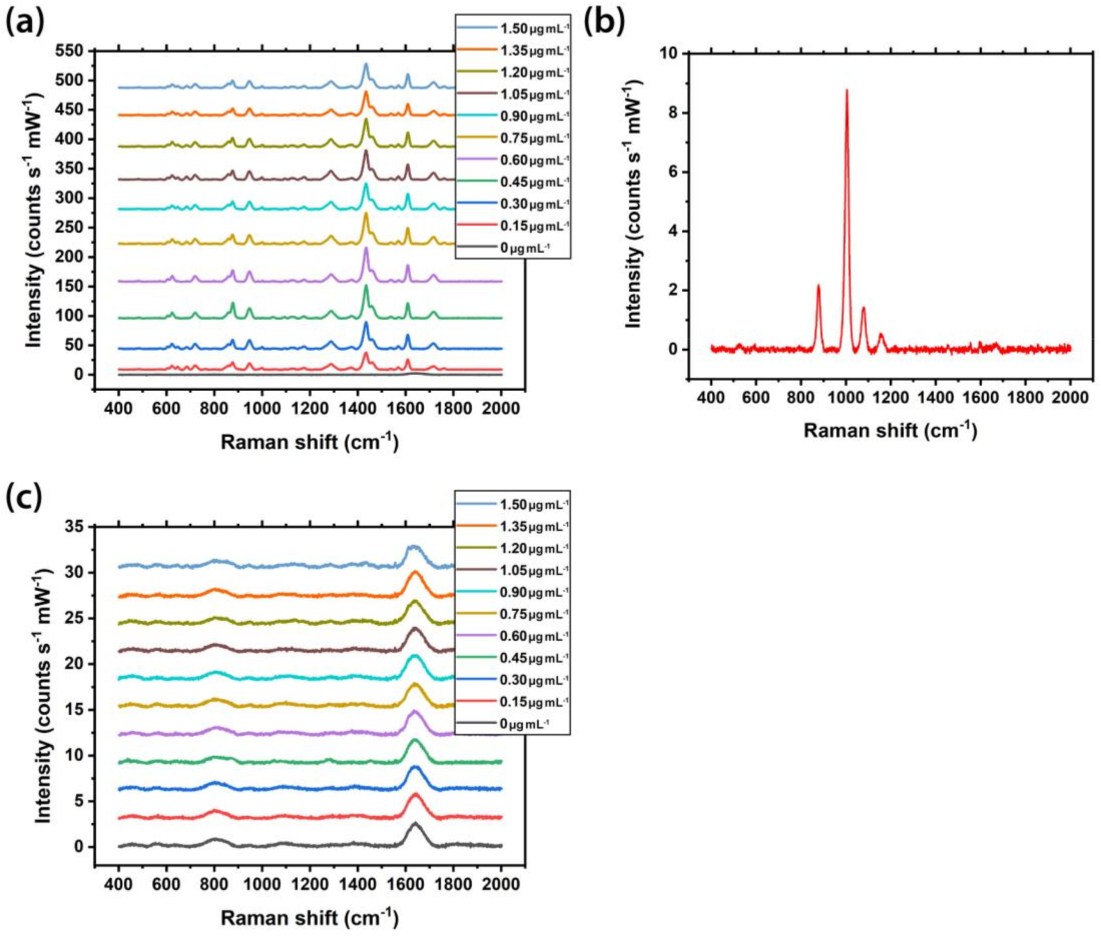

Figure 5.10. (a) SERS spectra of CRN in water with concentrations from 0 to 1.50 μg mL^{-1} in the absence of CB7. (b) Raman spectrum of SU. (c) SERS spectra of CRN in 2000-fold diluted SU with concentrations from 0 to 1.50 μg mL^{-1} in the absence of CB7.

5.5 SERS sensing of CB7-CRN complexes in urinalysis

Subsequently, SERS detection of CRN was performed in SU, i.e. in the presence of other biomolecules and proteins, as to explore its potential for point-of-care and clinical applications. The Raman signals observed in the prepared SU could be attributed to urea and phosphate, however, no Raman signals of CRN could be observed (Figure 5.10b). The prepared SU was then highly diluted with water (1000 – 5000-fold) for SERS titrations of CRN, meaning only a very small volume of sample is required for this highly sensitive detection scheme. This has particular important implications to point-of-care monitoring of patients in critical conditions who often fail to excrete a normal volume of urine, together with other benefits such as minimising the matrix effect.

As a control experiment, no SERS signals of CRN can be observed in diluted SU in the absence of CB7, probably due to preferential surface crowding by other biomolecules and proteins present in the complex matrix (Figure 5.10c). SERS titrations of CRN were first performed in 1000-fold diluted SU with CRN concentrations from 0 to 3.00 μg mL^{-1} (26.5 μM). Good correlations (R^2 ~ 0.81 – 0.94) between the SERS intensity and log concentration of CRN were found but the error bars are relatively large for the samples containing high CRN concentrations (Figure 5.11). The presence of excess [CRN-H]$^+$ with a constant CB7 concentration of 10 μM caused a shift in the aggregation kinetics, resulting in faster aggregation of Au NPs and thus a narrower measurement window.

SERS titrations were then performed in 2000-fold diluted SU with CRN concentrations from 0 to 1.50 μg mL^{-1} (13.3 μM), as to avoid the shift in aggregation kinetics resulted from the relatively high ratio of CRN to CB7. Strong correlations ($R^2 >$ 0.95) between the SERS intensity and log concentration of CRN were found for all characteristic CRN peaks with very small error bars (Figure 5.12), indicating the high reproducibility (i.e. < 5% error) of the SERS signals in our sensing scheme, which allows selective detection of a particular analyte in a complex matrix via formation of host-guest complexes (Figure 5.12a).

Finally, to test the detection limit, SERS titrations were performed in 5000-fold diluted SU with CRN concentrations from 0 to 0.60 μg mL^{-1} (5.3 μM). Strong correlations ($R^2 \sim 0.88 – 0.96$) between the SERS intensity and log concentration of CRN were found for all characteristic CRN peaks with small error bars (Figure 5.13). Notably, the CRN signals can still be observed in the SERS spectra even when the concentration is down to 0.06 μg mL^{-1} (0.53 μM) with a SNR of 4.8, implying that the actual detection limit could be down to 12.5 ng mL^{-1} (111 nM) which is the lowest among all previous reports.

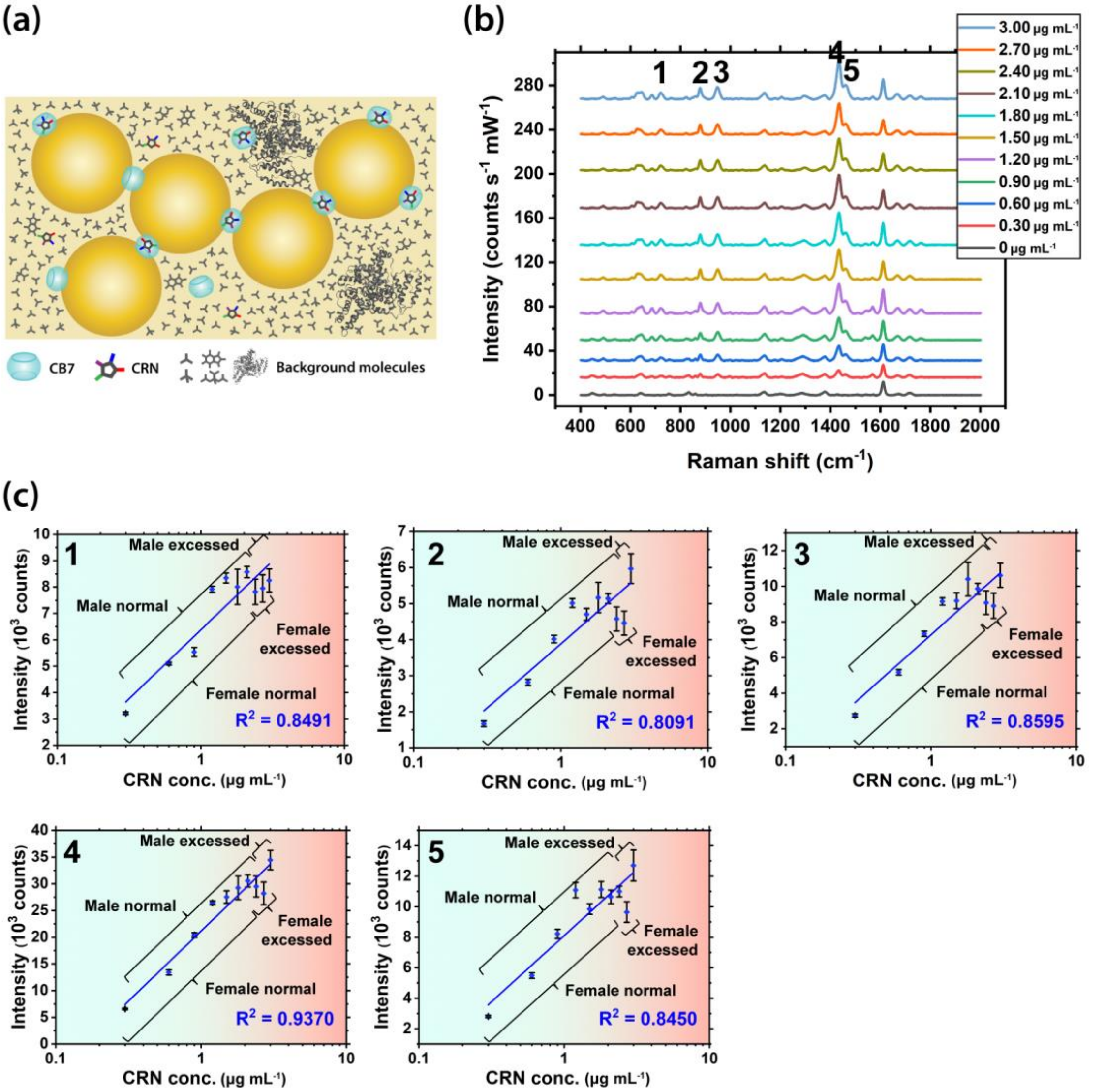

Figure 5.11. (a) Schematic illustration of the precise plasmonic hotspots within Au NP: CB7 nanoaggregates for CRN detection in 1000-fold diluted SU (not to scale). (b) SERS spectra of CRN in 1000-fold diluted SU with concentrations from 0 to 3.00 μg mL^{-1} (26.5 μM). Spectra were baseline corrected and offset for clarity. (c) Corresponding plots of SERS intensity of the five characteristic CRN peaks in (b) against CRN concentration. Logarithmic fittings were performed to reveal correlation between SERS intensity and CRN concentration. (Note: 1 μg mL^{-1} in measurement samples corresponds to 1000 μg mL^{-1} of the actual CRN concentration in undiluted patient samples.)

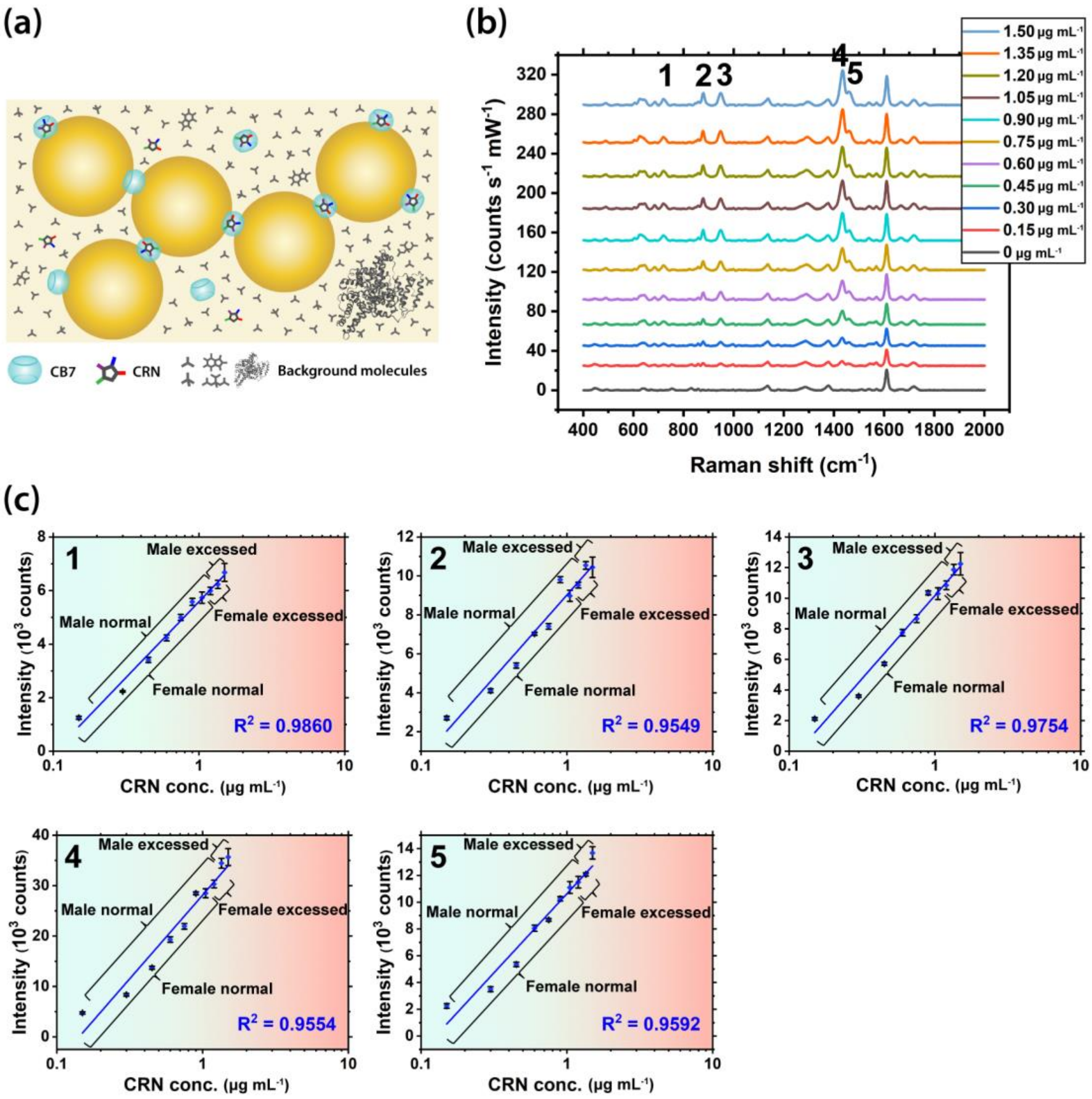

Figure 5.12. (a) Schematic illustration of the precise plasmonic hotspots within Au NP: CB7 nanoaggregates for CRN detection in 2000-fold diluted SU (not to scale). (b) SERS spectra of CRN in 2000-fold diluted SU with concentrations from 0 to 1.50 μg mL^{-1} (13.3 μM). Spectra were baseline corrected and offset for clarity. (c) Corresponding plots of SERS intensity of the five characteristic CRN peaks in (b) against CRN concentration. Logarithmic fittings were performed to reveal correlation between SERS intensity and CRN concentration. (Note: 1 μg mL^{-1} in measurement samples corresponds to 2000 μg mL^{-1} of the actual CRN concentration in undiluted patient samples.)

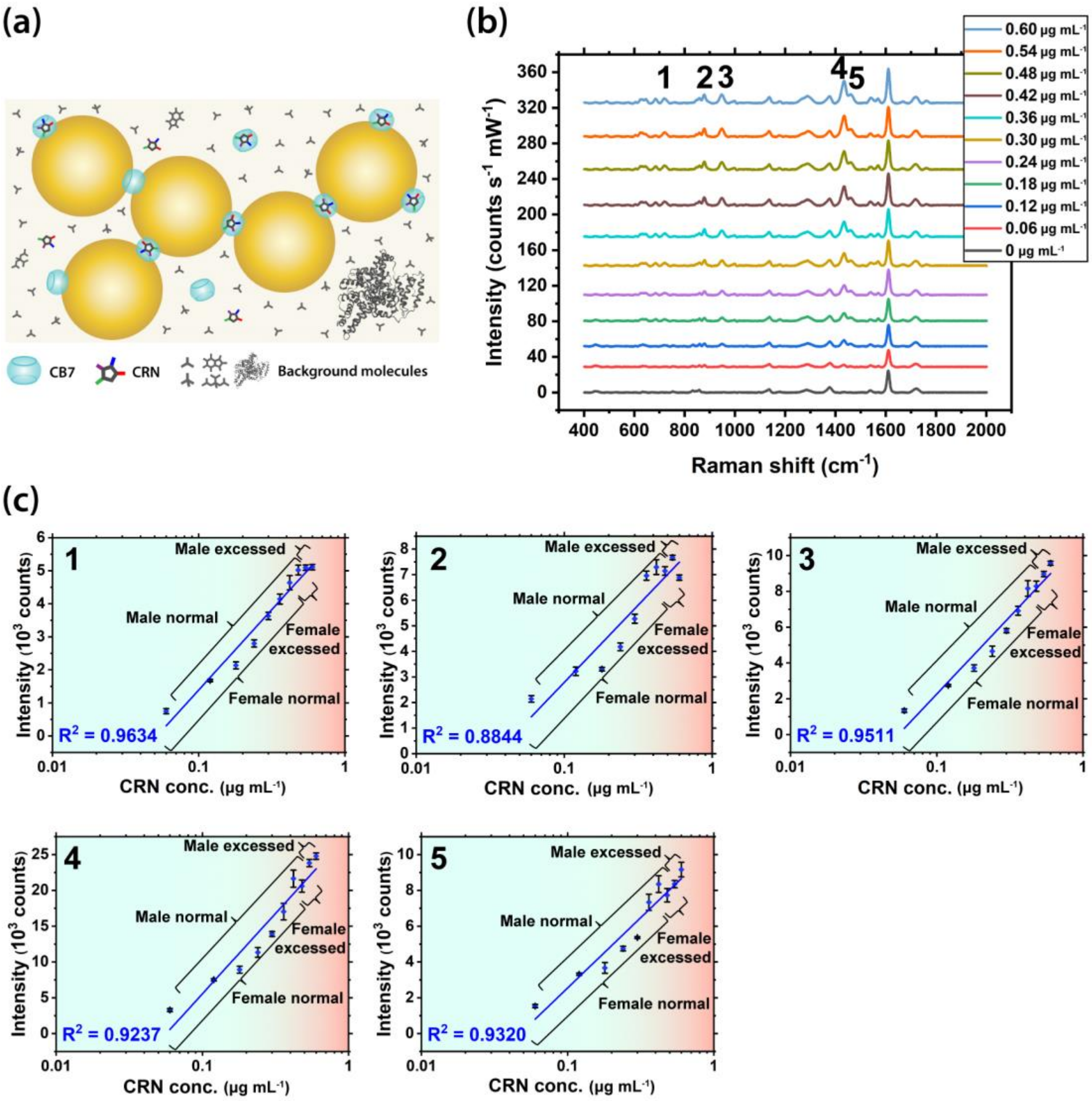

Figure 5.13. (a) Schematic illustration of the precise plasmonic hotspots within Au NP: CB7 nanoaggregates for CRN detection in 5000-fold diluted SU (not to scale). (b) SERS spectra of CRN in 5000-fold diluted SU with concentrations from 0 to 0.60 μg mL^{-1} (5.3 μM). Spectra were baseline corrected and offset for clarity. (c) Corresponding plots of SERS intensity of the five characteristic CRN peaks in (b) against CRN concentration. Logarithmic fittings were performed to reveal correlation between SERS intensity and CRN concentration. (Note: 1 μg mL^{-1} in measurement samples corresponds to 5000 μg mL^{-1} of the actual CRN concentration in undiluted patient samples.)

5.6 Matrix effect on SERS signals

The signal perturbation from other biomolecules and proteins on the SERS signals of CRN in diluted SU (i.e. matrix effect) was studied. The CRN signals in 2000-fold diluted SU are 34.0% – 52.6% lower than those in water at the same concentration of 0.60 μg mL^{-1} (Figure 5.14), probably due to competitive binding between CRN and other biomolecules to CB7 and Au NPs in the matrix.[183] For instance, uric acid can form host-guest complexes with CB7[272] while phosphate may also bind to the surface of Au NPs. Nevertheless, the matrix effect on the SERS signals of CRN can be minimised by increasing the dilution factor and thus recovering the CRN signals in the absence of other biomolecules and proteins (i.e. in water) and increasing the SNR.

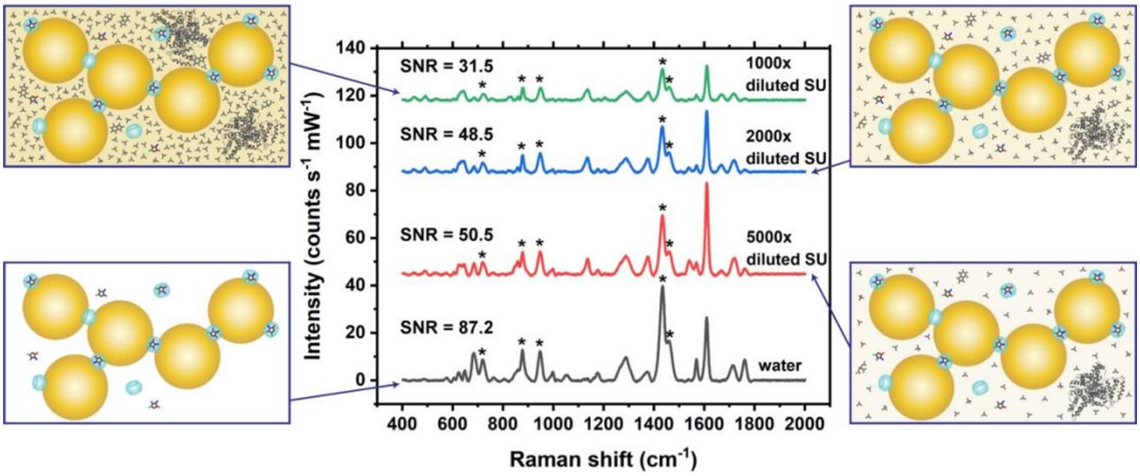

Figure 5.14. SERS spectra of 0.60 μg mL^{-1} CRN in water and sequentially diluted SU. Insets: Schematic illustrations of the Au NP: CB7 nanoaggregates for CRN detection in water and sequentially diluted SU, showing the matrix differences (not to scale).

5.7 Conclusions

In this Chapter, a novel multi-spectroscopic sensing platform based on UV-Vis spectroscopy and SERS for an important urinary biomarker CRN has been developed. The key binding parameters of the CB7-CRN complex have been quantified using NMR, and UV-Vis titrations, and supported by DFT molecular models. The dual-triggered self-assembly of the plasmonic substrate by a combination of carbonyl portal binding of CB7 and the electrostatic effects of CRN allows rapid quantification via two independent spectral signatures (i.e. UV-Vis and SERS) from a single sample solution, enhancing the data consistency and measurement throughput. Notably, the CRN signals are selectively enhanced in SERS via formation of precise plasmonic hotspots and host-guest complexation with CB7. The quantification of CRN of clinically relevant levels has been demonstrated in highly diluted SU with rapid response, high sensitivity (detection limit of 111 nM) and reproducibility (within 5% error). Our detection scheme is also tolerant against the presence of other biomolecules and proteins in SU, making it promising for point-of-care and clinical applications.

Chapter 6. Conclusions and Outlook

This Chapter concluded the research outcomes and provided insights into the possible future directions.

6.1 Conclusions

Surface-enhanced Raman spectroscopy (SERS) is a powerful technique that has found itself a wide range of applications in sensing and related research. The high sensitivity, specificity and portability of the SERS sensors are particularly useful for real-time and on-site detection of trace analyte targets, as opposed to the classical techniques which are bulky and more prone to false signals. In this research, we have demonstrated facile fabrication of reproducible SERS substrates via aqueous self-assembly of gold nanoparticles (Au NPs) mediated by the highly symmetric and rigid macrocycles, cucurbiturils (CBs), allowing the formation of precise plasmonic hotspots within the Au NP: CB nanoaggregates. Novel host-guest complexes of CBs and various small molecules, including explosives, drugs and biomarkers, have been investigated using different experimental and computational approaches. Subsequent molecular recognitions of the analyte targets enabled by CBs have been demonstrated using the Au NP: CB SERS substrates, for potential applications in different areas such as homeland security, environmental monitoring, therapeutic drug monitoring and early disease diagnostics.

While CBs are known to have strong preferences for positively charged guests that can be fully or mostly encapsulated within its cavity, neutral guests such as 2,4-dinitrotoluene (DNT), a bulky explosive marker, are much rarer. The novel host-guest complexation between CB and poly-substituted aromatics has provided new insights into the scenario of bulky guests in the Au NP: CB system, which has not been properly addressed in the previous reports. Notably, the SERS signals of bulky guests can be detected when they are not localised within but just in close proximity to the plasmonic nanojunctions between Au NPs, hence extending the range of attractive analyte targets for the Au NP: CB SERS system.

Interestingly, the aqueous self-assembly of the Au NP: CB nanoaggregates can be dual-triggered by a combination of carbonyl portal binding of CB7 and the electrostatic effects of the analyte targets such as creatinine (CRN), an important biomarker, in contrast to the previous Au NP: CB systems where the aggregation of Au NPs is only mediated by the portal binding of CB7 onto the Au NP surfaces. This has provided fundamental insights into the aggregation kinetics which can be modified using the host-guest complex itself, thus opening new possibilities for designing Au NP: CB SERS systems.

While CB7 can fully or almost fully encapsulate a wide variety of positively charged molecules such as methylxanthines (MeX), CB8 is capable of fully encapsulating small guests within its relatively larger cavity and localise them at the centre of the plasmonic hotspots within the Au NP: CB8 nanoaggregates for stronger SERS enhancement as in the case of caffeine (CAF). This has also illustrated the possibility to quantify analyte targets via formation of 1:1 CB8 host-guest complexes in the Au NP: CB SERS system, in addition to the more common routes of utilising 1:1 CB7 or 1:1:1 CB8 host-guest complexation.

Quantitative SERS detection of various analyte targets, ranging from neutral and bulky nitroexplosives (DNT) to positively charged drug molecules (MeX) and biomarkers (CRN), has been demonstrated systematically via formation of CB host-guest complexes and localisation of the analyte molecules in close proximity to or within the precise plasmonic nanojunctions between the Au NPs. The tolerance of the Au NP: CB SERS system against signal perturbation from background molecules has been demonstrated by multiple proof-of-concept experiments. For instance, DNT can be detected in the presence of model organic contaminants while CRN of clinically relevant concentrations can be quantified in the presence of proteins and other biomolecules (i.e. synthetic urine). The capability of the SERS system to distinguish structurally similar molecules has also been verified by multiplexed detection of drug isomers, theobromine (TBR) and theophylline (TPH). Therefore, the Au NP: CB SERS system has great potentials to be extended to multiplexed detection of a wide variety of attractive analyte targets in complex media for in-field and point-of-care applications.

6.2 Future work

The reproducibility, responsiveness, high sensitivity and robustness of the Au NP: CB system in the SERS detection of attractive analyte targets including explosives, drugs and biomarkers have been demonstrated in this research. However, the ability of the SERS system to simultaneously detect multiple analyte molecules in complex media with high sensitivity remains the major challenge towards practical applications. For instance, on-site detection of bulky guests using the Au NP: CB system is hindered by the current detection limit while quantitative multiplexed detection of a wide variety of CB guests in complex media is disfavoured by the labour-intensive procedures. Further research efforts are thus required to address these issues, such as increasing the SERS enhancement by means of new approaches or techniques and incorporating advanced data analytical methods.

While the detection limit of Au NP: CB SERS system is excellent for point-of-care sensing of drugs and biomarkers, machine learning methods such as artificial neural network[5,15] should be adopted to simultaneously quantify tens of analyte molecules in complex media such as blood serum and urine, paving the way towards practical applications.

Anisotropic nanostructures such as Au nanostars (Au NSs) have intrinsically more plasmonic hotspots than spherical NPs due to the presence of sharp tips or edges.[22,75] The SERS signals can be further enhanced by attaching CBs onto the Au NSs via aqueous self-assembly. Meanwhile, the NPs on mirror geometry (NPoM)[181] can be applied to deposit Au NSs on a glass slide or metal surface sandwiched by CBs, where multi-layered SERS substrates can be fabricated via alternate coating of Au NSs and CBs, as to increase the durability and overcome the shortcomings of limited measurement window of the solution-based methods. The performance of the SERS sensor can be improved further by incorporating techniques such as photo-induced enhanced Raman spectroscopy (PIERS)[205] and electrochemical SERS (EC-SERS)[241]. For instance, CB can bind to semiconductor quantum dots,[149] which provides an opportunity for PIERS sensing.

With the continuous research efforts by our group and others in enhancing the SERS signals of attractive analyte targets in the Au NP: CB system and developing advanced analytical tools to probe the complex situations, we expect the Au NP: CB SERS system to be ready for real sample testing or applications in real environments in this new decade.

References

(1) Lee, T.-C.; Scherman, O. A. Formation of Dynamic Aggregates in Water by Cucurbit[5]uril Capped with Gold Nanoparticles. *Chem. Commun.* **2010**, *46*, 2438–2440.

(2) Taylor, R. W.; Lee, T.-C.; Scherman, O. A.; Esteban, R.; Aizpurua, J.; Huang, F. M.; Baumberg, J. J.; Mahajan, S. Precise Subnanometer Plasmonic Junctions for SERS within Gold Nanoparticle Assemblies Using Cucurbit[*n*]uril " Glue ". *ACS Nano* **2011**, *5*, 3878–3887.

(3) Kasera, S.; Biedermann, F.; Baumberg, J. J.; Scherman, O. A.; Mahajan, S. Quantitative SERS Using the Sequestration of Small Molecules Inside Precise Plasmonic Nanoconstructs. *Nano Lett.* **2012**, *12*, 5924–5928.

(4) Taylor, R. W.; Coulston, R. J.; Biedermann, F.; Mahajan, S.; Baumberg, J. J.; Scherman, O. A. In Situ SERS Monitoring of Photochemistry within a Nanojunction Reactor. *Nano Lett.* **2013**, *13*, 5985–5990.

(5) Kasera, S.; Herrmann, L. O.; del Barrio, J.; Baumberg, J. J.; Scherman, O. A. Quantitative Multiplexing with Nano-Self-Assemblies in SERS. *Sci. Rep.* **2014**, *4*, 6785.

(6) Ghosh, T. K.; Prelas, M. A.; Viswanath, D. S.; Loyalka, S. K. *Science and Technology of Terrorism and Counterterrorism, 2nd Edition* **2009**.

(7) Fatah, A. A.; Arcilesi, R. D.; McClintock, J. A.; Lattin, C. H.; Helinski, M. S.; Hutchings, M. Guide for the Selection of Explosives Detection and Blast Mitigation Equipment for Emergency First Responders. *Guide 105-07* **2008**.

(8) Wells, K.; Bradley, D. A. A Review of X-Ray Explosives Detection Techniques for Checked Baggage. *Appl. Radiat. and Isot.* **2012**, *70*, 1729–1746.

(9) Miceli, J. N.; Aravind, M. K.; Ferrell, W. J. Analysis of Caffeine: Comparison of

the Manual Enzyme Multiplied Immunoassay (EMIT), Automated EMIT, and High-Performance Liquid Chromatography Procedures. *Ther. Drug Monit.* **1984**, *6*, 344–347.

(10) Chang, J.; Gotcher, S.; Gushaw, J. B. Homogeneous Enzyme Immunoassay for Theophylline in Serum and Plasma. *Clin. Chem.* **1982**, *28*, 361–367.

(11) Willard, M. D.; Tvedten, H. *Small Animal Clinical Diagnosis by Laboratory Methods, 4th Edition* **2004**.

(12) Scott, N. R.; Chakraborty, J.; Marks, V. Determination of Caffeine, Theophylline and Theobromine in Serum and Saliva Using High-Performance Liquid Chromatography. *Ann. Clin. Biochem.***1984**, *21*, 120–124.

(13) Engvall, E. [28] Enzyme Immunoassay ELISA and EMIT. *Methods Enzymol.* **1980**, *70*, 419–439.

(14) Sturgeon, C. M.; Viljoen, A. Analytical Error and Interference in Immunoassay: Minimizing Risk. *Ann. Clin. Biochem*. **2011**, *48*, 418–432.

(15) Alharbi, O.; Xu, Y.; Goodacre, R. Simultaneous Multiplexed Quantification of Caffeine and Its Major Metabolites Theobromine and Paraxanthine Using Surface-Enhanced Raman Scattering. *Anal. Bioanal. Chem.* **2015**, *407*, 8253–8261.

(16) Jaffe, M. Ueber Den Niederschlag, Welchen Pikrinsaure in Normalem Harn Erzeugt Und Uber Eine Neue Reaction Des Kreatinins. *Z. Physiol. Chem.* **1886**, *10*, 391–400.

(17) Folin, O.; Morris, J. L. On The Determination of Creatinine and Creatine in Urine. *J. Biol. Chem.* **1914**, *17*, 469–473.

(18) Gangopadhyay, D.; Sharma, P.; Nandi, R.; Das, M.; Ghosh, S.; Singh, R. K. In Vitro Concentration Dependent Detection of Creatinine: A Surface Enhanced Raman Scattering and Fluorescence Study. *RSC Adv.* **2016**, *6*, 112562–112567.

(19) Raman, C. V.; Krishnan, K. S. A New Type of Secondary Radiation. *Nature* **1928**, *121*, 501–502.

(20) Kauffmann, T. H.; Kokanyan, N.; Fontana, M. D. Use of Stokes and Anti-Stokes Raman Scattering for New Applications. *J. Raman Spectrosc.* **2019**, *50*, 418–424.

(21) Hallmark, V. M.; Campion, A. Selection Rules for Surface Raman Spectroscopy: Experimental Results. *J. Chem. Phys.* **1986**, *84*, 2933–2941.

(22) Langer, J.; Jimenez de Aberasturi, D.; Aizpurua, J.; Alvarez-Puebla, R. A.; Auguie, B.; Baumberg, J. J.; Bazan, G. C.; Bell, S. E. J.; Boisen, A.; Brolo, A. G.; et al. Present and Future of Surface-Enhanced Raman Scattering. *ACS Nano* **2020**, *14*, 28–117.

(23) Jehlicka, J.; Edwards, H. G. M. Raman Spectroscopy as a Tool for the Non-Destructive Identification of Organic Minerals in the Geological Record. *Org. Geochem.* **2008**, *39*, 371–386.

(24) Paudel, A.; Raijada, D.; Rantanen, J. Raman Spectroscopy in Pharmaceutical Product Design. *Adv. Drug Deliv. Rev.* **2015**, *89*, 3–20.

(25) Stuart, B. H. Polymer Crystallinity Studied Using Raman Spectroscopy. *Vib. Spectrosc.* **1996**, *10*, 79–87.

(26) Fleischmann, M.; Hendra, P. J.; McQuillan, A. J. Raman Spectra of Pyridine Adsorbed at a Silver Electrode. *Chem. Phys. Lett.* **1974**, *26*, 163–166.

(27) Jeanmaire, D. L.; Van Duyne, R. P. Surface Raman Spectroelectrochemistry: Part I. Heterocyclic, Aromatic, and Aliphatic Amines Adsorbed on the Anodized Silver Electrode. *J. Electroanal. Chem.* **1977**, *84*, 1–20.

(28) Albrecht, M. G.; Creighton, J. A. Anomalously Intense Raman Spectra of Pyridine at a Silver Electrode. *J. Am. Chem. Soc.* **1977**, *99*, 5215–5217.

(29) Pilot, R.; Signorini, R.; Durante, C.; Orian, L.; Bhamidipati, M.; Fabris, L. A

Review on Surface-Enhanced Raman Scattering. *Biosensors* **2019**, *9*, 57.

(30) Ding, S.-Y.; Yi, J.; Li, J.-F.; Ren, B.; Wu, D.-Y.; Panneerselvam, R.; Tian, Z.-Q. Nanostructure-Based Plasmon-Enhanced Raman Spectroscopy for Surface Analysis of Materials. *Nat. Rev. Mater*. **2016**, *1*, 16021.

(31) Zong, C.; Xu, M.; Xu, L.-J.; Wei, T.; Ma, X.; Zheng, X.-S.; Hu, R.; Ren, B. Surface-Enhanced Raman Spectroscopy for Bioanalysis: Reliability and Challenges. *Chem. Rev*. **2018**, *118*, 4946–4980.

(32) Le Ru, E. C.; Grand, J.; Felidj, N.; Aubard, J.; Levi, G.; Hohenau, A.; Krenn, J. R.; Blackie, E.; Etchegoin, P. G. Experimental Verification of the SERS Electromagnetic Model beyond the $|E|^4$ Approximation: Polarization Effects. *J. Phys. Chem. C* **2008**, *112*, 8117–8121.

(33) Fazio, B.; D'Andrea, C.; Bonaccorso, F.; Irrera, A.; Calogero, G.; Vasi, C.; Gucciardi, P. G.; Allegrini, M.; Toma, A.; Chiappe, D.; et al. Re-Radiation Enhancement in Polarized Surface-Enhanced Resonant Raman Scattering of Randomly Oriented Molecules on Self-Organized Gold Nanowires. *ACS Nano* **2011**, *5*, 5945–5956.

(34) De Abajo, F. J. G. Nonlocal Effects in the Plasmons of Strongly Interacting Nanoparticles, Dimers, and Waveguides. *J. Phys. Chem. C* **2008**, *112*, 17983–17987.

(35) Lombardi, J. R.; Birke, R. L. A Unified View of Surface-Enhanced Raman Scattering. *Acc. Chem. Res.* **2009**, *42*, 734–742.

(36) Jensen, L.; Aikens, C. M.; Schatz, G. C. Electronic Structure Methods for Studying Surface-Enhanced Raman Scattering. *Chem. Soc. Rev.* **2008**, *37*, 1061–1073.

(37) Morton, S. M.; Jensen, L. Understanding the Molecule-Surface Chemical Coupling in SERS. *J. Am. Chem. Soc.* **2009**, *131*, 4090–4098.

(38) Gieseking, R. L.; Ratner, M. A.; Schatz, G. C. Semiempirical Modeling of Ag Nanoclusters: New Parameters for Optical Property Studies Enable Determination of Double Excitation Contributions to Plasmonic Excitation. *J. Phys. Chem. A* **2016**, *120*, 4532–4549.

(39) Ding, S.-Y.; You, E.-M.; Tian, Z.-Q.; Moskovits, M. Electromagnetic Theories of Surface-Enhanced Raman Spectroscopy. *Chem. Soc. Rev*. **2017**, *46*, 4042–4076.

(40) Le Ru, E. C.; Grand, J.; Sow, I.; Somerville, W. R. C.; Etchegoin, P. G.; Treguer-Delapierre, M.; Charron, G.; Felidj, N.; Levi, G.; Aubard, J. A Scheme for Detecting Every Single Target Molecule with Surface-Enhanced Raman Spectroscopy. *Nano Lett.* **2011**, *11*, 5013–5019.

(41) Le Ru, E. C.; Etchegoin, P. G. Chapter 4 - SERS Enhancement Factors and Related Topics. *Principles of Surface-Enhanced Raman Spectroscopy* **2009**, p.185–264.

(42) McMahon, J. M.; Li, S.; Ausman, L. K.; Schatz, G. C. Modeling the Effect of Small Gaps in Surface-Enhanced Raman Spectroscopy. *J. Phys. Chem. C* **2012**, *116*, 1627–1637.

(43) Huang, Y.; Zhou, Q.; Hou, M.; Ma, L.; Zhang, Z. Nanogap Effects on Near- and Far-Field Plasmonic Behaviors of Metallic Nanoparticle Dimers. *Phys. Chem. Chem. Phys.* **2015**, *17*, 29293–29298.

(44) Zhu, W.; Crozier, K. B. Quantum Mechanical Limit to Plasmonic Enhancement as Observed by Surface-Enhanced Raman Scattering. *Nat. Commun.* **2014**, *5*, 5228.

(45) Hajisalem, G.; Nezami, M. S.; Gordon, R. Probing the Quantum Tunneling Limit of Plasmonic Enhancement by Third Harmonic Generation. *Nano Lett.* **2014**, *14*, 6651–6654.

(46) Freestone, I.; Meeks, N.; Sax, M.; Higgitt, C. The Lycurgus Cup – A Roman Nanotechnology. *Gold Bull.* **2007**, *40*, 270–277.

(47) Cao, G. *Nanostructures and Nanomaterials – Synthesis, Properties and Applications. 2nd Edition* **2010**.

(48) Mie, G. Beitrage Zur Optik Truber Medien, Speziell Kolloidaler Metallosungen. *Ann. Phys.* **1908**, *330*, 337–445.

(49) Ghosh, S. K.; Pal, T. Interparticle Coupling Effect on the Surface Plasmon Resonance of Gold Nanoparticles: From Theory to Applications. *Chem. Rev*. **2007**, *107*, 4797–4862.

(50) Huang, X.; El-Sayed, M. A. Gold Nanoparticles: Optical Properties and Implementations in Cancer Diagnosis and Photothermal Therapy. *J. Adv. Res*. **2010**, *1*, 13–28.

(51) Zhang, J. Z.; Noguez, C. Plasmonic Optical Properties and Applications of Metal Nanostructures. *Plasmonics* **2008**, *3*, 127–150.

(52) Arnold, M. D.; Blaber, M. G. Optical Performance and Metallic Absorption in Nanoplasmonic Systems. *Opt. Express* **2009**, *17*, 3835–3847.

(53) Blaber, M. G.; Arnold, M. D.; Ford, M. J. A Review of the Optical Properties of Alloys and Intermetallics for Plasmonics. *J. Phys.: Condens. Matter* **2010**, *22*, 143201.

(54) Amendola, V.; Pilot, R.; Frasconi, M.; Marago, O. M.; Iati, M. A. Surface Plasmon Resonance in Gold Nanoparticles: A Review. *J. Phys.: Condens. Matter* **2017**, *29*, 203002.

(55) Kim, M.; Lee, J.-H.; Nam, J.-M. Plasmonic Photothermal Nanoparticles for Biomedical Applications. *Adv. Sci*. **2019**, *6*, 1900471.

(56) Jain, P. K.; Lee, K. S.; El-Sayed, I. H.; El-Sayed, M. A. Calculated Absorption and Scattering Properties of Gold Nanoparticles of Different Size, Shape, and Composition: Applications in Biological Imaging and Biomedicine. *J. Phys. Chem.*

B **2006**, *110*, 7238–7248.

(57) Morsin, M.; Salleh, M. M.; Umar, A. A.; Sahdan, M. Z. Gold Nanoplates for a Localized Surface Plasmon Resonance-Based Boric Acid Sensor. *Sensors* **2017**, *17*, 947.

(58) Kobayashi, H.; Ogawa, M.; Alford, R.; Choyke, P. L.; Urano, Y. New Strategies for Fluorescent Probe Design in Medical Diagnostic Imaging. *Chem. Rev.* **2010**, *110*, 2620–2640.

(59) Virga, A.; Ferrante, C.; Batignani, G.; De Fazio, D.; Nunn, A. D. G.; Ferrari, A. C.; Cerullo, G.; Scopigno, T. Coherent Anti-Stokes Raman Spectroscopy of Single and Multi-Layer Graphene. *Nat. Commun.* **2019**, *10*, 3658.

(60) Krishna, R.; Unsworth, T. J.; Edge, R. Raman Spectroscopy and Microscopy, *Reference Module in Materials Science and Materials Engineering* **2016**.

(61) Robert, B. Resonance Raman Spectroscopy. *Photosynth. Res.* **2009**, *101*, 147–155.

(62) Novak, V.; Sebestík, J.; Bour, P. Theoretical Modeling of the Surface-Enhanced Raman Optical Activity. *J. Chem. Theory Comput.* **2012**, *8*, 1714–1720.

(63) Abdali, S.; Blanch, E. W. Surface Enhanced Raman Optical Activity (SEROA). *Chem. Soc. Rev.* **2008**, *37*, 980–992.

(64) Wu, D.-Y.; Li, J.-F.; Ren, B.; Tian, Z.-Q. Electrochemical Surface-Enhanced Raman Spectroscopy of Nanostructures. *Chem. Soc. Rev.* **2008**, 37, 1025–1041.

(65) Shao, F.; Zenobi, R. Tip-Enhanced Raman Spectroscopy: Principles, Practice, and Applications to Nanospectroscopic Imaging of 2D Materials. *Anal. Bioanal. Chem*. **2019**, *411*, 37–61.

(66) Verma, P. Tip-Enhanced Raman Spectroscopy: Technique and Recent Advances. *Chem. Rev.* **2017**, *117*, 6447–6466.

(67) Turkevich, J.; Stevenson, P. C.; Hillier, J. A Study of the Nucleation and Growth

Processes in the Synthesis of Colloidal Gold. *Discuss. Faraday Soc.* **1951**, *11*, 55–75.

(68) Pillai, Z. S.; Kamat, P. V. What Factors Control the Size and Shape of Silver Nanoparticles in the Citrate Ion Reduction Method? *J. Phys. Chem. B* **2004**, *108*, 945–951.

(69) Michaels, A. M.; Jiang, J.; Brus, L. Ag Nanocrystal Junctions as the Site for Surface-Enhanced Raman Scattering of Single Rhodamine 6G Molecules. *J. Phys. Chem. B* **2000**, *104*, 11965–11971.

(70) Park, S. Y.; Lee, J.-S.; Georganopoulou, D.; Mirkin, C. A.; Schatz, G. C. Structures of DNA-Linked Nanoparticle Aggregates. *J. Phys. Chem. B* **2006**, *110*, 12673–12681.

(71) Aslan, K.; Luhrs, C. C.; Perez-Luna, V. H. Controlled and Reversible Aggregation of Biotinylated Gold Nanoparticles with Streptavidin. *J. Phys. Chem. B* **2004**, *108*, 15631–15639.

(72) Wang, Z.; Zong, S.; Yang, J.; Song, C.; Li, J.; Cui, Y. One-Step Functionalized Gold Nanorods as Intracellular Probe with Improved SERS Performance and Reduced Cytotoxicity. *Biosens. Bioelectron.* **2010**, *26*, 241–247.

(73) Scarabelli, L.; Coronado-Puchau, M.; Giner-Casares, J. J.; Langer, J.; Liz-Marzan, L. M. Monodisperse Gold Nanotriangles: Size Control, Large-Scale Self-Assembly, and Performance in Surface-Enhanced Raman Scattering. *ACS Nano* **2014**, *8*, 5833–5842.

(74) McLellan, J. M.; Siekkinen, A.; Chen, J.; Xia, Y. Comparison of the Surface-Enhanced Raman Scattering on Sharp and Truncated Silver Nanocubes. *Chem. Phys. Lett.* **2006**, *427*, 122–126.

(75) Khoury, C. G.; Vo-Dinh, T. Gold Nanostars for Surface-Enhanced Raman

Scattering: Synthesis, Characterization and Optimization. *J. Phys. Chem. C* **2008**, *112*, 18849–18859.

(76) Lim, D.-K.; Jeon, K.-S.; Hwang, J.-H.; Kim, H.; Kwon, S.; Suh, Y. D.; Nam, J.-M. Highly Uniform and Reproducible Surface-Enhanced Raman Scattering from DNA-Tailorable Nanoparticles with 1-nm Interior Gap. *Nat. Nanotechnol.* **2011**, *6*, 452–460.

(77) Zhou, J.; Xiong, Q.; Ma, J.; Ren, J.; Messersmith, P. B.; Chen, P.; Duan, H. Polydopamine-Enabled Approach toward Tailored Plasmonic Nanogapped Nanoparticles: From Nanogap Engineering to Multifunctionality. *ACS Nano* **2016**, *10*, 11066–11075.

(78) Johnson, C. J.; Dujardin, E.; Davis, S. A.; Murphy, C. J.; Mann, S. Growth and Form of Gold Nanorods Prepared by Seed-Mediated, Surfactant-Directed Synthesis. *J. Mater. Chem.* **2002**, *12*, 1765–1770.

(79) Sun, Y.; Xia, Y. Shape-Controlled Synthesis of Gold and Silver Nanoparticles. *Science* **2002**, *298*, 2176–2179.

(80) Skrabalak, S. E.; Chen, J.; Sun, Y.; Lu, X.; Au, L.; Cobley, C. M.; Xia, Y. Gold Nanocages: Synthesis, Properties, and Applications. *Acc. Chem. Res.* **2008**, *41*, 1587–1595.

(81) Xie, J.; Zhang, Q.; Lee, J. Y.; Wang, D. I. C. The Synthesis of SERS-Active Gold Nanoflower Tags for In Vivo Applications. *ACS Nano* **2008**, *2*, 2473–2480.

(82) Hu, J.; Jiang, R.; Zhang, H.; Guo, Y.; Wang, J.; Wang, J. Colloidal Porous Gold Nanoparticles. *Nanoscale* **2018**, *10*, 18473–18481.

(83) Cai, J.; Raghavan, V.; Bai, Y. J.; Zhou, M. H.; Liu, X. L.; Liao, C. Y.; Ma, P.; Shi, L.; Dockery, P.; Keogh, I.; et al. Controllable Synthesis of Tetrapod Gold Nanocrystals with Precisely Tunable Near-Infrared Plasmon Resonance towards

Highly Efficient Surface Enhanced Raman Spectroscopy Bioimaging. *J. Mater. Chem. B* **2015**, *3*, 7377–7385.

(84) Hurst, S. J.; Lytton-Jean, A. K. R.; Mirkin, C. A. Maximizing DNA Loading on a Range of Gold Nanoparticle Sizes. *Anal. Chem.* **2006**, *78*, 8313–8318.

(85) Fan, M.; Andrade, G. F. S.; Brolo, A. G. A Review on the Fabrication of Substrates for Surface Enhanced Raman Spectroscopy and Their Applications in Analytical Chemistry. *Anal. Chim. Acta* **2011**, *693*, 7–25.

(86) Masuda, H.; Fukuda, K. Ordered Metal Nanohole Arrays Made by a Two-Step Replication of Honeycomb Structures of Anodic Alumina. *Science* **1995**, *268*, 1466–1468.

(87) Kahl, M.; Voges, E.; Kostrewa, S.; Viets, C.; Hill, W. Periodically Structured Metallic Substrates for SERS. *Sens. Actuators, B* **1998**, *51*, 285–291.

(88) Grabar, K. C.; Freeman, R. G.; Hommer, M. B.; Natan, M. J. Preparation and Characterization of Au Colloid Monolayers. *Anal. Chem.* **1995**, *67*, 735–743.

(89) Freeman, R. G.; Grabar, K. C.; Allison, K. J.; Bright, R. M.; Davis, J. A.; Guthrie, A. P.; Hommer, M. B.; Jackson, M. A.; Smith, P. C.; Walter, D. G.; et al. Self-Assembled Metal Colloid Monolayers: An Approach to SERS Substrates. *Science* **1995**, *267*, 1629–1632.

(90) Musick, M. D.; Keating, C. D.; Lyon, L. A.; Botsko, S. L.; Pena, D. J.; Holliway, W. D.; McEvoy, T. M.; Richardson, J. N.; Natan, M. J. Metal Films Prepared by Stepwise Assembly. 2. Construction and Characterization of Colloidal Au and Ag Multilayers. *Chem. Mater.* **2000**, *12*, 2869–2881.

(91) Li, J. F.; Huang, Y. F.; Ding, Y.; Yang, Z. L.; Li, S. B.; Zhou, X. S.; Fan, F. R.; Zhang, W.; Zhou, Z. Y.; Wu, D. Y.; et al. Shell-Isolated Nanoparticle-Enhanced Raman Spectroscopy. *Nature* **2010**, *474*, 392–395.

(92) Faraday, M. X. The Bakerian Lecture–Experimental Relations of Gold (and Other Metals) to Light. *Philos. Trans. Royal Soc.* **1857**, *147*, 145–181.

(93) Jeong, H.-H.; Choi, E.; Ellis, E.; Lee, T.-C. Recent Advances in Gold Nanoparticles for Biomedical Applications: From Hybrid Structures to Multi-Functionality. *J. Mater. Chem. B* **2019**, *7*, 3480–3496.

(94) Frens, G. Controlled Nucleation for the Regulation of the Particle Size in Monodisperse Gold Suspensions. *Nat. Phys. Sci.* **1973**, *241*, 20–22.

(95) Kimling, J.; Maier, M.; Okenve, B.; Kotaidis, V.; Ballot, H.; Plech, A. Turkevich Method for Gold Nanoparticle Synthesis Revisited. *J. Phys. Chem. B* **2006**, *110*, 15700–15707.

(96) Pong, B.-K.; Elim, H. I.; Chong, J.-X.; Ji, W.; Trout, B. L.; Lee, J.-Y. New Insights on the Nanoparticle Growth Mechanism in the Citrate Reduction of Gold(III) Salt: Formation of the Au Nanowire Intermediate and Its Nonlinear Optical Properties. *J. Phys. Chem. C* **2007**, *111*, 6281–6287.

(97) Kumar, S.; Gandhi, K. S.; Kumar, R. Modeling of Formation of Gold Nanoparticles by Citrate Method. *Ind. Eng. Chem. Res.* **2007**, *46*, 3128–3136.

(98) Ji, X.; Song, X.; Li, J.; Bai, Y.; Yang, W.; Peng, X. Size Control of Gold Nanocrystals in Citrate Reduction: The Third Role of Citrate. *J. Am. Chem. Soc.* **2007**, *129*, 13939–13948.

(99) Polte, J.; Ahner, T. T.; Delissen, F.; Sokolov, S.; Emmerling, F.; Thunemann, A. F.; Kraehnert, R. Mechanism of Gold Nanoparticle Formation in the Classical Citrate Synthesis Method Derived from Coupled In Situ XANES and SAXS Evaluation. *J. Am. Chem. Soc.* **2010**, *132*, 1296–1301.

(100) Ojea-Jimenez, I.; Bastus, N. G.; Puntes, V. Influence of the Sequence of the Reagents Addition in the Citrate-Mediated Synthesis of Gold Nanoparticles. *J.*

Phys. Chem. C **2011**, *115*, 15752–15757.

(101) Bastus N. G.; Comenge, J.; Puntes, V. Kinetically Controlled Seeded Growth Synthesis of Citrate-Stabilized Gold Nanoparticles of up to 200 nm : Size Focusing versus Ostwald Ripening. *Langmuir* **2011**, *27*, 11098–11105.

(102) Daruich De Souza, C.; Ribeiro Nogueira, B.; Rostelato, M. E. C. M. Review of the Methodologies Used in the Synthesis Gold Nanoparticles by Chemical Reduction. *J. Alloys Compd*. **2019**, *798*, 714–740.

(103) Brust, M.; Walker, M.; Bethell, D.; Schiffrin, D. J.; Whyman, R. Synthesis of Thiol-Derivatised Gold Nanoparticles in a Two-Phase Liquid-Liquid System. *J. Chem. Soc., Chem. Commun.* **1994**, 801–802.

(104) Liz-Marzan, L. M. Gold Nanoparticle Research Before and After the Brust-Schiffrin Method. *Chem. Commun*. **2013**, *49*, 16–18.

(105) Zhao, P.; Li, N.; Astruc, D. State of the Art in Gold Nanoparticle Synthesis. *Coord. Chem. Rev*. **2013**, *257*, 638–665.

(106) Bernard, L.; Kamdzhilov, Y.; Calame, M.; Van der Molen, S. J.; Liao, J.; Schönenberger, C. Spectroscopy of Molecular Junction Networks Obtained by Place Exchange in 2D Nanoparticle Arrays. *J. Phys. Chem. C* **2007**, *111*, 18445–18450.

(107) Bhattacharjee, R. R.; Mandal, T. K. Polymer-Mediated Chain-Like Self-Assembly of Functionalized Gold Nanoparticles. *J. Colloid Interface Sci.* **2007**, *307*, 288–295.

(108) Lee, S. H.; Bae, K. H.; Kim, S. H.; Lee, K. R.; Park, T. G. Amine-Functionalized Gold Nanoparticles as Non-Cytotoxic and Efficient Intracellular SiRNA Delivery Carriers. *Int. J. Pharm.* **2008**, *364*, 94–101.

(109) Teyssandier, J.; De Feyter, S.; Mali, K. S. Host-Guest Chemistry in Two-

Dimensional Supramolecular Networks. *Chem. Commun.* **2016**, *52*, 11465–11487.

(110) Pedersen, C. J. Cyclic Polyethers and Their Complexes with Metal Salts. *J. Am. Chem. Soc.* **1967**, *89*, 7017–7036.

(111) Bohmer, V. Calixarenes, Macrocycles with (Almost) Unlimited Possibilities. *Angew. Chem. Int. Ed.* **1995**, *34*, 713–745.

(112) Del Valle, E. M. M. Cyclodextrins and Their Uses: A Review. *Process Biochem.* **2004**, *39*, 1033–1046.

(113) Lagona, J.; Mukhopadhyay, P.; Chakrabarti, S.; Isaacs, L. The Cucurbit[*n*]uril Family. *Angew. Chem. Int. Ed.* **2005**, *44*, 4844–4870.

(114) Biedermann, F.; Uzunova, V. D.; Scherman, O. A.; Nau, W. M.; De Simone, A. Release of High-Energy Water as an Essential Driving Force for the High-Affinity Binding of Cucurbit[*n*]urils. *J. Am. Chem. Soc.* **2012**, *134*, 15318–15323.

(115) Behrend, R.; Meyer, E.; Rusche, F. I. Ueber Condensationsproducte aus Glycoluril und Formaldehyd. *Justus Liebigs Ann. Chem.* **1905**, *339*, 1–37.

(116) Freeman, W. A.; Mock, W. L.; Shih, N. Y. Cucurbituril. *J. Am. Chem. Soc.* **1981**, *103*, 7367–7368.

(117) Kim, J.; Jung, I.-S.; Kim, S.-Y.; Lee, E.; Kang, J.-K.; Sakamoto, S.; Yamaguchi, K.; Kim, K. New Cucurbituril Homologues: Syntheses, Isolation, Characterization, and X-ray Crystal Structures of Cucurbit[*n*]uril (*n* = 5, 7, and 8). *J. Am. Chem. Soc.* **2000**, *122*, 540–541.

(118) Day, A.; Arnold, A. P.; Blanch, R. J.; Snushall, B. Controlling Factors in the Synthesis of Cucurbituril and Its Homologues. *J. Org. Chem.* **2001**, *66*, 8094–8100.

(119) Day, A. I.; Blanch, R. J.; Arnold, A. P.; Lorenzo, S.; Lewis, G. R.; Dance, I. A Cucurbituril-Based Gyroscane: A New Supramolecular Form. *Angew. Chem. Int. Ed.* **2002**, *41*, 275–277.

(120) Masson, E.; Ling, X.; Joseph, R.; Kyeremeh-Mensah, L.; Lu, X. Cucurbituril Chemistry: A Tale of Supramolecular Success. *RSC Adv.* **2012**, *2*, 1213–1247.

(121) Assaf, K. I.; Nau, W. M. Cucurbiturils: From Synthesis to High-Affinity Binding and Catalysis. *Chem. Soc. Rev.* **2015**, *44*, 394–418.

(122) Liu, S.; Zavalij, P. Y.; Isaacs, L. Cucurbit[10]uril. *J. Am. Chem. Soc.* **2005**, *127*, 16798–16799.

(123) Isaacs, L. Cucurbit[*n*]urils: From Mechanism to Structure and Function. *Chem. Commun.* **2009**, 619–629.

(124) Pisani, M. J.; Zhao, Y.; Wallace, L.; Woodward, C. E.; Keene, F. R.; Day, A. I.; Collins, J. G. Cucurbit[10]uril Binding of Dinuclear Platinum(II) and Ruthenium(II) Complexes: Association/Dissociation Rates from Seconds to Hours. *Dalton Trans.* **2010**, *39*, 2078–2086.

(125) Cheng, X.-J.; Liang, L.-L.; Chen, K.; Ji, N.-N.; Xiao, X.; Zhang, J.-X.; Zhang, Y.-Q.; Xue, S.-F.; Zhu, Q.-J.; Ni, X.-L.; et al. Twisted Cucurbit[14]uril. *Angew. Chem. Int. Ed.* **2013**, *52*, 7252–7255.

(126) Li, Q.; Qiu, S.-C.; Zhang, J.; Chen, K.; Huang, Y.; Xiao, X.; Zhang, Y.; Li, F.; Zhang, Y.-Q.; Xue, S.-F.; et al. Twisted Cucurbit[*n*]urils. *Org. Lett.* **2016**, *18*, 4020–4023.

(127) Zhao, J.; Kim, H.-J.; Oh, J.; Kim, S.-Y.; Lee, J. W.; Sakamoto, S.; Yamaguchi, K.; Kim, K. Cucurbit[*n*]uril Derivatives Soluble in Water and Organic Solvents. *Angew. Chem. Int. Ed.* **2001**, *40*, 4233–4235.

(128) Jon, S. Y.; Selvapalam, N.; Oh, D. H.; Kang, J.-K.; Kim, S.-Y.; Jeon, Y. J.; Lee, J. W.; Kim, K. Facile Synthesis of Cucurbit[*n*]uril Derivatives via Direct Functionalization: Expanding Utilization of Cucurbit[*n*]uril. *J. Am. Chem. Soc.* **2003**, *125*, 10186–10187.

(129) Lu, L.-B.; Yu, D.-H.; Zhang, Y.-Q.; Zhu, Q.-J.; Xue, S.-F.; Tao, Z. Supramolecular Assemblies Based on Some New Methyl-Substituted Cucurbit[5]urils through Hydrogen Bonding. *J. Mol. Struct.* **2008**, *885*, 70–75.

(130) Lewin, V.; Rivollier, J.; Coudert, S.; Buisson, D.-A.; Baumann, D.; Rousseau, B.; Legrand, F.-X.; Kourilova, H.; Berthault, P.; Dognon, J.-P.; et al. Synthesis of Cucurbit[6]uril Derivatives and Insights into Their Solubility in Water. *Eur. J. Org. Chem.* **2013**, *2013*, 3857–3865.

(131) Robinson, E. L.; Zavalij, P. Y.; Isaacs, L. Synthesis of a Disulfonated Derivative of Cucurbit[7]uril and Investigations of Its Ability to Solubilise Insoluble Drugs. *Supramol. Chem.* **2015**, *27*, 288–297.

(132) Vinciguerra, B.; Cao, L.; Cannon, J. R.; Zavalij, P. Y.; Fenselau, C.; Isaacs, L. Synthesis and Self-Assembly Processes of Monofunctionalized Cucurbit[7]uril. *J. Am. Chem. Soc.* **2012**, *134*, 13133–13140.

(133) Vinciguerra, B.; Zavalij, P. Y.; Isaacs, L. Synthesis and Recognition Properties of Cucurbit[8]uril Derivatives. *Org. Lett.* **2015**, *17*, 5068–5071.

(134) Isaacs, L.; Park, S.-K.; Liu, S.; Ko, Y. H.; Selvapalam, N.; Kim, Y.; Kim, H.; Zavalij, P. Y.; Kim, G.-H.; Lee, H.-S.; et al. The Inverted Cucurbit[*n*]uril Family. *J. Am. Chem. Soc.* **2005**, *127*, 18000–18001.

(135) Huang, W.-H.; Liu, S.; Zavalij, P. Y.; Isaacs, L. Nor-Seco-Cucurbit[10]uril Exhibits Homotropic Allosterism. *J. Am. Chem. Soc.* **2006**, *128*, 14744–14745.

(136) Huang, W.-H.; Zavalij, P. Y.; Isaacs, L. Chiral Recognition inside a Chiral Cucurbituril. *Angew. Chem. Int. Ed.* **2007**, *46*, 7425–7427.

(137) Svec, J.; Necas, M.; Sindelar, V. Bambus[6]uril. *Angew. Chem. Int. Ed.* **2010**, *49*, 2378–2381.

(138) Miyahara, Y.; Goto, K.; Oka, M.; Inazu, T. Remarkably Facile Ring-Size Control

in Macrocyclization: Synthesis of Hemicucurbit[6]uril and Hemicucurbit[12]uril. *Angew. Chem. Int. Ed.* **2004**, *43*, 5019–5022.

(139) Flinn, A.; Hough, G. C.; Stoddart, J. F.; Williams, D. J. Decamethylcucurbit[5]uril. *Angew. Chem. Int. Ed.* **1992**, *31*, 1475–1477.

(140) Cong, H.; Ni, X. L.; Xiao, X.; Huang, Y.; Zhu, Q.-J.; Xue, S.-F.; Tao, Z.; Lindoy, L. F.; Wei, G. Synthesis and Separation of Cucurbit[*n*]urils and Their Derivatives. *Org. Biomol. Chem.* **2016**, *14*, 4335–4364.

(141) Nau, W. M.; Florea, M.; Assaf, K. I. Deep inside Cucurbiturils: Physical Properties and Volumes of Their Inner Cavity Determine the Hydrophobic Driving Force for Host-Guest Complexation. *Isr. J. Chem.* **2011**, *51*, 559–577.

(142) Lee, J. W.; Samal, S.; Selvapalam, N.; Kim, H.-J.; Kim, K. Cucurbituril Homologues and Derivatives: New Opportunities in Supramolecular Chemistry. *Acc. Chem. Res.* **2003**, *36*, 621–630.

(143) Szejtli, J. Introduction and General Overview of Cyclodextrin Chemistry. *Chem. Rev.* **1998**, *98*, 1743–1754.

(144) Mecozzi, S.; Rebek, J. The 55 % Solution: A Formula for Molecular Recognition in the Liquid State. *Chem. – Eur. J.* **1998**, *4*, 1016–1022.

(145) Thomas, C. R.; Ferris, D. P.; Lee, J.-H.; Choi, E.; Cho, M. H.; Kim, E. S.; Stoddart, J. F.; Shin, J.-S.; Cheon, J.; Zink, J. I. Noninvasive Remote-Controlled Release of Drug Molecules In Vitro Using Magnetic Actuation of Mechanized Nanoparticles. *J. Am. Chem. Soc.* **2010**, *132*, 10623–10625.

(146) Tonga, G. Y.; Jeong, Y.; Duncan, B.; Mizuhara, T.; Mout, R.; Das, R.; Kim, S. T.; Yeh, Y. C.; Yan, B.; Hou, S.; et al. Supramolecular Regulation of Bioorthogonal Catalysis in Cells Using Nanoparticle-Embedded Transition Metal Catalysts. *Nat. Chem.* **2015**, *7*, 597–603.

(147) Lee, T.-C.; Kalenius, E.; Lazar, A. I.; Assaf, K. I.; Kuhnert, N.; Grun, C. H.; Janis, J.; Scherman, O. A.; Nau, W. M. Chemistry inside Molecular Containers in the Gas Phase. *Nat. Chem.* **2013**, *5*, 376–382.

(148) Ellis, E.; Moorthy, S.; Chio, W.-I. K.; Lee, T.-C. Artificial Molecular and Nanostructures for Advanced Nanomachinery. *Chem. Commun.* **2018**, *54*, 4075–4090.

(149) Peveler, W. J.; Jia, H.; Jeen, T.; Rees, K.; Macdonald, T. J.; Xia, Z.; Chio, W.-I. K.; Moorthy, S.; Parkin, I. P.; Carmalt, C. J.; et al. Cucurbituril-Mediated Quantum Dot Aggregates Formed by Aqueous Self-Assembly for Sensing Applications. *Chem. Commun.* **2019**, *55*, 5495–5498.

(150) Mock, W. L.; Shih, N. Y. Host-Guest Binding Capacity of Cucurbituril. *J. Org. Chem.* **1983**, *48*, 3618–3619.

(151) Freeman, W. A. Structures of the *p*-xylylenediammonium Chloride and Calcium Hydrogensulfate Adducts of the Cavitand “Cucurbituril”, $C_{36}H_{36}N_{24}O_{12}$. *Acta Crystallogr. B* **1984**, *40*, 382–387.

(152) Shetty, D.; Khedkar, J. K.; Park, K. M.; Kim, K. Can We Beat the Biotin–Avidin Pair?: Cucurbit[7]uril-Based Ultrahigh Affinity Host–Guest Complexes and Their Applications. *Chem. Soc. Rev.* **2015**, *44*, 8747–8761.

(153) Buschmann, H.-J.; Cleve, E.; Jansen, K.; Wego, A.; Schollmeyer, E. Complex Formation between Cucurbit[*n*]urils and Alkali, Alkaline Earth and Ammonium Ions in Aqueous Solution. *J. Incl. Phenom. Macrocycl. Chem.* **2001**, *40*, 117–120.

(154) Buschmann, H.-J.; Cleve, E.; Jansen, K.; Schollmeyer, E. Determination of Complex Stabilities with Nearly Insoluble Host Molecules: Cucurbit[5]uril, Decamethylcucurbit[5]uril and Cucurbit[6]uril as Ligands for the Complexation of Some Multicharged Cations in Aqueous Solution. *Anal. Chim. Acta* **2001**, *437*,

157–163.

(155) Kellersberger, K. A.; Anderson, J. D.; Ward, S. M.; Krakowiak, K. E.; Dearden, D. V. Encapsulation of N_2, O_2, Methanol, or Acetonitrile by Decamethylcucurbit[5]uril$(NH_4^+)_2$ Complexes in the Gas Phase: Influence of the Guest on “Lid” Tightness. *J. Am. Chem. Soc.* **2001**, *123*, 11316–11317.

(156) Tuncel, D.; Cindir, N.; Koldemir, U. [5]Rotaxane and [5]Pseudorotaxane Based on Cucurbit[6]uril and Anchored to a Meso-tetraphenyl Porphyrin. *J. Incl. Phenom. Macrocycl. Chem.* **2006**, *55*, 373–380.

(157) Barrow, S. J.; Kasera, S.; Rowland, M. J.; del Barrio, J.; Scherman, O. A. Cucurbituril-Based Molecular Recognition. *Chem. Rev*. **2015**, *115*, 12320–12406.

(158) Ong, W.; Kaifer, A. E. Unusual Electrochemical Properties of the Inclusion Complexes of Ferrocenium and Cobaltocenium with Cucurbit[7]uril. *Organometallics* **2003**, *22*, 4181–4183.

(159) Rekharsky, M. V.; Mori, T.; Yang, C.; Ko, Y. H.; Selvapalam, N.; Kim, H.; Sobransingh, D.; Kaifer, A. E.; Liu, S.; Isaacs, L.; et al. A Synthetic Host-Guest System Achieves Avidin-Biotin Affinity by Overcoming Enthalpy – Entropy Compensation. *Proc. Natl. Acad. Sci. U. S. A.* **2007**, *104*, 20737–20742.

(160) Liu, S.; Ruspic, C.; Mukhopadhyay, P.; Chakrabarti, S.; Zavalij, P. Y.; Isaacs, L. The Cucurbit[*n*]uril Family: Prime Components for Self-Sorting Systems. *J. Am. Chem. Soc.* **2005**, *127*, 15959–15967.

(161) Moghaddam, S.; Yang, C.; Rekharsky, M.; Ko, Y. H.; Kim, K.; Inoue, Y.; Gilson, M. K. New Ultrahigh Affinity Host−Guest Complexes of Cucurbit[7]uril with Bicyclo[2.2.2]octane and Adamantane Guests: Thermodynamic Analysis and Evaluation of M2 Affinity Calculations. *J. Am. Chem. Soc.* **2011**, *133*, 3570–3581.

(162) Cao, L.; Sekutor, M.; Zavalij, P. Y.; Mlinaric-Majerski, K.; Glaser, R.; Isaacs, L.

Cucurbit[7]uril·Guest Pair with an Attomolar Dissociation Constant. *Angew. Chem. Int. Ed.* **2014**, *53*, 988–993.

(163) Green, N. M. Avidin. 1. The Use of [^{14}C]Biotin for Kinetic Studies and for Assay. *Biochem. J.* **1963**, *89*, 585–591.

(164) Murray, J.; Kim, K.; Ogoshi, T.; Yao, W.; Gibb, B. C. The Aqueous Supramolecular Chemistry of Cucurbit[*n*]urils, Pillar[*n*]arenes and Deep-Cavity Cavitands. *Chem. Soc. Rev.* **2017**, *46*, 2479–2496.

(165) Kim, H.-J.; Heo, J.; Jeon, W. S.; Lee, E.; Kim, J.; Sakamoto, S.; Yamaguchi, K.; Kim, K. Selective Inclusion of a Hetero-Guest Pair in a Molecular Host: Formation of Stable Charge-Transfer Complexes in Cucurbit[8]uril. *Angew. Chem. Int. Ed.* **2001**, *40*, 1526–1529.

(166) Rauwald, U.; Scherman, O. A. Supramolecular Block Copolymers with Cucurbit[8]uril in Water. *Angew. Chem. Int. Ed.* **2008**, *47*, 3950–3953.

(167) Liu, Y.; Huang, Z.; Liu, K.; Kelgtermans, H.; Dehaen, W.; Wang, Z.; Zhang, X. Porphyrin-Containing Hyperbranched Supramolecular Polymers: Enhancing $^1O_2$-Generation Efficiency by Supramolecular Polymerization. *Polym. Chem.* **2014**, *5*, 53–56.

(168) Isaacs, L. Stimuli Responsive Systems Constructed Using Cucurbit[*n*]uril-Type Molecular Containers. *Acc. Chem. Res.* **2014**, *47*, 2052–2062.

(169) Macartney, D. H. Encapsulation of Drug Molecules by Cucurbiturils: Effects on Their Chemical Properties in Aqueous Solution. *Isr. J. Chem.* **2011**, *51*, 600–615.

(170) Yang, X.; Liu, F.; Zhao, Z.; Liang, F.; Zhang, H.; Liu, S. Cucurbit[10]uril-Based Chemistry. *Chin. Chem. Lett.* **2018**, *29*, 1560–1566.

(171) Corma, A.; Garcia, H.; Montes-Navajas, P.; Primo, A.; Calvino, J. J.; Trasobares, S. Gold Nanoparticles in Organic Capsules: A Supramolecular Assembly of Gold

Nanoparticles and Cucurbituril. *Chem. – Eur. J.* **2007**, *13*, 6359–6364.

(172) Lee, T.-C.; Scherman, O. A. A Facile Synthesis of Dynamic Supramolecular Aggregates of Cucurbit[*n*]uril (*n* =5–8) Capped with Gold Nanoparticles in Aqueous Media. *Chem. – Eur. J.* **2012**, *18*, 1628–1633.

(173) An, Q.; Li, G.; Tao, C.; Li, Y.; Wu, Y.; Zhang, W. A General and Efficient Method to Form Self-Assembled Cucurbit[*n*]uril Monolayers on Gold Surfaces. *Chem. Commun.* **2008**, 1989–1991.

(174) Huang, T.; Meng, F.; Qi, L. Facile Synthesis and One-Dimensional Assembly of Cyclodextrin-Capped Gold Nanoparticles and Their Applications in Catalysis and Surface-Enhanced Raman Scattering. *J. Phys. Chem. C* **2009**, *113*, 13636–13642.

(175) Mahajan, S.; Lee, T.-C.; Biedermann, F.; Hugall, J. T.; Baumberg, J. J.; Scherman, O. A. Raman and SERS Spectroscopy of Cucurbit[*n*]urils. *Phys. Chem. Chem. Phys.* **2010**, *12*, 10429–10433.

(176) Jones, S. T.; Taylor, R. W.; Esteban, R.; Abo-Hamed, E. K.; Bomans, P. H. H.; Sommerdijk, N. A. J. M.; Aizpurua, J.; Baumberg, J. J.; Scherman, O. A. Gold Nanorods with Sub-Nanometer Separation Using Cucurbit[*n*]uril for SERS Applications. *Small* **2014**, *10*, 4298–4303.

(177) Zhang, J.; Coulston, R. J.; Jones, S. T.; Geng, J.; Scherman, O. A.; Abell, C. One-Step Fabrication of Supramolecular Microcapsules from Microfluidic Droplets. *Science* **2012**, *335*, 690–694.

(178) Coulston, R. J.; Jones, S. T.; Lee, T.-C.; Appel, E. A.; Scherman, O. A. Supramolecular Gold Nanoparticle–Polymer Composites Formed in Water with Cucurbit[8]uril. *Chem. Commun.* **2011**, *47*, 164–166.

(179) de Nijs, B.; Carnegie, C.; Szabo, I.; Grys, D.-B.; Chikkaraddy, R.; Kamp, M.; Barrow, S. J.; Readman, C.A.; Kleemann, M.-E.; Scherman, O. A.; et al. Inhibiting

Analyte Theft in Surface-Enhanced Raman Spectroscopy Substrates: Subnanomolar Quantitative Drug Detection. *ACS Sensors* **2019**, *4*, 2988–2996.

(180) Tao, C.-A.; An, Q.; Zhu, W.; Yang, H.; Li, W.; Lin, C.; Xu, D.; Li, G. Cucurbit[*n*]urils as a SERS Hot-Spot Nanocontainer through Bridging Gold Nanoparticles. *Chem. Commun.* **2011**, *47*, 9867–9869.

(181) Sigle, D. O.; Kasera, S.; Herrmann, L. O.; Palma, A.; de Nijs, B.; Benz, F.; Mahajan, S.; Baumberg, J. J.; Scherman, O. A. Observing Single Molecules Complexing with Cucurbit[7]uril through Nanogap Surface-Enhanced Raman Spectroscopy. *J. Phys. Chem. Lett.* **2016**, *7*, 704–710.

(182) Carnegie, C.; Chikkaraddy, R.; Benz, F.; de Nijs, B.; Deacon, W. M.; Horton, M.; Wang, W.; Readman, C.; Barrow, S. J.; Scherman, O. A.; et al. Mapping SERS in CB:Au Plasmonic Nanoaggregates. *ACS Photonics* **2017**, *4*, 2681–2686.

(183) Villa, J. E. L.; Poppi, R. J. A Portable SERS Method for the Determination of Uric Acid Using a Paper-Based Substrate and Multivariate Curve Resolution. *Analyst* **2016**, *141*, 1966–1972.

(184) Peveler, W. J.; Roldan, A.; Hollingsworth, N.; Porter, M. J.; Parkin, I. P. Multichannel Detection and Differentiation of Explosives with a Quantum Dot Array. *ACS Nano* **2016**, *10*, 1139–1146.

(185) Peveler, W. J.; Jaber, S. B.; Parkin, I. P. Nanoparticles in Explosives Detection - the State-of-the-Art and Future Directions. *Forensic Sci. Med. Pathol.* **2017**, *13*, 490–494.

(186) Cecchini, M. P.; Turek, V. A.; Paget, J.; Kornyshev, A. A.; Edel, J. B. Self-Assembled Nanoparticle Arrays for Multiphase Trace Analyte Detection. *Nat. Mater.* **2013**, *12*, 165–171.

(187) Thomas, S. W.; Joly, G. D.; Swager, T. M. Chemical Sensors Based on Amplifying

Fluorescent Conjugated Polymers. *Chem. Rev.* **2007**, *107*, 1339–1386.

(188) Zapata, F.; Lopez-Lopez, M.; Garcia-Ruiz, C. Detection and Identification of Explosives by Surface Enhanced Raman Scattering. *Appl. Spectrosc. Rev.* **2016**, *51*, 227–262.

(189) Zhu, W.; Li, W.; Wang, C.; Cui, J.; Yang, H.; Jiang, Y.; Li, G. CB[8]-Based Rotaxane as a Useful Platform for Sensitive Detection and Discrimination of Explosives. *Chem. Sci.* **2013**, *4*, 3583–3590.

(190) Zhu, W.; Wang, C.; Li, W.; Tao, C. A.; Cui, J.; Yang, H.; Jiang, Y.; Li, G. A New Strategy for Selective Detection of Nitrated Explosives Based on a Confinement Effect of Nanocavity. *J. Mater. Chem. A* **2013**, *1*, 11741–11747.

(191) Liu, X.; Zhao, L.; Shen, H.; Xu, H.; Lu, L. Ordered Gold Nanoparticle Arrays as Surface-Enhanced Raman Spectroscopy Substrates for Label-Free Detection of Nitroexplosives. *Talanta* **2011**, *83*, 1023–1029.

(192) Smith, K. D.; McCord, B. R.; MacCrehan, W. A.; Mount, K.; Rowe, W. F. Detection of Smokeless Powder Residue on Pipe Bombs by Micellar Electrokinetic Capillary Electrophoresis. *J. Forensic Sci.* **1999**, *44*, 789–794.

(193) Amaral, H. I. F.; Fernandes, J.; Berg, M.; Schwarzenbach, R. P.; Kipfer, R. Assessing TNT and DNT Groundwater Contamination by Compound-Specific Isotope Analysis and ^{3}H–^{3}He Groundwater Dating: A Case Study in Portugal. *Chemosphere* **2009**, *77*, 805–812.

(194) Berg, M.; Bolotin, J.; Hofstetter, T. B. Compound-Specific Nitrogen and Carbon Isotope Analysis of Nitroaromatic Compounds in Aqueous Samples Using Solid-Phase Microextraction Coupled to GC/IRMS. *Anal. Chem.* **2007**, *79*, 2386–2393.

(195) Kalderis, D.; Juhasz, A. L.; Boopathy, R.; Comfort, S. Soils Contaminated with Explosives: Environmental Fate and Evaluation of State-of-the-Art Remediation

Processes (IUPAC Technical Eport). *Pure App. Chem*. **2011**, *83*, 1407–1484.

(196) Lent, E. M.; Crouse, L. C. B.; Quinn, M. J.; Wallace, S. M. Comparison of the Repeated Dose Toxicity of Isomers of Dinitrotoluene. *Int. J. Toxicol.* **2012**, *31*, 143–157.

(197) Lent, E. M. Chapter 6 – Wildlife Toxicity Assessment for 2,4-Dinitrotoluene and 2,6-Dinitrotoluene. *Wildlife Toxicity Assessments for Chemicals of Military Concern.* **2015**, 107–146.

(198) Tchounwou, P. B.; Wilson, B. A.; Ishaque, A. B.; Schneider, J. Transcriptional Activation of Stress Genes and Cytotoxicity in Human Liver Carcinoma Cells (HepG2) Exposed to 2,4,6-Trinitrotoluene, 2,4-Dinitrotoluene, and 2,6-Dinitrotoluene. *Environ. Toxicol.* **2001**, *16*, 209–216.

(199) Sabbioni, G.; Jones, C. R.; Sepai, O.; Hirvonen, A.; Norppa, H.; Jarventaus, H.; Glatt, H.; Pomplun, D.; Yan, H.; Brooks, L. R.; et al. Biomarkers of Exposure, Effect, and Susceptibility in Workers Exposed to Nitrotoluenes. *Cancer Epidemiol. Biomark. Prev.* **2006**, *15*, 559–566.

(200) Chen, W.; Zuckerman, N. B.; Konopelski, J. P.; Chen, S. Pyrene-Functionalized Ruthenium Nanoparticles as Effective Chemosensors for Nitroaromatic Derivatives. *Anal. Chem.* **2010**, *82*, 461–465.

(201) Jiang, Y.; Zhao, H.; Zhu, N.; Lin, Y.; Yu, P.; Mao, L. A Simple Assay for Direct Colorimetric Visualization of Trinitrotoluene at Picomolar Levels Using Gold Nanoparticles. *Angew. Chem. Int. Ed.* **2008**, *47*, 8601–8604.

(202) Riskin, M.; Tel-Vered, R.; Bourenko, T.; Granot, E.; Willner, I. Imprinting of Molecular Recognition Sites through Electropolymerization of Functionalized Au Nanoparticles: Development of an Electrochemical TNT Sensor Based on π-Donor-Acceptor Interactions. *J. Am. Chem. Soc.* **2008**, *130*, 9726–9733.

(203) Matsumoto, K.; Torimaru, A.; Ishitobi, S.; Sakai, T.; Ishikawa, H.; Toko, K.; Miura, N.; Imato, T. Preparation and Characterization of a Polyclonal Antibody from Rabbit for Detection of Trinitrotoluene by a Surface Plasmon Resonance Biosensor. *Talanta* **2005**, *68*, 305–311.

(204) Fang, Y.; Seong, N.-H.; Dlott, D. D. Measurement of the Distribution of Site Enhancements in Surface-Enhanced Raman Scattering. *Science* **2008**, *321*, 388–392.

(205) Ben-Jaber, S.; Peveler, W. J.; Quesada-Cabrera, R.; Cortes, E.; Sotelo-Vazquez, C.; Abdul-Karim, N.; Maier, S. A.; Parkin, I. P. Photo-Induced Enhanced Raman Spectroscopy for Universal Ultra-Trace Detection of Explosives, Pollutants and Biomolecules. *Nat. Commun.* **2016**, *7*, 12189.

(206) Ben-Jaber, S.; Peveler, W. J.; Quesada-Cabrera, R.; Sol, C. W. O.; Papakonstantinou, I.; Parkin, I. P. Sensitive and Specific Detection of Explosives in Solution and Vapour by Surface-Enhanced Raman Spectroscopy on Silver Nanocubes. *Nanoscale* **2017**, *9*, 16459–16466.

(207) Chio, W.-I. K.; Peveler, W. J.; Assaf, K. I.; Moorthy, S.; Nau, W. M.; Parkin, I. P.; Olivo, M.; Lee, T.-C. Selective Detection of Nitroexplosives Using Molecular Recognition within Self-Assembled Plasmonic Nanojunctions. *J. Phys. Chem. C* **2019**, *123*, 15769–15776.

(208) Phelan, J. M.; Barnett, J. L. Solubility of 2,4-Dinitrotoluene and 2,4,6-Trinitrotoluene in Water. *J. Chem. Eng. Data* **2001**, *46*, 375–376.

(209) Biedermann, F.; Nau, W. M.; Schneider, H.-J. The Hydrophobic Effect Revisited – Studies with Supramolecular Complexes Imply High-Energy Water as a Noncovalent Driving Force. *Angew. Chem. Int. Ed.* **2014**, *53*, 11158–11571.

(210) Liu, T.; Schneider, H.-J. Additivity and Quantification of Dispersive Interactions

– from Cyclopropyl to Nitro Groups: Measurements on Porphyrin Derivatives. *Angew. Chem. Int. Ed.* **2002**, *41*, 1368–1370.

(211) Fierro-Mercado, P. M.; Hernandez-Rivera, S. P. Highly Sensitive Filter Paper Substrate for SERS Trace Explosives Detection. *Int. J. Spectrosc.* **2012**, *2012*, 7.

(212) Carey, D. M.; Korenowski, G. M. Measurement of the Raman Spectrum of Liquid Water. *J. Chem. Phys.* **1998**, *108*, 2669–2675.

(213) Martinez-Pinilla, E.; Onatibia-Astibia, A.; Franco, R. The Relevance of Theobromine for the Beneficial Effects of Cocoa Consumption. *Front. Pharmacol.* **2015**, *6*, 30.

(214) Sanphui, P.; Nangia, A. Salts and Co-Crystals of Theobromine and Their Phase Transformations in Water. *J. Chem. Sci.* **2014**, *126*, 1249–1264.

(215) Sugimoto, N.; Miwa, S.; Hitomi, Y.; Nakamura, H.; Tsuchiya, H.; Yachie, A. Theobromine, the Primary Methylxanthine Found in Theobroma Cacao, Prevents Malignant Glioblastoma Proliferation by Negatively Regulating Phosphodiesterase-4, Extracellular Signal-Regulated Kinase, Akt/Mammalian Target of Rapamycin Kinase, and Nuclear Fact. *Nutr. Cancer* **2014**, *66*, 419–423.

(216) Bispo, M. S.; Veloso, M. C. C.; Pinheiro, H. L. C.; De Oliveira, R. F. S.; Reis, J. O. N.; De Andrade, J. B. Simultaneous Determination of Caffeine, Theobromine, and Theophylline by High-Performance Liquid Chromatography. *J. Chromatogr. Sci.* **2002**, *40*, 45–48.

(217) Holmgren, P.; Norden-Pettersson, L.; Ahlner, J. Caffeine Fatalities - Four Case Reports. *Forensic Sci. Int.* **2004**, *139*, 71–73.

(218) Cortinovis, C.; Caloni, F. Household Food Items Toxic to Dogs and Cats. *Front. Vet. Sci*. **2016**, *3*. 26.

(219) Huck, C. W.; Guggenbichler, W.; Bonn, G. K. Analysis of Caffeine, Theobromine

and Theophylline in Coffee by Near Infrared Spectroscopy (NIRS) Compared to High-Performance Liquid Chromatography (HPLC) Coupled to Mass Spectrometry. *Anal. Chim. Acta* **2005**, *538*, 195–203.

(220) Brunetto, M. R.; Gutierrez, L.; Delgado, Y.; Gallignani, M.; Zambrano, A.; Gomez, A.; Ramos, G.; Romero, C. Determination of Theobromine, Theophylline and Caffeine in Cocoa Samples by a High-Performance Liquid Chromatographic Method with On-Line Sample Cleanup in a Switching-Column System. *Food Chem.* **2007**, *100*, 459–467.

(221) Carvalho, J. J.; Weller, M. G.; Panne, U.; Schneider, R. J. A Highly Sensitive Caffeine Immunoassay Based on a Monoclonal Antibody. *Anal. Bioanal. Chem.* **2010**, *396*, 2617–2618.

(222) Chiem, N.; Harrison, D. J. Microchip-Based Capillary Electrophoresis for Immunoassays: Analysis of Monoclonal Antibodies and Theophylline. *Anal. Chem.* **1997**, *69*, 373–378.

(223) Gupta, V. K.; Jain, A. K.; Shoora, S. K. Multiwall Carbon Nanotube Modified Glassy Carbon Electrode as Voltammetric Sensor for the Simultaneous Determination of Ascorbic Acid and Caffeine. *Electrochim. Acta* **2013**, *93*, 248–253.

(224) Peng, Y.; Zhang, W.; Chang, J.; Huang, Y.; Chen, L.; Deng, H.; Huang, Z.; Wen, Y. A Simple and Sensitive Method for the Voltammetric Analysis of Theobromine in Food Samples Using Nanobiocomposite Sensor. *Food Anal. Methods* **2017**, *10*, 3375–3384.

(225) Bates, F.; del Valle, M. Voltammetric Sensor for Theophylline Using Sol–Gel Immobilized Molecularly Imprinted Polymer Particles. *Microchim. Acta* **2015**, *182*, 933–942.

(226) Xu, W.; Kim, T.-H.; Zhai, D.; Er, J. C.; Zhang, L.; Kale, A. A.; Agrawalla, B. K.; Cho, Y.-K.; Chang, Y.-T. Make Caffeine Visible: A Fluorescent Caffeine "Traffic Light" Detector. *Sci. Rep.* **2013**, *3*, 2255.

(227) Mahapatra, A. K.; Sahoo, P.; Goswami, S.; Chantrapromma, S.; Fun, H.-K. Fluorescence Sensing of Theobromine by Simple 2,6-diamino-pyridine and the Novel Cyclic Chair-Like Hydrogen-Bonded Tetramer of Its Diacetyl Derivative. *Tetrahedron Lett.* **2009**, *50*, 89–92.

(228) Liu, P.; Liu, R.; Guan, G.; Jiang, C.; Wang, S.; Zhang, Z. Surface-Enhanced Raman Scattering Sensor for Theophylline Determination by Molecular Imprinting on Silver Nanoparticles. *Analyst* **2011**, *136*, 4152–4158.

(229) Zheng, H.; Ni, D.; Yu, Z.; Liang, P.; Chen, H. Fabrication of Flower-Like Silver Nanostructures for Rapid Detection of Caffeine Using Surface Enhanced Raman Spectroscopy. *Sens. Actuators, B* **2016**, *231*, 423–430.

(230) Wu, M.; Li, H.; Lv, D.; Lu, F. Dynamic-SERS Spectroscopy for the in Situ Discrimination of Xanthine Analogues in Ternary Mixture. *Anal. Bioanal. Chem.* **2017**, *409*, 5569–5579.

(231) Kang, J.; Gu, H.; Zhong, L.; Hu, Y.; Liu, F. The pH Dependent Raman Spectroscopic Study of Caffeine. *Spectrochim. Acta A* **2011**, *78*, 757–762.

(232) Pavel, I.; Szeghalmi, A.; Moigno, D.; Cinta, S.; Kiefer, W. Theoretical and pH Dependent Surface Enhanced Raman Spectroscopy Study on Caffeine. *Biopolymers* **2003**, *72*, 25–37.

(233) Hu, R.; Tang, R.; Xu, J.; Lu, F. Chemical Nanosensors Based on Molecularly-Imprinted Polymers Doped with Silver Nanoparticles for the Rapid Detection of Caffeine in Wastewater. *Anal. Chim. Acta* **2018**, *1034*, 176–183.

(234) Kurokawa, Y.; Imai, Y.; Tamai, Y. Surface-Enhanced Raman Scattering

Observations on Bipyridine, Phthalimide, Phenylethylamine and Theobromine by Using a Fine Silver Particle-Doped Cellulose Gel Film. *Analyst* **1997**, *122*, 941–944.

(235) Lee, W. W. Y.; Silverson, V. A. D.; McCoy, C. P.; Donnelly, R. F.; Bell, S. E. J. Preaggregated Ag Nanoparticles in Dry Swellable Gel Films for Off-the-Shelf Surface-Enhanced Raman Spectroscopy. *Anal. Chem.* **2014**, *86*, 8106–8113.

(236) Chen, X.; Gu, H.; Shen, G.; Dong, X.; Kang, J. Spectroscopic Study of Surface Enhanced Raman Scattering of Caffeine on Borohydride-Reduced Silver Colloids. *J. Mol. Struct.* **2010**, *975*, 63–68.

(237) Sato-Berru, R.; Redon, R.; Vazquez-Olmos, A.; Saniger, J. M. Silver Nanoparticles Synthesized by Direct Photoreduction of Metal Salts. Application in Surface-Enhanced Raman Spectroscopy. *J. Raman Spectrosc.* **2009**, *40*, 376–380.

(238) Li, Y.-T.; Yang, Y.-Y.; Sun, Y.-X.; Cao, Y.; Huang, Y.-S.; Han, S. Electrochemical Fabrication of Reduced MoS_2-Based Portable Molecular Imprinting Nanoprobe for Selective SERS Determination of Theophylline. *Microchim. Acta* **2020**, *187*, 203.

(239) Hughes, J.; Izake, E. L.; Lott, W. B.; Ayoko, G. A.; Sillence, M. Ultra Sensitive Label Free Surface Enhanced Raman Spectroscopy Method for the Detection of Biomolecules. *Talanta* **2014**, *130*, 20–25.

(240) Ameku, W. A.; de Araujo, W. R.; Rangel, C. J.; Ando, R. A.; Paixao, T. R. L. C. Gold Nanoparticle Paper-Based Dual-Detection Device for Forensics Applications. *ACS Appl. Nano Mater.* **2019**, *2*, 5460–5468.

(241) Velicka, M.; Adomaviciute, S.; Zacharovas, E.; Sablinskas, V. Application of Label-Free SERS and EC-SERS for Detection of Traces of Drugs in Biological Fluids. *Proc. SPIE* **2020**, *11257*, 112570S.

(242) Wu, J.; Isaacs, L. Cucurbit[7]uril Complexation Drives Thermal *trans-cis*-Azobenzene Isomerization and Enables Colorimetric Amine Detection. *Chem. – Eur. J.* **2009**, *15*, 11675–11680.

(243) Edwards, H. G. M.; Munshi, T.; Anstis, M. Raman Spectroscopic Characterisations and Analytical Discrimination between Caffeine and Demethylated Analogues of Pharmaceutical Relevance. *Spectrochim. Acta A* **2005**, *61*, 1453–1459.

(244) Gunasekaran, S.; Sankari, G.; Ponnusamy, S. Vibrational Spectral Investigation on Xanthine and Its Derivatives – Theophylline, Caffeine and Theobromine. *Spectrochim. Acta A* **2005**, *61*, 117–127.

(245) Heise, H. M.; Voigt, G.; Lampen, P.; Kupper, L.; Rudloff, S.; Werner, G. Multivariate Calibration for the Determination of Analytes in Urine Using Mid-Infrared Attenuated Total Reflection Spectroscopy. *Appl. Spectrosc.* **2001**, *55*, 434–443.

(246) Saatkamp, C. J.; de Almeida, M. L.; Bispo, J. A. M.; Pinheiro, A. L. B.; Fernandes, A. B.; Silveira, L. Quantifying Creatinine and Urea in Human Urine through Raman Spectroscopy Aiming at Diagnosis of Kidney Disease. *J. Biomed. Opt.* **2016**, *21*, 37001.

(247) Bell, T. W.; Hou, Z.; Luo, Y.; Drew, M. G.; Chapoteau, E.; Czech, B. P.; Kumar, A. Detection of Creatinine by a Designed Receptor. *Science* **1995**, *269*, 671−674.

(248) Wang, T.-L.; Chiang, H. K.; Lu, H.-H.; Peng F.-Y. Semi-Quantitative Surface Enhanced Raman Scattering Spectroscopic Creatinine Measurement in Human Urine Samples. *Opt. Quant. Electron.* **2005**, *37*, 1415−1422.

(249) McMurdy, J. W.; Berger, A. J. Raman Spectroscopy-Based Creatinine Measurement in Urine Samples from a Multipatient Population. *Appl. Spectrosc.*

2003, *57*, 522−525.

(250) Lad, U.; Khokhar, S.; Kale, G. M. Electrochemical Creatinine Biosensors. *Anal. Chem.* **2008**, *80*, 7910−7917.

(251) Yan, S.-L.; Lin, P.-Z.; Hsiao, M.-W. Separation of Urea, Uric Acid, Creatine, and Creatinine by Micellar Electrokinetic Capillary Chromatography with Sodium Cholate. *J. Chromatogr. Sci.* **1999**, *37*, 45−50.

(252) Premasiri, W. R.; Clarke, R. H.; Womble, M. E. Urine Analysis by Laser Raman Spectroscopy. *Lasers Surg. Med*. **2001**, *28*, 330−334.

(253) Chen, J.-C.; Kumar, A. S.; Chung, H.-H.; Chien, S.-H.; Kuo, M.-C.; Zen, J.-M. An Enzymeless Electrochemical Sensor for the Selective Determination of Creatinine in Human Urine. *Sens. Actuators, B* **2006**, *115*, 473−480.

(254) Bonsnes, R. W.; Taussky, H. H. On the Colorimetric Determination of Creatinine by the Jaffe Reaction. *J. Biol. Chem.* **1945**, *158*, 581−591.

(255) Du, H.; Chen. R.; Du, J.; Fan, J.; Peng, X. Gold Nanoparticle-Based Colorimetric Recognition of Creatinine with Good Selectivity and Sensitivity. *Ind. Eng. Chem. Res*. **2016**, *55*, 12334−12340.

(256) Weber, J. A.; van Zanten, A. P. Interferences in Current Methods for Measurements of Creatinine. *Clin. Chem*. **1991**, *37*, 695−700.

(257) Liotta, E.; Gottardo, R.; Bonizzato, L.; Pascali, J. P.; Bertaso, A.; Tagliaro, F. Rapid and Direct Determination of Creatinine in Urine Using Capillary Zone Electrophoresis. *Clin. Chem. Acta* **2009**, *409*, 52−55.

(258) Zuo, Y.; Wang, C.; Zhou, J.; Sachdeva, A.; Ruelos, V. C. Simultaneous Determination of Creatinine and Uric Acid in Human Urine by High-Performance Liquid Chromatography. *Anal. Sci*. **2008**, *24*, 1589−1592.

(259) Li, X.; Fang, X.; Yu, Z.; Sheng, G.; Wu, M.; Fu, J.; Chen, H. Direct Quantification

of Creatinine in Human Urine by Using Isotope Dilution Extractive Electrospray Ionization Tandem Mass Spectrometry. *Anal. Chim. Acta* **2012**, *748*, 53−57.

(260) Bonifacio, A.; Cervo, S.; Sergo, V. Label-Free Surface-Enhanced Raman Spectroscopy of Biofluids: Fundamental Aspects and Diagnostic Applications. *Anal. Bioanal. Chem.* **2015**, *407*, 8265−8277.

(261) Yu, B.; Ge, M.; Li, P.; Xie, Q.; Yang, L. Development of Surface-Enhanced Raman Spectroscopy Application for Determination of Illicit Drugs: Towards a Practical Sensor. *Talanta* **2019**, *191*, 1−10.

(262) Kong, K.; Kendall, C.; Stone, N.; Notingher, I. Raman Spectroscopy for Medical Diagnostics − From In-Vitro Biofluid Assays to In-Vivo Cancer Detection. *Adv. Drug Deliv. Rev.* **2015**, *89*, 121−134.

(263) Wang, Y.; Chen, J.; Wu, Y.; Chen, Y.; Pan, J.; Lei, J.; Chen, Y.; Sun, L.; Feng, S.; Chen, R. Surface-Enhanced Raman Spectroscopy of Creatinine in Silver Colloid. *Proc. SPIE*, **2011**, *8329*, 83290K.

(264) Wang, H.; Malvadkar, N.; Koytek, S.; Bylander, J.; Reeves, W. B.; Demirel, M. C. Quantitative Analysis of Creatinine in Urine by Metalized Nanostructured Parylene. *J. Biomed. Opt.* **2010**, *15*, 027004.

(265) Li, M.; Du, Y.; Zhao, F.; Zeng, J.; Mohan, C.; Shih, W.-C. Reagent- and Separation-Free Measurements of Urine Creatinine Concentration Using Stamping Surface Enhanced Raman Scattering (S-SERS). *Biomed. Opt. Express* **2015**, *6*, 849−858.

(266) Zhang, H.; Li, G.; Li, S.; Xu, L.; Tian, Y.; Jiao, A.; Liu, X.; Chen, F.; Chen, M. Boron Nitride/Gold Nanocomposites for Crystal Violet and Creatinine Detection by Surface-Enhanced Raman Spectroscopy. *Appl. Surf. Sci.* **2018**, *457*, 684–694.

(267) Lu, Y.; Wu, C.; You, R.; Wu, Y.; Shen, H.; Zhu, L.; Feng, S. Superhydrophobic

Silver Film as a SERS Substrate for the Detection of Uric Acid and Creatinine. *Biomed. Opt. Express* **2018**, *9*, 4988−4997.

(268) Chamuah, N.; Saikia, A.; Joseph, A. M.; Nath, P. Blu-ray DVD as SERS Substrate for Reliable Detection of Albumin, Creatinine and Urea in Urine. *Sens. Actuators, B* **2019**, *285*, 108−115.

(269) Chio, W.-I. K.; Moorthy, S.; Perumal, J.; Dinish, U. S.; Parkin, I. P.; Olivo, M.; Lee, T.-C. Dual-Triggered Nanoaggregates of Cucurbit[7]uril and Gold Nanoparticles for Multi-Spectroscopic Quantification of Creatinine in Urinalysis. *J. Mater. Chem. C.* **2020**, *8*, 7051−7058.

(270) Eisner, C.; Faulhaber-Walter, R.; Wang, Y.; Leelahavanichkul, A.; Yuen, P. S. T.; Mizel, D.; Star, R. A.; Briggs, J. P.; Levine, M.; Schnermann, J. Major Contribution of Tubular Secretion to Creatinine Clearance in Mice. *Kidney Int.* **2010**, *77*, 519−526.

(271) Valadbeigi, Y.; Ilbeigi, V.; Tabrizchi, M. Effect of Mono- and Di-hydration on the Stability and Tautomerisms of Different Tautomers of Creatinine: A Thermodynamic and Mechanistic Study. *Comput. Theor. Chem.* **2015**, *1061*, 27−35.

(272) Chio, W.-I. K.; Davison, G.; Jones, T.; Liu, J.; Parkin, I. P.; Lee, T.-C. Quantitative SERS Detection of Uric Acid via Formation of Precise Plasmonic Nanojunctions within Aggregates of Gold Nanoparticles and Cucurbit[*n*]uril. *J. Vis. Exp.* **2020**. (Accepted)

Appendix

A.1 Synthesis of Au NPs

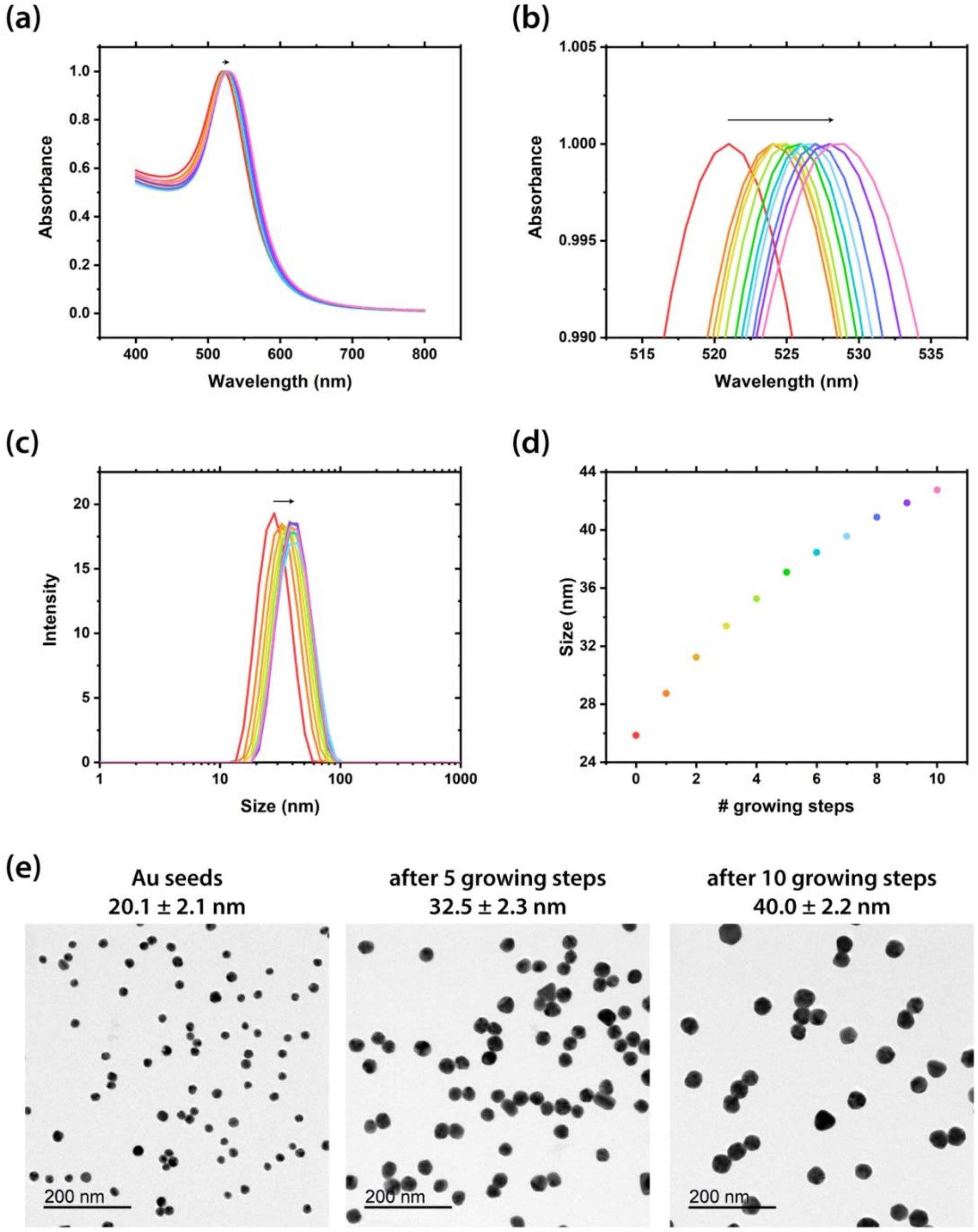

Figure A.1. (a) UV-Vis spectra of Au NPs and (b) zoom-in spectra showing the shifting of the LSPR peaks. (c) Hydrodynamic size of Au NPs determined by dynamic light scattering and (d) corresponding plot of particle size as a function of number of growing steps. (e) TEM images showing the size of Au seeds and Au NPs after 5 and 10 growing steps.

A.2 Coordinates of the CB7-DNT inclusion complex

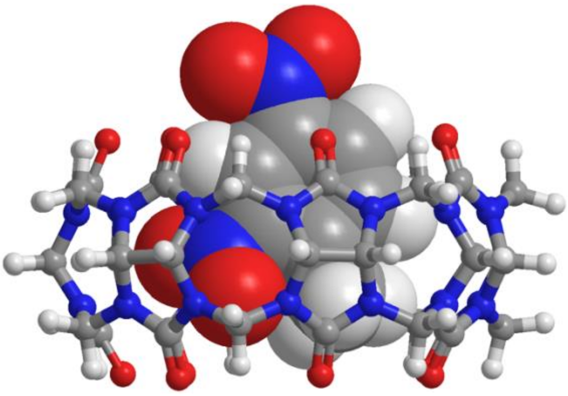

Table A.1. Coordinates of the CB7-DNT inclusion complex in water. The geometry was optimised at the CPCM/wB97X-D/6-311+G** level of theory. Energy = −4892.9663 hartree.

Atom (Centre Nr.)	**Coordinates (Å)**		
	X	**Y**	**Z**
N(1)	1.449	3.012	-3.809
C(2)	1.114	4.346	-3.371
C(3)	-0.432	4.377	-3.45
N(4)	-0.771	3.034	-3.862
C(5)	0.338	2.265	-4.114
N(6)	1.381	4.615	-1.977
C(7)	0.237	4.888	-1.265
N(8)	-0.835	4.721	-2.107
O(9)	0.338	1.13	-4.558
O(10)	0.186	5.24	-0.099
N(11)	-3.038	2.408	-3.315
C(12)	-3.803	3.446	-2.657
C(13)	-4.929	2.658	-1.942
N(14)	-4.725	1.302	-2.386
C(15)	-3.634	1.174	-3.206
N(16)	-3.126	4.12	-1.577
C(17)	-3.668	3.825	-0.349
N(18)	-4.665	2.9	-0.54
O(19)	-3.27	0.157	-3.769

O(20)	-3.344	4.328	0.713
N(21)	5.509	-0.966	-0.523
C(22)	5.913	-0.592	0.811
C(23)	5.426	-1.78	1.681
N(24)	4.684	-2.594	0.741
C(25)	4.829	-2.158	-0.552
N(26)	5.213	0.54	1.378
C(27)	4.53	0.211	2.524
N(28)	4.636	-1.144	2.705
O(29)	4.441	-2.739	-1.552
O(30)	3.958	0.992	3.264
N(31)	-1.596	-4.311	2.123
C(32)	-2.195	-4.026	3.412
C(33)	-3.581	-3.446	3.039
N(34)	-3.659	-3.656	1.617
C(35)	-2.497	-4.165	1.093
N(36)	-1.573	-2.957	4.149
C(37)	-2.334	-1.815	4.167
N(38)	-3.484	-2.061	3.453
O(39)	-2.302	-4.466	-0.071
O(40)	-2.053	-0.777	4.74
N(41)	-5.546	-0.445	-0.927
C(42)	-6.109	0.018	0.321
C(43)	-5.819	-1.159	1.295
N(44)	-5.145	-2.127	0.46
C(45)	-5.013	-1.704	-0.837
N(46)	-5.435	1.136	0.939
C(47)	-4.796	0.791	2.101
N(48)	-5	-0.548	2.316
O(49)	-4.546	-2.353	-1.758
O(50)	-4.193	1.55	2.842
C(51)	4.19	-3.911	1.061
C(52)	-2.167	5.174	-1.781
C(53)	4.191	-1.81	3.902
C(54)	-2.08	2.691	-4.353
N(55)	3.611	2.203	-3.092
C(56)	4.326	3.139	-2.253
C(57)	5.279	2.227	-1.438
N(58)	5.041	0.911	-1.986
C(59)	4.111	0.927	-2.997
N(60)	3.534	3.793	-1.239
C(61)	3.876	3.398	0.03
N(62)	4.837	2.426	-0.077
O(63)	3.799	-0.018	-3.699
O(64)	3.423	3.85	1.067
C(65)	2.781	2.623	-4.193

C(66)	2.7	4.94	-1.495
C(67)	5.549	1.906	1.059
C(68)	5.879	-0.231	-1.707
C(69)	-5.687	0.249	-2.178
C(70)	-5.579	2.503	0.503
C(71)	-4.872	-3.484	0.859
C(72)	-4.643	-1.204	3.546
N(73)	0.846	-3.096	4.204
C(74)	1.377	-4.242	3.503
C(75)	2.844	-3.84	3.208
N(76)	2.94	-2.51	3.761
C(77)	1.783	-2.108	4.381
N(78)	0.82	-4.464	2.188
C(79)	1.754	-4.321	1.19
N(80)	2.933	-3.914	1.768
O(81)	1.622	-1.073	5.004
O(82)	1.577	-4.544	0.006
C(83)	-0.388	-3.135	4.948
C(84)	-0.43	-5.152	1.988
H(85)	1.607	5.089	-4.004
H(86)	-0.827	5.106	-4.164
H(87)	-4.166	4.171	-3.39
H(88)	-5.938	2.993	-2.2
H(89)	6.993	-0.428	0.847
H(90)	6.235	-2.362	2.131
H(91)	-2.241	-4.934	4.021
H(92)	-4.419	-3.936	3.543
H(93)	-7.172	0.24	0.196
H(94)	-6.715	-1.6	1.739
H(95)	4.933	-4.429	1.676
H(96)	4.056	-4.451	0.125
H(97)	-2.108	5.755	-0.861
H(98)	-2.52	5.816	-2.593
H(99)	4.068	-1.06	4.683
H(100)	4.962	-2.524	4.204
H(101)	-1.985	1.801	-4.973
H(102)	-2.454	3.52	-4.962
H(103)	4.842	3.882	-2.868
H(104)	6.337	2.49	-1.535
H(105)	2.706	1.79	-4.89
H(106)	3.258	3.473	-4.693
H(107)	2.591	5.491	-0.562
H(108)	3.198	5.574	-2.235
H(109)	5.304	2.525	1.921
H(110)	6.624	1.966	0.863
H(111)	5.816	-0.91	-2.557

H(112)	6.911	0.113	-1.595
H(113)	-5.569	-0.48	-2.978
H(114)	-6.689	0.684	-2.228
H(115)	-5.404	3.151	1.36
H(116)	-6.604	2.642	0.146
H(117)	-4.795	-4.089	-0.043
H(118)	-5.708	-3.844	1.467
H(119)	-5.496	-1.804	3.879
H(120)	-4.432	-0.435	4.288
H(121)	1.279	-5.143	4.116
H(122)	3.587	-4.497	3.668
H(123)	-0.356	-2.337	5.688
H(124)	-0.46	-4.101	5.458
H(125)	-0.498	-5.97	2.714
H(126)	-0.431	-5.563	0.979
C(127)	1.801	-0.544	-1.022
C(128)	1.508	-1.589	-1.879
C(129)	0.178	-1.896	-2.124
C(130)	-0.856	-1.204	-1.523
C(131)	-0.514	-0.155	-0.688
C(132)	0.806	0.221	-0.412
C(133)	1.204	1.346	0.495
N(134)	-1.634	0.549	-0.061
O(135)	-1.554	1.754	0.071
O(136)	-2.589	-0.119	0.289
N(137)	-0.147	-2.992	-3.04
O(138)	-1.317	-3.174	-3.324
O(139)	0.769	-3.666	-3.473
H(140)	2.835	-0.301	-0.809
H(141)	2.305	-2.156	-2.338
H(142)	-1.893	-1.462	-1.699
H(143)	0.588	1.39	1.395
H(144)	2.247	1.223	0.786
H(145)	1.098	2.303	-0.022

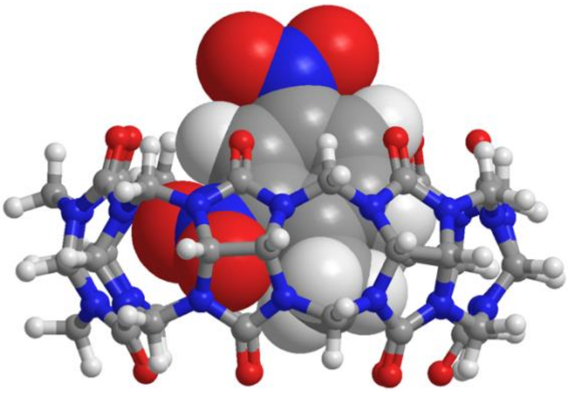

Table A.2. Coordinates of the CB7-DNT inclusion complex in gas phase. The geometry was optimised at the wB97X-D/6-311+G** level of theory. Energy = −4892.7629 hartree.

Atom (Centre Nr.)	**Coordinates (Å)**		
	X	**Y**	**Z**
N(1)	1.101	2.858	-3.642
C(2)	0.984	4.275	-3.395
C(3)	-0.549	4.533	-3.483
N(4)	-1.06	3.288	-3.977
C(5)	-0.104	2.295	-4.039
N(6)	1.321	4.711	-2.072
C(7)	0.212	5.105	-1.335
N(8)	-0.897	4.902	-2.134
O(9)	-0.269	1.166	-4.422
O(10)	0.233	5.59	-0.234
N(11)	-3.354	2.784	-3.378
C(12)	-3.995	3.792	-2.569
C(13)	-5.064	2.977	-1.78
N(14)	-5.059	1.702	-2.444
C(15)	-4.043	1.584	-3.375
N(16)	-3.205	4.393	-1.536
C(17)	-3.527	3.925	-0.274
N(18)	-4.572	3.029	-0.426
O(19)	-3.836	0.642	-4.094
O(20)	-3.042	4.288	0.765
N(21)	5.358	-1.019	-0.315
C(22)	5.868	-0.532	0.946
C(23)	5.478	-1.665	1.943
N(24)	5.004	-2.715	1.084
C(25)	4.953	-2.341	-0.246
N(26)	5.225	0.627	1.493
C(27)	4.43	0.337	2.587

N(28)	4.5	-1.032	2.794
O(29)	4.646	-3.042	-1.175
O(30)	3.828	1.132	3.259
N(31)	-1.279	-4.292	1.983
C(32)	-2.023	-4.11	3.201
C(33)	-3.354	-3.462	2.719
N(34)	-3.21	-3.414	1.29
C(35)	-2.012	-3.952	0.857
N(36)	-1.501	-3.15	4.133
C(37)	-2.345	-2.064	4.316
N(38)	-3.378	-2.196	3.405
O(39)	-1.683	-4.139	-0.286
O(40)	-2.224	-1.202	5.145
N(41)	-5.582	-0.188	-0.99
C(42)	-5.935	0.135	0.36
C(43)	-5.53	-1.139	1.151
N(44)	-4.715	-1.861	0.201
C(45)	-4.846	-1.355	-1.085
N(46)	-5.171	1.172	1.013
C(47)	-4.631	0.75	2.214
N(48)	-4.856	-0.616	2.302
O(49)	-4.449	-1.872	-2.095
O(50)	-4.116	1.438	3.056
C(51)	4.607	-4.028	1.521
C(52)	-2.195	5.391	-1.744
C(53)	4.034	-1.605	4.031
C(54)	-2.41	3.077	-4.419
N(55)	3.208	1.923	-2.906
C(56)	4.047	2.921	-2.279
C(57)	5.041	2.07	-1.44
N(58)	4.796	0.732	-1.891
C(59)	3.751	0.652	-2.795
N(60)	3.422	3.767	-1.304
C(61)	3.818	3.476	-0.011
N(62)	4.665	2.378	-0.083
O(63)	3.412	-0.33	-3.401
O(64)	3.521	4.084	0.983
C(65)	2.34	2.236	-4.014
C(66)	2.661	4.949	-1.621
C(67)	5.447	1.979	1.057
C(68)	5.63	-0.396	-1.585
C(69)	-5.927	0.598	-2.144
C(70)	-5.318	2.571	0.713
C(71)	-4.317	-3.228	0.389
C(72)	-4.554	-1.366	3.487
N(73)	0.907	-3.318	4.408

C(74)	1.536	-4.357	3.645
C(75)	3.001	-3.858	3.498
N(76)	2.9	-2.472	3.888
C(77)	1.705	-2.195	4.538
N(78)	1.113	-4.502	2.269
C(79)	2.186	-4.493	1.394
N(80)	3.304	-4.118	2.121
O(81)	1.436	-1.192	5.143
O(82)	2.168	-4.799	0.231
C(83)	-0.395	-3.406	5.014
C(84)	-0.122	-5.137	1.886
H(85)	1.563	4.838	-4.14
H(86)	-0.816	5.344	-4.175
H(87)	-4.429	4.57	-3.212
H(88)	-6.07	3.416	-1.831
H(89)	6.952	-0.367	0.876
H(90)	6.325	-2.025	2.544
H(91)	-2.166	-5.08	3.7
H(92)	-4.245	-4.051	2.985
H(93)	-7.008	0.364	0.42
H(94)	-6.388	-1.753	1.461
H(95)	5.346	-4.402	2.239
H(96)	4.602	-4.664	0.634
H(97)	-2.056	5.917	-0.797
H(98)	-2.559	6.093	-2.506
H(99)	3.727	-0.782	4.679
H(100)	4.863	-2.156	4.501
H(101)	-2.408	2.216	-5.091
H(102)	-2.732	3.973	-4.968
H(103)	4.54	3.533	-3.047
H(104)	6.094	2.336	-1.611
H(105)	2.1	1.292	-4.508
H(106)	2.877	2.893	-4.718
H(107)	2.594	5.543	-0.707
H(108)	3.203	5.515	-2.392
H(109)	5.169	2.641	1.879
H(110)	6.516	2.099	0.831
H(111)	5.454	-1.153	-2.352
H(112)	6.68	-0.075	-1.616
H(113)	-5.895	-0.069	-3.007
H(114)	-6.946	0.978	-2.009
H(115)	-4.956	3.123	1.583
H(116)	-6.384	2.792	0.552
H(117)	-4.014	-3.609	-0.589
H(118)	-5.171	-3.813	0.763
H(119)	-5.423	-1.994	3.732

H(120)	-4.379	-0.652	4.294
H(121)	1.451	-5.317	4.172
H(122)	3.712	-4.388	4.147
H(123)	-0.44	-2.653	5.803
H(124)	-0.503	-4.407	5.451
H(125)	-0.281	-6.029	2.511
H(126)	-0.017	-5.436	0.841
C(127)	1.671	-1.093	-0.764
C(128)	1.335	-2.23	-1.483
C(129)	0.072	-2.308	-2.043
C(130)	-0.861	-1.3	-1.891
C(131)	-0.469	-0.174	-1.188
C(132)	0.799	-0.016	-0.613
C(133)	1.243	1.206	0.142
N(134)	-1.469	0.889	-1.066
O(135)	-1.094	2.044	-1.132
O(136)	-2.63	0.56	-0.913
N(137)	-0.295	-3.496	-2.834
O(138)	-1.378	-3.495	-3.378
O(139)	0.518	-4.396	-2.901
H(140)	2.657	-1.018	-0.319
H(141)	2.039	-3.042	-1.606
H(142)	-1.853	-1.387	-2.319
H(143)	0.506	1.538	0.874
H(144)	2.177	0.999	0.667
H(145)	1.401	2.037	-0.548

A.3 Binding energy of the CB7-DNT inclusion complex

Table A.3. Binding energies, in kcal mol^{-1}, of the CB7-DNT inclusion complex, optimised at various levels of theory.

Method	**Water model**	**Energy / kcal mol^{-1}**
wB97X-D/6-311+G**	-	−36.9
wB97X-D/6-31G*	-	−38.9
MMFF94	-	−34.7
wB97X-D/6-311+G**	CPCM[a]	−26.9
wB97X-D/6-31G*	CPCM[a]	−30.3

[a] Calculation was performed in the presence of solvent with the dielectric constant of water (78) using the CPCM model in Spartan'16.

A.4 Coordinates of the [CB7-CAF-H]$^+$ inclusion complex

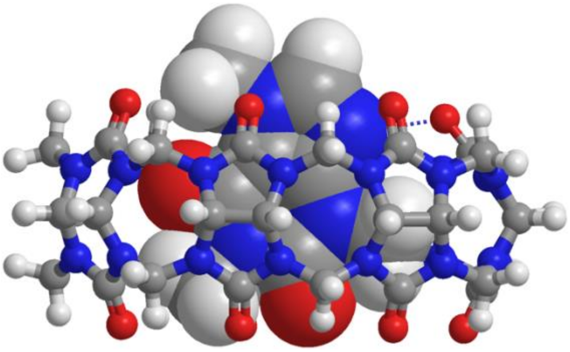

Table A.4. Coordinates of the [CB7-CAF-H]$^+$ inclusion complex in gas phase. The geometry was optimised at the wB97X-D/6-31G* level of theory. Energy = −4891.8067 hartree.

Atom (Centre Nr.)	**Coordinates (Å)**		
	X	**Y**	**Z**
N(1)	2.273	2.622	-4.201
C(2)	1.862	3.947	-3.815
C(3)	0.317	3.822	-3.659
N(4)	0.040	2.474	-4.073
C(5)	1.182	1.795	-4.475
N(6)	2.282	4.388	-2.513
C(7)	1.252	4.446	-1.593
N(8)	0.093	4.097	-2.257
O(9)	1.227	0.709	-4.995
O(10)	1.344	4.780	-0.431
N(11)	-2.219	1.854	-3.436
C(12)	-2.859	2.961	-2.777
C(13)	-4.146	2.337	-2.160
N(14)	-4.069	0.959	-2.555
C(15)	-2.970	0.686	-3.353
N(16)	-2.155	3.479	-1.633
C(17)	-2.838	3.271	-0.444
N(18)	-4.001	2.601	-0.752
O(19)	-2.727	-0.359	-3.909
O(20)	-2.486	3.654	0.652
N(21)	5.370	-1.396	-0.830
C(22)	5.705	-1.066	0.523
C(23)	4.759	-1.978	1.363
N(24)	3.898	-2.583	0.373
C(25)	4.335	-2.317	-0.924
N(26)	5.347	0.262	0.961

C(27)	4.468	0.258	2.031
N(28)	4.119	-1.053	2.263
O(29)	3.920	-2.818	-1.939
O(30)	4.099	1.226	2.662
N(31)	-2.379	-4.424	2.335
C(32)	-2.912	-3.888	3.558
C(33)	-4.347	-3.415	3.157
N(34)	-4.397	-3.694	1.745
C(35)	-3.273	-4.349	1.279
N(36)	-2.297	-2.681	4.050
C(37)	-3.171	-1.613	4.105
N(38)	-4.365	-2.034	3.562
O(39)	-3.115	-4.814	0.175
O(40)	-2.948	-0.537	4.615
N(41)	-5.385	-0.520	-1.154
C(42)	-6.063	0.130	-0.064
C(43)	-6.234	-1.012	0.992
N(44)	-5.616	-2.142	0.351
C(45)	-5.165	-1.867	-0.926
N(46)	-5.314	1.129	0.653
C(47)	-5.070	0.785	1.969
N(48)	-5.589	-0.477	2.163
O(49)	-4.711	-2.661	-1.716
O(50)	-4.569	1.500	2.809
C(51)	3.186	-3.815	0.626
C(52)	-1.181	4.525	-1.740
C(53)	3.441	-1.432	3.472
C(54)	-1.264	2.031	-4.500
N(55)	4.560	1.883	-3.797
C(56)	5.245	2.723	-2.853
C(57)	6.035	1.700	-1.963
N(58)	5.562	0.424	-2.434
C(59)	4.731	0.530	-3.540
N(60)	4.405	3.407	-1.891
C(61)	4.594	2.957	-0.611
N(62)	5.636	2.067	-0.623
O(63)	4.268	-0.383	-4.178
O(64)	3.964	3.311	0.374
C(65)	3.576	2.324	-4.752
C(66)	3.645	4.609	-2.143
C(67)	6.078	1.440	0.596
C(68)	6.033	-0.868	-1.993
C(69)	-5.181	0.047	-2.456
C(70)	-5.080	2.463	0.192
C(71)	-5.535	-3.469	0.897
C(72)	-5.484	-1.140	3.434

N(73)	0.115	-2.654	3.878
C(74)	0.670	-3.885	3.370
C(75)	2.078	-3.459	2.862
N(76)	2.181	-2.085	3.270
C(77)	1.017	-1.609	3.853
N(78)	0.044	-4.423	2.200
C(79)	0.833	-4.323	1.068
N(80)	2.006	-3.668	1.437
O(81)	0.847	-0.491	4.294
O(82)	0.576	-4.759	-0.029
C(83)	-1.043	-2.628	4.736
C(84)	-1.173	-5.194	2.224
H(85)	2.169	4.679	-4.575
H(86)	-0.243	4.539	-4.278
H(87)	-3.067	3.770	-3.494
H(88)	-5.077	2.788	-2.531
H(89)	6.772	-1.248	0.711
H(90)	5.295	-2.752	1.932
H(91)	-2.910	-4.659	4.342
H(92)	-5.146	-3.962	3.675
H(93)	-7.019	0.550	-0.409
H(94)	-7.285	-1.240	1.220
H(95)	3.872	-4.534	1.105
H(96)	2.866	-4.208	-0.343
H(97)	-1.009	4.920	-0.737
H(98)	-1.579	5.324	-2.388
H(99)	3.254	-0.516	4.036
H(100)	4.099	-2.096	4.055
H(101)	-1.133	1.060	-4.985
H(102)	-1.665	2.756	-5.228
H(103)	5.890	3.444	-3.369
H(104)	7.124	1.777	-2.065
H(105)	3.449	1.506	-5.466
H(106)	3.958	3.212	-5.270
H(107)	3.634	5.200	-1.226
H(108)	4.149	5.172	-2.938
H(109)	5.949	2.165	1.402
H(110)	7.142	1.196	0.487
H(111)	5.846	-1.568	-2.811
H(112)	7.110	-0.810	-1.791
H(113)	-4.979	-0.782	-3.138
H(114)	-6.095	0.573	-2.768
H(115)	-4.826	3.064	1.068
H(116)	-5.997	2.855	-0.272
H(117)	-5.448	-4.160	0.054
H(118)	-6.453	-3.683	1.459

H(119)	-6.408	-1.698	3.623
H(120)	-5.360	-0.363	4.191
H(121)	0.699	-4.640	4.169
H(122)	2.897	-4.048	3.300
H(123)	-1.021	-1.687	5.291
H(124)	-0.974	-3.473	5.439
H(125)	-1.119	-5.904	3.062
H(126)	-1.228	-5.739	1.279
C(127)	-1.291	-0.253	0.815
N(128)	-0.849	-0.983	-0.295
C(129)	0.334	-0.794	-1.020
N(130)	1.178	0.250	-0.593
C(131)	0.813	0.983	0.484
C(132)	-0.343	0.778	1.186
N(133)	1.475	2.024	1.070
C(134)	0.728	2.441	2.111
N(135)	-0.367	1.714	2.203
O(136)	-2.347	-0.476	1.380
O(137)	0.624	-1.483	-1.965
C(138)	-1.419	1.852	3.213
C(139)	2.404	0.515	-1.324
C(140)	-1.704	-2.068	-0.795
H(141)	2.377	2.446	0.809
H(142)	0.999	3.254	2.764
H(143)	-2.371	2.033	2.717
H(144)	-1.474	0.933	3.796
H(145)	-1.156	2.696	3.851
H(146)	2.472	-0.222	-2.126
H(147)	2.380	1.520	-1.756
H(148)	3.268	0.416	-0.659
H(149)	-2.560	-2.131	-0.131
H(150)	-2.035	-1.847	-1.811
H(151)	-1.154	-3.009	-0.792

A.5 Coordinates of the [CB7-TBR-H]$^+$ inclusion complex

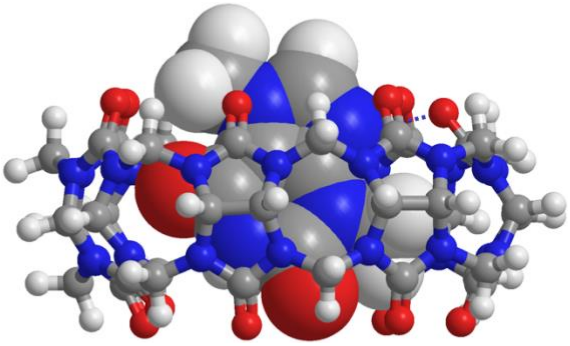

Table A.5. Coordinates of the [CB7-TBR-H]$^+$ inclusion complex in gas phase. The geometry was optimised at the wB97X-D/6-31G* level of theory. Energy = −4852.5047 hartree.

Atom (Centre Nr.)	**Coordinates (Å)**		
	X	**Y**	**Z**
N(1)	1.894	2.815	-4.508
C(2)	1.709	4.228	-4.291
C(3)	0.150	4.365	-4.211
N(4)	-0.314	3.031	-4.470
C(5)	0.714	2.112	-4.503
N(6)	2.153	4.747	-3.023
C(7)	1.111	5.048	-2.167
N(8)	-0.062	4.846	-2.868
O(9)	0.582	0.906	-4.577
O(10)	1.203	5.492	-1.043
N(11)	-2.524	2.322	-3.807
C(12)	-3.048	3.276	-2.881
C(13)	-3.972	2.405	-1.980
N(14)	-3.855	1.078	-2.524
C(15)	-3.051	1.050	-3.660
N(16)	-2.102	3.858	-1.957
C(17)	-2.358	3.489	-0.652
N(18)	-3.409	2.584	-0.665
O(19)	-2.884	0.115	-4.401
O(20)	-1.796	3.902	0.342
N(21)	5.136	-1.363	-0.800
C(22)	5.395	-0.894	0.527
C(23)	4.691	-1.954	1.426
N(24)	3.969	-2.773	0.483
C(25)	4.325	-2.485	-0.834
N(26)	4.753	0.344	0.909

C(27)	3.888	0.187	1.972
N(28)	3.876	-1.156	2.299
O(29)	4.023	-3.128	-1.809
O(30)	3.282	1.068	2.552
N(31)	-2.201	-4.883	2.381
C(32)	-2.744	-4.456	3.645
C(33)	-4.087	-3.760	3.231
N(34)	-4.208	-4.071	1.832
C(35)	-3.072	-4.685	1.322
N(36)	-2.017	-3.396	4.300
C(37)	-2.598	-2.170	4.112
N(38)	-3.834	-2.370	3.549
O(39)	-2.888	-5.010	0.174
O(40)	-2.115	-1.091	4.416
N(41)	-4.836	-0.538	-1.008
C(42)	-5.331	0.129	0.160
C(43)	-5.583	-1.031	1.169
N(44)	-5.003	-2.177	0.512
C(45)	-4.731	-1.911	-0.836
N(46)	-4.377	0.976	0.850
C(47)	-4.185	0.583	2.160
N(48)	-4.924	-0.567	2.359
O(49)	-4.497	-2.730	-1.686
O(50)	-3.519	1.163	2.991
C(51)	3.480	-4.089	0.810
C(52)	-1.340	5.054	-2.261
C(53)	3.361	-1.628	3.547
C(54)	-1.642	2.668	-4.882
N(55)	3.930	1.792	-3.697
C(56)	4.803	2.687	-2.983
C(57)	5.491	1.734	-1.961
N(58)	5.161	0.427	-2.446
C(59)	4.203	0.458	-3.448
N(60)	4.174	3.677	-2.150
C(61)	4.220	3.345	-0.814
N(62)	4.879	2.132	-0.711
O(63)	3.744	-0.496	-4.028
O(64)	3.821	4.018	0.112
C(65)	3.141	2.180	-4.828
C(66)	3.526	4.879	-2.615
C(67)	5.293	1.638	0.568
C(68)	5.729	-0.810	-1.990
C(69)	-4.847	0.054	-2.321
C(70)	-4.189	2.366	0.517
C(71)	-5.217	-3.540	0.946
C(72)	-4.826	-1.321	3.570

N(73)	0.413	-3.433	4.357
C(74)	0.937	-4.464	3.508
C(75)	2.295	-3.872	3.039
N(76)	2.203	-2.481	3.438
C(77)	1.122	-2.248	4.268
N(78)	0.225	-4.690	2.270
C(79)	1.084	-4.601	1.167
N(80)	2.296	-4.113	1.628
O(81)	0.868	-1.210	4.841
O(82)	0.822	-4.927	0.037
C(83)	-0.815	-3.538	5.085
C(84)	-0.939	-5.550	2.197
H(85)	2.161	4.799	-5.112
H(86)	-0.270	5.065	-4.944
H(87)	-3.582	4.078	-3.412
H(88)	-5.023	2.734	-1.989
H(89)	6.478	-0.819	0.702
H(90)	5.392	-2.564	2.015
H(91)	-2.877	-5.303	4.328
H(92)	-4.960	-4.122	3.786
H(93)	-6.240	0.702	-0.076
H(94)	-6.648	-1.207	1.378
H(95)	4.268	-4.658	1.328
H(96)	3.237	-4.580	-0.136
H(97)	-1.152	5.574	-1.319
H(98)	-1.957	5.687	-2.914
H(99)	3.061	-0.758	4.136
H(100)	4.161	-2.170	4.076
H(101)	-1.581	1.786	-5.524
H(102)	-2.062	3.508	-5.451
H(103)	5.507	3.173	-3.674
H(104)	6.582	1.858	-1.908
H(105)	2.918	1.264	-5.381
H(106)	3.719	2.864	-5.466
H(107)	3.540	5.589	-1.786
H(108)	4.108	5.279	-3.454
H(109)	4.944	2.355	1.315
H(110)	6.391	1.574	0.606
H(111)	5.582	-1.548	-2.782
H(112)	6.802	-0.660	-1.815
H(113)	-4.636	-0.744	-3.038
H(114)	-5.849	0.472	-2.514
H(115)	-3.663	2.832	1.352
H(116)	-5.176	2.843	0.394
H(117)	-5.209	-4.165	0.049
H(118)	-6.192	-3.618	1.443

H(119)	-5.801	-1.771	3.791
H(120)	-4.555	-0.621	4.362
H(121)	1.038	-5.402	4.071
H(122)	3.166	-4.346	3.513
H(123)	-0.809	-2.740	5.830
H(124)	-0.852	-4.511	5.587
H(125)	-0.840	-6.350	2.945
H(126)	-0.960	-5.983	1.193
C(127)	0.344	1.466	-0.922
N(128)	-0.307	0.463	-1.634
C(129)	-1.036	-0.629	-1.160
N(130)	-1.098	-0.746	0.242
C(131)	-0.582	0.250	1.002
C(132)	0.095	1.330	0.502
N(133)	-0.616	0.377	2.363
C(134)	0.013	1.527	2.677
N(135)	0.445	2.119	1.583
O(136)	1.021	2.319	-1.466
O(137)	-1.560	-1.429	-1.891
C(138)	1.174	3.387	1.519
C(139)	-1.655	-1.948	0.834
H(140)	-0.151	0.451	-2.647
H(141)	-1.127	-0.188	3.055
H(142)	0.142	1.892	3.682
H(143)	0.746	4.002	0.728
H(144)	1.062	3.883	2.483
H(145)	2.224	3.190	1.313
H(146)	-2.619	-1.737	1.304
H(147)	-1.800	-2.675	0.034
H(148)	-0.955	-2.356	1.572

A.6 Coordinates of the [CB7-TPH-H]$^+$ inclusion complex

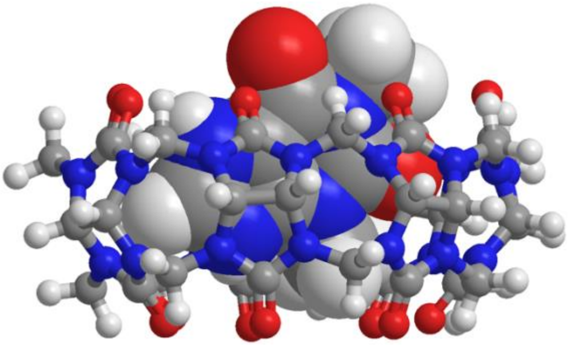

Table A.6. Coordinates of the [CB7-TPH-H]$^+$ inclusion complex in gas phase. The geometry was optimised at the wB97X-D/6-31G* level of theory. Energy = −4852.4856 hartree.

Atom (Centre Nr.)	Coordinates (Å)		
	X	Y	Z
N(1)	1.890	3.173	-4.253
C(2)	1.623	4.421	-3.578
C(3)	0.079	4.392	-3.387
N(4)	-0.337	3.311	-4.231
C(5)	0.724	2.595	-4.757
N(6)	2.113	4.520	-2.236
C(7)	1.128	4.302	-1.289
N(8)	-0.077	4.178	-1.960
O(9)	0.661	1.679	-5.538
O(10)	1.297	4.262	-0.089
N(11)	-2.573	2.572	-3.626
C(12)	-3.142	3.352	-2.569
C(13)	-4.325	2.478	-2.074
N(14)	-4.015	1.187	-2.642
C(15)	-3.063	1.273	-3.647
N(16)	-2.329	3.485	-1.375
C(17)	-3.053	3.143	-0.232
N(18)	-4.239	2.574	-0.646
O(19)	-2.748	0.404	-4.424
O(20)	-2.715	3.358	0.909
N(21)	4.909	-1.292	-1.085
C(22)	5.704	-1.125	0.114
C(23)	4.942	-2.015	1.141
N(24)	4.094	-2.821	0.312
C(25)	3.951	-2.284	-0.947
N(26)	5.654	0.180	0.708

C(27)	4.790	0.234	1.795
N(28)	4.247	-1.034	1.956
O(29)	3.139	-2.610	-1.791
O(30)	4.561	1.203	2.479
N(31)	-1.985	-4.821	2.400
C(32)	-2.639	-4.126	3.468
C(33)	-4.018	-3.754	2.855
N(34)	-3.756	-3.884	1.438
C(35)	-2.607	-4.607	1.179
N(36)	-2.109	-2.822	3.816
C(37)	-3.137	-1.891	3.956
N(38)	-4.261	-2.435	3.362
O(39)	-2.226	-5.008	0.104
O(40)	-3.068	-0.843	4.552
N(41)	-5.026	-0.581	-1.334
C(42)	-5.890	-0.190	-0.254
C(43)	-5.916	-1.451	0.671
N(44)	-4.951	-2.321	0.049
C(45)	-4.451	-1.822	-1.137
N(46)	-5.386	0.840	0.617
C(47)	-5.301	0.430	1.936
N(48)	-5.590	-0.921	1.968
O(49)	-3.696	-2.390	-1.895
O(50)	-5.095	1.144	2.892
C(51)	3.484	-4.064	0.705
C(52)	-1.306	4.490	-1.264
C(53)	3.609	-1.360	3.218
C(54)	-1.698	3.080	-4.643
N(55)	4.093	2.204	-3.897
C(56)	4.944	2.878	-2.955
C(57)	5.726	1.711	-2.272
N(58)	4.931	0.558	-2.641
C(59)	4.018	0.847	-3.657
N(60)	4.277	3.498	-1.824
C(61)	4.759	3.047	-0.617
N(62)	5.687	2.056	-0.873
O(63)	3.311	0.045	-4.216
O(64)	4.420	3.442	0.481
C(65)	3.171	2.839	-4.815
C(66)	3.487	4.708	-1.882
C(67)	6.338	1.346	0.208
C(68)	5.308	-0.809	-2.383
C(69)	-4.939	0.082	-2.603
C(70)	-5.304	2.229	0.266
C(71)	-4.746	-3.693	0.416
C(72)	-5.480	-1.681	3.186

N(73)	0.308	-2.704	3.687
C(74)	0.976	-3.964	3.446
C(75)	2.360	-3.528	2.889
N(76)	2.390	-2.109	3.103
C(77)	1.174	-1.627	3.578
N(78)	0.445	-4.785	2.399
C(79)	1.219	-4.775	1.256
N(80)	2.300	-3.928	1.505
O(81)	0.937	-0.477	3.872
O(82)	1.035	-5.405	0.243
C(83)	-0.875	-2.622	4.520
C(84)	-0.764	-5.564	2.498
H(85)	1.977	5.271	-4.177
H(86)	-0.415	5.328	-3.685
H(87)	-3.449	4.341	-2.939
H(88)	-5.309	2.829	-2.419
H(89)	6.742	-1.435	-0.060
H(90)	5.599	-2.647	1.754
H(91)	-2.710	-4.769	4.356
H(92)	-4.830	-4.430	3.157
H(93)	-6.880	0.086	-0.644
H(94)	-6.896	-1.946	0.705
H(95)	4.246	-4.646	1.245
H(96)	3.191	-4.603	-0.199
H(97)	-1.067	4.592	-0.203
H(98)	-1.690	5.452	-1.645
H(99)	3.377	-0.410	3.704
H(100)	4.314	-1.928	3.845
H(101)	-1.663	2.338	-5.444
H(102)	-2.114	4.022	-5.028
H(103)	5.589	3.602	-3.467
H(104)	6.761	1.608	-2.619
H(105)	2.985	2.135	-5.629
H(106)	3.660	3.739	-5.210
H(107)	3.517	5.147	-0.882
H(108)	3.940	5.400	-2.603
H(109)	6.422	2.046	1.042
H(110)	7.338	1.053	-0.128
H(111)	4.803	-1.424	-3.132
H(112)	6.397	-0.916	-2.484
H(113)	-4.588	-0.645	-3.339
H(114)	-5.945	0.433	-2.882
H(115)	-5.136	2.773	1.199
H(116)	-6.249	2.558	-0.187
H(117)	-4.393	-4.228	-0.469
H(118)	-5.706	-4.116	0.748

H(119)	-6.323	-2.379	3.250
H(120)	-5.537	-0.961	4.005
H(121)	1.041	-4.538	4.381
H(122)	3.207	-4.011	3.399
H(123)	-0.917	-1.618	4.950
H(124)	-0.774	-3.361	5.331
H(125)	-0.760	-6.105	3.451
H(126)	-0.742	-6.275	1.669
C(127)	0.151	1.780	2.068
N(128)	-1.077	1.116	2.204
C(129)	-1.518	0.017	1.479
N(130)	-0.612	-0.565	0.565
C(131)	0.558	0.072	0.340
C(132)	0.950	1.190	1.016
N(133)	1.541	-0.214	-0.575
C(134)	2.507	0.719	-0.449
N(135)	2.166	1.564	0.505
O(136)	0.482	2.725	2.744
O(137)	-2.625	-0.469	1.597
C(138)	-0.992	-1.765	-0.177
C(139)	-1.934	1.642	3.274
H(140)	1.598	-1.003	-1.218
H(141)	3.405	0.740	-1.044
H(142)	2.707	2.385	0.800
H(143)	-1.858	-2.193	0.321
H(144)	-1.272	-1.528	-1.207
H(145)	-0.173	-2.489	-0.160
H(146)	-1.947	2.726	3.190
H(147)	-2.935	1.242	3.165
H(148)	-1.512	1.340	4.233

A.7 Coordinates of the [CB8-CAF-H]$^+$ inclusion complex

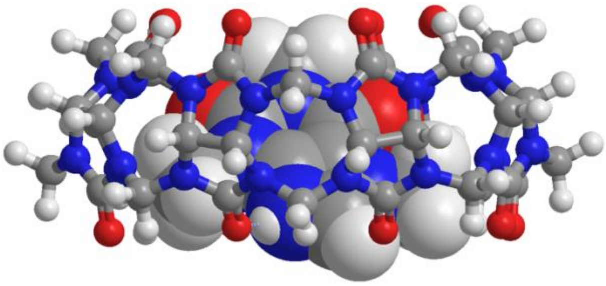

Table A.7. Coordinates of the [CB8-CAF-H]$^+$ inclusion complex in gas phase. The geometry was optimised at the wB97X-D/6-31G* level of theory. Energy = −5493.3988 hartree.

Atom (Centre Nr.)	**Coordinates (Å)**		
	X	**Y**	**Z**
N(1)	6.304	-0.903	-0.010
C(2)	6.669	-0.154	-1.189
C(3)	6.111	-1.041	-2.335
N(4)	5.890	-2.299	-1.699
C(5)	5.981	-2.220	-0.315
N(6)	5.992	1.099	-1.385
C(7)	4.939	0.991	-2.259
N(8)	4.922	-0.305	-2.746
O(9)	5.859	-3.133	0.462
O(10)	4.185	1.889	-2.590
N(11)	4.312	-3.714	-2.887
C(12)	3.796	-3.087	-4.058
C(13)	2.484	-3.868	-4.331
N(14)	2.240	-4.525	-3.069
C(15)	3.384	-4.548	-2.277
N(16)	3.318	-1.717	-3.902
C(17)	2.015	-1.589	-4.340
N(18)	1.550	-2.831	-4.678
O(19)	3.559	-5.206	-1.283
O(20)	1.394	-0.537	-4.453
N(21)	-1.944	2.867	4.780
C(22)	-2.409	4.071	4.131
C(23)	-3.680	3.569	3.400
N(24)	-3.990	2.347	4.076
C(25)	-2.926	1.895	4.845
N(26)	-1.598	4.574	3.062
C(27)	-2.025	4.125	1.831
N(28)	-3.214	3.434	2.030

O(29)	-2.892	0.871	5.487
O(30)	-1.496	4.347	0.760
N(31)	-5.662	-2.702	0.056
C(32)	-6.114	-2.572	-1.293
C(33)	-5.289	-3.649	-2.051
N(34)	-4.211	-3.920	-1.125
C(35)	-4.504	-3.454	0.156
N(36)	-5.743	-1.360	-1.996
C(37)	-5.134	-1.617	-3.204
N(38)	-4.930	-2.985	-3.271
O(39)	-3.906	-3.722	1.170
O(40)	-4.870	-0.812	-4.071
N(41)	-0.110	-5.109	-2.936
C(42)	-0.860	-4.867	-4.127
C(43)	-2.332	-4.924	-3.644
N(44)	-2.197	-4.734	-2.210
C(45)	-0.893	-5.001	-1.793
N(46)	-0.770	-3.521	-4.662
C(47)	-2.030	-2.998	-4.933
N(48)	-2.952	-3.862	-4.381
O(49)	-0.515	-5.155	-0.658
O(50)	-2.259	-1.990	-5.562
C(51)	-5.267	1.687	4.051
C(52)	4.222	-0.593	-3.970
C(53)	-4.132	3.290	0.931
C(54)	5.644	-3.542	-2.375
N(55)	6.049	0.493	1.955
C(56)	6.308	1.886	1.781
C(57)	5.455	2.544	2.896
N(58)	4.501	1.501	3.215
C(59)	4.935	0.261	2.749
N(60)	5.760	2.499	0.582
C(61)	5.051	3.654	0.880
N(62)	4.918	3.709	2.252
O(63)	4.465	-0.817	3.018
O(64)	4.654	4.475	0.080
C(65)	6.767	-0.571	1.316
C(66)	6.337	2.331	-0.725
C(67)	4.322	4.826	2.938
C(68)	3.674	1.546	4.397
C(69)	1.248	-5.565	-2.904
C(70)	0.346	-3.059	-5.436
C(71)	-3.288	-5.006	-1.296
C(72)	-4.369	-3.608	-4.432
N(73)	-5.835	0.569	-0.532
C(74)	-6.424	0.375	0.757

C(75)	-5.857	1.560	1.580
N(76)	-4.704	1.973	0.790
C(77)	-4.759	1.426	-0.493
N(78)	-5.961	-0.771	1.508
C(79)	-5.576	-0.423	2.791
N(80)	-5.574	0.965	2.848
O(81)	-4.023	1.707	-1.416
O(82)	-5.329	-1.175	3.704
C(83)	-6.294	-0.062	-1.736
C(84)	-6.316	-2.134	1.201
N(85)	0.770	4.850	3.488
C(86)	1.107	4.207	4.742
C(87)	2.592	3.816	4.520
N(88)	2.979	4.629	3.401
C(89)	1.892	5.207	2.770
N(90)	0.470	2.957	5.006
C(91)	1.279	1.876	4.705
N(92)	2.512	2.390	4.278
O(93)	1.930	5.914	1.785
O(94)	1.007	0.711	4.852
C(95)	-0.497	5.478	3.227
C(96)	-0.804	2.810	5.653
H(97)	7.757	-0.003	-1.239
H(98)	6.798	-1.149	-3.185
H(99)	4.521	-3.135	-4.883
H(100)	2.563	-4.594	-5.153
H(101)	-2.601	4.866	4.865
H(102)	-4.527	4.267	3.452
H(103)	-7.201	-2.728	-1.348
H(104)	-5.856	-4.565	-2.271
H(105)	-0.619	-5.612	-4.898
H(106)	-2.830	-5.879	-3.862
H(107)	-6.050	2.438	4.221
H(108)	-5.269	0.959	4.866
H(109)	3.637	0.292	-4.227
H(110)	4.956	-0.783	-4.771
H(111)	-3.577	3.505	0.015
H(112)	-4.948	4.026	1.042
H(113)	5.810	-4.340	-1.648
H(114)	6.356	-3.640	-3.205
H(115)	7.384	2.095	1.863
H(116)	6.035	2.832	3.783
H(117)	6.642	-1.474	1.918
H(118)	7.830	-0.294	1.285
H(119)	5.972	3.159	-1.337
H(120)	7.433	2.379	-0.663

H(121)	4.960	5.081	3.793
H(122)	4.296	5.662	2.235
H(123)	4.284	1.880	5.254
H(124)	3.320	0.528	4.580
H(125)	1.434	-6.015	-1.926
H(126)	1.375	-6.327	-3.688
H(127)	0.040	-2.116	-5.894
H(128)	0.592	-3.782	-6.229
H(129)	-2.845	-5.207	-0.317
H(130)	-3.829	-5.901	-1.645
H(131)	-4.539	-2.935	-5.275
H(132)	-4.884	-4.560	-4.607
H(133)	-7.520	0.375	0.676
H(134)	-6.562	2.396	1.691
H(135)	-6.011	0.565	-2.584
H(136)	-7.391	-0.122	-1.677
H(137)	-6.037	-2.723	2.078
H(138)	-7.401	-2.209	1.039
H(139)	0.953	4.900	5.582
H(140)	3.236	4.028	5.386
H(141)	-0.752	6.165	4.047
H(142)	-0.372	6.049	2.304
H(143)	-0.881	3.594	6.422
H(144)	-0.835	1.829	6.131
C(145)	-0.676	1.160	1.111
N(146)	-1.646	0.160	1.022
C(147)	-2.109	-0.444	-0.151
N(148)	-1.338	-0.273	-1.307
C(149)	-0.339	0.639	-1.269
C(150)	-0.031	1.379	-0.163
N(151)	0.541	0.998	-2.256
C(152)	1.361	1.946	-1.755
N(153)	1.033	2.193	-0.501
O(154)	-0.406	1.733	2.151
O(155)	-3.114	-1.120	-0.179
C(156)	1.615	3.224	0.358
C(157)	-1.842	-0.844	-2.555
C(158)	-2.320	-0.215	2.269
H(159)	0.692	0.538	-3.162
H(160)	2.192	2.386	-2.285
H(161)	2.446	3.696	-0.165
H(162)	0.836	3.955	0.574
H(163)	1.956	2.757	1.284
H(164)	-2.217	-1.845	-2.338
H(165)	-2.649	-0.228	-2.960
H(166)	-1.026	-0.915	-3.276

H(167)	-1.587	-0.207	3.075
H(168)	-3.103	0.510	2.486
H(169)	-2.753	-1.207	2.150

A.8 Coordinates of the [CB8-TBR-H]$^+$ inclusion complex

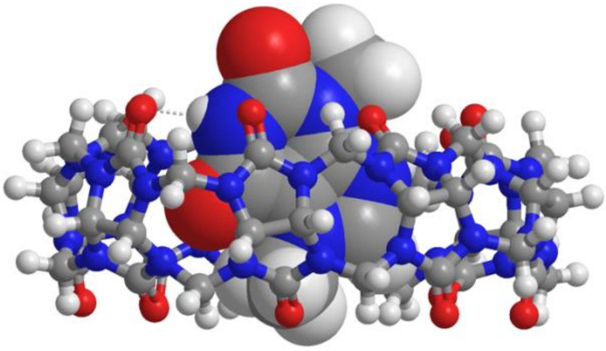

Table A.8. Coordinates of the [CB8-TBR-H]$^+$ inclusion complex in gas phase. The geometry was optimised at the wB97X-D/6-31G* level of theory. Energy = −5454.0728 hartree.

Atom (Centre Nr.)	**Coordinates (Å)**		
	X	**Y**	**Z**
N(1)	4.974	0.168	-1.145
C(2)	5.488	1.178	-0.239
C(3)	5.204	2.475	-1.026
N(4)	5.101	2.024	-2.377
C(5)	4.878	0.656	-2.443
N(6)	4.739	1.354	0.970
C(7)	3.773	2.329	0.830
N(8)	3.961	2.917	-0.418
O(9)	4.678	0.007	-3.443
O(10)	2.937	2.649	1.648
N(11)	4.124	3.668	-3.884
C(12)	3.607	4.769	-3.123
C(13)	2.532	5.380	-4.068
N(14)	2.334	4.313	-5.022
C(15)	3.293	3.317	-4.934
N(16)	2.825	4.412	-1.948
C(17)	1.546	4.953	-2.002
N(18)	1.426	5.637	-3.191
O(19)	3.412	2.367	-5.669
O(20)	0.695	4.855	-1.140

N(21)	-2.243	-5.195	3.726
C(22)	-2.607	-4.477	4.927
C(23)	-3.809	-3.620	4.445
N(24)	-4.202	-4.275	3.231
C(25)	-3.240	-5.159	2.767
N(26)	-1.675	-3.498	5.394
C(27)	-1.999	-2.218	4.982
N(28)	-3.221	-2.300	4.315
O(29)	-3.295	-5.816	1.756
O(30)	-1.376	-1.210	5.215
N(31)	-4.488	0.076	-1.887
C(32)	-5.148	1.346	-1.788
C(33)	-4.539	2.164	-2.949
N(34)	-3.307	1.438	-3.202
C(35)	-3.355	0.151	-2.669
N(36)	-4.785	2.149	-0.639
C(37)	-4.500	3.458	-1.008
N(38)	-4.387	3.470	-2.393
O(39)	-2.561	-0.738	-2.895
O(40)	-4.412	4.412	-0.273
N(41)	-0.050	3.977	-5.300
C(42)	-1.049	4.988	-5.100
C(43)	-2.323	4.165	-4.767
N(44)	-1.758	2.873	-4.385
C(45)	-0.416	2.797	-4.706
N(46)	-0.891	5.775	-3.898
C(47)	-2.026	5.775	-3.101
N(48)	-2.929	4.914	-3.708
O(49)	0.315	1.834	-4.512
O(50)	-2.212	6.440	-2.112
C(51)	-5.371	-3.970	2.460
C(52)	3.439	4.235	-0.652
C(53)	-4.013	-1.106	4.189
C(54)	5.260	2.863	-3.531
N(55)	4.665	-1.794	0.233
C(56)	5.224	-1.677	1.546
C(57)	4.708	-2.943	2.273
N(58)	3.582	-3.333	1.440
C(59)	3.656	-2.742	0.186
N(60)	4.668	-0.617	2.360
C(61)	4.332	-1.080	3.631
N(62)	4.406	-2.461	3.584
O(63)	2.999	-3.024	-0.792
O(64)	4.083	-0.396	4.594
C(65)	5.251	-1.237	-0.950
C(66)	5.086	0.753	2.228

C(67)	4.136	-3.287	4.731
C(68)	2.944	-4.619	1.585
C(69)	1.237	4.196	-5.928
C(70)	0.292	6.479	-3.508
C(71)	-2.549	1.664	-4.397
C(72)	-4.237	4.677	-3.157
N(73)	-5.019	0.630	1.225
C(74)	-5.693	-0.593	0.906
C(75)	-5.537	-1.440	2.192
N(76)	-4.413	-0.788	2.840
C(77)	-4.197	0.484	2.333
N(78)	-5.023	-1.423	-0.074
C(79)	-4.948	-2.747	0.350
N(80)	-5.312	-2.758	1.686
O(81)	-3.463	1.334	2.790
O(82)	-4.671	-3.700	-0.337
C(83)	-5.354	1.906	0.669
C(84)	-5.093	-1.166	-1.487
N(85)	0.685	-4.037	5.386
C(86)	0.972	-5.268	4.686
C(87)	2.346	-4.959	4.033
N(88)	2.819	-3.848	4.797
C(89)	1.812	-3.251	5.545
N(90)	0.141	-5.572	3.559
C(91)	0.699	-5.153	2.375
N(92)	1.978	-4.696	2.648
O(93)	1.926	-2.276	6.248
O(94)	0.182	-5.244	1.277
C(95)	-0.496	-3.785	6.164
C(96)	-1.177	-6.148	3.633
H(97)	6.551	1.015	-0.013
H(98)	5.986	3.241	-0.927
H(99)	4.408	5.469	-2.854
H(100)	2.850	6.304	-4.566
H(101)	-2.861	-5.177	5.736
H(102)	-4.648	-3.599	5.155
H(103)	-6.237	1.215	-1.861
H(104)	-5.165	2.193	-3.852
H(105)	-1.142	5.619	-5.991
H(106)	-3.012	4.047	-5.613
H(107)	-6.236	-3.907	3.131
H(108)	-5.508	-4.794	1.757
H(109)	2.680	4.420	0.111
H(110)	4.247	4.979	-0.543
H(111)	-3.404	-0.273	4.548
H(112)	-4.916	-1.199	4.816

H(113)	5.458	2.213	-4.386
H(114)	6.121	3.522	-3.361
H(115)	6.321	-1.613	1.495
H(116)	5.444	-3.757	2.324
H(117)	4.845	-1.764	-1.815
H(118)	6.340	-1.398	-0.906
H(119)	4.596	1.310	3.029
H(120)	6.178	0.836	2.349
H(121)	4.870	-4.102	4.751
H(122)	4.257	-2.657	5.614
H(123)	3.720	-5.386	1.747
H(124)	2.421	-4.831	0.649
H(125)	1.474	3.345	-6.571
H(126)	1.137	5.096	-6.545
H(127)	0.013	7.056	-2.623
H(128)	0.618	7.167	-4.298
H(129)	-1.873	0.816	-4.517
H(130)	-3.227	1.705	-5.266
H(131)	-4.451	5.511	-2.485
H(132)	-4.964	4.666	-3.979
H(133)	-6.738	-0.398	0.627
H(134)	-6.420	-1.427	2.846
H(135)	-4.970	2.685	1.330
H(136)	-6.452	1.986	0.619
H(137)	-4.571	-1.986	-1.985
H(138)	-6.142	-1.152	-1.824
H(139)	0.993	-6.120	5.379
H(140)	3.057	-5.795	4.084
H(141)	-0.719	-4.646	6.809
H(142)	-0.268	-2.914	6.783
H(143)	-1.190	-6.826	4.497
H(144)	-1.356	-6.718	2.719
C(145)	0.012	-1.786	0.626
N(146)	-0.007	-2.839	-0.278
C(147)	0.208	-2.840	-1.654
N(148)	0.399	-1.571	-2.235
C(149)	0.337	-0.487	-1.436
C(150)	0.162	-0.522	-0.078
N(151)	0.452	0.830	-1.797
C(152)	0.355	1.583	-0.676
N(153)	0.184	0.788	0.368
O(154)	-0.091	-1.939	1.829
O(155)	0.225	-3.852	-2.308
C(156)	-0.002	1.212	1.763
C(157)	0.678	-1.451	-3.659
H(158)	-0.058	-3.774	0.137

H(159)	0.515	1.189	-2.759
H(160)	0.407	2.666	-0.646
H(161)	0.419	2.211	1.875
H(162)	-1.066	1.200	2.006
H(163)	0.525	0.510	2.406
H(164)	0.721	-2.463	-4.058
H(165)	-0.125	-0.896	-4.148
H(166)	1.639	-0.953	-3.814

A.9 Coordinates of the [CB8-TPH-H]$^+$ inclusion complex

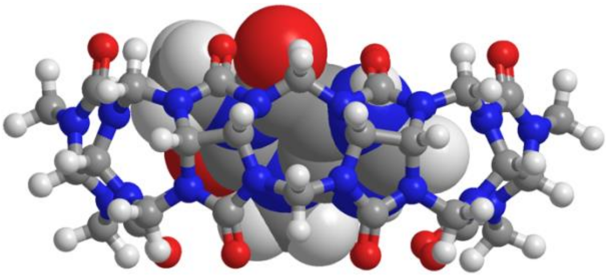

Table A.9. Coordinates of the [CB8-TPH-H]$^+$ inclusion complex in gas phase. The geometry was optimised at the wB97X-D/6-31G* level of theory. Energy = −5454.0750 hartree.

Atom (Centre Nr.)	**Coordinates (Å)**		
	X	**Y**	**Z**
N(1)	0.462	5.739	-1.080
C(2)	-0.685	6.181	-0.316
C(3)	-1.864	5.665	-1.178
N(4)	-1.260	5.458	-2.460
C(5)	0.119	5.440	-2.397
N(6)	-0.872	5.516	0.934
C(7)	-1.742	4.441	0.825
N(8)	-2.274	4.466	-0.465
O(9)	0.889	5.243	-3.307
O(10)	-2.011	3.653	1.701
N(11)	-2.657	4.042	-3.847
C(12)	-3.864	3.664	-3.179
C(13)	-4.368	2.463	-4.019
N(14)	-3.173	2.074	-4.737
C(15)	-2.208	3.059	-4.719
N(16)	-3.698	3.075	-1.860
C(17)	-4.411	1.875	-1.762

N(18)	-4.852	1.554	-3.026
O(19)	-1.185	3.096	-5.363
O(20)	-4.645	1.278	-0.735
N(21)	4.795	-2.145	3.354
C(22)	4.021	-2.521	4.515
C(23)	3.218	-3.744	3.997
N(24)	3.953	-4.141	2.837
C(25)	4.859	-3.182	2.423
N(26)	2.992	-1.596	4.887
C(27)	1.781	-1.925	4.321
N(28)	1.892	-3.181	3.758
O(29)	5.603	-3.245	1.476
O(30)	0.781	-1.224	4.354
N(31)	-0.197	-5.630	-2.252
C(32)	-1.552	-6.073	-2.114
C(33)	-2.300	-5.272	-3.215
N(34)	-1.363	-4.209	-3.523
C(35)	-0.089	-4.499	-3.043
N(36)	-2.242	-5.659	-0.911
C(37)	-3.464	-5.064	-1.192
N(38)	-3.514	-4.878	-2.562
O(39)	0.931	-3.908	-3.306
O(40)	-4.336	-4.802	-0.397
N(41)	-3.175	-0.303	-5.215
C(42)	-4.368	-1.035	-4.929
C(43)	-3.854	-2.492	-4.766
N(44)	-2.429	-2.308	-4.583
C(45)	-2.028	-1.025	-4.941
N(46)	-4.998	-0.788	-3.649
C(47)	-5.222	-1.954	-2.942
N(48)	-4.584	-2.971	-3.629
O(49)	-0.890	-0.634	-5.069
O(50)	-5.895	-2.075	-1.942
C(51)	3.802	-5.402	2.158
C(52)	-3.586	3.888	-0.677
C(53)	0.712	-4.025	3.679
C(54)	-1.983	5.294	-3.694
N(55)	2.385	5.541	0.382
C(56)	2.225	5.989	1.737
C(57)	3.363	5.245	2.484
N(58)	3.625	4.128	1.580
C(59)	3.051	4.347	0.339
N(60)	1.051	5.478	2.417
C(61)	1.371	4.967	3.669
N(62)	2.759	4.905	3.733
O(63)	3.126	3.592	-0.620

O(64)	0.600	4.672	4.547
C(65)	1.799	6.160	-0.782
C(66)	-0.295	5.946	2.175
C(67)	3.439	4.349	4.872
C(68)	4.809	3.303	1.685
C(69)	-3.131	1.032	-5.730
C(70)	-5.691	0.417	-3.299
C(71)	-1.493	-3.393	-4.704
C(72)	-4.675	-4.344	-3.221
N(73)	-0.809	-5.834	1.030
C(74)	0.488	-6.394	0.821
C(75)	1.307	-5.838	2.013
N(76)	0.520	-4.681	2.414
C(77)	-0.793	-4.797	1.942
N(78)	1.237	-5.897	-0.316
C(79)	2.534	-5.556	0.040
N(80)	2.581	-5.561	1.428
O(81)	-1.745	-4.151	2.307
O(82)	3.462	-5.346	-0.703
C(83)	-2.014	-6.260	0.375
C(84)	0.946	-6.277	-1.676
N(85)	3.593	0.744	5.008
C(86)	4.957	0.950	4.551
C(87)	4.892	2.413	4.055
N(88)	3.782	2.954	4.779
C(89)	2.973	1.955	5.301
N(90)	5.340	0.220	3.381
C(91)	5.097	0.939	2.229
N(92)	4.683	2.221	2.626
O(93)	1.943	2.106	5.912
O(94)	5.228	0.563	1.090
C(95)	3.178	-0.441	5.716
C(96)	5.821	-1.140	3.372
H(97)	-0.677	7.271	-0.180
H(98)	-2.699	6.375	-1.255
H(99)	-4.570	4.506	-3.144
H(100)	-5.174	2.720	-4.720
H(101)	4.668	-2.744	5.375
H(102)	3.152	-4.569	4.720
H(103)	-1.613	-7.163	-2.242
H(104)	-2.525	-5.862	-4.115
H(105)	-5.094	-0.911	-5.745
H(106)	-4.051	-3.128	-5.641
H(107)	3.882	-6.208	2.899
H(108)	4.623	-5.476	1.441
H(109)	-3.803	3.244	0.178

H(110)	-4.329	4.703	-0.715
H(111)	-0.163	-3.391	3.843
H(112)	0.775	-4.775	4.487
H(113)	-1.254	5.371	-4.503
H(114)	-2.716	6.108	-3.775
H(115)	2.289	7.083	1.794
H(116)	4.271	5.844	2.630
H(117)	2.406	5.903	-1.654
H(118)	1.841	7.246	-0.619
H(119)	-0.902	5.554	2.993
H(120)	-0.321	7.045	2.196
H(121)	4.355	4.923	5.050
H(122)	2.766	4.456	5.725
H(123)	5.663	3.942	1.959
H(124)	4.992	2.855	0.705
H(125)	-2.188	1.162	-6.266
H(126)	-3.970	1.152	-6.430
H(127)	-6.262	0.189	-2.396
H(128)	-6.381	0.706	-4.105
H(129)	-0.511	-2.954	-4.902
H(130)	-1.786	-4.032	-5.555
H(131)	-5.502	-4.412	-2.511
H(132)	-4.889	-4.961	-4.103
H(133)	0.430	-7.492	0.799
H(134)	1.408	-6.549	2.847
H(135)	-2.862	-5.976	1.003
H(136)	-1.976	-7.355	0.280
H(137)	1.825	-6.005	-2.266
H(138)	0.786	-7.364	-1.737
H(139)	5.678	0.786	5.364
H(140)	5.806	2.990	4.246
H(141)	3.915	-0.703	6.489
H(142)	2.227	-0.197	6.194
H(143)	6.468	-1.263	4.252
H(144)	6.412	-1.288	2.465
C(145)	-1.419	-0.613	1.123
N(146)	-1.952	-0.701	-0.172
C(147)	-1.605	0.087	-1.268
N(148)	-0.493	0.940	-1.140
C(149)	0.133	0.991	0.061
C(150)	-0.282	0.282	1.151
N(151)	1.256	1.684	0.442
C(152)	1.512	1.392	1.735
N(153)	0.593	0.553	2.175
O(154)	-1.836	-1.225	2.078
O(155)	-2.218	0.043	-2.313

C(156)	-0.156	1.803	-2.273
C(157)	-3.056	-1.643	-0.389
H(158)	1.867	2.275	-0.134
H(159)	2.353	1.780	2.293
H(160)	0.560	0.096	3.100
H(161)	-0.818	2.673	-2.282
H(162)	0.882	2.132	-2.194
H(163)	-0.280	1.237	-3.197
H(164)	-3.077	-2.335	0.451
H(165)	-4.002	-1.104	-0.459
H(166)	-2.870	-2.180	-1.322

A.10 Binding energies of the [CB-MeX-H]$^+$ inclusion complexes

Table A.10. Binding energies, in kcal mol^{-1}, of the [CB-MeX-H]$^+$ inclusion complexes, optimised at the wB97X-D/6-31G* level of theory.

Structure	**Energy/ Hartree**	**Energy / kcal mol^{-1}**	**Binding energy / kcal mol^{-1}**
CB7	-4211.1343	-2642524.6517	
CB8	-4812.7175	-3020023.5319	
[CAF-H]$^+$	-680.5313	-427039.5438	
[TBR-H]$^+$	-641.2288	-402376.8512	
[TPH-H]$^+$	-641.2215	-402372.2503	
[CB7-CAF-H]$^+$	-4891.8067	-3069652.7048	-88.5093
[CB7-TBR-H]$^+$	-4852.5047	-3044990.3687	-88.8658
[CB7-TPH-H]$^+$	-4852.4856	-3044978.3738	-81.4718
[CB8-CAF-H]$^+$	-5493.3988	-3447157.1832	-94.1075
[CB8-TBR-H]$^+$	-5454.0728	-3422479.7843	-79.4012
[CB8-TPH-H]$^+$	-5454.0750	-3422481.1624	-85.3801

A.11 Coordinates of the [CB7-CRN-H]$^+$ inclusion complex

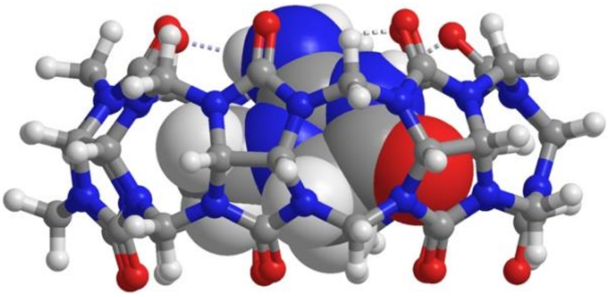

Table A.11. Coordinates of the [CB7-CRN-H]$^+$ inclusion complex in water. The geometry was optimised at the CPCM/wB97X-D/6-31G* level of theory. Energy = −4607.8120 hartree.

Atom (Centre Nr.)	Coordinates (Å)		
	X	Y	Z
N(1)	0.026	4.901	1.316
C(2)	0.581	5.635	0.209
C(3)	2.099	5.31	0.287
N(4)	2.168	4.295	1.316
C(5)	0.954	4.102	1.944
N(6)	0.207	5.145	-1.101
C(7)	1.301	4.769	-1.853
N(8)	2.412	4.859	-1.044
O(9)	0.748	3.381	2.905
O(10)	1.288	4.452	-3.029
N(11)	4.141	2.897	1.263
C(12)	5.015	3.186	0.141
C(13)	5.748	1.835	-0.063
N(14)	5.477	1.119	1.153
C(15)	4.51	1.734	1.915
N(16)	4.356	3.4	-1.118
C(17)	4.38	2.28	-1.919
N(18)	5.106	1.314	-1.254
O(19)	4.085	1.356	2.992
O(20)	3.885	2.177	-3.027
N(21)	-5.588	1.366	1.076
C(22)	-6.007	0.908	-0.223
C(23)	-6.092	-0.636	-0.046
N(24)	-5.409	-0.846	1.218
C(25)	-5.21	0.334	1.905
N(26)	-5.015	1.051	-1.278
C(27)	-4.675	-0.155	-1.835

N(28)	-5.393	-1.136	-1.202
O(29)	-4.798	0.438	3.046
O(30)	-3.868	-0.33	-2.742
N(31)	0.15	-4.502	1.318
C(32)	0.452	-5.42	0.238
C(33)	1.972	-5.207	0.03
N(34)	2.376	-4.481	1.202
C(35)	1.298	-4.027	1.929
N(36)	-0.117	-5.045	-1.029
C(37)	0.782	-4.368	-1.814
N(38)	2.007	-4.436	-1.198
O(39)	1.341	-3.352	2.942
O(40)	0.54	-3.81	-2.88
N(41)	5.56	-1.314	1.047
C(42)	5.748	-1.83	-0.287
C(43)	4.981	-3.191	-0.252
N(44)	4.482	-3.255	1.098
C(45)	4.825	-2.155	1.851
N(46)	5.078	-1.105	-1.346
C(47)	4.009	-1.786	-1.851
N(48)	3.969	-3.027	-1.27
O(49)	4.582	-1.995	3.034
O(50)	3.225	-1.387	-2.709
C(51)	-5.285	-2.119	1.882
C(52)	3.75	4.64	-1.528
C(53)	-5.327	-2.517	-1.605
C(54)	3.407	3.924	1.954
N(55)	-2.349	4.445	1.168
C(56)	-2.923	4.94	-0.07
C(57)	-4.182	4.053	-0.233
N(58)	-4.342	3.457	1.063
C(59)	-3.247	3.666	1.874
N(60)	-2.164	4.66	-1.257
C(61)	-2.652	3.577	-1.95
N(62)	-3.789	3.138	-1.29
O(63)	-3.109	3.269	3.017
O(64)	-2.192	3.108	-2.975
C(65)	-1.286	5.137	1.855
C(66)	-1.057	5.454	-1.72
C(67)	-4.742	2.293	-1.96
C(68)	-5.517	2.745	1.491
C(69)	6.142	-0.098	1.549
C(70)	5.554	0.124	-1.925
C(71)	3.746	-4.359	1.648
C(72)	3.235	-4.108	-1.87
N(73)	-2.505	-4.633	-0.971

C(74)	-3.002	-4.681	0.379
C(75)	-4.317	-3.859	0.301
N(76)	-4.24	-3.251	-1.012
C(77)	-3.233	-3.796	-1.781
N(78)	-2.212	-3.952	1.355
C(79)	-2.965	-2.986	2
N(80)	-4.204	-2.943	1.403
O(81)	-3.037	-3.586	-2.966
O(82)	-2.598	-2.306	2.943
C(83)	-1.428	-5.439	-1.474
C(84)	-1.095	-4.561	2.041
H(85)	0.352	6.702	0.301
H(86)	2.721	6.17	0.556
H(87)	5.682	4.023	0.374
H(88)	6.828	1.933	-0.218
H(89)	-6.951	1.377	-0.516
H(90)	-7.113	-1.027	-0.012
H(91)	0.174	-6.446	0.5
H(92)	2.547	-6.132	-0.075
H(93)	6.814	-1.927	-0.515
H(94)	5.61	-4.059	-0.476
H(95)	-6.217	-2.685	1.78
H(96)	-5.104	-1.907	2.936
H(97)	3.702	4.64	-2.618
H(98)	4.388	5.463	-1.19
H(99)	-5.182	-2.55	-2.686
H(100)	-6.281	-2.99	-1.353
H(101)	3.17	3.539	2.947
H(102)	4.034	4.821	2.051
H(103)	-3.14	6.011	0.005
H(104)	-5.083	4.608	-0.518
H(105)	-1.293	4.789	2.889
H(106)	-1.478	6.217	1.833
H(107)	-0.94	5.277	-2.789
H(108)	-1.3	6.509	-1.549
H(109)	-4.328	2.049	-2.939
H(110)	-5.688	2.836	-2.091
H(111)	-5.527	2.754	2.581
H(112)	-6.4	3.269	1.113
H(113)	6.106	-0.157	2.637
H(114)	7.185	-0.035	1.222
H(115)	5.188	0.18	-2.951
H(116)	6.65	0.093	-1.933
H(117)	3.736	-4.22	2.729
H(118)	4.258	-5.296	1.406
H(119)	3.881	-4.994	-1.892

H(120)	2.979	-3.822	-2.891
H(121)	-3.149	-5.718	0.699
H(122)	-5.224	-4.465	0.393
H(123)	-1.452	-5.364	-2.561
H(124)	-1.589	-6.48	-1.176
H(125)	-1.339	-5.61	2.258
H(126)	-0.951	-4.022	2.978
C(127)	0.178	-0.343	0.99
C(128)	1.387	-0.834	0.216
N(129)	0.891	-1.325	-0.986
C(130)	-0.454	-1.097	-1.078
N(131)	-0.902	-0.521	0.032
C(132)	-2.283	-0.192	0.32
N(133)	-1.16	-1.432	-2.137
O(134)	2.546	-0.808	0.546
H(135)	0.299	0.701	1.291
H(136)	0.015	-0.965	1.877
H(137)	-2.934	-0.975	-0.076
H(138)	-2.556	0.778	-0.106
H(139)	-2.412	-0.165	1.403
H(140)	1.501	-1.535	-1.783
H(141)	-2.136	-1.156	-2.264
H(142)	-0.768	-2.115	-2.781
H(143)	-1.279	-1.185	-1.82

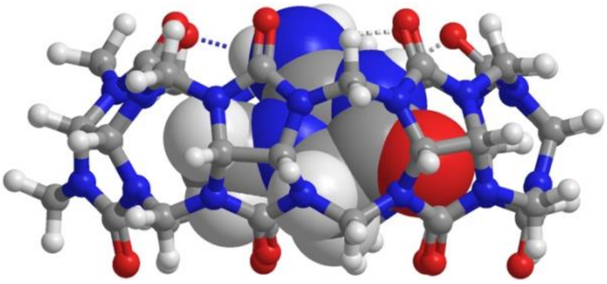

Table A.12. Coordinates of the [CB7-CRN-H]$^+$ inclusion complex in gas phase. The geometry is optimised at the wB97X-D/6-31G* level of theory. Energy = −4607.6597 hartree.

Atom (Centre Nr.)	**Coordinates (Å)**		
	X	**Y**	**Z**
N(1)	-0.907	4.745	1.359
C(2)	-0.428	5.585	0.3
C(3)	1.119	5.429	0.395

N(4)	1.284	4.315	1.305
C(5)	0.083	3.938	1.888
N(6)	-0.715	5.127	-1.039
C(7)	0.433	5.001	-1.812
N(8)	1.51	5.192	-0.965
O(9)	-0.069	3.085	2.735
O(10)	0.476	4.814	-3.005
N(11)	3.486	3.309	1.285
C(12)	4.297	3.871	0.226
C(13)	5.319	2.734	-0.031
N(14)	5.26	1.962	1.171
C(15)	4.135	2.255	1.925
N(16)	3.651	4.028	-1.044
C(17)	3.889	2.954	-1.887
N(18)	4.78	2.118	-1.226
O(19)	3.808	1.742	2.967
O(20)	3.449	2.801	-3.001
N(21)	-5.866	0.445	0.993
C(22)	-6.094	-0.106	-0.311
C(23)	-5.883	-1.635	-0.092
N(24)	-5.165	-1.667	1.165
C(25)	-5.274	-0.462	1.855
N(26)	-5.09	0.2	-1.317
C(27)	-4.529	-0.935	-1.85
N(28)	-5.124	-2.021	-1.248
O(29)	-4.946	-0.266	2.999
O(30)	-3.669	-0.981	-2.714
N(31)	0.963	-4.298	1.294
C(32)	1.39	-5.233	0.275
C(33)	2.861	-4.808	0.035
N(34)	3.184	-4.047	1.203
C(35)	2.053	-3.668	1.902
N(36)	0.776	-5.039	-1.008
C(37)	1.525	-4.194	-1.802
N(38)	2.751	-4.048	-1.195
O(39)	2.003	-2.958	2.877
O(40)	1.173	-3.691	-2.855
N(41)	5.817	-0.405	0.999
C(42)	6.037	-0.865	-0.345
C(43)	5.505	-2.338	-0.307
N(44)	5.064	-2.498	1.049
C(45)	5.256	-1.363	1.825
N(46)	5.24	-0.258	-1.389
C(47)	4.275	-1.097	-1.872
N(48)	4.463	-2.337	-1.304
O(49)	5.053	-1.27	3.01

O(50)	3.417	-0.832	-2.701
C(51)	-4.814	-2.867	1.882
C(52)	2.868	5.167	-1.44
C(53)	-4.771	-3.368	-1.61
C(54)	2.521	4.083	2.013
N(55)	-3.201	3.979	1.163
C(56)	-3.807	4.412	-0.079
C(57)	-4.891	3.325	-0.303
N(58)	-5.056	2.751	0.998
C(59)	-4.021	3.099	1.857
N(60)	-2.991	4.306	-1.253
C(61)	-3.207	3.127	-1.936
N(62)	-4.266	2.475	-1.298
O(63)	-3.888	2.737	3.001
O(64)	-2.626	2.739	-2.922
C(65)	-2.241	4.774	1.888
C(66)	-2.001	5.268	-1.666
C(67)	-4.997	1.464	-2.008
C(68)	-6.083	1.82	1.376
C(69)	6.161	0.894	1.512
C(70)	5.443	1.062	-1.931
C(71)	4.524	-3.695	1.617
C(72)	3.89	-3.511	-1.894
N(73)	-1.656	-4.983	-0.924
C(74)	-2.115	-5.028	0.436
C(75)	-3.556	-4.45	0.341
N(76)	-3.577	-3.866	-0.983
C(77)	-2.499	-4.273	-1.753
N(78)	-1.457	-4.12	1.352
C(79)	-2.37	-3.283	1.988
N(80)	-3.613	-3.522	1.429
O(81)	-2.345	-4.072	-2.937
O(82)	-2.122	-2.505	2.881
C(83)	-0.469	-5.621	-1.422
C(84)	-0.246	-4.489	2.051
H(85)	-0.778	6.617	0.443
H(86)	1.627	6.32	0.79
H(87)	4.758	4.818	0.541
H(88)	6.344	3.09	-0.207
H(89)	-7.095	0.156	-0.675
H(90)	-6.816	-2.209	-0.035
H(91)	1.272	-6.273	0.608
H(92)	3.558	-5.647	-0.088
H(93)	7.1	-0.788	-0.606
H(94)	6.267	-3.087	-0.561
H(95)	-5.636	-3.594	1.824

H(96)	-4.661	-2.57	2.922
H(97)	2.816	5.167	-2.531
H(98)	3.382	6.073	-1.093
H(99)	-4.593	-3.394	-2.687
H(100)	-5.625	-4.013	-1.365
H(101)	2.288	3.522	2.922
H(102)	2.954	5.06	2.287
H(103)	-4.212	5.429	0.014
H(104)	-5.846	3.723	-0.675
H(105)	-2.213	4.371	2.904
H(106)	-2.57	5.823	1.918
H(107)	-1.837	5.143	-2.739
H(108)	-2.409	6.27	-1.47
H(109)	-4.468	1.286	-2.948
H(110)	-6.017	1.819	-2.22
H(111)	-6.142	1.837	2.466
H(112)	-7.035	2.153	0.948
H(113)	6.165	0.799	2.6
H(114)	7.163	1.172	1.162
H(115)	5.05	1.071	-2.95
H(116)	6.527	1.246	-1.955
H(117)	4.508	-3.537	2.697
H(118)	5.173	-4.548	1.379
H(119)	4.669	-4.285	-1.954
H(120)	3.551	-3.256	-2.9
H(121)	-2.079	-6.057	0.819
H(122)	-4.345	-5.209	0.44
H(123)	-0.52	-5.565	-2.511
H(124)	-0.472	-6.672	-1.107
H(125)	-0.323	-5.545	2.361
H(126)	-0.173	-3.856	2.938
C(127)	0.371	-0.197	1.005
C(128)	1.622	-0.517	0.206
N(129)	1.173	-1.131	-0.968
C(130)	-0.19	-1.094	-1.034
N(131)	-0.695	-0.55	0.07
C(132)	-2.108	-0.4	0.361
N(133)	-0.864	-1.576	-2.059
O(134)	2.772	-0.305	0.482
H(135)	0.34	0.855	1.307
H(136)	0.327	-0.823	1.905
H(137)	-2.645	-1.292	0.027
H(138)	-2.522	0.485	-0.132
H(139)	-2.237	-0.312	1.441
H(140)	1.787	-1.228	-1.786
H(141)	-1.858	-1.398	-2.217

H(142)	-0.375	-2.153	-2.739
H(143)	-0.997	-1.226	-1.788

A.12 Binding energies of the [CB7-CRN-H]$^+$ inclusion complexes

Table A.13. Binding energies, in kcal mol^{-1}, of the [CB7-CRN-H]$^+$ inclusion complexes in gas phase and in water, optimised at the wB97X-D/6-31G* level of theory.

Structure	**Water model**	**Energy/ Hartree**	**Energy / kcal mol^{-1}**	**Binding energy / kcal mol^{-1}**
CB7		-4211.134	-2642524.652	
[CRN-H]$^+$		-396.390	-248738.298	
[CB7-CRN-H]$^+$		-4607.660	-2891347.954	-85.004
CB7	CPCM	-4211.273	-2642611.447	
[CRN-H]$^+$	CPCM	-396.482	-248795.928	
[CB7-CRN-H]$^+$	CPCM	-4607.812	-2891443.496	-36.121